

**A NUMERICAL INVESTIGATION OF METABOLIC
REDUCTIVE DECHLORINATION IN
DNAPL SOURCE ZONES**

by

John Anthony Christ

A dissertation submitted in partial fulfillment
of the requirements for the degree of
Doctor of Philosophy
(Environmental Engineering)
in The University of Michigan
2005

Doctoral Committee:

Professor Linda M. Abriola, Chair

Professor Peter Adriaens

Associate Professor Avery H. Demond

Assistant Professor Maria Cruz Da Silva Castro

Associate Professor Frank E. Löffler, Georgia Institute of Technology

20050722 063

“Twenty years from now you will be more disappointed by the things you didn't do than by the ones you did do. So throw off the bowlines. Sail away from the safe harbor. Catch the trade winds in your sails. Explore. Dream. Discover.”

- Mark Twain

JUL 18 2005

REPORT DOCUMENTATION PAGE

Form Approved
OMB No. 0704-0188

Public reporting burden for this collection of information is estimated to average 1 hour per response, including the time for reviewing instructions, searching existing data sources, gathering and maintaining the data needed, and completing and reviewing the collection of information. Send comments regarding this burden estimate or any other aspect of this collection of information, including suggestions for reducing this burden, to Washington Headquarters Services, Directorate for Information Operations and Reports, 1215 Jefferson Davis Highway, Suite 1204, Arlington, VA 22202-4302, and to the Office of Management and Budget, Paperwork Reduction Project (0704-0188), Washington, DC 20503.

1. AGENCY USE ONLY (Leave blank)		2. REPORT DATE 13.Jul.05	3. REPORT TYPE AND DATES COVERED DISSERTATION	
4. TITLE AND SUBTITLE A NUMERICAL INVESTIGATION OF METABOLIC REDUCTIVE DECHLORINATION IN DNAPL SOURCE ZONES			5. FUNDING NUMBERS	
6. AUTHOR(S) CAPT CHRIST JOHN A				
7. PERFORMING ORGANIZATION NAME(S) AND ADDRESS(ES) UNIVERSITY OF MICHIGAN			8. PERFORMING ORGANIZATION REPORT NUMBER CI04-1134	
9. SPONSORING/MONITORING AGENCY NAME(S) AND ADDRESS(ES) THE DEPARTMENT OF THE AIR FORCE AFIT/CIA, BLDG 125 2950 P STREET WPAFB OH 45433			10. SPONSORING/MONITORING AGENCY REPORT NUMBER	
11. SUPPLEMENTARY NOTES				
12a. DISTRIBUTION AVAILABILITY STATEMENT Unlimited distribution In Accordance With AFI 35-205/AFIT Sup 1			12b. DISTRIBUTION CODE DISTRIBUTION STATEMENT A Approved for Public Release Distribution Unlimited	
13. ABSTRACT (Maximum 200 words)				
14. SUBJECT TERMS			15. NUMBER OF PAGES 291	
			16. PRICE CODE	
17. SECURITY CLASSIFICATION OF REPORT	18. SECURITY CLASSIFICATION OF THIS PAGE	19. SECURITY CLASSIFICATION OF ABSTRACT	20. LIMITATION OF ABSTRACT	

ABSTRACT

A NUMERICAL INVESTIGATION OF METABOLIC REDUCTIVE DECHLORINATION IN DNAPL SOURCE ZONES

by

John Anthony Christ

Chair: Linda M. Abriola

Among the most intractable environmental remediation problems are those involving the release of dense non-aqueous phase liquids (DNAPLs), such as chlorinated solvents, to the subsurface. Research efforts have focused on the use of numerical models to investigate reductions in contaminant concentrations due to partial mass removal and improvements in the performance of complementary source zone remediation technologies. Previous numerical investigations, however, have been limited to two-dimensional systems. Furthermore, a lack of models capable of simulating the most promising complementary technology, metabolic reductive dechlorination, has limited its application. This work developed and applied compositional multiphase numerical simulators to examine the influence of dimensionality (two-dimensions versus three-dimensions) on DNAPL source zone simulations and to investigate the benefits of stimulating metabolic reductive dechlorination at a chlorinated ethene-DNAPL contaminated site.

Results from the dimensionality investigation showed that the simulation of DNAPL migration, entrapment, and dissolution in two dimensions provided reasonable approximations to the behavior simulated in three dimensions. Commonly employed

saturation distribution and mass recovery metrics were approximately equivalent. Flux-averaged concentrations simulated in two dimensions, however, tended to be three to four times higher than those simulated in three dimensions. This difference was attributed to dilution at the down gradient boundary. An alternative metric, mass flux reduction, however, yielded better agreement.

To investigate the application of complementary mass removal technologies, an existing multiphase compositional simulator was modified to incorporate eight chemical components and four microbial populations: a fermentative population, two dechlorinating populations, and a competitor population. Monod kinetics, modified to incorporate electron donor thresholds, electron acceptor competition, and competitor inhibition, were used to simulate microbial growth and component degradation. This simulator was used to explore enhancements in DNAPL dissolution due to metabolic reductive dechlorination in one- and two-dimensional non-uniformly contaminated domains. Simulation results demonstrated the potential for this technology to accelerate interphase mass transfer. The level of enhancement was affected by the dechlorination rate, DNAPL zone length, and DNAPL zone configuration. The length of time dissolution enhancement persisted at the quasi-steady-state value (maximum), however, was generally less than 50 percent of the longevity of the source.

ABSTRACT

A NUMERICAL INVESTIGATION OF METABOLIC REDUCTIVE DECHLORINATION IN DNAPL SOURCE ZONES

by

John Anthony Christ

Chair: Linda M. Abriola

Among the most intractable environmental remediation problems are those involving the release of dense non-aqueous phase liquids (DNAPLs), such as chlorinated solvents, to the subsurface. Research efforts have focused on the use of numerical models to investigate reductions in contaminant concentrations due to partial mass removal and improvements in the performance of complementary source zone remediation technologies. Previous numerical investigations, however, have been limited to two-dimensional systems. Furthermore, a lack of models capable of simulating the most promising complementary technology, metabolic reductive dechlorination, has limited its application. This work developed and applied compositional multiphase numerical simulators to examine the influence of dimensionality (two-dimensions versus three-dimensions) on DNAPL source zone simulations and to investigate the benefits of stimulating metabolic reductive dechlorination at a chlorinated ethene-DNAPL contaminated site.

Results from the dimensionality investigation showed that the simulation of DNAPL migration, entrapment, and dissolution in two dimensions provided reasonable approximations to the behavior simulated in three dimensions. Commonly employed

saturation distribution and mass recovery metrics were approximately equivalent. Flux-averaged concentrations simulated in two dimensions, however, tended to be three to four times higher than those simulated in three dimensions. This difference was attributed to dilution at the down gradient boundary. An alternative metric, mass flux reduction, however, yielded better agreement.

To investigate the application of complementary mass removal technologies, an existing multiphase compositional simulator was modified to incorporate eight chemical components and four microbial populations: a fermentative population, two dechlorinating populations, and a competitor population. Monod kinetics, modified to incorporate electron donor thresholds, electron acceptor competition, and competitor inhibition, were used to simulate microbial growth and component degradation. This simulator was used to explore enhancements in DNAPL dissolution due to metabolic reductive dechlorination in one- and two-dimensional non-uniformly contaminated domains. Simulation results demonstrated the potential for this technology to accelerate interphase mass transfer. The level of enhancement was affected by the dechlorination rate, DNAPL zone length, and DNAPL zone configuration. The length of time dissolution enhancement persisted at the quasi-steady-state value (maximum), however, was generally less than 50 percent of the longevity of the source.

© John A. Christ

All Rights Reserved

2005

TABLE OF CONTENTS

DEDICATION.....	ii
ACKNOWLEDGEMENTS.....	iii
LIST OF TABLES.....	x
LIST OF FIGURES.....	xii
LIST OF APPENDICES.....	xvii
CHAPTER I INTRODUCTION.....	1
CHAPTER II BACKGROUND AND LITERATURE REVIEW.....	8
II.A INTRODUCTION.....	8
II.B PHYSICO-CHEMICAL PROCESSES.....	9
II.C BIOLOGICAL PROCESSES.....	13
II.D COMPOSITIONAL MULTIPHASE MODELS.....	21
II.E ILLUSTRATIVE CALCULATION.....	33
II.F CONCLUSIONS AND RESEARCH OBJECTIVES.....	39
CHAPTER III MODEL DEVELOPMENT.....	45
III.A INTRODUCTION.....	45
III.B PHASE MASS BALANCE EQUATIONS.....	46
III.C COMPONENT MASS BALANCE EQUATIONS.....	49
III.D CONSTITUTIVE RELATIONSHIPS.....	50

III.E NUMERICAL IMPLEMENTATION.....	65
CHAPTER IV DIMENSIONALITY EFFECTS ON SIMULATIONS OF DNAPL MIGRATION AND ENTRAPMENT IN NONUNIFORM POROUS MEDIA.....	74
IV.A INTRODUCTION.....	74
IV.B METHODS.....	76
IV.C RESULTS AND ANALYSIS.....	84
IV.D CONCLUSIONS.....	105
CHAPTER V DIMENSIONALITY EFFECTS ON SIMULATIONS OF DNAPL MASS RECOVERY IN NONUNIFORM POROUS MEDIA.....	107
V.A INTRODUCTION.....	107
V.B METHODS.....	109
V.C RESULTS AND ANALYSIS.....	115
V.D CONCLUSIONS.....	144
CHAPTER VI MODELING METABOLIC REDUCTIVE DECHLORINATION IN BATCH SYSTEMS.....	147
VI.A INTRODUCTION.....	147
VI.B MODEL DEVELOPMENT.....	149
VI.C APPLICATIONS.....	165
VI.D CONCLUSIONS.....	184
CHAPTER VII MODELING METABOLIC REDUCTIVE DECHLORINATION IN DNAPL SOURCE ZONES.....	189
VII.A INTRODUCTION.....	189
VII.B MODEL DEVELOPMENT.....	191
VII.C SOURCE ZONE DECHLORINATION SIMULATIONS.....	199
VII.D CONCLUSIONS.....	235

CHAPTER VIII CONCLUSIONS AND RECOMMENDATIONS FOR FUTURE	
WORK.....	239
VIII.A CONCLUSIONS.....	239
VIII.B FUTURE WORK.....	246
APPENDICES.....	249
APPENDIX A UTCHEM VALIDATION.....	250
APPENDIX B MISER SOLUTION SCHEME.....	260
APPENDIX C SATURATION DISTRIBUTION COMPARISON.....	261
APPENDIX D FLUX-AVERAGED CONCENTRATIONS.....	265
BIBLIOGRAPHY.....	269

LIST OF TABLES

Table II.1: Parameters used in example source zone remediation calculations.....	36
Table II.2: Calculated source longevities in years for natural gradient dissolution, source zone bioremediation, and SEAR + bioremediation of all four hypothetical source zones.....	37
Table III.1: Summary of numerical models employed in this dissertation.....	73
Table IV.1: Numerical simulation input parameters for 2-D and 3-D numerical simulations using UTCHEM.....	82
Table IV.2: Statistics for saturation distribution metrics in 2-D and 3-D realizations ($\sigma^2 \ln(k) = 0.29$).....	87
Table IV.3: Saturation distribution metrics for three alternative realizations subject to three different spill volumes.....	91
Table IV.4: Saturation distribution metrics for three alternative realizations subject to two different release rates.....	92
Table IV.5: Spearman rank correlation coefficients for 2-D and 3-D simulation comparisons.....	98
Table IV.6: Statistics for saturation distribution metrics in 2-D and 3-D realizations with $\sigma^2 \ln(K) = 1.0$	104
Table V.1: Numerical simulation input parameters for 2-D and 3-D mass recovery simulations in non-uniform permeability fields.....	113

Table V.2: Average difference $\bar{\Delta}$ in percent, maximum difference Δ_{max} in percent, and average of the squared difference (ASD) between 2-D and 3-D percent flux reduction curves.....	127
Table V.3: 2D and 3D source longevity statistics for mass recovery simulations.....	131
Table V.4: Mean (\pm 95 % Confidence Interval) 2-D and 3-D mass transfer parameter values.....	140
Table VI.1: Biological degradation expressions.....	157
Table VI.2: Dechlorination kinetic parameters for pure and mixed culture simulations.....	172
Table VI.3: Best fit kinetic coefficients for <i>Sulfurospirillum multivorans</i> in the presence of 500 mg/L, 1000 mg/L, and 5000 mg/L of TWEEN 80 surfactant.....	178
Table VII.1: 1-D column properties for base case metabolic reductive dechlorination simulation.....	202
Table VII.2: Component <i>c</i> physical properties for metabolic reductive dechlorination simulations.....	203
Table VII.3: Biomass phase properties for metabolic reductive dechlorination simulations.....	203
Table VII.4: Biological degradation parameters for metabolic reductive dechlorination simulations.....	204
Table VII.5: Model parameters used in non-uniform biomass simulations.....	209
Table A.1: Fluid and Matrix properties for numerical simulation experiments.....	253
Table A.2: Constitutive relation properties for model simulations.....	254
Table C.1: 2D and 3D saturation distribution metrics for all 16 realizations.....	261

LIST OF FIGURES

Figure I.1: Hypothetical DNAPL source zone showing the formation of residual saturation zones, high saturation pool zones, and a possible flushing remediation scenario.....	3
Figure II.1: Representation of biophase attached to porous media as an (a) biofilm and (b) discrete microcolonies.....	27
Figure II.2: Depiction of DNAPL source zone conceptual models used in the example calculations.....	35
Figure II.3: Percent of DNAPL mass remaining as a function of time for three alternative remediation strategies in LGP scenario.....	38
Figure III.1: Conceptual model of relevant phases, components, and interphase mass transfer mechanisms.....	47
Figure III.2: Representative hysteretic soil moisture characteristic.....	54
Figure III.3: Illustrative example of Monod degradation kinetics for two hypothetical microbial populations.....	63
Figure III.4: Comparison of two-dimensional simulation results using MT3DMS-MODFLOW (solid line) and MISER (closed diamonds) in terms of flux-weighted contaminant concentrations versus percent mass removal.....	68
Figure IV.1: Model domain conceptualization for 2-D and 3-D simulations.....	80
Figure IV.2: Saturation profiles simulated in (a) 2D using UTCHEM and (b) in the same 2D slice extracted from a 3D UTCHEM simulation.....	86
Figure IV.3: Box plot comparing 2-D, “2-D in 3-D”, and 3-D metric distributions for all 16 permeability realizations: (a) S_o^{max} , (b) σ_{xx}^2 , and (c) σ_{zz}^2	88

Figure IV.4: Q-Q plot comparing saturation CDF's generated using all contaminated cells ($s_o > 0.0001$) in 2-D and 3-D domains.....	93
Figure IV.5: Scatterplot of 2-D versus "2-D in 3-D" (open boxes) and 3-D (closed boxes) ganglia-to-pool (GTP) mass ratios.....	95
Figure IV.6: Scatterplot of realization ranks based on metric values.....	97
Figure IV.7: Scatterplot of σ_{xx}^2 v. σ_{yy}^2 metrics for 16 3-D simulations.....	101
Figure V.1: Representative initial saturation distributions in (a) 3-D and (b) 2-D.....	114
Figure V.2: Temporal evolution of a 3-D DNAPL source zone under natural gradient dissolution conditions.....	117
Figure V.3: Temporal evolution of a 2-D DNAPL source zone under natural gradient dissolution conditions.....	118
Figure V.4: Flux-weighted concentration at the effluent boundary plotted as a function of percent mass removal for all 16 (a) 3-D and (b) 2-D realizations.....	119
Figure V.5: Flux-weighted concentration at the effluent boundary as a function of percent mass removal.....	122
Figure V.6: Percent flux reduction at the effluent boundary as a function of percent mass removal.....	126
Figure V.7: (a) Flux-weighted concentration and (b) percent flux reduction at the effluent boundary as a function of percent mass removal.....	129
Figure V.8: Flux-weighted concentration at the effluent boundary as a function of percent mass removal for 2-D and 3-D simulations at three different hydraulic gradients.....	130
Figure V.9: Box plot of source longevity for the ensemble of two and three dimensional simulations.....	132
Figure V.10: Scatterplot of 2-D versus 3-D source longevity values.....	133
Figure V.11: Source longevity plotted against (a) the maximum organic saturation and (b) the initial ganglia-to-pool mass ratio.....	134

Figure V.12: Numerical simulation (bold line) and upscaled mode (solid line) of the flux weighted concentration at the effluent boundary as a function of percent mass removal for 2-D and 3-D simulations.....	143
Figure VI.1: Conceptual model of metabolic reductive dechlorination, synergistic, and competing processes.....	152
Figure VI.2: Example diagram of simplex optimization method for two parameter ($k = 2$) optimization.....	164
Figure VI.3: (a) Hydrogen, (b) chloroethenes, (c) acetate, and (d) biomass concentrations as a function of time.....	170
Figure VI.4: (a) Fermentable substrate and Hydrogen, (b) chloroethenes, (c) acetate, and (d) biomass concentrations as a function of time.....	171
Figure VI.5: PCE dechlorination to cis-DCE by <i>Sulfurospirillum multivorans</i> pure culture.....	175
Figure VI.6: cis-DCE dechlorination to ethene by <i>Dehalococcoides etheneogenes</i> BAV1 pure culture.....	176
Figure VI.7: Simulated and experimental chloroethene concentrations during metabolic reductive dechlorination by <i>Sulfurospirillum multivorans</i> in the presence of (a) 500 mg/L, (b) 1000 mg/L, and (c) 5000 mg/L of TWEEN 80 surfactant.....	177
Figure VI.8: Simulated and experimental chloroethene concentrations for aqueous-organic phase batch system of Yang and McCarty [2000].....	185
Figure VI.9: Simulated and experimental results for a two-phase (PCE-water) batch experiment.....	186
Figure VII.1: Comparison of numerical model developed in this work to analytical solution of Clement [2001].....	198
Figure VII.2: Comparison of simulated (solid line) and experimental (filled symbols) results for a one-dimensional column contaminated with PCE-DNAPL [Yang and McCarty, 2002].....	205
Figure VII.3: Simulation results for the equilibrium initial condition and the zero contaminant concentration initial condition.....	212

Figure VII.4: Dissolution enhancement as a function of time for three alternative k_{max}^{PCE} values.....	222
Figure VII.5: NAPL configuration (shaded area) for simulations in sections VII.C.3.iii and VI.C.3.iv.....	223
Figure VII.6: Dissolution enhancement factor as a function of time for the 60 cm, 30 cm, 20 cm, and 10 cm NAPL zone length.....	224
Figure VII.7: Dissolution enhancement factor as a function of time for alternative NAPL source configurations.....	228
Figure VII.8: Bioenhanced dissolution as a function of time for 30 cm (Base case), 20 cm, and 10 cm NAPL zone lengths.....	229
Figure VII.9: Percent of DNAPL mass remaining as a function of time for three alternative remediation strategies in the LGP scenario (Figure II.2) with a transient bioenhanced dissolution factor.....	230
Figure VII.10: Total chloroethene concentration as a function of time for base case simulation and a simulation that includes back partitioning of dechlorination products (e.g., <i>cis</i> -DCE) into the residual PCE-NAPL.....	233
Figure VII.11: PCE and <i>cis</i> -DCE concentrations for the alternative primary substrate amendment strategy simulation discussed in section VII.C.4.ii.....	236
Figure A.1: (a) Hydraulic conductivity field used in reported simulations and (b) M-VALOR hysteretic benchmark simulation.....	254
Figure A.2: (a) Non-hysteretic saturation – capillary pressure – relative permeability model simulation using UTCHEM and (b) hysteretic simulation using MVALOR.....	255
Figure A.3: Saturation profile for hysteretic simulation using the unmodified version of UTCHEM.....	256
Figure A.4: Organic saturation profile simulated using (a) the modified version of UTCHEM and (b) MVALOR.....	259
Figure B.1: Solution scheme used in version of MISER modified to simulate DNAPL source zone metabolic reductive dechlorination.....	260

Figure C.1: Saturation profile simulation in (a) 2-D and (b) the same 2-D slice extracted from 3-D.....	262
Figure D.1: Flux-averaged concentration curves for all 16 realizations.....	265

LIST OF APPENDICES

APPENDIX A UTCHEM VALIDATION.....	250
APPENDIX B MISER SOLUTION SCHEME.....	260
APPENDIX C SATURATION DISTRIBUTION COMPARISON.....	261
APPENDIX D FLUX-AVERAGED CONCENTRATIONS.....	265

CHAPTER I

INTRODUCTION

Past improper disposal practices, both legal and illegal, have resulted in a legacy of environmental contamination of soils, surface water, and groundwater. Among the most intractable of these environmental contamination scenarios are those involving the release of dense non-aqueous phase liquids (DNAPLs), such as chlorinated solvents, to the subsurface. DNAPLs are water-immiscible organic liquids that, when spilled, have the potential to contaminate large volumes of groundwater with carcinogenic and mutagenic organic chemicals at concentrations orders-of-magnitude above their safe drinking water standards [US EPA, 2003]. The region of the aquifer contaminated with DNAPL is usually termed the "source zone" [NRC, 2004]. According to the U.S. Environmental Protection Agency, approximately sixty percent of all superfund sites contain DNAPL source zones [US EPA, 2003] and if all U.S. contaminated sites are considered, the number of DNAPL sites is approximately 15,000 to 25,000 [US EPA, 2003]. A total life cycle cost just for containment of contamination at these sites using traditional hydraulic systems (e.g., pump-and-treat) has been put as high as \$50 to \$100 billion [US EPA, 2003] and the remediation of these sites has been estimated to take anywhere from decades to centuries [Mackay and Cherry, 1989]. Given that almost half

of the US population obtains its drinking water from subsurface aquifers [Hutson et al., 2004], alternative methods to reduce exposure to DNAPLs in the subsurface are clearly needed.

A hypothetical DNAPL source zone is depicted in Figure I.1. When spilled in sufficient amounts, DNAPLs migrate downward under gravitational and capillary forces until a low permeability layer/capillary barrier impedes the downward migration [Mercer and Cohen, 1990]. During migration, hysteretic capillary forces cause organic contaminants to become immobilized as discontinuous globules or ganglia [US EPA, 1990]. In addition, heterogeneity and nonuniformity in soil properties may cause DNAPLs to pool to high saturations at interfaces of textural contrast [Essaid and Hess, 1993; Dekker and Abriola, 2000a; Saenton et al., 2002]. The subsurface distribution of DNAPL, often termed the source zone architecture, controls the rate and extent of DNAPL dissolution, the down gradient aqueous phase contaminant concentrations, and the success of remediation methods [Sale and McWhorter, 2001; Lemke et al., 2004b].

Recent work has focused on source zone remediation methods that accelerate DNAPL dissolution or destroy contaminants *in situ* using physico-chemical processes [Henry et al., 2003]. Many of these technologies have demonstrated significant DNAPL mass removal [Fountain et al., 1995; Abriola et al., 2005]. However, no technology has been shown capable of complete mass removal [NRC, 2004]. Thus, a small fraction of DNAPL remains entrapped in the porous medium, where it continues to serve as a source of down gradient contamination [Fountain et al., 1995; Sale and McWhorter, 2001]. Consequently, some authors have questioned the benefit of partial source zone mass removal [e.g. Cherry et al., 1997; Freeze and McWhorter, 1997; Freeze, 2000]. Following an in-depth assessment,

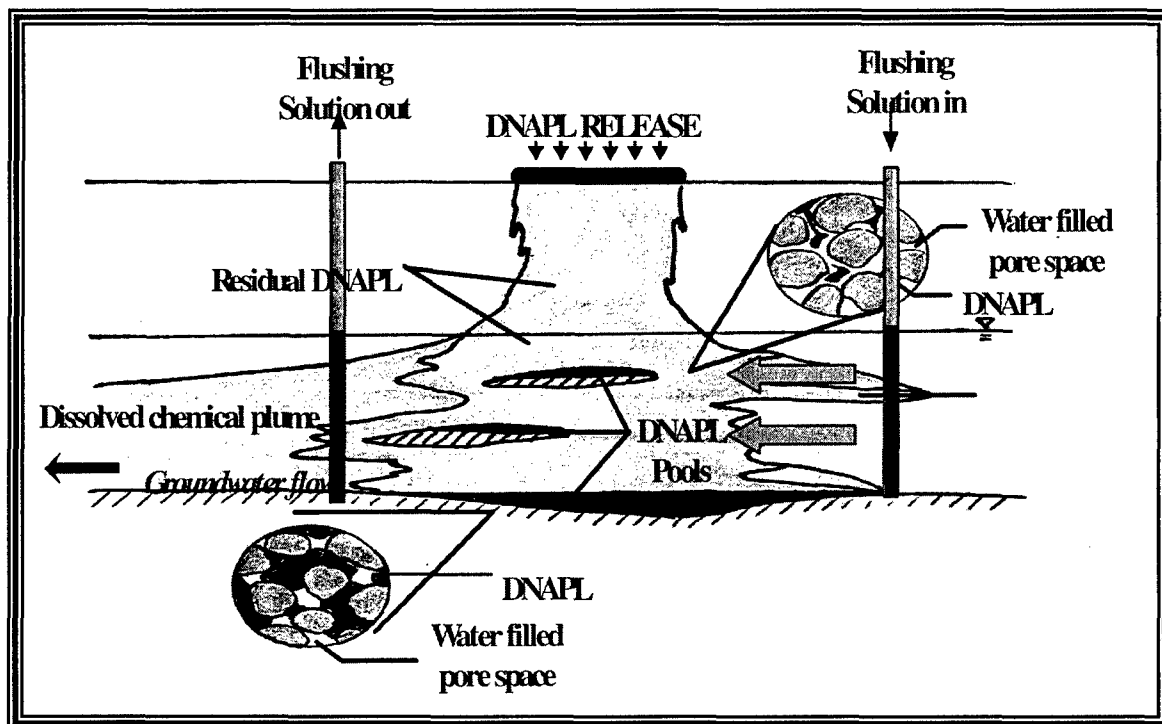


Figure I.1: Hypothetical DNAPL source zone showing the formation of residual saturation zones, high saturation pool zones, and a possible flushing remediation scenario (modified from Kueper and Frind, 1991).

however, a recently convened expert panel concluded that there are a number of benefits to partial source zone mass removal, including (i) mitigation of human exposure and adverse ecological impacts due to reductions in volume, toxicity, and mobility of the DNAPL, (ii) reductions in life-cycle site costs, (iii) mitigation of public stakeholder concerns and portrayal of a positive environmental image, (iv) reduction in future uncertainty in transaction costs, and (v) improvement in the performance of complementary source zone remediation technologies [US EPA, 2003]. These conclusions were based on existing numerical, experimental, and field investigations found in the published literature [e.g., Martel et al., 1998; Jawitz et al., 2000; Londergan et al., 2001; Rao et al., 2002; Yang and McCarty, 2002].

Of particular importance were conclusions drawn from numerical simulations of the fate and transport of DNAPLs in the subsurface [e.g., Faust et al., 1989; Bradford et al., 1998; Dekker and Abriola, 2000b; Whittaker et al., 2000; Lemke et al., 2004b]. Such numerical simulations have been used to quantify the benefits of partial source zone mass removal. For example, numerical simulations have shown that one- to two-orders-of-magnitude reductions in mass discharge may be achieved at moderate levels of source zone DNAPL mass removal (e.g., 60-90%) [Rao et al., 2002; Rao and Jawitz, 2003; Lemke and Abriola, 2004b], supporting conclusions (i), (ii), and (v) reached by the expert panel. The applicability of these numerical investigations to actual field scenarios, however, is questionable due to the utilization of simplifying assumptions, foremost of which is the assumption that two-dimensional simulations provide reasonable approximations to three-dimensional behavior [e.g., Whittaker et al., 2000; Lemke et al., 2004b]. Computational demands of simulating the fate and transport of DNAPL in three dimensions have led most researchers to conduct numerical investigations in two-

dimensional domains [e.g., Kueper and Gerhard, 1995; Rathfelder et al., 2001; Lemke et al., 2004a]. No study, however, has rigorously investigated the affects of dimensionality on multiphase simulations to determine the error that may be introduced into the numerical simulations and, consequently, the conclusions founded on those simulations.

Furthermore, there is a lack of capability to investigate potential enhancements in complementary technologies following partial mass removal [Stroo et al., 2003; US EPA, 2003; NRC, 2004]. Foremost among the potentially complementary technologies enhanced by partial mass removal is source zone bioremediation, which may enhance DNAPL dissolution and reduce aqueous phase contaminant concentrations [de Blanc et al., 1997; Zoller, 1998; Zoller and Rubin, 2001; Rao et al. 2002; Stroo et al., 2003; NRC, 2004]. Until recently, it was believed that high contaminant concentrations typical of a DNAPL source zone would be toxic to indigenous microorganisms [Abelson, 1990; Bouwer, 1994]. However, degradation in anaerobic environments typical of a treated source zone is well known [Vogel et al., 1987; McCarty and Semprini, 1994] and recent research on chlorinated aliphatic hydrocarbons has demonstrated that metabolic reductive dechlorination (chlororespiration) in the presence of nonaqueous phase chlorinated contaminants is possible [Nielsen and Keasling 1999; Carr et al., 2000; Cope and Hughes, 2001; Yang and McCarty, 2000, 2002]. Existing tools capable of investigating the benefits of implementing complementary technologies (e.g., aggressive mass removal followed by metabolic reductive dechlorination) are limited to single phase numerical simulators [e.g., Wagner et al., 2002]. Although these models are capable tools for investigating degradation in aqueous phase plumes down gradient of a DNAPL source zone, as highlighted by a recent National Research Council expert panel [NRC, 2004], they are incapable of simulating potential enhancements in DNAPL dissolution due to biological activity. Thus, there is a need to

develop numerical simulators capable of investigating processes such as metabolic reductive dechlorination in chlorinated-DNAPL source zones to determine potential benefits of implementing complementary technologies [NRC, 2004].

The goal of this research was to improve the understanding of the benefits of partial source zone mass removal from chlorinated-DNAPL source zones by (i) determining the effects of dimensionality on multiphase numerical simulations of DNAPL migration, entrapment, and dissolution in nonuniform subsurface environments and (ii) developing and applying a compositional multiphase flow and transport model capable of simulating metabolic reductive dechlorination in a chlorinated-DNAPL source zone. Existing numerical simulators were modified to enable the comparison of DNAPL simulations in two and three dimensions. An existing multi-dimensional, multi-phase compositional simulator was modified to incorporate dechlorination kinetics. Dechlorination kinetics were adapted from the literature and validated against laboratory data collected by collaborating colleagues at the Georgia Institute of Technology and data published in the literature. The full model was validated using batch and column data in the published literature. Finally, this model was applied under a variety of source zone scenarios to explore the potential benefits of metabolic reductive dechlorination in DNAPL source zones.

This doctoral dissertation is comprised of eight chapters. Chapter II provides a comprehensive review of both compositional multiphase simulator and metabolic reductive dechlorination literature. The mathematical and numerical modeling framework that provides the foundation for the simulators employed and developed in this study is described in detail in Chapter III. Chapters IV and V describe a rigorous investigation of the effects of dimensionality on DNAPL migration, entrapment, and

dissolution in two- and three-dimensional systems. This dimensionality study improves the interpretation of existing numerical simulations and supports the decision to develop the source zone bioremediation model in two rather than three dimensions. Chapter VI uses the developed kinetic model to investigate metabolic reductive dechlorination kinetics in laboratory systems with and without NAPL. Finally, Chapter VII describes efforts to validate the multi-dimensional, multiphase metabolic reductive dechlorination model against one-dimensional laboratory data from the published literature and also presents a sensitivity analysis on the influence of source zone conditions on metabolic reductive dechlorination. Chapter VIII provides conclusions and future areas for research.

CHAPTER II

BACKGROUND AND LITERATURE REVIEW

II.A INTRODUCTION

Investigation of the benefits of partial mass removal from DNAPL source zones, the research goal stated in Chapter I, requires a thorough understanding of the physical, chemical, and biological processes ongoing in a source zone, as well as the capabilities of existing multiphase compositional simulators. Given the importance of physical-chemical processes to the success of most remediation strategies [NRC, 2004], this chapter begins with a review of literature related to the migration, entrapment, and dissolution of DNAPLs in the subsurface. This section is followed by a review of source zone biological processes, focusing specifically on the stimulation of metabolic reductive dechlorination in the source zone. The state-of-the-art in compositional multiphase simulators is provided to set the context for the modeling undertaken in this work. Conclusions and gaps in understanding are highlighted in the final sections through the interpretation of a simplified modeling problem. Research objectives are also proposed to eliminate selected gaps in understanding and aid in the attainment of the stated goal. Literature related to the investigation of dimensionality effects on multiphase simulations is reviewed in Chapter IV.

II.B PHYSICO-CHEMICAL PROCESSES

As described in Chapter I and depicted in Figure I.1, DNAPL source zones will have a nonuniform architecture composed of low (residual) saturation regions containing ganglia and high saturation regions containing pools, that will govern contaminant discharge from the source area (i.e., contaminant plume development). Considerable research has focused on understanding the processes that affect the formation of the source zone architecture and the forces controlling local- and field-scale dissolution.

II.B.1 Source Zone Architecture

Regulations preventing the introduction of contaminants into the subsurface preclude the systematic investigation of DNAPL source zones at the field-scale. Thus, numerical simulations have become the primary method for investigating processes that control the migration, entrapment, and dissolution of DNAPLs. These investigations have considered the influence of spill characteristics [Kueper and Gerhard, 1995; Dekker and Abriola, 2000a], spatial heterogeneity in soil properties [Essaid and Hess, 1993; Dekker and Abriola, 2000a; Lemke et al., 2004a], capillary forces [Dekker and Abriola, 2000a; Lemke et al., 2004a; Phelan et al., 2004], and NAPL composition [Bradford et al., 1998; Phelan et al., 2004] on the nature and extent of DNAPL contamination. Observations of entrapment due to capillary forces and pooling above textural interfaces in numerical simulations have been supported by results from controlled release field-studies that demonstrate a highly non-uniform saturation distribution (i.e., source zone architecture) even in relatively uniform sandy aquifers [e.g., Poulsen and Kueper, 1992; Kueper et al., 1993].

An advantage to performing numerical simulations is the ability to perfectly quantify source zone metrics that may indicate DNAPL source zone behavior. Metrics have been used to quantify the magnitude of source zone saturations and the spatial distribution of DNAPL mass within the source zone region [Essaid et al., 1993; Essaid and Hess, 1993; Kueper and Gerhard, 1995; Dekker and Abriola, 2000; Lemke et al., 2004a]. Spatial saturation distribution metrics have generally focused on the computation of first and second spatial moments (see Section IV.B.3) [e.g., Kueper and Gerhard, 1995]. More recently, source zone saturation distributions have been quantified using a metric that considers the magnitude and distribution of DNAPL saturations, the ganglia-to-pool (GTP) mass ratio [Lemke et al., 2004b]. The GTP mass ratio uses a threshold saturation consistent with the maximum residual organic saturation to quantify the ratio of DNAPL mass entrapped as ganglia below the threshold saturation to the mass pooled above the threshold saturation. Lemke et al. [2004b] showed that the distribution of DNAPL mass quantified using this metric will have a controlling influence on contaminant dissolution from a source area. For an ensemble of 200 DNAPL distribution realizations developed using hydraulic property geostatistical data from a DNAPL contaminated site in Oscoda, MI [Abriola et al., 2005], the GTP was found to range between ~ 1 and ∞ , with typical values between 2 and 20. These values indicate that the source zones for this relatively uniform aquifer material consisted primarily of ganglia zones. In aquifers with greater heterogeneity and/or source zones that have aged (i.e., ganglia have preferentially dissolved), the source zone will likely be dominated by DNAPL pools resulting in lower GTP mass ratios.

II.B.2 DNAPL Source Zone Dissolution

Considering that the timescale of a DNAPL release is typically small relative to the time required for the DNAPL to completely dissolve into the flowing aqueous phase, the final source zone architecture when DNAPL migration ceases is expected to control contaminant dissolution. Due to variability in the source zone architecture, methods for quantifying dissolution from both residual saturation and pooled regions are required.

DNAPL dissolution kinetics have been the focus of a number of laboratory-scale [Miller et al., 1990; Powers et al., 1992; Geller and Hunt, 1993; Imhoff et al., 1994; Powers et al., 1994, 1998; Kim and Chrysikopoulos, 1999; Saba and Illangasekare, 2000; Nambi and Powers, 2000, 2003], field-scale [Frind et al., 1999; Broholm et al., 1999, 2005; Rivett and Feenstra, 2004], and numerical modeling [Mayer and Miller, 1996; Unger et al., 1998; Zhu and Sykes, 2000; Parker and Park, 2004] studies. Generally, DNAPL dissolution kinetics are described by assuming local equilibrium [e.g., Soerens et al., 1998; Sale and McWhorter, 2001; Rao and Jawitz, 2003] or by using a linearized, rate-limited, interphase mass transfer expression [White et al., 1995; Delshad et al., 1996; Abriola et al., 1997; Rathfelder et al., 2000]. Local equilibrium assumptions typically employ Raoult's law to relate contaminant concentrations in the organic and aqueous phases [Weber and DiGiano, 1996]. In contrast, rate-limited mass transfer expressions employ a lumped mass transfer coefficient to quantify the rate of interphase mass transfer between the organic and aqueous phases [Weber and Digiano, 1996]. These lumped coefficients are commonly correlated to groundwater velocity, contaminant properties, and DNAPL saturation. Lumped mass transfer correlations have been derived for a variety of experimental systems including dissolution of residual NAPL blobs [e.g.,

Miller et al., 1990; Geller and Hunt, 1993; Powers et al., 1994; Imhoff et al., 1994], dissolution from high initial saturation ganglia regions [e.g., Nambi and Powers, 2000, 2003], and interphase mass exchange from DNAPL pools [e.g., Kim and Chrysikopoulos, 1999; Chrysikopoulos and Kim, 2000].

Local-scale mass transfer correlations have been incorporated into compositional multiphase, numerical simulators to explore DNAPL dissolution under a variety of natural and engineered subsurface conditions [Mayer and Miller, 1996; Dekker and Abriola, 2000b; Zhu and Sykes, 2000; Taylor et al., 2001; Rathfelder et al., 2001; Phelan et al., 2004; Lemke et al., 2004b] and to successfully simulate laboratory investigations [Rathfelder et al., 2001; Brusseau et al., 2002], despite some experimental evidence suggesting the use of correlations derived from one-dimensional column dissolution experiments could result in significant prediction errors [Saba and Illangasekare, 2000; Saenton et al., 2002]. Numerical investigations that have compared the effect of the mass transfer correlation on field-scale simulations have shown that differences in simulation results due to the form of the mass transfer correlation are only observed at high levels of mass removal (>90% mass removal) [Mayer and Miller, 1996; Unger et al., 1998; Zhu and Sykes, 2000]. More recent work has focused on using these numerical simulators to develop correlations that describe dissolution using field-scale source zone properties such as bulk aqueous phase flow and GTP mass ratio [Dekker, 1996; Zhu and Sykes, 2004; Parker and Park, 2004].

An area of research that has only recently been investigated is the effect of biological activity on the rate of DNAPL dissolution. Degradation of aqueous phase contaminants adjacent to the DNAPL has been demonstrated to enhance the dissolution

from the DNAPL to the aqueous phase, reducing source longevity [Cope and Hughes, 2001; Yang and McCarty, 2000; 2002; Adamson et al., 2004; Chu et al., 2004]. This process has been termed *bioenhanced dissolution* since it (i) increases the driving force for mass transfer from the DNAPL to the aqueous phase and (ii) degrades the parent compounds (e.g., PCE) to lesser chlorinated products that have higher aqueous phase solubilities [Adamson et al., 2003, 2004; Chu et al., 2004; NRC, 2004]. Experimental dissolution enhancement factors, quantified as the ratio of the total chloroethene flux in the effluent of a biotic and abiotic column, have ranged between one (i.e., no enhancement) and six [Cope and Hughes, 2001; Yang and McCarty, 2000, 2002; Adamson et al., 2004]. Understanding the processes affecting the degree of dissolution enhancement will require an understanding of the rates and limitations of biological degradation processes.

II.C BIOLOGICAL PROCESSES

The disappearance of chlorinated ethenes and the presence of chlorinated degradation products at contaminated groundwater sites in the 1980's inspired researchers to investigate biotic and abiotic transformation processes [Vogel et al., 1987; McCarty and Semprini, 1994]. As early as 1980, researchers identified links between existing microbial metabolism and the fortuitous oxidation of chlorinated hydrocarbons [Higgins et al., 1980]. As more work was completed, researchers recognized three pathways for biotransformation of chlorinated compounds: (i) use of the chlorinated hydrocarbon as a source of carbon and energy under aerobic and anaerobic conditions [Hartmans et al., 1985; Hartmans and deBont, 1992; Bradley and Chappelle, 1996;

Bradley et al., 1998; Verce et al., 2000, 2001; Coleman et al., 2002a, 2002b], (ii) cometabolism of the chlorinated hydrocarbon, either aerobically or anaerobically [Ensign et al., 1992; Hopkins et al., 1993; Anderson and McCarty, 1997; Chauhan et al., 1998; Ryoo et al., 2001; Shim et al., 2001], and (iii) metabolic reductive dechlorination (chlororespiration), in which the chlorinated compound serves as a metabolic electron acceptor for energy generation [Löffler et al., 1996, 1999; Holliger, 1998]. Aerobic metabolic oxidation is a productive pathway for removal of lesser chlorinated ethenes (i.e., *cis*-dichloroethene (*cis*-DCE) and vinyl chloride (VC)), however, no organisms that grow with tetrachloroethene (PCE) or trichloroethene (TCE) as a carbon source have been identified. Aerobic cometabolism can act on all chloroethenes [Ryoo et al., 2001; Shim et al., 2001], however the need for a primary substrate such as methane or toluene and the fact that the degradation of the target compounds can only be indirectly controlled are major drawbacks of this approach. Anaerobic cometabolic reductive dechlorination of PCE has been observed under methanogenic [Fathepure and Boyd, 1988a, b], acetogenic [Terzenbach and Blaut, 1994], and sulfidogenic conditions [Cole et al., 1995]. However, due to low rates and incomplete reductive dechlorination, this process is least likely to contribute to detoxification of contaminated subsurface environments. The metabolic reductive dechlorination pathway (chlororespiration) is a strict anaerobic process that requires an electron donor. The chlororespiratory pathway is promising in that it can lead to efficient dechlorination to ethene and achieve complete detoxification [e.g., Nielsen and Keasling, 1999].

II.C.1 Metabolic Reductive Dechlorination (Chlororespiration)

The ability to use chloroethenes as energy-yielding electron acceptors is distributed among several bacterial groups including different subdivisions of the proteobacteria, the gram-positive bacteria, and the Chloriflexi (formerly green non-sulfur bacteria). Organisms capable of metabolic reductive dechlorination have been isolated from contaminated and pristine sites [Hollinger et al., 1993; Krumholz et al., 1996; Sharma and McCarty, 1996; Maymo-Gatell et al., 1997; Kengen et al., 1999; Löffler et al., 2000; He et al., 2003b; Sung et al., 2003]. They are generally anaerobic with only one organism exhibiting facultative behavior to date [Sharma and McCarty, 1996]. Bacterial populations capable of gaining energy from reductive dechlorination of chloroethenes have been classified into a number of phylogenetic groups including *Dehalobater*, *Sulfurospirillum*, *Desulfuromonas*, *Desulfitobacterium*, *Clostridium*, and *Dehalococcoides* [Löffler et al., 2003]. This broad range of organisms capable of chlororespiration is encouraging for post-treatment bioremediation; however, the majority of these organisms are incapable of complete dechlorination of chloroethenes to ethene [Löffler et al., 2003, Major et al., 2003]. At many sites, dichloroethenes (primarily *cis*-DCEs), and in some cases VC, accumulate. There is an apparent link between the presence of members of the *Dehalococcoides* group and complete dechlorination (e.g., ethene formation) [Maymo-Gatell et al., 1997, 2001; Hendrickson et al., 2002; He et al., 2003a,b; Cupples et al., 2003]. These findings have important ramifications for source zone bioremediation. Although a variety of microorganisms are capable of PCE-to-*cis*-DCE dechlorination, complete detoxification requires the presence and activity of *Dehalococcoides* populations [Hendrickson et al., 2002]. Recent field

demonstrations have shown that even when *Dehalococcoides* populations are not present, however, chlororespiration may be stimulated through bioaugmentation [Ellis et al., 2000; Major et al., 2002; Lendvay et al., 2003; Adamson et al., 2003].

To sustain the reductive dechlorination process, an electron donor must be provided. Chlororespiring populations depend on the activity of fermentative organisms to convert organic materials into suitable electron donors [DiStefano et al., 1992; He et al., 2002]. A variety of substrates including pentanol, ethanol, lactate, propionate, butyrate, oleate and olive oil have been shown to produce suitable electron donors (e.g., acetate, hydrogen) to support chlororespiring populations [Fennell et al., 1997; Carr and Hughes, 1998; Yang and McCarty, 1998, 2002; He et al., 2002]. Chlororespiring populations are highly competitive hydrogen utilizers, and outcompete methanogens, acetogens, and sulfate-reducing populations for this electron donor [Löffler et al., 1999]. Thus, substrates that result in slow release (or production) of hydrogen are advantageous because the majority of reducing equivalents is directed towards the process of interest [Smatlak et al., 1996; Ballapragada et al., 1997; Fennell et al., 1997; Fennell and Gossett, 1998; He et al., 2002]. It should be noted that all approaches that increase the flux of hydrogen in a subsurface environment will also result in an increased flux of acetate. Although *Dehalococcoides* populations require hydrogen as electron donor, acetate has been implicated as a relevant source of low concentrations of hydrogen through syntrophic oxidation [Schink, 1997; He et al., 2002].

II.C.2 Metabolic Reductive Dechlorination in Multiphase Systems

Despite the novelty of source zone bioremediation [Stroo et al., 2003], a number of studies have recently appeared which investigate chlororespiration in aqueous-NAPL phase systems (~ 0.9 mM or 150 mg/L for PCE). Chlororespiration in the presence of non-aqueous phase PCE has been observed in batch [Nielsen and Keasling, 1999; Yang and McCarty, 2000; Carr et al., 2000; Sung et al., 2003; Adamson et al., 2004], column [Cope and Hughes, 2001; Yang and McCarty, 2002], multi-dimensional laboratory [Adamson et al., 2003], and field-scale studies [Mravik et al., 2003; Ramsburg et al., 2004]. Modeling studies have also been conducted assuming idealized one- and two-dimensional domains [Chu et al., 2003, 2004]. The goal of these experimental and modeling studies has generally been to demonstrate dechlorination of near-solubility contaminant concentrations consistent with the presence of a DNAPL and to quantify enhancements in dissolution due to dechlorinating activity (see section II.B.2).

Nielsen and Keasling [1999] demonstrated complete reductive dechlorination (e.g. ethene formation) at saturated PCE concentrations in batch systems. The majority of reducing equivalents from the electron donor, glucose, was consumed by reductive dechlorination, probably due to the inhibition of other microbial processes, such as methanogenesis, by the high chloroethene concentrations. Yang and McCarty [2000] also reported degradation of PCE in batch systems where concentrations of PCE approached aqueous solubility. However, dechlorination stalled at *cis*-DCE. This lack of complete dechlorination was also observed in a separate experiment that found *cis*-DCE accumulated until PCE had been exhausted [Adamson et al., 2004] and a large-scale laboratory experiment demonstrated that VC production from *cis*-DCE degradation was

limited to down-gradient regions of the experimental domain [Adamson et al., 2003]. Reasons for the accumulation of *cis*-DCE are unclear. Adamson et al. [2004] suggest PCE is a more energetic electron acceptor that will be used preferentially (i.e., electron acceptor competition). Yu et al. [2005], however, demonstrate that PCE concentrations up to approximately half the solubility concentration had very little effect on *cis*-DCE dechlorination in two separate cultures. They suggest chloroethene self-inhibition as a second alternative [Yu and Semprini, 2004]. This hypothesis is based on limited evidence showing that at high concentrations typical of a DNAPL source zone, chloroethene self-inhibition may occur [Maillard et al., 2003; Yu and Semprini, 2004].

In column studies, a nonuniform distribution of organisms and NAPL has been shown to result in significant competition and bioclogging due to fermentative and competitor growth [Yang and McCarty, 2002]. The partitioning of chlorinated degradation products (TCE, *cis*-DCE, VC) into the non-aqueous phase has also been observed and may impact the bioavailability of the lesser chlorinated ethenes [Cope and Hughes, 2001; Adamson et al., 2004]; though these observations were primarily made in mixed NAPL systems consisting of PCE in an organic carrier phase. Efforts to overcome electron donor competition and bioclogging in column experiments have generally focused on alteration of the substrate amendment strategy [Cope and Hughes, 2001; Yang and McCarty, 2002]. As discussed in the previous section, substrates that result in the slow release of the electron donor (e.g., hydrogen) provide a competitive advantage to the dechlorinating populations. When an electron donor is added in sufficient concentrations, dissolution enhancements in one-dimensional columns have been as high as a factor of six [e.g., Cope and Hughes, 2001].

Recent observations from pilot-scale field studies indicate that residual flushing solutions (e.g., surfactant) following active physico-chemical treatment may provide an alternative source of electron donor capable of stimulating indigenous metabolic reductive dechlorinating populations. For example, following the implementation of surfactant enhanced aquifer remediation (SEAR) at a tetrachloroethene (PCE)-contaminated DNAPL site in Oscoda, MI, Ramsburg et al. [2004] observed the formation of PCE degradation products and the continued decline in source zone PCE concentrations 450 days after SEAR completion. The degradation of residual surfactant appeared to stimulate the metabolic reductive dechlorination process [Ramsburg et al., 2004]. A similar study that used co-solvent flushing to treat a PCE-contaminated DNAPL site in Jacksonville, FL also showed PCE degradation product formation following source zone treatment [Mravik et al., 2003]. The occurrence of this phenomenon was fortuitous, however. Future design and implementation of metabolic reductive dechlorination as a source zone management strategy will likely require mathematical models capable of simulating the germane processes.

Recent modeling studies have attempted to better understand the factors that may affect the magnitude of dissolution enhancement in NAPL contaminated media [Seagren et al., 1993, 1994; Chu et al., 2003, 2004; Gupta and Seagren, 2005]. Biological clogging, influent electron donor concentration, inhibition kinetics, and NAPL configuration are all factors that have been examined using these models. The application of these models to experimental or field-scale systems, however, has been limited due to the use of idealized modeling domains, simplified degradation kinetics, and the assumption of steady-state conditions. These models typically assume

dissolution from fully saturated DNAPL pools placed along the flow domain boundary. Dechlorination rate limitations such as electron donor supply are often ignored and the assumption of steady-state conditions prohibits the simulation of changes in the rate of dissolution as the DNAPL dissolves. Each of these limitations is expected to affect the predicted enhancement of dissolution. The consideration of these limitations will likely require the use of numerical modeling methods that are capable of simulating the spatial-temporal distribution of multiple components and phases.

II.C.3 Metabolic Reductive Dechlorination Summary

This brief review of the metabolic reductive dechlorination literature highlights the factors important in the successful application of this technology at chlorinated-DNAPL source zone sites. Experimental results indicate that electron donor limitations, microbial ecology (e.g., PCE-to-*cis*DCE and *cis*DCE-to-ethene dechlorinating populations), and contaminant toxicity are all factors that must be considered when investigating bioenhanced dissolution due to metabolic reductive dechlorination. These factors, however, have generally been neglected in existing models developed to examine bioenhanced dissolution. Additionally, existing models were found to employ simplifying assumptions that limit their application to highly idealized systems. Thus, there is a need to develop a new compositional multiphase model to enable the systematic investigation of bioenhanced dissolution under rate-limited dissolution and dechlorination conditions.

II.D COMPOSITIONAL MULTIPHASE MODELS

Models that simulate multiphase flow have been used for a number of decades in the petroleum and geothermal industries. However, it wasn't until the early 1980's that these techniques were adapted to simulate contaminant spill scenarios [Mercer and Cohen, 1990]. Multiphase flow models are generally divided into three categories: (i) those that assume a sharp interface between the migrating fluids (Buckley-Leverett models); (ii) those that incorporate capillarity (black-oil models); and (iii) those that consider interphase transport of mass (compositional models) [Abriola, 1989]. In this work, the third category is further divided into models that include or exclude biotransformation processes. It should be noted that models that exclude biotransformation processes can be of the second or third type (i.e., black-oil or compositional), while models that include biotransformation processes must be of the third type to account for interphase partitioning of contaminants, since degradation is consistently assumed proportional to aqueous phase concentrations.

II.D.1 Multiphase Models Without Biotransformation

Although earlier works developed and applied models of the flow of immiscible phases [Faust, 1985; Osborne and Sykes, 1986] and mass transport from an immobile NAPL phase [Fried et al., 1979], Abriola and Pinder [1985a,b] were the first to develop a model that combined flow of immiscible phases with miscible organic transport [Abriola, 1989]. Their model considered two- and three-phase flow of a two-component NAPL in the saturated and unsaturated zone and allowed for partitioning of one of the components into the gas or aqueous phase. However, fluid entrapment due to hysteresis was

neglected. A model that followed shortly thereafter [Corapcioglu and Baehr, 1987; Baehr and Corapcioglu, 1987] had somewhat similar capabilities (mass transfer and biotransformation), however, the NAPL was considered immobile at residual levels in the unsaturated zone and uniform in the saturated zone. Subsequently, Kaluarachchi and Parker [1992] developed a model for two-component NAPL transport in a two-dimensional, three-phase system.

Over the last decade, models have attempted to relax many of the assumptions applied in earlier work. Sleep and Sykes [1993] developed a model capable of simultaneous water, organic, and air phase flow with interphase mass transfer for an arbitrary number of components. Phase densities and viscosities were modeled as functions of phase composition. Kueper and Frind [1991] developed a two-phase model capable of modeling heterogeneous porous media properties. Abriola et al. [1992] developed a three-phase, two-dimensional model that included fluid entrapment due to hysteresis (VALOR). Falta et al. [1992] extended an existing three-dimensional model to solve the multiphase flow equations for nonisothermal conditions. The development of this model was necessitated by the proposal of a novel source zone treatment technology: enhanced steam injection. White et al. [1995] and Lenhard et al. [1995] presented a three-dimensional, three-phase compositional model that incorporated fluid entrapment and hysteresis in constitutive functions (STOMP). This model has been used successfully to simulate DNAPL infiltration and entrapment in a heterogeneous porous matrix [Oostrom et al., 1999].

More recently, the development of source zone flushing technologies has prompted the development of models with more sophisticated interphase partitioning.

Early models capable of SEAR simulation assumed local thermodynamic equilibrium among phases [e.g. Wilson, 1989; Wilson and Clarke, 1991], however experimental observations suggested that rate limitations must be considered [e.g., Pennell et al., 1993]. In conjunction with early experiments, Abriola et al. [1993] developed a model to describe rate-limited mass transfer during surfactant solubilization experiments. The model was implemented in one-dimension and agreed well with column effluent data. This model served as the first among many that considered more complex mass transfer and transformation processes associated with source zone treatment [e.g., Delshad et al., 1996; Abriola et al., 1997; Dekker and Abriola, 2000b]. These models are reviewed in detail in section II.D.3.

II.D.2 Modeling the Biophase

Before reviewing compositional multiphase simulators capable of modeling source zone remediation and biotransformation processes, it is important to understand the alternative methods that have been developed to account for the presence of an active biophase. While bioaugmentation has stimulated research into the transport and activity of unattached microorganisms [Taylor and Jaffe, 1990; Ellis et al., 2000; Rogers and Logan, 2000; Major et al., 2002, 2003; Lendvay et al., 2003; Adamson et al., 2003] these processes are left for future work. The following discussion and work only considers the attached biophase.

Although methods for modeling biotransformations without explicitly accounting for the growth of a microbial population have been used [Schaerlaekens et al., 1999], these methods are limited in application to steady-state systems. Simulating transient

bacterial growth typically assumes one of the following: (i) that the pore scale geometrical configuration of the attached bacteria consists of a biofilm covering the individual porous medium grains, (ii) that the configuration of the attached bacteria takes the form of attached microcolonies, or (iii) that the pore scale geometrical configuration of bacteria can be neglected [Baveye and Valocchi, 1989]. When modeling substrate diffusion into the attached biophase, these assumptions are important. However, if bacteria are assumed to respond directly to bulk aqueous phase substrate concentrations, all three methods can be shown to give equivalent results [Baveye and Valocchi, 1989].

Early studies tended to support the microcolony representation of the biophase (see references in Baveye and Valocchi, 1989); however, more recent studies have indicated a biofilm configuration may be a more accurate representation of reality (see Figure II.1a). Using etched glass to simulate a porous medium, Vayenas et al. [2002] visualized the development of a biofilm at the pore scale. This biofilm developed near the source of the contaminant and grew at a mildly decreasing thickness with distance away from the contaminant source. Nambi et al. [2003] reported similar behavior when studying anaerobic dechlorination of PCE in silicon-based micromodels. These experimental observations indicate that the assumption that a biofilm is a uniform thickness and completely covers the solid aquifer material is a reasonable approximation. However, for the favorable conditions considered in these experiments such as excess electron donor and no solvent toxicity, biofilm growth was significant directly adjacent to the contaminant source. This observation indicates that the assumption that concentration gradients within the biofilm are negligible could lead to overly-optimistic degradation predictions [Odencrantz et al., 1990]. As the biofilm grows, the rate of degradation will

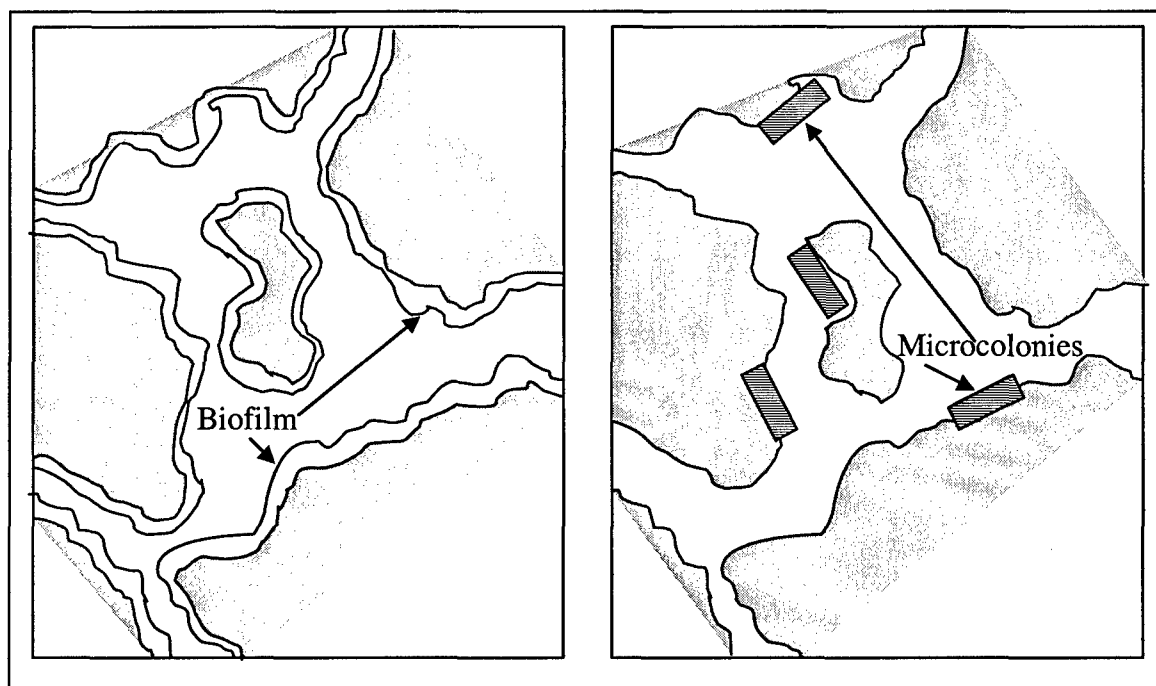
likely become dominated by the rate of contaminant and electron donor diffusion within the biofilm. The importance of these observations in macro-scale systems is unclear, however. In larger scale systems, it is likely that other factors such as electron donor supply and solvent toxicity will limit the growth of the biofilm, making the assumption of no concentration gradient within the biofilm valid.

An alternative to the biofilm configuration is the microcolony representation of the biophase (see Figure II.1 b). In the microcolony conceptualizations, the biophase is assumed to be comprised of cylindrical microcolonies of a given radius and thickness with a constant cell mass density [Baveye and Valocchi, 1989]. The biomass density is defined by the number of colonies per unit volume of the porous medium. Two options for modeling growth of the biophase exist for this representation: (i) the individual microcolonies are assumed to grow in size and (ii) the microcolonies are all a constant size, but the number of microcolonies increases as the biophase grows [Baveye and Valocchi, 1989]. Similar to the biofilm model, the substrate is assumed to be transferred from the bulk fluid to the biophase through a thin immobile fluid layer. Although one can visualize microcolonies growing in three dimensions, transfer of substrate to the biophase is generally assumed to only take place perpendicular to the flat, circular microcolony surface.

Both of the geometrical configurations of the biophase described above have been used successfully to simulate substrate uptake and degradation. A biofilm configuration was used by Anderson and McCarty [1994] to simulate cometabolic transformation of TCE. They showed that external mass transfer limitations in a water film surrounding the biofilm (i.e., an external mass transfer limitation) were important when the bulk fluid was

not adequately mixed or when the bulk fluid concentration of the cometabolite (TCE) was low. Microcolony models have been used to simulate microbial growth and substrate transformation due to aerobic, heterotrophic microorganisms [Molz et al., 1986]. For example, a one-dimensional microcolony based transport model successfully simulated transport and biotransformation of benzene and toluene in a variably saturated sandy aquifer analog [Abriola et al., 1991; Chen et al., 1992].

Despite these successes, models commonly neglect the geometry of the biophase and mass transfer limitations (external and internal) and simply treat the biotransformation reactions as sinks in the aqueous phase transport equations (macroscopic model). When employing this method, the effect of biophase growth on flow is usually neglected. This modeling approach has been implemented in a number of models that simulate reductive dechlorination in single-phase systems (Hossain and Corapcioglu, 1994; Cirpka, 1995; Tonnaer et al., 1997; Clement et al., 1998) where the transformation of PCE is modeled using first-order (e.g., Clement et al., 1998) or mixed-order (e.g., Michaelis-Menton) reactions (Hossain and Corapcioglu, 1994; Tonnaer et al., 1997). The assumption that the biophase does not influence aqueous phase flow is typically justified based on the relatively low concentrations, and consequently low rates of microbial growth, found in migrating plumes. In a source zone, however, significant contaminant concentrations, which may stimulate microbial growth, may occur [e.g., Yang and McCarty, 2002].



(a)

(b)

Figure II.1. Representation of biophase attached to porous media as an (a) biofilm and (b) discrete microcolonies. In both representations it is assumed that a thin immobile water phase separates the biophase from the bulk aqueous phase (after Baveye and Valocchi, 1989).

As mentioned in section II.C.2, observations of biological clogging in the laboratory and the field have motivated the development of methods to simulate the effects of microbial growth on aqueous phase flow. Permeability and porosity correction factors, which account for the reduction in aqueous phase flow due to significant growth of a biophase, have been derived using methods similar to those used to derive relative permeability expressions used in organic-aqueous-gas phase flow systems [Taylor et al., 1990; Vandevivere et al., 1995; Clement et al., 1996; Seki and Miyazaki, 2001]. These correction factors are typically derived as functions of the porous media properties and microbial growth concentrations assuming flow through idealized capillaries or packed spherical grains, and differ depending on whether a biofilm, a microcolony, or a macroscopic biophase configuration is assumed. Yet, Clement et al. [1996] demonstrated that all three modeling methods give practically identical results. A mathematical description of these correction factors is provided in Chapter III.

As this brief review has shown, mathematical models of the biophase and its effects on flow, transport, and transformation vary widely in complexity. Biophase models may include or neglect mass transfer limitations between the aqueous and biophase, may assume or neglect a biophase geometrical configuration, and may simulate or ignore the effects of the biophase on aqueous phase flow and transport. In this work, mass transfer limitations and the biophase geometrical configuration are ignored; however, the effects of biophase growth on the flow field are modeled. The decision to ignore mass transfer limitations (i.e., to employ a macroscopic biophase model) is supported by modeling study results that demonstrate mass transfer limitations are insignificant under typical aquifer conditions [Odencrantz et al., 1990; MacDonald et al.,

1999] and that when mass transfer is ignored, the differences in biophase configurations are immaterial [Baveye and Valocchi, 1989; Lensing, 1998]. It is important to note, however, that, as discussed above, the simulation of significant biological clogging may require the incorporation of mass transfer limitations to account for internal diffusion within a thick biophase.

II.D.3 Multiphase Models that Consider Biotransformation

A handful of existing multiphase models are capable of simulating biotransformation in conjunction with NAPL dissolution. These models evolved out of soil vapor extraction (SVE) and bioventing (BV) applications (e.g., Abriola et al., 1997; Mackinnon et al., 1997). The literature on these and other models are reviewed below to demonstrate the similarities and differences between existing models and the model developed as part of this work.

Shortly after publication of the Abriola and Pinder (1985a) model, Corapcioglu et al. (1991) developed a model that considered simultaneous flow of water and an immiscible fluid. This model allowed for mass transfer between the NAPL and aqueous phase (i.e., dissolution), between the solid and aqueous phase (i.e., sorption), and degradation of aqueous phase chloroethenes (PCE, TCE, DCE, VC) under methanogenic conditions. Sorption and dissolution were modeled using the assumption of local equilibrium and Michaelis-Menton kinetics were used to model reductive dechlorination. Microorganisms were assumed to have an undefined geometrical configuration that did not affect flow or transport and were assumed to respond directly to bulk aqueous phase contaminant concentrations (see section II.D.2). Primary substrate and nutrients were

assumed to be in excess. Although the model was developed to simulate multiphase flow in three-dimensions, the model was solved using a one-dimensional finite difference scheme that assumed the NAPL was immobile at residual saturation in a region outside of the domain. These assumptions resulted in a model that was essentially a single (aqueous) phase transport simulator similar to those referenced in section II.D.2. In a later study, Malone et al. [1993] solved for sequential degradation of non-chlorinated hydrocarbons in a one-dimensional flowing aqueous phase system undergoing fast and slow mass transfer from two regions of an immobile organic phase. Steady aqueous phase flow was assumed, which reduced the specification of the problem to single-phase transport with a two-compartment source. Microorganism growth in response to first-order contaminant transformation was modeled; however, the effects of microbial growth on flow were neglected. Mackinnon et al. [1997] made similar assumptions; however, advective component transport was permitted to occur in the gas rather than in the aqueous phase and mass transfer limitations were assumed to exist between the aqueous and biophases. Gallo and Manzini [2001] solved for both two-phase flow (aqueous-organic) and aqueous phase transport of a single component in two dimensions using a finite-element/ finite-volume nested iteration routine. This model included several alternative biomass models and considered the effects of microbial growth on aqueous phase flow in the biofilm formulation [Gallo and Hassanizadeh, 2000, 2002]. It was incapable, however, of simulating reductive dechlorination due to its limitation to a single organic component.

Unlike the models discussed previously, which have seen only limited application, three models have evolved and been applied to the simulation of DNAPL

source-zone remediation: TMVOCBio [Battistelli, 2004], the University of Texas compositional simulator (UTCHEM) [Delshad et al., 1996; UTCHEM, 2000], and the Michigan subsurface environmental simulator (MISER) [Abriola et al., 1997; Rathfelder et al., 2000; Dekker and Abriola, 2000b].

TMVOCBio, based on the original TMVOC compositional multiphase simulator [Pruess and Battistelli, 2002], is designed to simulate aerobic and anaerobic degradation of multiple contaminants in an equilibrated (no rate-limitations), three-phase (gas-aqueous-NAPL) flowing system. Microbial growth is considered, but the effects of growth on the flow field (i.e., porosity and permeability) are neglected. TMVOCBio has been used to successfully simulate aerobic degradation of toluene in a one-dimensional laboratory column and has been compared to results from a field-scale study of dechlorination in a migrating PCE plume [Battistelli, 2004]. This model has not been used to simulate metabolic reductive dechlorination in a DNAPL source zone, however.

UTCHEM is a three-dimensional (3-D), four-phase (aqueous, organic, gas, emulsion), multi-component simulator that evolved out of the petroleum industry. This model is capable of simulating immiscible/miscible flow of all four phases, non-isothermal conditions, and aerobic/anaerobic biodegradation [Delshad et al., 1996; UTCHEM, 2000]. Microbial degradation is modeled assuming both attached microcolonies subject to external mass-transfer resistance and unattached immobile biomass that respond directly to bulk aqueous phase concentrations. The model has been used extensively [Brown et al., 1994; Freeze et al., 1995; Delshad et al., 2000; Roeder and Falta, 2001; Saenton et al., 2002; Ouyang et al., 2002] and has been benchmarked for simplified problems against analytical solutions and lab-scale studies [UTCHEM, 2000].

It has been used to simulate aerobic cometabolism of TCE down gradient of a DNAPL source zone; however, UTCHEM has not been used to simulate metabolic reductive dechlorination within a chloroethene-DNAPL source zone.

MISER, originally developed for SVE/BV design [Abriola et al., 1997; Rathfelder et al., 2000] and later modified to simulate surfactant flushing [Dekker and Abriola, 2000b], is a two-dimensional, three-phase (aqueous-organic-gas), multi-component simulator capable of simulating aerobic degradation of multiple contaminants flowing in the aqueous phase. Microbial growth and the corresponding biophase volume are computed, however, the volume of the biophase is assumed to be negligible when compared to the volume of the other phases so that the effects of microbial growth on flow and transport are negligible. MISER has been linked to a two-phase (aqueous-organic) immiscible flow model, the Michigan-vertical and lateral organic phase redistribution (M-VALOR) simulator [Abriola et al., 1992], to successfully model soil vapor extraction, bioventing, and surfactant flushing at both the laboratory- and field-scale [Abriola et al., 1997; Dekker and Abriola, 2000b; Rathfelder et al., 2000; Rathfelder et al., 2001; Taylor et al., 2003; Abriola et al., 2005]. MISER has been verified against one- and two-dimensional analytical solutions [Abriola et al., 1997] and lab-scale sandbox studies [e.g. Taylor et al., 2003] and was published under partial sponsorship of the U.S. Environmental Protection Agency (EPA/600/R-97/099). In its current form, however, MISER is incapable of simulating enhancements in dissolution due to metabolic reductive dechlorination.

II.E ILLUSTRATIVE CALCULATION

Before concluding this chapter, an example calculation may prove helpful in illustrating the physico-chemical and biological processes important in a DNAPL source zone. This example can also illustrate the potential benefits of stimulating metabolic reductive dechlorination in a DNAPL source zone and serve as a motivation for the integration of metabolic reductive dechlorination into an existing compositional multiphase simulator presented in later chapters.

This example calculation evaluated the source longevity in years, defined as the time to remove 99.9% of the NAPL mass for three alternative remediation strategies: natural gradient dissolution (i.e., containment), source zone bioremediation, and SEAR followed by source zone bioremediation, in four alternative source zone scenarios, diagramed in Figure II.2. Each scenario assumed a different source zone architecture, however, the amounts of mass in the source zone, the source zone volume, the aqueous phase contaminant solubility during a given dissolution process, and the average hydraulic flux through the source zone were identical. Scenario characteristics were based on a recent pilot-scale SEAR demonstration in Oscoda, MI [Lemke et al., 2004a; Abriola et al., 2005] (see Table II.1). Given that no existing model is capable of simulating dissolution enhancement due to source zone dechlorination (see Section II.D.3), enhancements in dissolution were modeled assuming a spatially and temporally constant bioenhanced dissolution factor equal to five. This value has been reported for column studies with uniformly distributed NAPL ganglia (e.g., Cope and Hughes, 2001).

The source zone scenarios depicted in Figure II.2 were selected to span the expected range of behavior in the field and are characterized by the ganglia-to-pool ratio

(GTP) discussed in Section II.B.1. Scenario 1 assumes NAPL is entrapped as residual ganglia at a uniform saturation throughout the source zone (Figure II.2a). This scenario has an infinite GTP (IGP) and would be characteristic of an ideal site that had perfectly uniform hydraulic properties and where DNAPL was released over a reasonably wide area. The cleanup of this site is modeled using a simplified hydraulic approach (Brusseau, 1996), which is based on mass-balance calculations. Scenario 2 is perhaps more realistic (Figure II.2b). It is representative of a situation with the majority of NAPL entrapped as residual ganglia (high GTP (HGP)), though some pooling has occurred due to permeability contrasts. This DNAPL saturation distribution was generated following the methods outlined by Lemke et al. [2004a]. Using this methodology, the release of NAPL into a uniform permeability field and the subsequent natural dissolution or SEAR is simulated using existing compositional simulators, MVALOR and MISER. Scenario 3 was also generated using the methodology of Lemke et al. [2004a] (Figure II.2c). Here, however, formation properties were configured so that the resultant saturation distribution was dominated by pools (low GTP (LGP)). Scenario 4 assumed all mass was immobilized in six idealized, rectangular, fully saturated pools with no ganglia remaining (Figure II.2d). This scenario is an extreme case where the GTP is equal to zero (ZGP). Cleanup in this scenario was modeled using an analytical solution to the 2D advection-dispersion equation following the methods of Johnson and Pankow [1992].

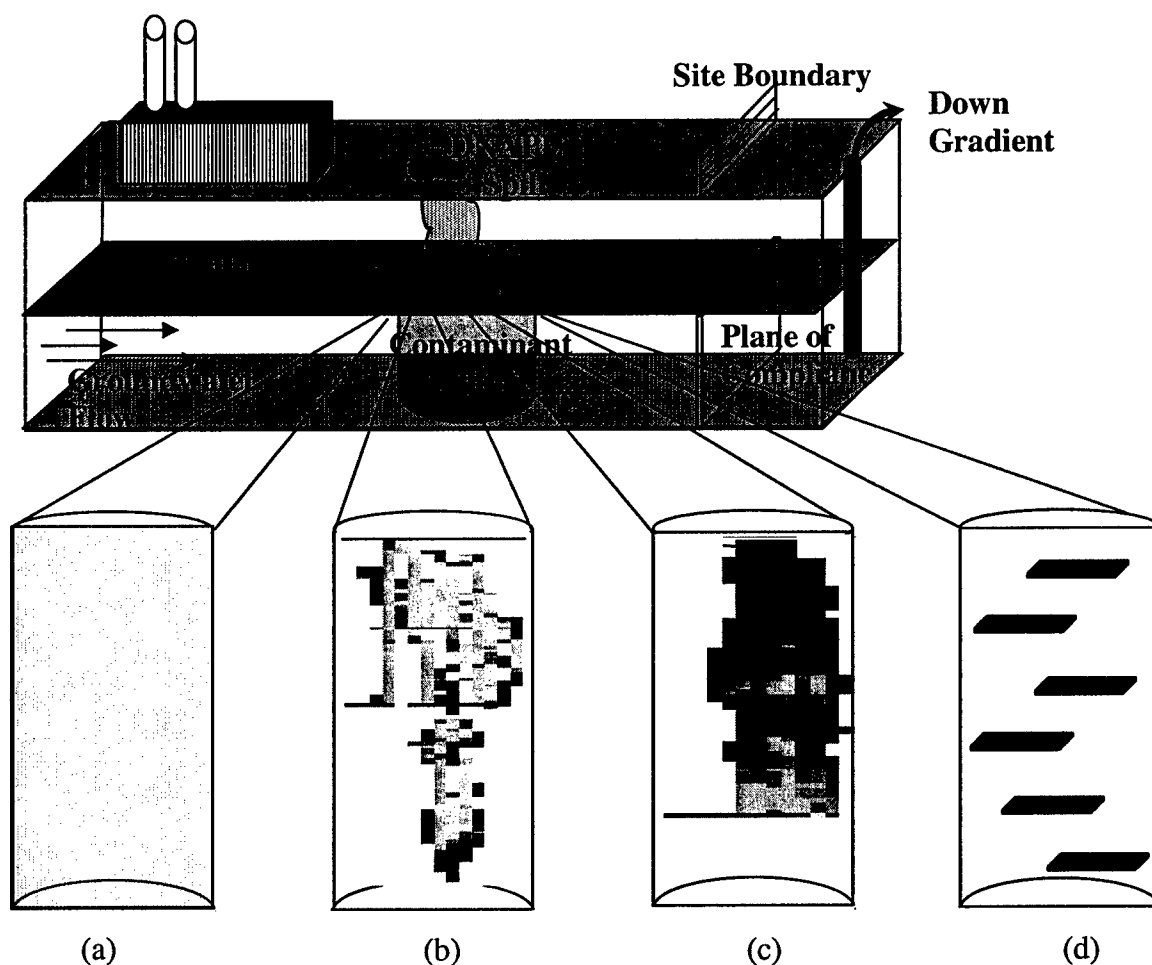


Figure II.2: Depiction of DNAPL source zone conceptual models used in the example calculations: a) infinite ganglia-to-pool ratio (IGP), b) high ganglia-to-pool ratio (HGP), c) low ganglia-to-pool ratio (LGP), and d) zero ganglia-to-pool ratio (OGP). All control volumes are the same size and contain equal amounts of PCE in the form of a NAPL.

Parameter	Value	Units	Reference
Values used in example calculations			
PCE spill volume	0.096	m ³	Lemke et al. [2004a]
Spill radius	0.797	m	Lemke et al. [2004a]
Spill depth	8.315	m	Lemke et al. [2004a]
Average NAPL saturation	0.017	-	Lemke et al. [2004a]
Porosity	0.36	-	Lemke et al. [2004a]
PCE density	1.623 x 10 ⁶	g/m ³	Verschuere[n] [1983]
Rate-limited Aqueous-phase PCE concentration	30 [†]	g/m ³	Abriola et al. [2005]
Length of surfactant flush	10	d	Abriola et al. [2005]
Bioenhanced dissolution factor	5 [†]	-	Carr et al. [2000] Cope and Hughes [2001] Yang and McCarty [2002]
Apparent PCE concentration during SEAR	5.4 x 10 ³	g/m ³	Abriola et al. [2005]
Groundwater Velocity	0.032	m/d	Lemke et al. [2004b]
SEAR Groundwater velocity	0.514	m/d	Abriola et al. [2005] Ramsburg et al. [2005]
Pore volume	5.9	m ³	calculated
Pool length	1	m	calculated
Pool depth	0.016	m	calculated
Number of independent pools	6	-	calculated
Vertical dispersivity	2.3 x 10 ⁻⁴	m	Johnson and Pankow [1992]
Aqueous solubility of PCE	150	g/m ³	Verschuere[n] [1983]
Equilibrium solubility of PCE in surfactant solution	26,880 [‡]	g/m ³	Taylor et al. [2001]
PCE bulk aqueous phase diffusion coefficient	5.7 x 10 ⁻⁵	m ² /d	Dekker and Abriola [2000b]

[†] Assumed based upon range of reported values

[‡] Reported weight solubilization ratio of 0.672 g PCE per g surfactant (4% Tween 80)

Table II.1: Parameters used in example source zone remediation calculations.

Years	Natural Gradient Dissolution	Source Zone Bioremediation ^a	SEAR + Bioremediation
Hydraulic Approach (HA)	36	7	0.01 ^b
High Ganglia-to-Pool ratio (HGP)	54	11	0.01 ^b
Low Ganglia-to-Pool ratio (LGP)	245	50	24
Pool Approach (PA)	817	163	157

^a Source-zone bioremediation calculations assume chlororespiring organisms are present in sufficient numbers and conditions for their activity are optimal (e.g., no nutrient or substrate limitations for duration of treatment)

^b 10-day SEAR (4% Tween) alone was sufficient for 99.9% removal of PCE-DNAPL mass

Table II.2 Calculated source longevity in years for natural gradient dissolution, source zone bioremediation, and SEAR + bioremediation of all four hypothetical source zones.

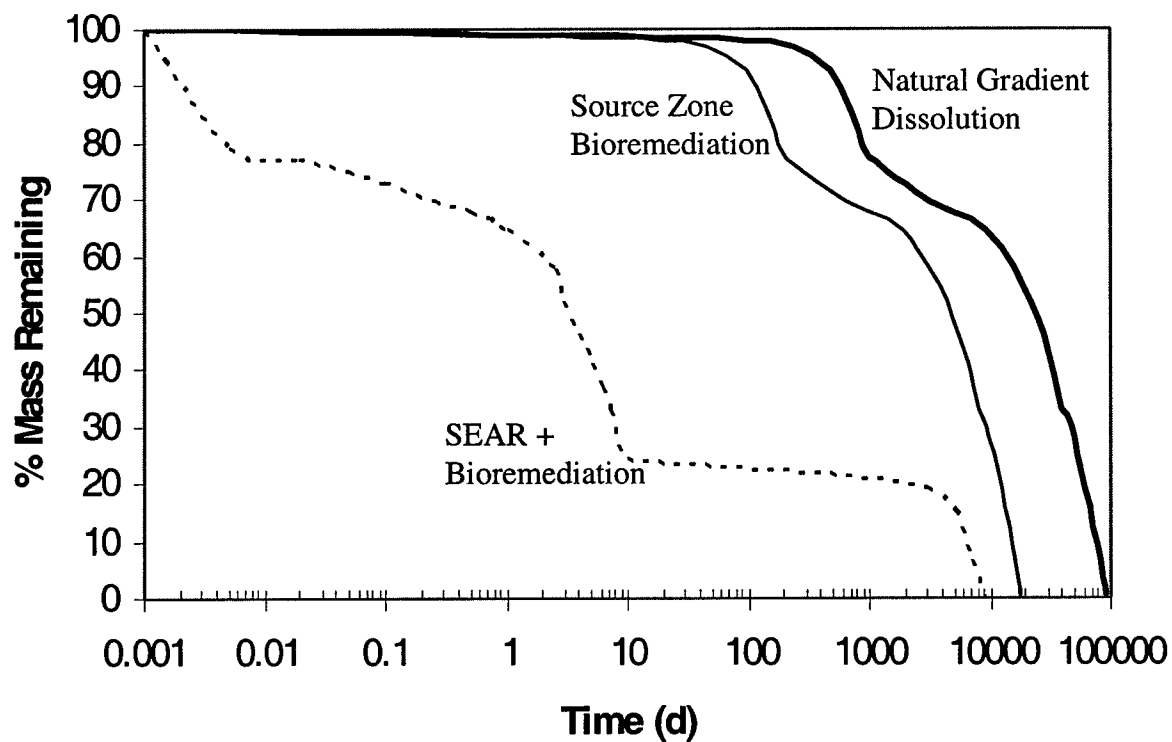


Figure II.3: Percent of DNAPL mass remaining as a function of time for three alternative remediation strategies in LGP scenario.

Calculated values of source longevity for each of the three management strategies for all four source zone scenarios are reported in Table II.2. As expected, the configuration of DNAPL in the source zone will control source longevity. However, regardless of the DNAPL configuration, source zone bioremediation, either when used as the sole strategy (method 2) or as a complementary technology to SEAR (method 3), will result in up to one order-of-magnitude reductions in source longevity. Moreover, Figure II.3 demonstrates that coupling complementary technologies can result in significant reductions in the mass remaining throughout a DNAPL source zone's life-cycle.

The results of the above modeling effort, although informative, are limited by the simplifying assumptions employed in these analyses. In particular, assuming a constant bioenhancement factor equal to observed enhancements in laboratory studies is problematic. As discussed in Sections II.B and II.C, enhancements in dissolution due to biological activity will depend upon a number of factors that vary spatially and temporally, such as the flow field, the DNAPL source zone architecture, and the type and concentrations of microbial populations metabolizing the contaminant. As discussed in Section II.D, compositional multiphase simulators provide the most promising tool for incorporating these factors into an assessment of source zone metabolic reductive dechlorination.

II.F CONCLUSIONS AND RESEARCH OBJECTIVES

This literature review, in conjunction with the illustrative example, demonstrated that biological activity can play an important role in the fate of chlorinated-DNAPL in the source zone. Experimental studies demonstrated that microbial reductive dechlorination

adjacent to a DNAPL enhances the rate of DNAPL dissolution, thus, reducing NAPL source longevity. The magnitude of enhancement observed in experimental studies has varied widely, however, due to dissolution and dechlorination rate limitations. Current modeling efforts to examine bioenhanced dissolution have been restricted to idealized systems with simplified biotransformation reactions. A lack of multiphase compositional simulators capable of modeling dissolution enhancement due to metabolic reductive dechlorination has limited the ability to systematically investigate factors affecting enhanced dissolution. Given the needs identified in the preceding sections, the following objectives were established:

Objective 1: Develop a conceptual model and mathematical framework that captures the necessary behavior to realistically represent reductive dechlorination in a source zone with and without active treatment.

Conceptual model development is a critical first step in any modeling investigation. Among the most important modeling questions are: (i) what is the appropriate dimensionality of the modeled system, and (ii) what is the appropriate level of biogeochemical complexity.

The majority of multiphase numerical modeling studies in the literature have been performed in two-dimensional (x-z cross section) systems [e.g., Kueper and Gerhard, 1995; Eassaid and Hess, 1993; Dekker and Abriola, 2000a; Lemke et al., 2004a]. No study, however, has considered the effect of dimensionality, two-dimensions versus three-dimensions, on multiphase system behavior to determine if conclusions drawn from

these two-dimensional studies remain valid in three-dimensional systems, particularly for systems, such as those considered here, where mass transfer is modeled.

The level of biogeochemical complexity incorporated into numerical simulators varies widely. Model complexity ranges from models that consider individual enzymatic reactions [e.g., Malliard et al., 2003] to models that ignore all biogeochemical behavior and simply assume first order decay of the chemical component [e.g., Clement et al., 1998]. The complexity of microbial reductive dechlorination precludes the use of either of these approaches. Rather, simulation of microbial reductive dechlorination will require the development of a conceptual model that relates multiple interacting chemical components, multiple active microbial species, and a transient biophase.

Objective 2: Integrate the conceptual model developed in Objective 1 into the numerical framework of an existing compositional multiphase model. Demonstrate model performance through mass balance computations and comparison to analytical solutions.

Previous modeling efforts have focused on either improving the understanding of physical-chemical processes in DNAPL source zones [e.g., Dekker and Abriola, 2000b; Lemke et al., 2004a] or simulating contaminant degradation in a migrating plume down-gradient of the source zone [e.g., Hossain and Corapcioglu, 1994; Tonnaer et al., 1997]. There is a need however, to develop models capable of simulating microbial reductive dechlorination in a DNAPL source zone where contaminant degradation can take place adjacent to the DNAPL (i.e., bioenhanced dissolution) [Stroo et al., 2003; NRC, 2004].

Several models reviewed in Section II.D.3 provide the necessary framework for a compositional multiphase simulator capable of modeling source zone metabolic reductive dechlorination. The version of MISER modified to simulate DNAPL source zone flushing remediation strategies [Dekker and Abriola, 2000b] was selected for modification in this work. This model was selected because of the level of complexity in its biodegradation module and its ability to simulate DNAPL dissolution using a physically-based model that reduces interfacial area as the DNAPL dissolves. MISER considers the biomass to be attached and neglects external biomass mass transfer limitations; however, it computes a biophase saturation, which can be incorporated into the flow part of the problem to simulate bioclogging. Although MISER is limited to 2-D, versus other multiphase simulators (e.g., UTCHEM) which are 3-D, a numerical study of PCE-DNAPL migration, entrapment, and dissolution undertaken as part of this dissertation (see Objective 1) will demonstrate that 2-D numerical simulations provide good approximations to 3-D simulations.

Given the lack of existing models capable of simulating source zone microbial reductive dechlorination, phase and component mass balances will be used to demonstrate model performance. The model will also be compared to an analytical solution that forms the foundation of the popular single-phase dechlorination model BIOCHLOR [Clement et al., 1998].

Objective 3: Assess model performance through comparison with data from existing batch and 1-D column studies in the literature.

Experimental evidence has demonstrated metabolic reductive dechlorination in batch and column studies with and without PCE as the DNAPL [e.g., Yang and McCarty, 1998, 2002]. Some simplified models have been applied to the simulation of aqueous-phase batch data [e.g., Fennell and Gossett, 1998; Carr et al., 2000]. These models have been used to evaluate alternative kinetic expressions and to identify metabolic reductive dechlorination kinetic coefficients.

Batch studies with and without PCE as the DNAPL will be simulated using the dechlorination kinetics developed as part of this work to demonstrate model performance. Published data from a 1-D column contaminated with PCE as the DNAPL [Yang and McCarty, 2002] will be used to assess the modified version of MISER. This comparison will demonstrate the ability of the model to simulate contaminant degradation and bioenhanced dissolution at the macroscopic scale.

Objective 4: Investigate bioenhanced dissolution through model simulation and sensitivity analyses to parameters such as, hydraulic conditions, microbial population concentration and distribution, and source zone characteristics.

Existing modeling investigations of bioenhanced dissolution have been restricted to highly idealized systems with simplified biotransformation reactions [Seagren et al., 1993, 1994; Chu et al., 2004; Gupta and Seagren, 2005]. Simplifying assumptions have rendered these models incapable of simulating most experimental and field-scale systems.

The model developed in this work, however, is capable of simulating bioenhanced dissolution at the scale of the experimental systems. Therefore, the model can be used to investigate system factors that may control the level of dissolution enhancement and to investigate potential reasons for the disparity in the reported experimental enhancement factors. These simulations will aid in the interpretation of existing experimental results and in the design of new bioenhanced dissolution experimental studies.

CHAPTER III

MODEL DEVELOPMENT

III.A INTRODUCTION

Numerical simulations performed in support of the objectives outlined in Section II.F require the simulation of multiple physical, chemical, and biological processes. Relevant processes are summarized in the conceptual model depicted in Figure III.1. Note, that Figure III.1 neglects the presence of a gas phase. While DNAPL may be entrapped in the unsaturated zone or the capillary fringe during migration, this study focuses on DNAPLs in the saturated zone. Figure III.1 also indicates that sorption from the aqueous phase to the solid phase and dissolution from the NAPL phase into the aqueous phase are the only interphase mass transfer mechanisms considered. The biophase is assumed to respond directly to bulk aqueous phase concentrations, eliminating the need to simulate substrate uptake (see Section II.D.2). The components listed in each of the phases indicate that biotransformation may only occur in the aqueous phase. Organic components must dissolve from the NAPL or desorb from the solid phase to come in contact with the electron donor, which can either be supplied directly or be obtained through the fermentation of primary substrates. Simulating this conceptual model requires the solution of phase and component mass balance equations, which are

coupled through constitutive relationships [Barry et al., 2002]. These equations and relationships are outlined below.

The following development is kept as general as possible to facilitate the simulation of scenarios with non-uniform DNAPL saturation distributions, non-uniform flow fields, density-dependent flow, and rate-limited interphase partitioning. However, some assumptions have been made in the following development to simplify the problem: (i) isothermal conditions, (ii) soil matrix compressibility is negligible, (iii) aqueous phase viscosity is independent of composition and pressure, (iv) saturated conditions (i.e., no gas phase) in an immobile soil matrix, (v) the aqueous phase is wetting, implying the solid phase is only in contact with the aqueous phase, (vi) the spill event timescale is small relative to the dissolution timescale, which allows for the initial DNAPL migration and entrapment simulation to be decoupled from the simulation of DNAPL dissolution and degradation [Barry et al., 2002; Lemke et al., 2004b; Phelan et al., 2004], and (vii) DNAPL is immobile once the DNAPL migration and entrapment simulation (spill release scenario) ceases. The derivation of the relevant equations provided in the present work follows closely that presented by Abriola et al. [1997] and Rathfelder et al. [2000]. Given that the numerical simulations performed in this work utilize several models, more detailed descriptions of model-specific processes are provided where appropriate.

III.B PHASE MASS BALANCE EQUATIONS

Bulk phase flow in a porous medium is usually described using macroscopically averaged equations [Abriola, 1989]:

$$\frac{\partial}{\partial t}(\varepsilon_\alpha \rho_\alpha^*) - \nabla \cdot [\varepsilon_\alpha \rho_\alpha^* \mathbf{V}^\alpha] = \phi \sum_c \sum_\beta E_{\alpha\beta}^{c*} + \sum_c R_\alpha^{c*} + \rho_\alpha^* Q_\alpha \quad (\text{III.1})$$

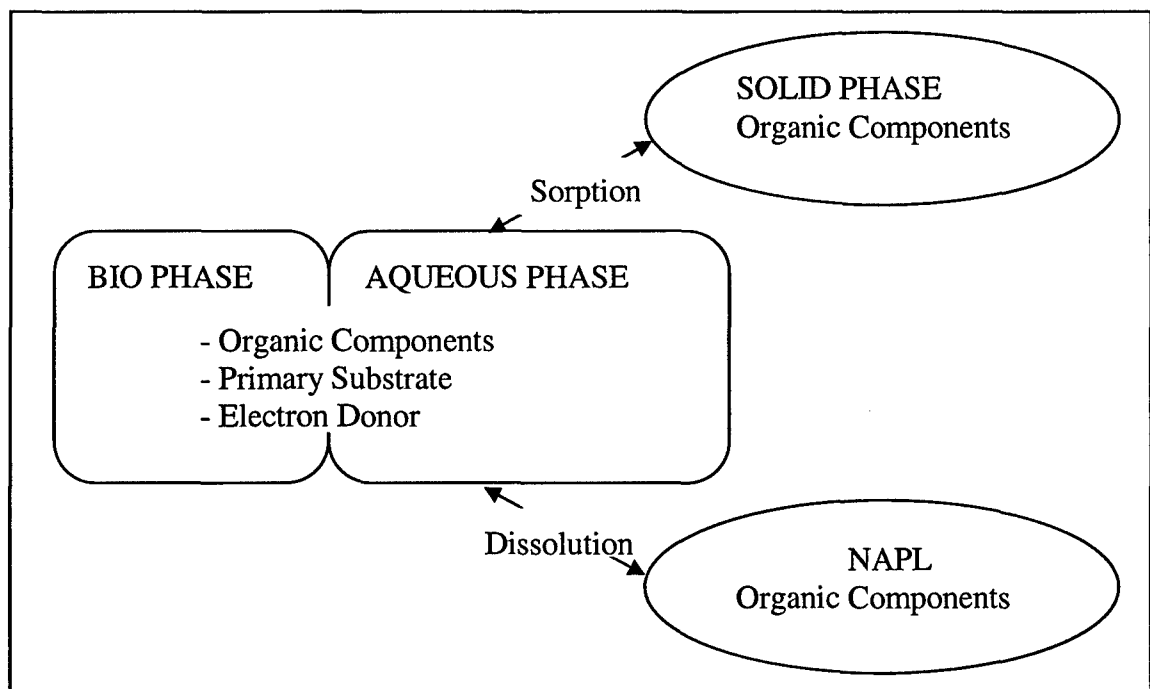


Figure III.1: Conceptual model of relevant phases, components, and interphase mass transfer mechanisms (adapted from Abriola et al., 1997).

where c denotes the component, α denotes the phase (a = aqueous, o = organic, b = biomass, s = soil), ε_α is the α -phase volume fraction, ρ_α^* is the α -phase mass density, V^α is the mass average α -phase velocity, ϕ is the matrix porosity, $E_{\alpha\beta}^{c*}$ is the mass rate of interphase mass transfer of component c from the β - to the α -phase (e.g., $\alpha = a$, $\beta = o$ or $\alpha = o$, $\beta = a$), R_α^{c*} is the mass rate of biological degradation of component c in the α -phase per unit pore volume, Q_α is an external source/sink of the α -phase, and t is time.

The mass average velocity of the α -phase is modeled using a modified version of Darcy's law:

$$q_\alpha = \phi S_\alpha V^\alpha = -\lambda_\alpha (\nabla P_\alpha - \rho_\alpha^* g \nabla z) \quad (\text{III.2})$$

which, when incorporated into equation (III.1) along with assumption (ii) in Section III.A and the substitution $\varepsilon_\alpha = \phi S_\alpha$, gives:

$$\phi \frac{\partial}{\partial t} (\rho_\alpha^* S_\alpha) - \nabla \cdot [\rho_\alpha^* \lambda_\alpha (\nabla P_\alpha - \rho_\alpha^* g \nabla z)] = \phi \sum_c \sum_\beta E_{\alpha\beta}^{c*} + \sum_c R_\alpha^{c*} + \rho_\alpha^* Q_\alpha \quad (\text{III.3})$$

where S_α and P_α are the α -phase saturation and pressure, $\lambda_\alpha = k k_{r\alpha} / \mu_\alpha$ is the α -phase mobility, k is the intrinsic permeability tensor, $k_{r\alpha}$ is the α -phase relative permeability, μ_α is the α -phase dynamic viscosity, g is the gravitational constant, and z denotes the positive downward vertical direction. Conservation of mass requires that $\sum_\alpha S_\alpha = 1$.

When simulating the initial spill event in this work (see Chapter IV), equation (III.3) is simplified by assuming immiscible flow and no reactions, so that bulk organic and aqueous phase flow can be described by:

$$\phi \frac{\partial}{\partial t} (\rho_a^* S_a) - \nabla \cdot [\rho_a^* \lambda_a (\nabla P_a - \rho_a^* g \nabla z)] = \rho_a^* Q_a \quad (\text{III.4a})$$

$$\phi \frac{\partial}{\partial t} (\rho_o^* S_o) - \nabla \cdot [\rho_o^* \lambda_o (\nabla P_o - \rho_o^* g \nabla z)] = \rho_o^* Q_a \quad (\text{III.4b})$$

III.C COMPONENT MASS BALANCE EQUATIONS

Simulating component concentrations in the bulk fluid phases (i.e., dissolution, transport, and degradation) requires the solution of a separate system of partial differential equations. In the following development, these mass balance equations are written in terms of the mole fraction of component c in the α phase (x_α^c):

$$\phi \frac{\partial}{\partial t} (S_\alpha \rho_\alpha x_\alpha^c) + \nabla \cdot \phi S_\alpha \rho_\alpha (x_\alpha^c V_\alpha - D_\alpha^c \nabla x_\alpha^c) = \phi \sum_\beta E_{\alpha\beta}^c + R_\alpha^c + Q_\alpha^c \quad (\text{III.5})$$

where ρ_α is the α -phase molar density, $E_{\alpha\beta}^c$ is the molar rate of interphase mass transfer of component c from the β to the α -phase, R_α^c is the molar rate of biological degradation of component c in the α -phase per unit pore volume, D_α^c is the hydrodynamic dispersion tensor, and Q_α^c is a source/sink of component c in the α phase. Mole fractions are constrained by $\sum_c x_\alpha^c = 1$.

The molar density of the α -phase is computed using Amagat's Law [Schwarzenbach et al., 2003], assuming the molar volume does not change due to intermolecular interaction of the mixture:

$$\rho_\alpha = \frac{1}{\sum_c \frac{x_\alpha^c MW_c}{\rho_c^*}} \quad (\text{III.6})$$

where MW_c and ρ_c^* are the molecular weight and mass density of component c , respectively.

The hydrodynamic dispersion tensor accounts for both mechanical dispersion and diffusion and is given by [Bear, 1972]:

$$\phi S_{\alpha} D_{\alpha}^c = \omega_T |q_{\alpha}| \delta_{LT} + (\omega_L - \omega_T) \frac{q_{\alpha L} q_{\alpha T}}{|q_{\alpha}|} + \phi S_{\alpha} \tau_{\alpha} D_{\alpha}^{cM} \delta_{LT} \quad (\text{III.7})$$

where ω_L and ω_T are the longitudinal and transverse dispersivity's, δ_{LT} is the Kronecker delta, D_{α}^{cM} is the molecular diffusion coefficient for component c in the α -phase, τ_{α} is the tortuosity, expressed using the relationship of Millington and Quirk [1961]:

$$\tau_{\alpha} = \frac{(\phi S_{\alpha})^{10/3}}{\phi^2} \quad (\text{III.8})$$

and $q_{\alpha L}$ and $q_{\alpha T}$ are components of the Darcy velocity in the longitudinal and transverse directions. Note, as is common in the multiphase modeling literature [e.g., Delshad et al., 1996], potential affects of saturation on the longitudinal and transverse dispersivities are neglected in this work.

III.D CONSTITUTIVE RELATIONSHIPS

As equations (III.1) and (III.5) indicate, phase and component mass balance equations are coupled through the phase saturation, pressure, mobility, molar density, average velocity, interphase exchange, and reaction terms. Therefore, closure of the system of governing equations requires the specification of constitutive relationships.

III.D.1 Capillary Pressure-Saturation Relationship

In this model, equations (III.4a) and (III.4b) are solved in terms of the aqueous phase pressure. This requires the use of the capillary pressure (P_c) (the pressure difference between the non-wetting (here, organic) and wetting (here, aqueous) fluids)

and the expansion of the temporal saturation derivatives in equation (III.4). A parametric representation of the capillary pressure-saturation relationship enables the quantification of the change in saturation due to the change in pressure ($\partial S_\alpha / \partial P_c$).

The capillary pressure can be related to the aqueous phase saturation using the Brooks and Corey [1964] parametric representation:

$$\overline{S}_a = \begin{cases} \left(\frac{P_b}{P_c} \right)^\lambda & \text{for } P_c \geq P_b \\ 1 & \text{for } P_c < P_b \end{cases} \quad (\text{III.9})$$

where P_b is the entry pressure of the porous medium, λ is the pore size index, and \overline{S}_a is the effective aqueous phase saturation, defined as a function of the actual aqueous phase saturation (S_a) and the residual aqueous phase saturation (S_{ar}) as defined by the primary drainage curve:

$$\overline{S}_a = \frac{S_a - S_{ar}}{1 - S_{ar}} \quad (\text{III.10})$$

This parametric representation was selected to avoid the significant capillary spreading that occurs when using the alternative, van Genuchten [1980] parametric representation [Rathfelder and Abriola, 1998].

Typically the entry pressure (P_b) is provided as an air-water entry pressure for a reference porous matrix. Leverett scaling is often used to correct the air-water entry pressure in the reference matrix (k_{ref} and ϕ_{ref}) to an organic-water entry pressure in an arbitrary porous matrix [Leverett, 1941]:

$$P_b = P_b^{air-water} \frac{\gamma_{ao}}{\sigma_{air-water}} \sqrt{\left(\frac{k_{ref}}{\phi_{ref}} \right) \left(\frac{\phi}{k} \right)} \quad (\text{III.11})$$

where γ_{ao} is the aqueous-organic phase interfacial tension, $\sigma_{air-water}$ is the air-water surface tension, and subscript *ref* refers to the soil properties of the reference air-water entry pressure ($P_b^{air-water}$).

Organic phase entrapment due to aqueous phase saturation reversal (hysteresis) is modeled using the method of Parker and Lenhard [1987]. This method idealizes the effective organic phase saturation (\bar{S}_o) as having a mobile fraction (\bar{S}_{of}) and an entrapped fraction (\bar{S}_{ot}):

$$\bar{S}_o = \frac{S_o}{1 - S_{ar}} = \bar{S}_{of} + \bar{S}_{ot} \quad (\text{III.12})$$

The organic phase saturation entrapped (\bar{S}_{ot}) due to saturation path reversal is computed by linearly interpolating a soil moisture characteristic scanning curve between the effective residual organic phase saturation (\bar{S}_{or}), which corresponds to the historical minimum effective aqueous phase saturation (\bar{S}_a^{\min}) (i.e., the reversal point), and zero:

$$\bar{S}_{ot} = \bar{S}_{or} \left(\frac{\bar{S}_a - \bar{S}_a^{\min}}{1 - \bar{S}_{or} - \bar{S}_a^{\min}} \right) \quad (\text{III.13})$$

\bar{S}_{or} is the effective residual organic phase saturation at zero capillary pressure and is computed as a function of the amount of water displaced at the saturation path reversal point (\bar{S}_a^{\min}) using the Land [1968] equation:

$$\bar{S}_{or} = \frac{1 - \bar{S}_a^{\min}}{1 + \left(1 - \bar{S}_a^{\min} \right) \left(\frac{1 - S_{ar} - S_{or}^{\max}}{S_{or}^{\max}} \right)} \quad (\text{III.14})$$

with S_{or}^{\max} representing the residual organic phase saturation defined by the primary imbibition curve. Figure III.2 depicts these saturation values on a representative soil moisture characteristic.

III.D.2 Relative Permeability-Saturation Relationship

Computation of phase mobilities (λ_α) requires the quantification of the relative permeability for the flowing organic and aqueous phases. The parametric model of Burdine [1953] is used to compute the aqueous phase relative permeability and is used in the derivation of the organic phase relative permeability. This model is commonly implemented in the Brooks and Corey [1964] capillary pressure framework [e.g., Lemke et al., 2004a]. The organic phase relative permeability has been modified following the method outlined in Rathfelder and Abriola [1998] to account for organic phase entrapment:

$$k_{ra} = \overline{S}_a^{\frac{2+3\lambda}{\lambda}} \quad (\text{III.15a})$$

$$k_{ro} = \left(1 - \overline{S}_a^{\frac{2+\lambda}{\lambda}}\right) \left(1 - \overline{\overline{S}}_a\right)^2 \quad (\text{III.15b})$$

where $\overline{\overline{S}}_a = \overline{S}_a + \overline{S}_{ot}$ is defined as the apparent aqueous phase saturation. The effect of organic entrapment on flow is included only in the organic phase relative permeability expression (eq. III.15b) due to the observation that organic phase entrapment has a negligible influence on the aqueous phase relative permeability [Lenhard et al., 1991].

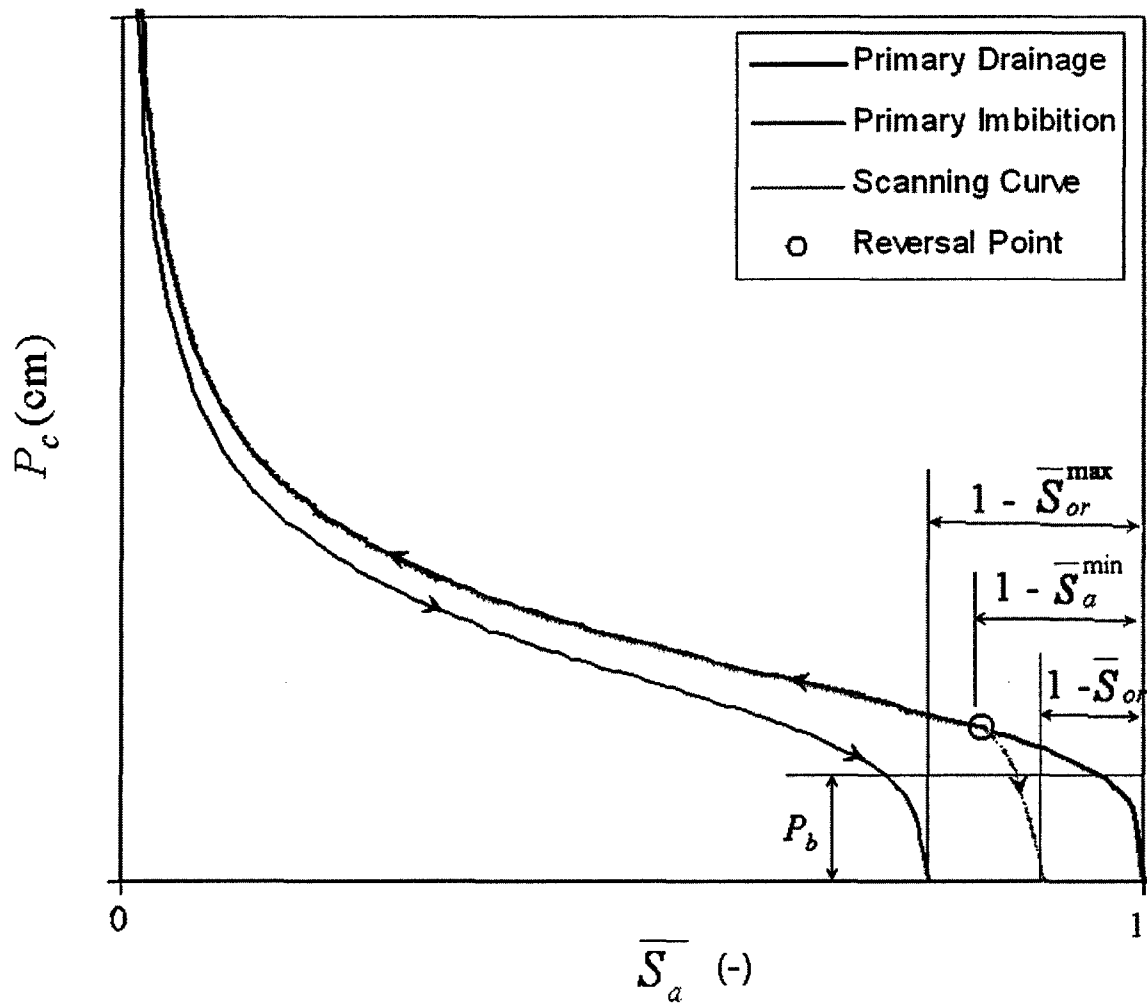


Figure III.2: Representative hysteretic soil moisture characteristic (after Parker and Lenhard [1987]).

III.D.3 Interphase Mass Exchange

Given that this work is limited to two-phase liquid flow and that the biophase is assumed to be fully penetrated (see Section II.D.2), interphase mass exchange is limited to DNAPL dissolution and solid phase sorption. DNAPL dissolution kinetics were discussed in Section II.B.2. As described there, DNAPL dissolution is generally represented mathematically using a linear driving force expression [Weber and DiGiano, 1996]:

$$E_{\alpha\beta}^c = -E_{\beta\alpha}^c = \frac{1}{MW_c} E_{\alpha\beta}^{c*} = \rho_\alpha \kappa_{\alpha\beta}^c (x_{\alpha\beta}^{c-e} - x_a^c) \quad (\text{III.16})$$

where $\kappa_{\alpha\beta}^c$ is the lumped mass transfer coefficient ($\kappa_{\alpha\beta}^c = \kappa^c \cdot a_{\alpha\beta}$) for component c between the α and β phases, κ^c is the mass transfer coefficient for component c through the controlling α -phase, $a_{\alpha\beta}$ is the specific interfacial area between the α and β phases, and $x_{\alpha\beta}^{c-e}$ is the mole fraction of component c in the α -phase at equilibrium with the β -phase, which is computed using Raoult's Law and the assumption that the activity coefficients equal one [Schwarzenbach et al., 2003]:

$$x_{\alpha\beta}^{c-e} = x_\beta^c C_\alpha^{c-sol} \quad (\text{III.17})$$

where C_α^{c-sol} is the solubility concentration of component c in the α -phase. As shown in equation (III.16), the interface between the two phases is assumed to have no mass, so that the mass lost from the β -phase is equal to the mass gained in the α -phase. Equilibrium mass transfer can be approximated using equation (III.16), by selecting a sufficiently large mass transfer coefficient ($\kappa_{\alpha\beta}^c$) (see Lang [2000]).

III.D.3.i Mass Transfer Coefficients ($\kappa_{\alpha\beta}^f$)

Mass transfer coefficients are generally expressed in terms of a Sherwood number (N_{Sh}) using correlations among dimensionless system parameters:

$$N_{Sh} = \frac{\kappa_{\alpha\beta}^f d_{50}^2}{D_a^{cM}} \quad (\text{III.18})$$

These correlations have been developed to describe DNAPL dissolution under a variety of experimental conditions (see section II.B.2) and are commonly implemented in macroscopic compositional multiphase simulators to compute the local- (grid-) scale mass transfer coefficient [Delshad et al., 1996; Dekker and Abriola, 2000b; Brusseau et al., 2002; Saenton et al., 2002; Parker and Park, 2004].

Implementation of the mass transfer coefficient in multiphase compositional simulators generally takes one of two forms. The first method of implementation utilizes mass transfer correlations that quantify a lumped mass transfer coefficient. In this method, the correlation accounts for the reduction in interfacial area ($a_{\alpha\beta}$) as the DNAPL dissolves. In the second method, the correlation is derived independently of the interfacial area ($a_{\alpha\beta}$) so that the interfacial area is modeled separately. Both methods are reviewed below since they are each applied in different models utilized in this dissertation.

III.D.3.i.1 Lumped Mass Transfer Coefficients ($\kappa_{\alpha\beta}^f$)

The simplest method to simulate rate-limited mass transfer uses a transient lumped mass transfer expression that correlates the lumped mass transfer coefficient

($\kappa_{\alpha\beta}$) to the organic phase saturation (S_o). Conditions under which lumped mass transfer correlations have been derived were reviewed in Section II.B.2.

A correlation developed by Powers et al. [1994] that incorporates the effects of the soil pore structure into the mass transfer correlation is among the most widely used [Mayer and Miller, 1996; Powers et al., 1998; Zhu and Sykes, 2000; Brusseau et al., 2002]:

$$N_{Sh} = 4.13(N_{Re})^{0.598} \left(\frac{d_{50}}{d_M} \right)^{0.673} U_i^{0.369} \left(\frac{S_o}{S_o^{t=0}} \right)^{\left(0.518 + 0.114 \left(\frac{d_{50}}{d_M} \right) + 0.10 U_i \right)} \quad (\text{III.19})$$

where N_{Re} is the Reynolds number $\left(N_{Re} = \frac{|q_a| \rho_a d_{50}}{\phi S_a \mu_a} \right)$, d_M is the diameter of a “medium” sand grain ($d_M = 0.05\text{cm}$), U_i is the uniformity index, and $S_o^{t=0}$ is the DNAPL saturation at time $t = 0$. The Powers correlation is based on transient dissolution from a NAPL that was imbibed and subsequently drained in a 1D column. The conditions under which the Powers correlation was developed are valid for the majority of the domains simulated in this dissertation: $0.0008 < S_o < 0.181$, $0.015 < N_{Re} < 0.23$ and $1.19 < U_i < 3.33$. Numerical simulation of DNAPL saturations greater than the upper limit of the Powers correlation account for only a very small fraction of the DNAPL contaminated cells (<1%). Thus, the use of this correlation for dissolution simulations performed in Chapter V of this dissertation was judged appropriate.

III.D.3.i.2 Non-lumped Mass Transfer Coefficients (κ)

A more rigorous alternative to simulating dissolution using a transient lumped mass transfer correlation [e.g., Powers et al., 1994] is to use a non-lumped mass transfer

coefficient (κ^c) and simulate the interfacial area (a_{ao}) between the organic and aqueous phases. This method provides the flexibility to simulate dissolution from a wide range of DNAPL saturations. It has been used in numerical studies of nonequilibrium dissolution [Powers et al., 1991] and field-scale DNAPL recovery [Dekker and Abriola, 2000b; Lemke et al., 2004b], and has been successfully calibrated to column dissolution data [Powers et al., 1994].

Modeling the mass transfer coefficient and the reduction in interfacial area separately facilitates the use of mass transfer coefficient correlations developed assuming steady-state dissolution. Using a steady-state analytical solution to the one-dimensional advection dispersion equation, Miller et al. [1990] derived the correlation:

$$N_{Sh} = 12N_{Re}^{0.75} N_{Sc}^{0.5} (\phi S_o)^{0.6} \quad (\text{III.20})$$

where N_{Sc} is the Schmidt number $\left(N_{Sc} = \frac{\mu_a}{\rho_a D_a^{cM}} \right)$. Powers et al. [1992] derived a similar expression using grain size parameters as a surrogate descriptor for the DNAPL saturation:

$$N_{Sh} = 57.7N_{Re}^{0.61} d_{50}^{0.64} U_i^{0.41} \quad (\text{III.21})$$

The difference in the correlations is attributed to the alternative methods used to emplace the DNAPL in the experimental systems. Miller et al. [1990] stirred NAPL into a water saturated glass bead medium resulting in a fairly uniform distribution of small spherical blobs. Powers et al. [1992] used an imbibition-drainage sequence to emplace the NAPL in aquifer soils resulting in a more heterogeneous distribution of NAPL blobs. The latter is more typical of a nonuniform DNAPL source zone. Hence, the Powers et al. [1992] correlation was employed for dissolution simulations presented in Chapter VII.

The Powers et al. [1992] correlation is for a steady-state system where changes in the DNAPL saturation are negligible. Thus, the transient nature of DNAPL dissolution is incorporated into simulations by explicitly modeling the change in interfacial area as the DNAPL dissolves. The change in saturation over a given numerical time-step is assumed small enough to allow for the use of the steady-state dissolution mass transfer coefficient, equation (III.21).

A diminishing sphere model is used to simulate the change in interfacial area as the DNAPL dissolves. In this method, the initial DNAPL saturation is assumed to be formed in m classes of spherical blobs. Each class represents a fraction (f_m) of the DNAPL saturation in a numerical cell with the same characteristic initial blob radius. The initial number of spherical blobs in each class (m) is computed from a balance on the DNAPL volume:

$$N_m^i = \frac{3\phi_m S_o^i (\Delta V)^i}{4\pi (r_m^i)^3} \quad (\text{III.22})$$

where the superscript i denotes values in the i^{th} -numerical grid-block, f_m denotes the fraction of the DNAPL saturation associated with the m -class, ΔV is the numerical grid-block volume, and r_m^i is the characteristic blob radius of class m in the i^{th} -grid-bloc. As the saturation decreases due to dissolution, the number of blobs in a class remains constant, but the blob radius (r_m^i) diminishes. This changes the specific interfacial area of DNAPL in the i^{th} -grid-block:

$$a_{ao}^i = \sum_m 3 \frac{\phi_m S_o^i}{r_m^i} \quad (\text{III.23})$$

In the limit, the DNAPL saturation in the m^{th} class will go to zero before the blob radius since the blob geometry is calculated using information from the previous time step.

Note that this development (equations III.22 and III.23) assumes that mass transfer may occur across the entire interfacial area. Some models that employ this method include a correction factor to account for the proportion of area actually in contact with the aqueous phase [e.g., Dekker and Abriola, 2000b]. In this dissertation, however, only the aqueous and organic phases are present (assumption iv in Section III.A) and the aqueous phase is wetting (assumption v in Section III.A), making the entire specific interfacial area available for mass transfer.

III.D.3.ii Solid Phase Sorption

Interphase mass transfer to the immobile solid phase is assumed to be from the aqueous phase only (i.e., aqueous phase is always wetting). Since this dissertation does not focus on the effects of sorption on simulated behavior, equilibrium was assumed and sorption was modeled using a linear isotherm. These simplifications enable the formulation of a retardation coefficient for each component c :

$$r_c = 1 + \frac{\rho_s^* K_d}{\phi} \quad (\text{III.27})$$

which can be substituted directly into the aqueous phase transport equation to account for the effects of sorption on contaminant transport:

$$\phi \frac{\partial}{\partial t} (r_c S_\alpha \rho_\alpha x_\alpha^c) + \nabla \cdot \phi S_\alpha \rho_\alpha (x_\alpha^c V_\alpha - D_\alpha^c \nabla x_\alpha^c) = \phi E_{ao}^c + R_\alpha^c \quad (\text{III.28})$$

The right hand side of equation (III.28) has been simplified to indicate that the rate-limited interphase partitioning is assumed to occur between the organic and aqueous phases only.

III.D.4 Biotransformation Reactions

Alternative methods for modeling the biophase were described in Section II.D.2. A conceptual box model and corresponding kinetic expressions describing metabolic reductive dechlorination are described in detail in Chapter VI. Therefore, this section outlines the necessary framework in which these kinetic expressions are solved.

In this dissertation, metabolic reductive dechlorination is assumed to be carried out by attached, immobile microbial populations that are able to respond directly to bulk aqueous phase concentrations. The use of these commonly employed assumptions [e.g., Hossain and Corapcioglu, 1994; Cirpka, 1995; Tonnaer et al., 1997; Clement et al., 1998] eliminates the need to assume and parameterize the attached biomass geometrical configuration [Baveye and Valocchi, 1989; Clement et al., 1996; Lensing, 1998] and to model the concentration gradient between the aqueous and biomass phases (i.e., E_{ab}^c). This allows the reaction term to be included as an internal source/sink in the flowing aqueous phase. Component degradation and microbial growth are modeled using Monod kinetic expressions, e.g.:

$$-R_a^c = k_{\max}^c X_j \frac{x_a^c}{K_S^c + x_a^c} \quad (\text{III.29a})$$

$$\frac{dX_j}{dt} = -X_j (Y^c R_a^c + b) \quad (\text{III.29b})$$

where k_{\max}^c is the component c molar maximum utilization rate, K_S^c is the molar half-saturation constant for substrate c , X_j is the mass concentration of microbial population j , Y^c is the yield of microbial mass per mole of substrate c degraded, and b is the first-order decay coefficient. The kinetic parameters (k_{\max}^c and K_S^c) quantify the affinity of a microbial population for the substrate c . As depicted in Figure III.3, a microbial

population with a low half-saturation constant will be better able to utilize the substrate than a microbial population with a higher half-saturation constant. However, at higher substrate concentrations, the microbial population with the greater maximum utilization rate will have better growth characteristics.

Commonly, the growth of biomass in the subsurface is assumed to have a negligible influence on the porosity and relative permeability of the porous medium [e.g., Delshad et al., 1996]. There is the potential for bioclogging in DNAPL source zones [Yang and McCarty, 2002], however. To account for the effects of microbial growth on aqueous phase flow and transport, the microbial concentrations are summed and used to compute a biophase saturation (S_b):

$$S_b = \frac{\sum_j X_j}{\phi \rho_b^*} \quad (\text{III.30})$$

where ρ_b^* is the biomass density, commonly assumed to be approximately equal to that of water [e.g., Abriola et al., 1997]. Recall, the saturations are constrained to sum to one (i.e., $S_a + S_o + S_b = 1$) so that the biophase saturation is assumed to reduce the aqueous phase saturation ($S_a = 1 - S_o - S_b$) [Chu et al., 2003]. When incorporated into the relative permeability computation (equation III.15), this reduced aqueous phase saturation accounts for the reduction in relative permeability due to microbial growth. This method of simulating bio-clogging can be shown equivalent to methods that have been derived in the literature using geometry-based permeability models [e.g., Clement et al., 1996; Chu et al., 2003, 2004].

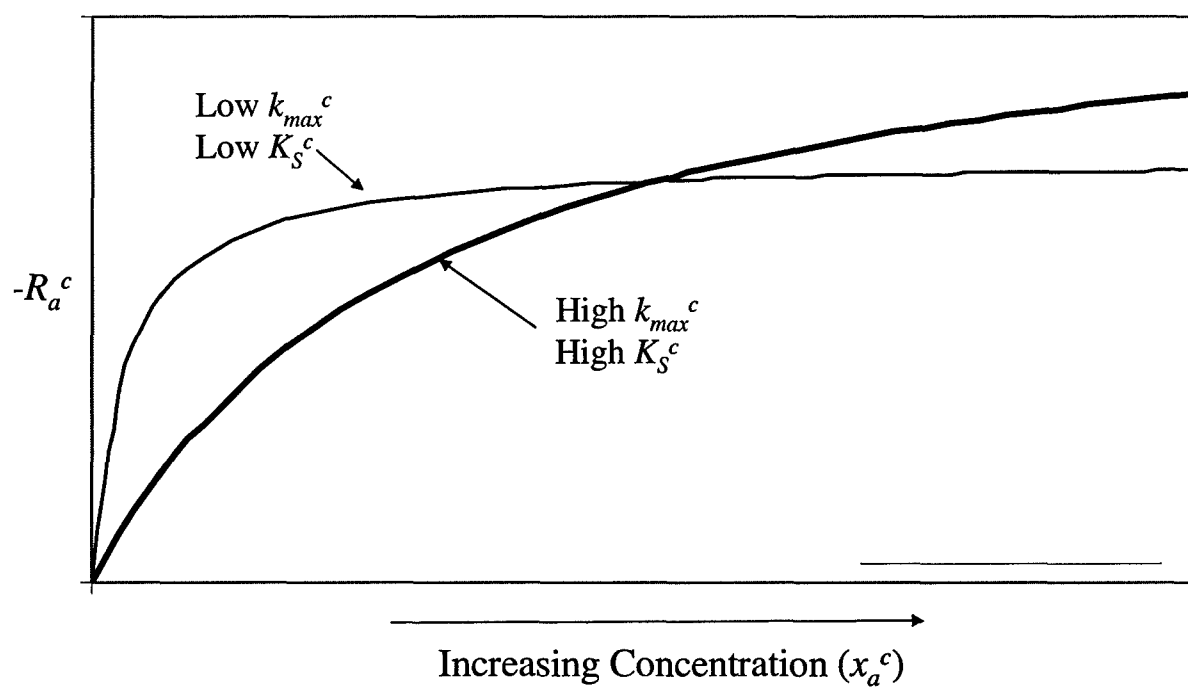


Figure III.3: Illustrative example of Monod degradation kinetics for two hypothetical microbial populations.

Existing models developed to account for reductions in porosity and permeability due to the accumulation of biomass in subsurface pores can be divided into three alternative groups: (i) biofilm based models [e.g., Taylor et al., 1990], (ii) micro-colony based models [e.g., Seki and Miyazaki, 2001], and (iii) macroscopic models [e.g., Clement et al., 1996]. Clement et al. [1996] demonstrated that, given typical aquifer conditions (e.g., particle size distribution, porosity), the biofilm and macroscopic models are equivalent with the same general form:

$$k_b = k \left(1 - \frac{\phi_f}{\phi} \right)^\xi \quad (\text{III.31})$$

where k_b is the permeability when biomass is present, ϕ is the volume fraction of the biomass ($=\phi S_b$), and ξ is a parameter related to the pore size distribution. For the conditions of their study, $\xi = 19/6$ was assumed; however, through a sensitivity analysis they demonstrated that reductions in permeability due to biomass growth were relatively insensitive to ξ . Models derived based on approximating a porous medium as a bundle of capillary tubes typical of relative permeability models (e.g., equation III.15) have also been shown to give the same relationship [Vandevivere et al., 1995]. One can show that the computation and incorporation of a biophase saturation into the relative permeability expression (equation III.15a) will result in similar expressions for biophase affected relative permeability.

To see this, equations (III.10) and (III.15a) are combined with the expression of the continuity of the phases (i.e., $S_a + S_o + S_b = 1$) to redefine the permeability of the aqueous phase:

$$kk_{ra} = k \left(\frac{S_a - S_{ar}}{1 - S_{ar}} \right)^{\frac{2+3\lambda}{\lambda}} = k \left(\frac{1 - S_o - S_b - S_{ar}}{1 - S_{ar}} \right)^{\frac{2+3\lambda}{\lambda}} \quad (\text{III.31})$$

In single phase systems where such descriptions of permeability reduction are commonly employed [e.g., Chu et al., 2003, 2004], S_o and S_{ar} are not considered and can be assumed to be zero. Hence, equation III.31 reduces to:

$$kk_{ra} = k(1 - S_b)^{\frac{2+3\lambda}{\lambda}} \quad (\text{III.32})$$

which is equivalent to equation (III.31) for $\xi = [(2 + 3\lambda)/\lambda]$. Experimental observations have indicated that a maximum reduction in permeability due to bioclogging occurs at $k_b/k \approx 0.001$ [Taylor and Jaffe, 1990; Dupin and McCarty, 2000]. At this ratio contaminant transport is assumed to be dominated by diffusion. A similar threshold is included in the relative permeability constitutive relationship when simulating a multiphase system (i.e., S_{ar} in eq. III.31). Constitutive relationships used in multiphase flow assume that upon reaching the residual aqueous phase saturation (S_{ar}), aqueous phase flow ceases ($k_{ra} = 0$) and component migration in the aqueous phase is due solely to diffusion (equation III.7).

III.E NUMERICAL IMPLEMENTATION

A number of multiphase compositional simulators developed to solve the mathematical framework outlined in the previous sections were employed in this dissertation. The 2-D University of Michigan – Vertical and Lateral Organic Redistribution (M-VALOR) simulator and a version of the 3-D University of Texas compositional multiphase simulator (UTCHEM) simplified to model immiscible two-phase flow (i.e., equation III.4) were used to investigate the influence of dimensionality

on DNAPL migration and entrapment (Chapter IV). The modular three-dimensional multi-species transport simulator (MT3DMS) was used to investigate the influence of dimensionality on DNAPL dissolution and mass recovery (Chapter V). Batch-DECHLOR, a model developed as part of this dissertation was used to simulate experimental metabolic reductive dechlorination data from the literature (Chapter VI). The University of Michigan subsurface environmental simulator (MISER) was modified to simulate metabolic reductive dechlorination kinetics in a DNAPL source zone and has been used to investigate bioenhanced dissolution in one-dimensional laboratory-scale columns (Chapter VII). These models are briefly described in the following sections and summarized in Table III.1.

III.E.1 UTCHEM and M-VALOR

UTCHEM is a three-dimensional, block-centered finite difference code that solves up to four phase mass balance equations (i.e., aqueous, organic, gas, and emulsion) and an unlimited number of component transport equations [Delshad et al., 1996]. The phase mass balance equations (e.g., III.4) are solved implicitly for pressure and back substitution is used to solve the component mass balance equations (III.5) for volumetric concentrations explicitly (see details in Chapter IV). UTCHEM is capable of simulating hysteretic DNAPL infiltration and entrapment, complex phase behavior, hydrogeochemical kinetics, and biological degradation. In this dissertation UTCHEM was used to simulate two-phase immiscible flow in nonuniform two- and three-dimensional domains. The ability of UTCHEM to simulate hysteretic infiltration and entrapment had not been verified against laboratory data or existing numerical simulation

results, however. Therefore, to provide validation for its application in this dissertation, two-dimensional DNAPL simulations generated using UTCHEM were benchmarked against simulations generated with M-VALOR [Rathfelder and Abriola, 1998]. M-VALOR is a two-dimensional block-centered finite difference multiphase flow code that has been used extensively to simulate two-dimensional, two-phase immiscible contaminant transport in lab and field-scale heterogeneous subsurface systems [Demond et al., 1996; Dekker and Abriola, 2000; Rathfelder et al., 2000; Rathfelder et al., 2003; Abriola et al., 2005].

Comparisons between two-dimensional saturation profiles generated with both models using identical input parameters led to the discovery of coding errors in the entrapment subroutine in UTCHEM. After modification of this subroutine to correctly simulate the two-phase capillary pressure – saturation – relative permeability relationship with entrapment, two-dimensional saturation distributions simulated using both models were essentially identical (maximum absolute difference in maximum organic saturation $< 2\%$), demonstrating that the modified version of UTCHEM was functioning properly. A detailed explanation of the UTCHEM coding errors and the corrections made are provided in Appendix A.

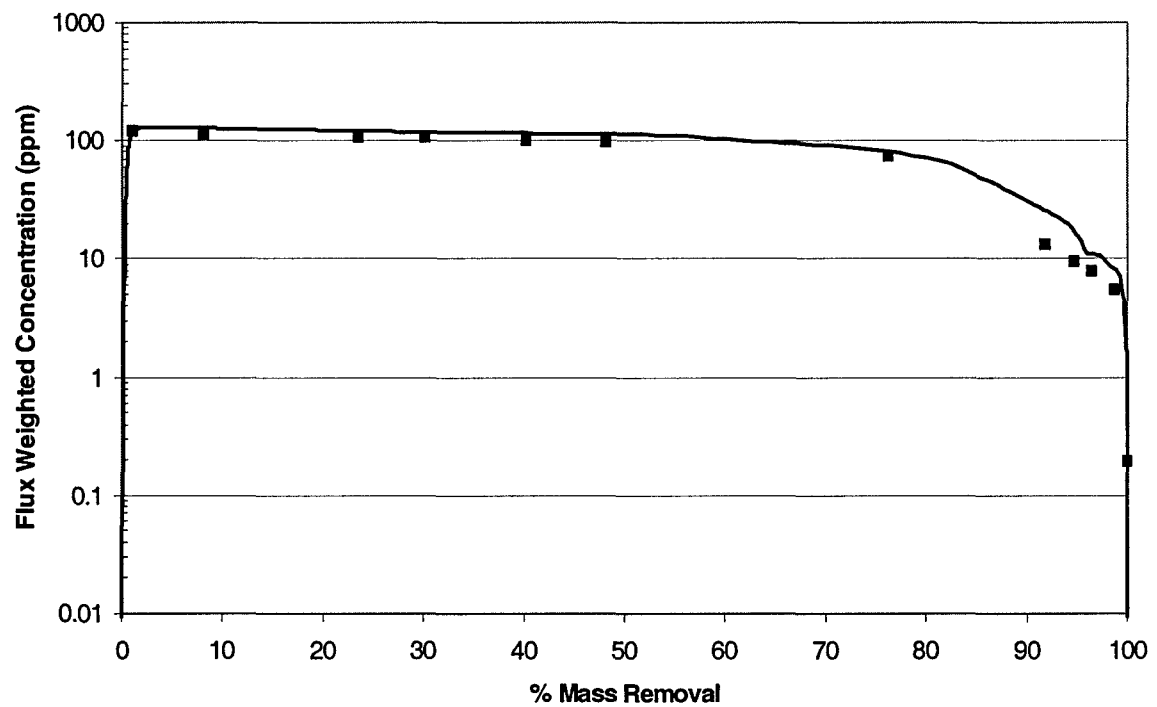


Figure III.4: Comparison of two-dimensional simulation results using MT3DMS-MODFLOW (solid line) and MISER (closed diamonds) in terms of flux-weighted contaminant concentrations versus percent mass removal.

III.E.2 MT3DMS

MT3DMS is a three-dimensional comprehensive transport model capable of simulating aqueous phase component advection, dispersion, and reaction (i.e., equation III.5) using standard finite difference methods, particle-tracking Eulerian-Lagrangian methods, or total-variation-diminishing finite volume methods [Zheng and Wang, 1999]. It is generally linked with MODFLOW [McDonald and Harbaugh, 1988], a three-dimensional block-centered finite difference code capable of simulating bulk aqueous phase flow (i.e., equation III.4). In its distributed form, MT3DMS-MODFLOW is incapable of simulating DNAPL source zones due to its lack of a simulated organic phase. In this dissertation, however, a version of MT3DMS-MODFLOW modified by Parker and Park [2004] to simulate dissolution from an immobile DNAPL phase was used. Aqueous phase mobility is corrected for the presence of an immobile organic phase using standard relative permeability expressions (e.g., equation III.15).

A comparison of flux-averaged aqueous phase concentrations due to dissolution from a PCE-DNAPL generated using the modified version of MT3DMS-MODFLOW and those generated using a compositional multiphase simulator (i.e., MISER) were demonstrated to have a root mean squared error less than 10 ppm (see Figure III.4). Flux-averaged aqueous phase concentrations are a commonly employed metric that quantifies the average contaminant concentration weighted by the proportion of aqueous phase flux associated with a given concentration across a down-gradient boundary (e.g., Lemke et al., 2004b). As shown in Figure III.4, the most significant difference in the flux averaged concentration data occurs at mass removal levels greater than 80 percent. This difference is likely caused by the difference between the mass transfer coefficient

correlations used in the two models. MT3DMS-MODFLOW uses the Powers et al. [1994] lumped mass transfer coefficient (i.e., equation III.19) while MISER uses the Powers et al. [1992] non-lumped mass transfer coefficient (see equation III.21 and discussion in Section III.D.3.i.2). At high levels of mass removal, the lumped mass transfer coefficient appears to result in slightly higher flux-averaged concentrations, which could be considered conservative in terms of contaminant mass flux or non-conservative in terms of source longevity. There is no evidence, however, that the effect of mass transfer coefficient selection on simulated results will differ with simulation dimensionality, which was the focus of the portion of this dissertation that utilized MT3DMS-MODFLOW.

III.E.3 Batch-DECHLOR

Batch-DECHLOR is a simulation-optimization model capable of fitting biological kinetic coefficients for aqueous and aqueous-NAPL batch data. The model is based on a simulation-optimization model developed in Dr. H. Scott Fogler's research group at the University of Michigan – Ann Arbor. This original model was modified to simulate metabolic reductive dechlorination of multiple chlorinated contaminants, growth of multiple microbial species, and dissolution from a DNAPL. The model incorporates existing solution routines provided in the high-level technical computing framework MATLAB. Ordinary differential equations describing the rate of change of component and microbial species concentrations are solved using one of the existing MATLAB solver subroutines (i.e., ode45 or ode15s). These solvers make use of explicit Runge-Kutta or numerical differentiation formulas to solve the system of equations [Hanselman and Littlefield, 2001]. Simulated results are compared to experimentally generated data

using absolute or root mean squared errors. An optimization solver subroutine in MATLAB (fminsearch), which is based on a simplex algorithm, is used to minimize the absolute or root mean squared error between the simulated and experimental data, by adjusting a vector of biological kinetic coefficients (e.g., k_{max}). Penalty functions are included to prevent the selection of nonphysical kinetic coefficients (e.g., values less than zero). This model is described in detail and used in Chapter VI to evaluate the ability of the dechlorination kinetics to model laboratory experiments provided in the literature and from collaborating colleagues at the Georgia Institute of Technology.

III.E.4 MISER

MISER, originally developed for soil vapor extraction/bioventing design [Abriola et al., 1997; Rathfelder et al., 2000] and later modified to simulate surfactant flushing [Dekker and Abriola, 2000b], is a two-dimensional, three-phase (aqueous-organic-gas), multi-component simulator capable of simulating aerobic degradation of multiple contaminants flowing in the aqueous phase. Linear Galerkin finite-elements are used to solve for NAPL dissolution (NAPL is assumed to be immobile), gas and aqueous phase flow, and contaminant transport. MISER has been linked to a two-phase (aqueous-organic) immiscible flow model (M-VALOR) [Abriola et al., 1992], to successfully model soil vapor extraction, bioventing, and surfactant flushing at both the laboratory- and field-scale [Abriola et al., 1997; Dekker and Abriola, 2000b; Rathfelder et al., 2000, 2001; Taylor et al., 2003; Lemke et al., 2004b].

For this dissertation, the biological degradation model in MISER was modified to enable the simulation of metabolic reductive dechlorination in a DNAPL source zone. This endeavor required the modification of multiple existing modules in MISER:

- Incorporation of kinetic expressions describing primary substrate fermentation, metabolic reductive dechlorination, and methanogenesis due to the activity of multiple microbial species
- Incorporation of multiple, spatially nonuniform microbial species capable of growing at different rates due to aqueous phase component transformations
- Computation of a biophase saturation to account for the effects of biomass growth on aqueous phase flow (i.e., aqueous phase relative permeability and saturation)
- Incorporation of a dynamic time-step adjustment to ensure good mass balance of aqueous phase components when bioreaction terms are lagged a time-step

Chapter VII provides a detailed explanation of the required modifications. These modifications enable the simulation of bioenhanced dissolution from immobile DNAPLs, a process no existing macroscopic compositional multiphase simulator is capable of doing [NRC, 2004]. Furthermore, the solution routine in MISER, which employs a sequential iterative algorithm to solve the phase and component mass balance equations, minimizes errors introduced using more traditional sequential non-iterative approaches (i.e., operator splitting, which decouples the transport and degradation processes) [Hammond et al., 2005]. The solution scheme implemented in MISER is diagrammed in Appendix B.

Model	Modeled Process	Dim.	Mass Transfer
M-VALOR	Two-phase immiscible DNAPL infiltration and entrapment (equation III.4)	2-D	immiscible
UTCHEM	Two-phase immiscible DNAPL infiltration and entrapment (equation III.4)	3-D	immiscible
MT3DMS	Dissolution from immobile NAPL and component transport (equation III.5)	3-D	Powers et al. [1994] lumped correlation (Section III.D.3.i.1)
Batch-DECHLOR	NAPL dissolution and aqueous phase dechlorination (equation III.5)	Batch	Powers et al. [1992] with diminishing sphere model (Section III.D.3.i.2)
MISER	Bulk aqueous phase flow, dissolution from an immobile NAPL, component transport and dechlorination (equations III.4 and III.5)	2-D	Powers et al. [1992] with diminishing sphere model (Section III.D.3.i.2)

Table III.1: Summary of numerical models employed in this dissertation.

CHAPTER IV

DIMENSIONALITY EFFECTS ON SIMULATIONS OF DNAPL MIGRATION AND ENTRAPMENT IN NONUNIFORM POROUS MEDIA

IV.A INTRODUCTION

As described in Chapter I, the bulk of the studies investigating the benefits of partial mass removal from DNAPL source zones has employed compositional multiphase models. These models have typically been used to simulate NAPL contaminant migration and dissolution in two-dimensional flow fields [Kueper and Frind, 1991; Essaid and Hess, 1993; Essaid et al., 1993; Brown et al., 1994; Kueper and Gerhard, 1995; Bradford et al., 1998; Dekker and Abriola, 2000a, b; Whittaker et al., 2000; Lemke et al., 2004a, b; Phelan et al., 2004], with relatively few studies undertaking three-dimensional simulations. Implicit in these 2-D investigations is the assumption that DNAPL migration and dissolution is relatively unaffected by the nominal 2-D domain width and porous medium property variability in the third dimension. However, to date, the validity of this assumption has not been systematically investigated. Existing modeling studies that have considered the third dimension typically have done so for a single realization and have neglected heterogeneity and/or hysteretic capillary effects [Faust et al., 1989; Brown et al., 1994; Panday et al., 1994; Edwards et al., 1999; Parker

and Park, 2004]. Guarnaccia and Pinder [1998] appear to be the only researchers to consider the effect of reduced model dimensionality on the prediction of the DNAPL distribution. However, they did so for a single homogeneous realization at the lab-scale (1m x 1m x 0.3m). Thus, no study has systematically investigated the effect of dimensionality on the simulation of infiltration and entrapment of DNAPL in field-scale nonuniform porous media. If it could be shown that 2-D simulations provide reasonable representations of 3-D behavior, then it would be justifiable to investigate DNAPL source zone processes in the more computationally efficient 2-D domain. Conversely, the identification of consistent differences between 2-D and 3-D simulations could lead to improved interpretations of 2D modeling and laboratory results.

The purpose of this portion of the dissertation is to investigate the effect of reduced dimensionality on simulated DNAPL saturation distributions using a suite of three-dimensional, statistically homogeneous, nonuniform permeability fields that is representative of a natural formation. DNAPL saturation distribution metrics are used to quantitatively compare predictions of DNAPL entrapment in two and three dimensions. Variations in contaminant recovery predictions due to reduced dimensionality (2-D v. 3-D) will be investigated in Chapter V. The results of these analyses will support the decision to use a 2-D model for the simulation of source zone metabolic reductive dechlorination (Chapter VII).

IV.B METHODS

DNAPL migration and entrapment simulations were performed in two and three dimensions using a version of UTCHEM [Delshad et al., 1996], modified to simulate hysteretic infiltration and entrapment in nonuniform permeability fields (Appendix A).

IV.B.1 Mathematical Model

Rather than solving the component mass balance equation in terms of mass of component c in phase α (i.e., equation III.5) as described in Section III.E.1, UTCHEM solves a conservation equation in terms of the overall volume of component c per unit pore volume (\tilde{C}_c) [Delshad et al., 1996]:

$$\frac{\partial}{\partial t}(\phi \tilde{C}_c \rho_c^*) = \nabla \cdot \left[\sum_{\alpha=1}^{n_p} \rho_c^* (C_c^\alpha \lambda_\alpha \cdot (\nabla P^\alpha - \rho^\alpha g \nabla z) - \phi S_\alpha D_c^\alpha \cdot \nabla C_c^\alpha) \right] + R_c \quad (\text{IV.1})$$

where

$$\tilde{C}_c = (1 - \hat{C}_c) \sum_{\alpha=1}^{n_p} S_\alpha C_c^\alpha + \hat{C}_c \quad (\text{IV.2})$$

n_p is the number of phases, ρ_c^* is the density of component c , C_c^α is the concentration of component c in phase α , \hat{C}_c is the sorbed concentration of component c , and all other parameters are as given in Section III.C. Development of equation IV.1 assumes slightly compressible porous media and fluids and accounts for mass transfer across phase boundaries. Simulation of DNAPL migration and entrapment in this chapter, however considers the immiscible flow of a pure DNAPL in the saturated zone. Thus, $C_c^\alpha = 0$ or 1, $\hat{C}_c = 0$, and $\tilde{C}_c = S_a$ or S_o , which reduces equation IV.1 to the phase mass balance equations for organic and aqueous phase flow (i.e., equation III.4). This simplified form

of equation IV.1 is solved using a uniform block-centered finite difference grid with the IMPES-type scheme described in Section III.E.1. Several upstream weighting options are available for the advection term. In this work, first order upstream weighting was selected to facilitate the comparison with M-VALOR, as described in Appendix A.

IV.B.2 Problem Description

To investigate the effect of reduced dimensionality on DNAPL saturation distributions, 21 3-D permeability realizations were selected from a suite of realizations developed by Lemke et al. [2004a]. These realizations are representative of a field-scale formation, whose properties are based on an aquifer located in Oscoda, Michigan, USA. This aquifer underlies a former dry cleaning business and is contaminated with PCE. It is composed of relatively homogeneous glacial outwash sands and was the site of a pilot-scale SEAR test designed to remove residual PCE from a known source zone [Abriola, et al., 2005]. The realizations were selected based on DNAPL mass distribution metrics (maximum organic saturation and vertical and lateral spreading) calculated from the results of 50 2-D PCE infiltration simulations generated using MVALOR [Lemke et al., 2004a]. Realizations representing the *minimum*, *mean*, and *maximum* values for three selected metrics (see below) were chosen to span the range of variability. Four additional realizations with metric values approximately corresponding to the 0.2, 0.4, 0.6, and 0.8 quantiles were selected for each metric. These selection criteria resulted in some duplication of the realizations chosen, so that the number of unique 3-D permeability realizations was actually 16. To facilitate direct comparisons between 2-D and 3-D simulations, the 2-D realizations used in this study were extracted directly from the center

x - z cross section of the 3-D simulation (Figure IV.1), resulting in 16 3-D and 16 2-D permeability realizations. This number of realizations is similar to the number employed for previous DNAPL saturation distribution studies [Kueper and Gerhard, 1995; Dekker and Abriola, 2000a], but was not large enough to ensure mean behavior in this subset of simulations reproduced mean behavior in the ensemble of 50 realizations simulated by Lemke et al. [2004a]. Mean maximum organic saturations and lateral spreading differed by 4 percent. Mean vertical spreading differed by 17 percent. These differences reflected the intent of this study to examine dimensionality effects on DNAPL simulations for a broad range of behavior, rather than trying to reproduce mean behavior observed in the ensemble of 50 simulations.

The size of the 3-D modeling domain (7.925m long (x) by 7.925m wide (y) by 9.754m deep (z)) was selected to be consistent with the installed remediation system and was oriented so that the center x - z cross-section (henceforth referred to as the center cross-section) connected the SEAR extraction well with the center injection well (Figure IV.1) [Lemke et al., 2004a]. To resolve the influence of capillary property variation at the modeled scale of heterogeneity (30.48 cm), the 3-D domain was discretized into 86,528 cells with 26 cells in the x -direction ($\Delta x = 30.48$ cm), 26 cells in the y -direction ($\Delta y = 30.48$ cm), and 128 cells in the z -direction ($\Delta z = 7.62$ cm). This level of spatial resolution represents a reasonable trade-off between model accuracy and computational demands [Rathfelder and Abriola, 1998; Glass et al., 2000; Lemke et al., 2004a]. In all simulations, the upper and lower boundaries of the domain were specified as no flow boundaries and the side boundaries were specified at a constant hydrostatic pressure corresponding to a constant organic liquid saturation equal to zero. The domain size was

sufficiently extensive such that no organic phase crossed the lateral boundaries during any simulation. A uniform saturation ($S_a = 1.0$) corresponding to hydrostatic conditions was specified at time $t = 0$.

Porous media properties of the selected realizations were based on 167 samples collected from vertical and directional cores at the Oscoda site [Abriola et al., 2005]. Statistically homogeneous, nonuniform permeability fields were generated using sequential Gaussian simulation (SGS) [Deutsch and Journel, 1998] following the procedure outlined by Lemke et al. [2004a]. These efforts utilized a zonal anisotropy model [Journel and Huijbregts, 1978] with a nugget effect and a spherical semivariogram. Variability in the horizontal plane was modeled as isotropic and a uniform vertical to horizontal permeability ratio of 0.5 was assigned to all cells to account for anisotropy due to aquifer stratification at a scale not resolved by the geostatistical methods. A uniform porosity of 0.36 was used in all simulations. The mean hydraulic conductivity, K , value was 16.8 m/d and the variance of the lognormal transformed K field ($\sigma^2 \ln(K)$) was 0.29 [Lemke et al., 2004a]. Soil properties are summarized in Table IV.1.

The P_c - S_α - $k_{r\alpha}$ relationship implemented in this work combined the Brooks-Corey [Brooks and Corey, 1964] P_c - S_α model with the Burdine [1953] $k_{r\alpha}$ -model integrated into the hysteretic entrapment model developed by Parker and Lenhard [1987] as described in Sections III.D.1 and III.D.2. A representative P_c - S_α soil moisture characteristic curve was derived from aquifer samples using the method of Haverkamp and Parlange [1986]. Capillary properties are summarized in Table IV.1. Leverett [1941] scaling (equation III.11) was used to scale this reference (*ref*) P_c - S_α curve to k and ϕ in each cell, with porosity assumed to be uniform ($\phi = \phi^{ef}$).

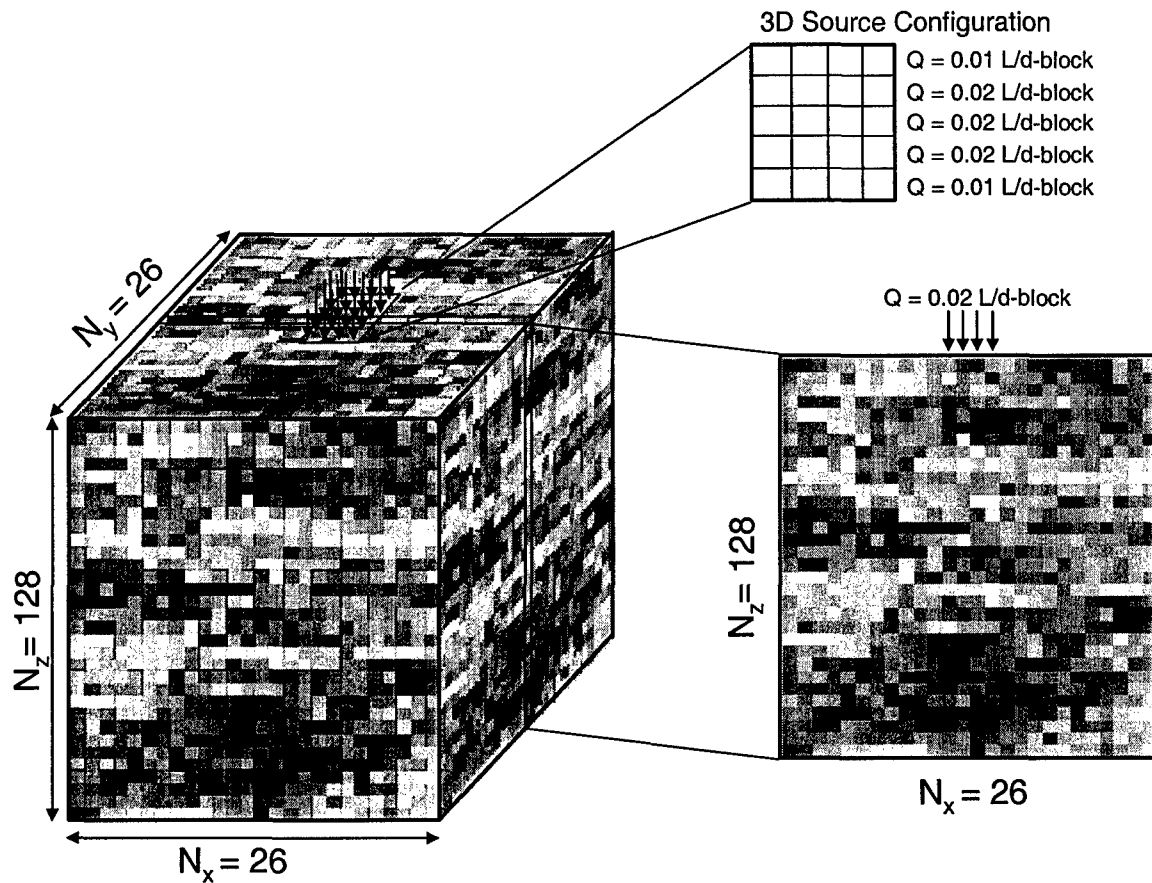


Figure IV.1: Model domain conceptualization for 2-D and 3-D simulations. The nominal width of the 2-D domain is equal to the width of the 3-D cross section and the release rate configuration in 3-D was selected so that the sum of the rows (x -direction) was equal to the sum of the columns (y -direction).

A hypothetical DNAPL spill, consistent with the suspected release from the former dry cleaner, was simulated in the 16 3-D realizations by releasing 128 liters of PCE over a 400 day period in a 4 x 5 cell area centered in the top layer of the 3-D model. As shown in Figure IV.1, the release rate in each cell block was selected to approximate a symmetric source by balancing the sum of the release rates in the x - and y -directions. For 2-D simulations, PCE was released at an equivalent rate (0.02 L/d) in each of the center four cells of the top layer of the center 2-D cross section (Figure IV.1), corresponding to a total of 32L of PCE released over the 400 day period. In all simulations the 400-day spill event was followed by a 330-day redistribution period to allow for organic entrapment.

IV.B.3 Saturation Distribution Metrics

To quantify the similarities and differences in saturation distributions simulated in 2-D and 3-D, four DNAPL mass distribution metrics were examined: (1) the maximum organic saturation (S_o^{max}), (2) the second spatial moment about the center of mass in the x -direction (σ_{xx}^2), (3) the second spatial moment about the center of mass in the z -direction (σ_{zz}^2), and (4) the saturation distribution ganglia-to-pool (GTP) mass ratio. Spatial moments are a commonly used metric for quantifying saturation distributions [Kueper and Frind, 1991; Essaid and Hess, 1993; Kueper and Gerhard, 1995; Lemke et al., 2004a] and may be defined as:

$$M_{ij} = \int_{-\infty}^{\infty} \int_{-\infty}^{\infty} n \rho_o s_o(x, z) x^i z^j dx dz \quad (IV.3)$$

Parameter		
Fluid Properties		
Density (g/cm ³)	Water	PCE
	0.999032	1.625
Viscosity (cP)	1.121	0.89
Compressibility (Pa ⁻¹)	4.4 x 10 ⁻¹⁰	0.0
Initial saturation	1.0	0.0
<i>P_c-s_α-k_{rα}</i> Model Parameters		
(Ref) Air entry pressure (kPa)	2.809	
Pore size index	2.0773	
Interfacial tensions		
Air/Water (dynes/cm)	72.75	
PCE/Water (dynes/cm)	47.8	
Irreducible water saturation	0.080	
Max residual organic saturation	0.151	
Matrix Properties		
Variogram parameters	Horizontal	Vertical
Nugget	0.333	0.333
Range (m)	7.0	1.07
Integral scale (m)	2.33	0.36
Porosity	0.36	
Reference permeability (μm ²)	19.7	
Domain Discretization		
Δx (m)	0.3048	
Δy (m)	0.3048	
Δz (m)	0.0726	

Table IV.1: Numerical simulation input parameters for 2-D and 3-D numerical simulations using UTCHEM.

The second spatial moment about the center of mass is then:

$$\sigma_{xx}^2 = \frac{M_{20}}{M_{00}} - X_{cm}^2 \quad \text{and} \quad \sigma_{zz}^2 = \frac{M_{02}}{M_{00}} - Z_{cm}^2 \quad (\text{IV.4})$$

where

$$X_{cm} = \frac{M_{10}}{M_{00}} \quad \text{and} \quad Z_{cm} = \frac{M_{01}}{M_{00}} \quad (\text{IV.5})$$

are the center of mass in the horizontal (X_{cm}) and vertical directions (Z_{cm}), respectively. In equations IV.3 to IV.5, x is the horizontal coordinate, z is the vertical coordinate, and i and j are the moment orders. M_{00} , the zeroth moment, is a measure of the organic mass in the domain.

The GTP mass ratio is a metric recently used to quantify the temporal evolution of a source zone [Lemke et al., 2004b] and is defined as the mass of PCE in cells with organic saturations less than the maximum residual organic saturation (ganglia) divided by the mass of PCE in cells with saturations greater than or equal to the maximum residual organic saturation (pools). This mass ratio may be a better indicator of subsequent dissolution behavior of DNAPL saturation distributions [Lemke et al., 2004b] than X_{cm} or Z_{cm} , which are reported here for completeness.

The metrics above were calculated for the saturation distributions simulated in the 16 selected 3-D permeability realizations and the 16 corresponding 2-D permeability realizations. In addition, 2-D saturation metrics for the center x - z cross section of each 3-D simulation were examined (2-D in 3-D). Statistical tests were used to determine the extent of similarity between the two- and three-dimensional DNAPL saturation distributions. The realizations were ranked according to their corresponding metric values to investigate migration and entrapment behavior for the ensemble of realizations.

The saturation structure of the 3-D simulations was also used to investigate the assumption of statistical isotropy of permeability imposed in the horizontal plane.

Finally, the influence of nonuniformity was further investigated by performing additional simulations in selected realizations with a higher degree of spatial variability. The three realizations that had previously generated the *min*, *mean*, and *max* s_o^{max} values (a normally distributed metric) in the center cross section of the 3-D domain were transformed by scaling the permeability field from $\sigma^2 \ln(K) = 0.29$ to $\sigma^2 \ln(K) = 1.0$.

IV.C RESULTS AND ANALYSIS

IV.C.1 Saturation distribution comparisons

Comparison of saturation distributions simulated in 2-D with those computed for the center x - z cross section of 3-D simulations illustrate some general similarities and differences that are typically encountered. Figure IV.2 depicts two representative PCE saturation distributions (all 16 simulations are depicted in Appendix C); one generated in 2-D (IV.2a) and the other in 3-D (IV.2b) using a profile extracted from the 3-D permeability realization. The 3-D realization has been sliced to reveal the center x - z cross section corresponding to the 2-D domain. Despite the presence of identical permeability fields and release rates in the cross-section, the appearance of the saturation distributions generated in 2-D and 3-D is quite different. The saturation distribution in the 3-D model appears more discontinuous, has a higher center of mass (Z_{cm}), and displays less spreading in the vertical direction. These characteristics are attributed to the movement of PCE out of the plane into adjacent sections and were generally observed in all 16 simulation comparisons. Note, however, that high saturation cells, indicative of

pools, appear at many of the same locations in both the 2-D and 3-D realizations. This observation is important, given the significance of pools in governing the persistence of DNAPL in a source zone [Anderson et al., 1992; Sale and McWhorter, 2001; Lemke et al., 2004b] and the influence pools have on the value of the distribution metrics.

Although the appearance of the saturation distributions simulated in 2-D and 3-D for a single realization can appear quite different (Figure IV.2), the behavior of the ensemble of realizations must be considered to assess the ability of 2-D simulations to adequately represent 3-D simulations. Ensemble statistics calculated for the saturation moment metrics described in Section IV.B.3 are reported in Table IV.2 for both 2-D simulations and 2-D cross sections extracted from 3-D simulations (2-D in 3-D). The mean spreading metric values calculated in 2-D simulations tend to be approximately 20-30% higher than the metrics derived from “2-D in 3-D” simulations. A paired t-test [Devore, 1995] confirmed that the 2-D simulation metrics are greater than the “2-D in 3-D” simulation metrics at the 98-99% (depending on the metric) confidence level. The variance in spreading metric values for this ensemble of 16 realizations is approximately twice as large in 2-D simulations as it is in 2-D cross sections extracted from 3-D simulations (2-D in 3-D). This variability is better visualized in Figure IV.3, which compares the distribution of metric values in 2-D and “2-D in 3-D” using box plots. In this figure each box represents the inter-quartile range and is separated by the median. The vertical lines extend to the minimum and maximum metric values and the points represent outliers as described in the figure caption. For the simulated conditions, the 2-D simulations tend to predict increased spreading in the lateral and vertical dimensions in addition to higher maximum saturations.

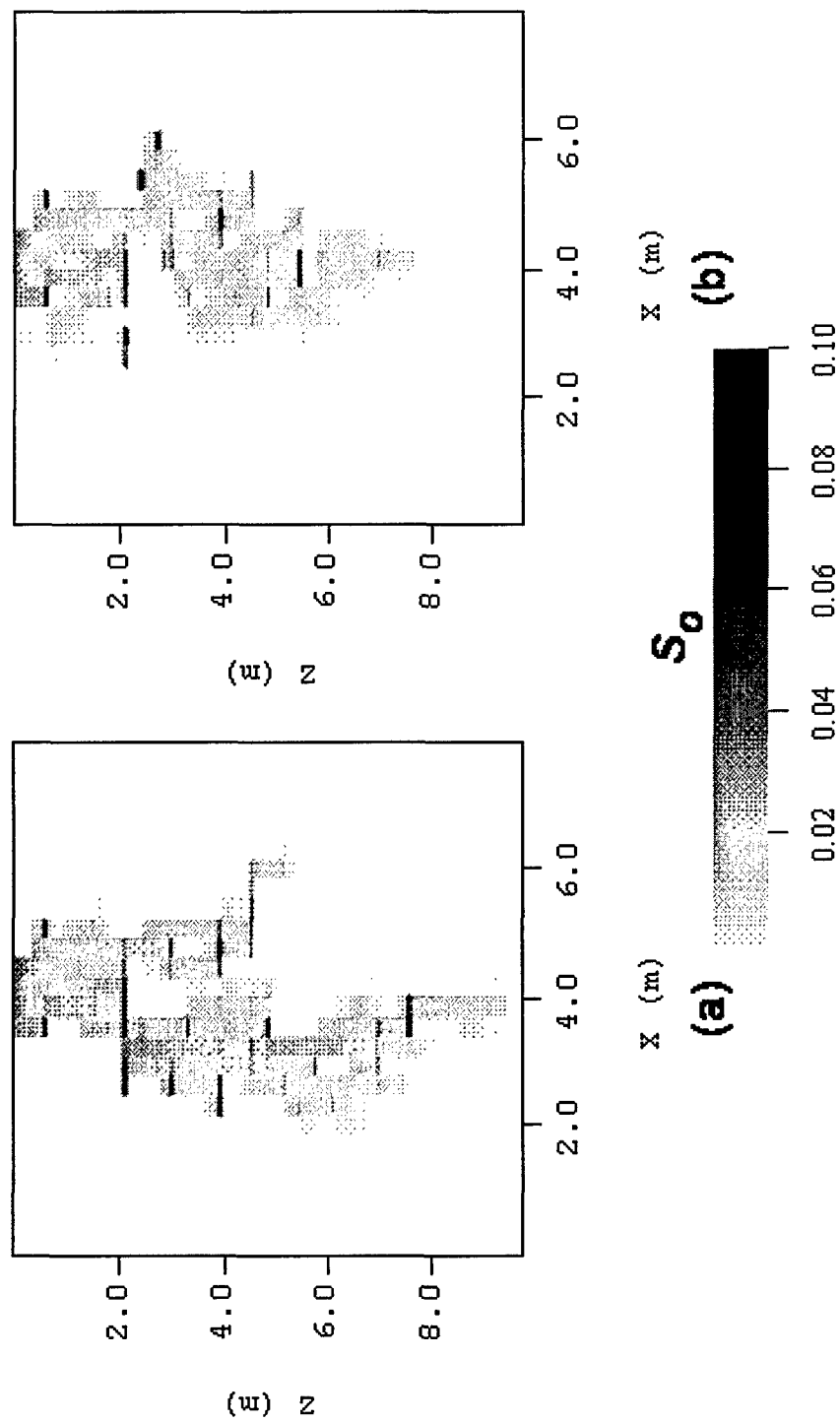


Figure IV.2: Saturation profiles simulated in (a) 2D using UTCHEM and (b) in the same 2D slice extracted from a 3D UTCHEM simulation.

Metric	Min	Mean	Max	Std. Dev.
2-D S_o^{\max}	0.172	0.363	0.626	0.127
2-D in 3-D ^a S_o^{\max}	0.134	0.277	0.442	0.101
3-D ^b S_o^{\max}	0.272	0.390	0.494	0.055
2-D X_{cm}	3.593	4.014	5.064	0.400
2-D in 3-D X_{cm}	3.531	3.939	4.320	0.250
3-D X_{cm}	3.671	3.943	4.339	0.166
2-D σ_{xx}^2	0.303	0.696	1.759	0.423
2-D in 3-D σ_{xx}^2	0.291	0.480	0.717	0.142
3-D σ_{xx}^2	0.304	0.444	0.584	0.092
2-D Z_{cm}	2.748	3.969	4.736	0.627
2-D in 3-D Z_{cm}	2.255	3.147	3.880	0.501
3-D Z_{cm}	2.527	3.275	4.252	0.403
2-D σ_{zz}^2	2.403	5.176	8.777	2.031
2-D in 3-D σ_{zz}^2	1.971	3.656	5.385	1.088
3-D σ_{zz}^2	2.018	3.790	7.797	1.372
2-D GTP	1.343	8.930	24.081	6.789
2-D in 3-D GTP ^c	2.880	18.631	∞	19.081
3-D GTP	3.874	10.324	23.05	5.160

^a Metrics calculated for center 2-D x - z cross section in 3-D simulation

^b Metrics calculated for entire 3-D domain

^c The one realization that resulted in an infinite GTP mass ratio was ignored for the statistical calculations.

Table IV.2: Statistics for saturation distribution metrics in 2-D and 3-D realizations ($\sigma^2 \ln(k) = 0.29$).

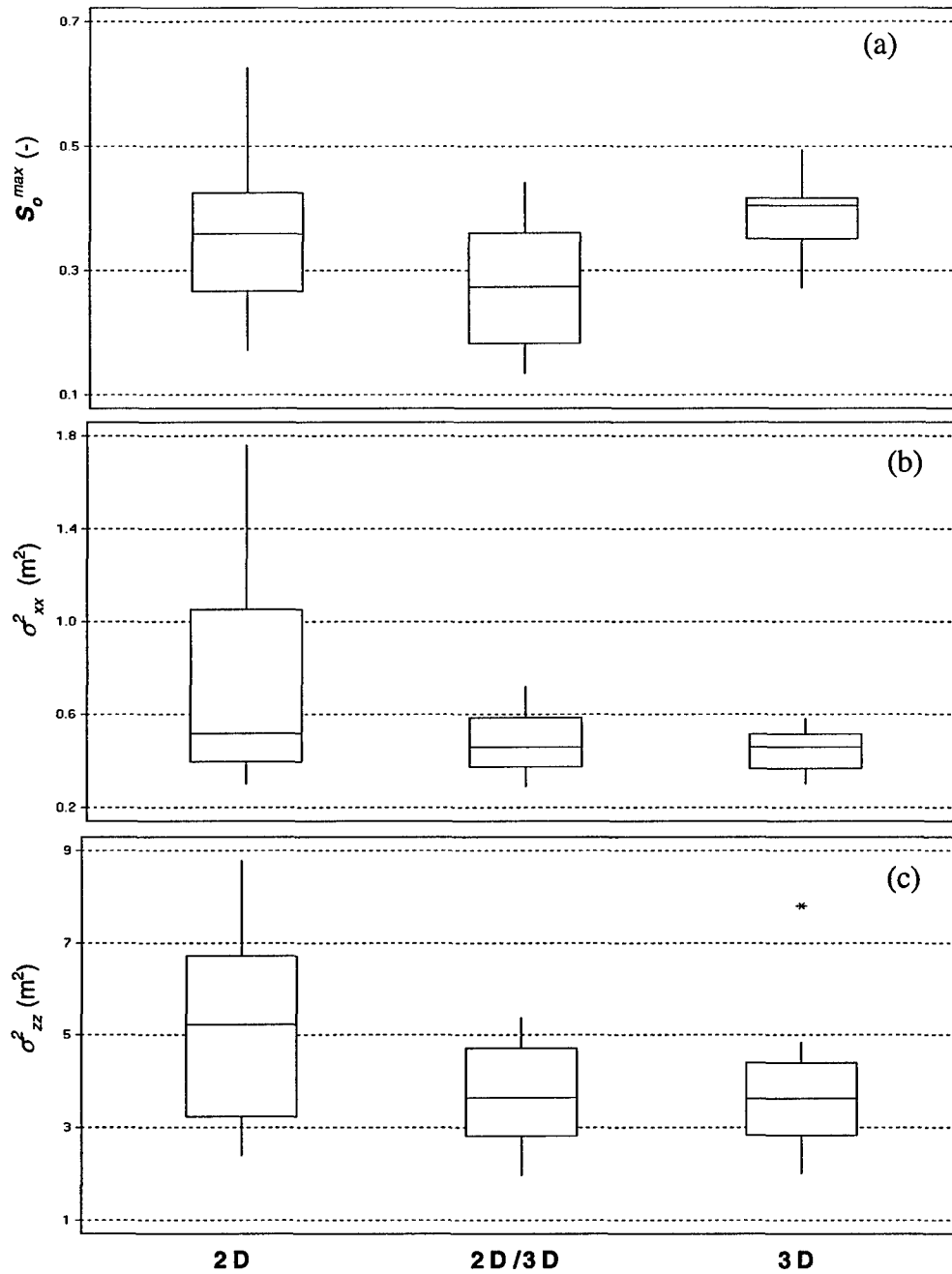


Figure IV.3: Box plot comparing 2-D, “2-D in 3-D”, and 3-D metric distributions for all 16 permeability realizations: (a) S_o^{max} , (b) σ_{xx}^2 , and (c) σ_{zz}^2 . The box extends from the $q_{0.25}$ to the $q_{0.75}$ quartile (inter quartile range - IQR) and is separated by the median. The whiskers extend from the box to the min and max metric value within $1.5 \cdot IQR$. An asterisk indicates a probable outlier (metric value $> 3 \cdot IQR$).

Alternatively, the ability of 2-D simulations to represent the saturation distributions simulated in the entire 3-D domain can be assessed by comparing saturation distribution spreading metrics calculated in 2-D and in 3-D. Statistics calculated for the ensemble of 3-D saturation distribution metrics are also given in Table IV.2. Mean metric values calculated in 3-D simulations are within 10-30% of metrics calculated in 2-D simulations and the 2-D metrics are slightly larger than the 3-D metrics. S_o^{max} is the only metric that does not follow this trend. Figure IV.3 shows that S_o^{max} for 2-D simulations are slightly lower than S_o^{max} calculated for the entire 3-D domain. A paired t-test [Devore, 1995] showed that, in contrast to the 2-D v. "2-D in 3-D" comparison, the 2-D and 3-D mean S_o^{max} values are equivalent at the 95% confidence level.

The equivalence of S_o^{max} in 2-D and 3-D, however, may be an artifact of the selected spill volume or source strength (release rate). Other investigators (e.g., Kueper and Gerhard [1995]) have demonstrated that saturation distribution metric values in 2-D simulations were sensitive to the release rate and spill volume. Therefore, to assess the influence of these factors on the S_o^{max} observation in this study, three realizations corresponding to the *min*, *mean*, and *max* S_o^{max} values simulated in "2-D in 3-D" were selected from the set of 16. Two additional spill volumes (64L and 192L) were simulated in each realization by adjusting the duration of the spill (i.e., the release rate remained unchanged) and one additional release rate was simulated by doubling the source strength to 0.64 l/d. Spill volume results are presented in Table IV.3 and release rate results are presented in Table IV.4. As shown in Table IV.3, an increase in spill volume resulted in an increase in the S_o^{max} value, however the increase was observed in both 2-D and 3-D, suggesting that the approximate equivalence of S_o^{max} in 2-D and 3-D is independent of

spill volume. The spreading metrics reported in Table IV.3 also support the general observation that lateral and vertical spreading in 2-D will, on average, be greater than that simulated in 3-D, regardless of the spill volume. For the range of source strengths considered here, S_o^{max} was insensitive to the release rate (Table IV.4). Spreading metrics decreased slightly due primarily to larger initial water displacement and subsequently more entrapment. Dimensionality did not appear to affect these results.

As an alternative to the comparison of selected metric values, a Q-Q plot can be used to compare the 2-D and 3-D saturation distributions directly. This plot is commonly found in the geostatistical literature [Goovaerts, 1997] and is based on the comparison of cumulative distribution functions. For this analysis, a cumulative distribution function (CDF) of PCE saturations was generated for each 2-D and 3-D realization using all cells in the domain with a saturation greater than 0.0001. The 2-D and 3-D CDFs were averaged separately to generate two ensemble CDF's that were then used to generate the Q-Q plot (Figure IV.4) [Goovaerts, 1997]. This figure compares the average saturation for each CDF quantile. Much like a normality test, the degree to which values plot along the 1:1 line is an indication of the similarity in distributions. An examination of Figure IV.4 shows that the ensemble CDF in two and three dimensions is visually similar, with the 2-D CDF generally resulting in saturations 15-50% higher at the same quantile. This observation, when combined with the results previously presented for the individual metrics, supports the premise that DNAPL infiltration and entrapment simulations conducted in 2-D domains will result in slightly higher estimates of NAPL saturations than simulations conducted in fully 3-D domains.

Spill Volume	S_o^{max} (-)		X_{cm} (m)		Z_{cm} (m)		σ_{xx}^2 (m ²)		σ_{zz}^2 (m ²)	
<i>min</i>	2-D	3-D	2-D	3-D	2-D	3-D	2-D	3-D	2-D	3-D
64L	0.217	0.332	3.941	4.060	2.654	2.236	0.279	0.242	2.444	2.197
128L	0.223	0.334	3.669	4.061	4.725	3.629	0.388	0.328	8.107	4.691
192L	0.498*	0.425	3.390	4.041	6.170	4.631	1.191	0.422	10.571	6.958
<i>mean</i>	2-D	3-D	2-D	3-D	2-D	3-D	2-D	3-D	2-D	3-D
64L	0.305	0.396	3.752	3.877	2.379	2.038	0.366	0.259	1.608	1.291
128L	0.354	0.397	3.758	3.865	3.579	3.164	1.115	0.464	2.882	2.613
192L	0.356	0.397	3.828	3.851	4.779	4.103	1.563	0.607	5.833	4.482
<i>max</i>	2-D	3-D	2-D	3-D	2-D	3-D	2-D	3-D	2-D	3-D
64L	0.436	0.441	3.820	3.879	2.557	2.109	0.199	0.224	2.359	1.684
128L	0.440	0.442	3.813	3.671	4.270	3.469	0.402	0.546	5.655	4.009
192L	0.472*	0.442	3.765	3.571	5.558	4.515	0.747	0.697	8.611	6.263

Note: In all 2-D cases the spill volume is ¼ the volume reported in the left hand column

*These saturations were larger than observed for other spill volumes due to pooling of NAPL on the bottom no-flow boundary.

Table IV.3: Saturation distribution metrics for three alternative realizations subject to three different spill volumes. Spill volumes were changed by increasing or decreasing the duration of the spill event. In all simulations the contaminant release rate in a given block remained unchanged.

Release Rate l/d	S_o^{max} (-)		X_{cm} (m)		Z_{cm} (m)		σ_{xx}^2 (m ²)		σ_{zz}^2 (m ²)	
<i>min</i>	2-D	3-D	2-D	3-D	2-D	3-D	2-D	3-D	2-D	3-D
0.32	0.223	0.334	3.669	4.061	4.725	3.629	0.388	0.328	8.107	4.691
0.64	0.227	0.337	3.714	4.052	4.005	3.140	0.364	0.291	5.859	3.761
<i>mean</i>	2-D	3-D	2-D	3-D	2-D	3-D	2-D	3-D	2-D	3-D
0.32	0.354	0.397	3.758	3.865	3.579	3.164	1.115	0.464	2.882	2.613
0.64	0.354	0.398	3.741	3.861	3.230	2.796	0.876	0.390	2.498	2.188
<i>max</i>	2-D	3-D	2-D	3-D	2-D	3-D	2-D	3-D	2-D	3-D
0.32	0.440	0.442	3.813	3.671	4.270	3.469	0.402	0.546	5.655	4.009
0.64	0.441	0.444	3.803	3.740	3.726	3.026	0.331	0.447	4.330	3.177

Note: In all 2-D cases the spill volume is ¼ the 3-D spill volume

Table IV.4: Saturation distribution metrics for three alternative realizations subject to two different release rates. In all simulations, spill volume remained unchanged.

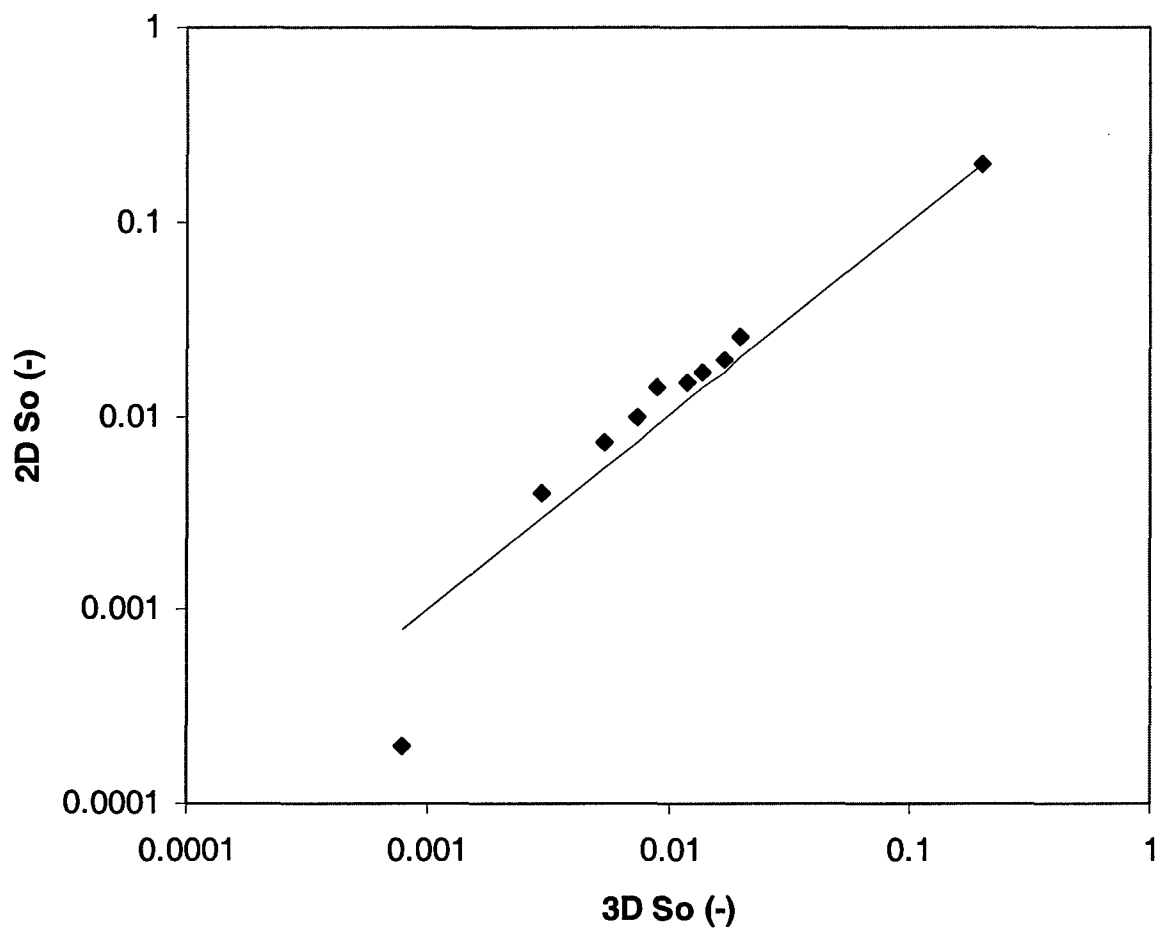


Figure IV.4: Q-Q plot comparing saturation CDF's generated using all contaminated cells ($s_o > 0.0001$) in 2-D and 3-D domains. Low value corresponds to 10th-percentile and may be an artifact of the large difference (~ 1 order-of-magnitude) in the number of cells with a quantifiable saturation in 2-D and 3-D domains.

In contrast to the spreading metrics discussed above, which quantify the spatial distribution of DNAPL saturation values in the domain, Lemke et al. [2004b] recently showed that long-term dissolution behavior can be significantly influenced by the distribution of mass between cells classified as pools and ganglia. This distribution of mass can be quantified by the GTP mass ratio defined in section IV.B.3. Figure IV.5 is a scatterplot of 3-D and “2-D in 3-D” versus 2-D GTP mass ratios for all 16 realizations considered in this study. From this figure, a positive trend in the simulated mass distribution is apparent. Despite the fact that several points do not follow the general trend, there is a statistically significant ($p\text{-value} = 0.0016$) positive correlation ($= 0.721$) between the 3-D and 2-D data (closed boxes) and the “2-D in 3-D” and 2-D data (open boxes, $\rho = 0.765$, $p\text{-value} = 0.0002$). In both the 3-D and “2-D in 3-D” comparisons, 75% of the data points fall above a 1:1 line, indicating that the mass distributions simulated in 2-D generally resulted in higher levels of mass trapped in pools, which could affect predictions of source longevity [Anderson et al., 1992; Sale and McWhorter, 2001].

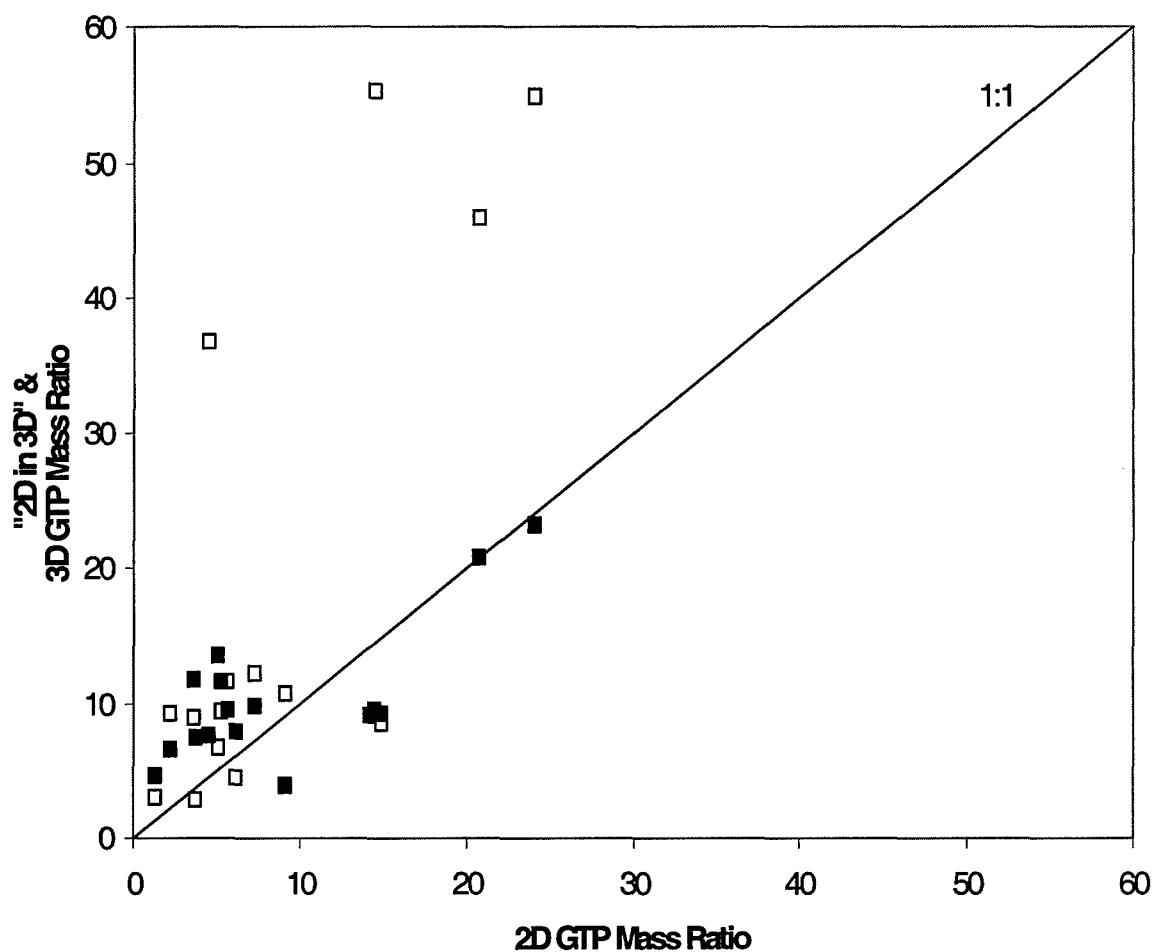


Figure IV.5: Scatterplot of 2-D versus “2-D in 3-D” (open boxes) and 3-D (closed boxes) ganglia-to-pool (GTP) mass ratios. Note, one “2-D in 3-D” realization had a GTP mass ratio = ∞ . This point is not shown.

IV.C.2 Realization rank calculations

To compare the degree of variability in metric values across the ensemble of realizations simulated in two and three dimensions, each realization was rank ordered according to its metric value. Ranks of the 2-D simulations were plotted against ranks of the corresponding 2-D cross sections extracted from 3-D simulations and ranks of the corresponding 3-D simulations (Figure IV.6). Spearman rank correlation coefficients [Statistix, 1996] for all combinations are given in Table IV.5. The rank correlation coefficients for 2-D simulations and 2-D cross sections extracted from 3-D simulations are significant at or above the 95% confidence level for all metrics, indicating that 2-D cross sections representing average or extreme metric values tended to reproduce average or extreme metric values in the corresponding 2-D cross section in the 3-D domain. The same is true when comparing 2-D and 3-D simulations except for the σ_{xx}^2 metric (Figure IV.6e). The lower statistical correlation of the metric between 2-D and 3-D simulations may result from the greater variability in spreading in the x -direction in 2-D simulations than in 3-D simulations. In fact, the metric standard deviation for the 3-D simulations is smallest for all 5 of the metrics in Table IV.2. Thus, evaluating behavior over the entire 3-D domain appears to have a smoothing effect on the metrics selected for analysis in this study.

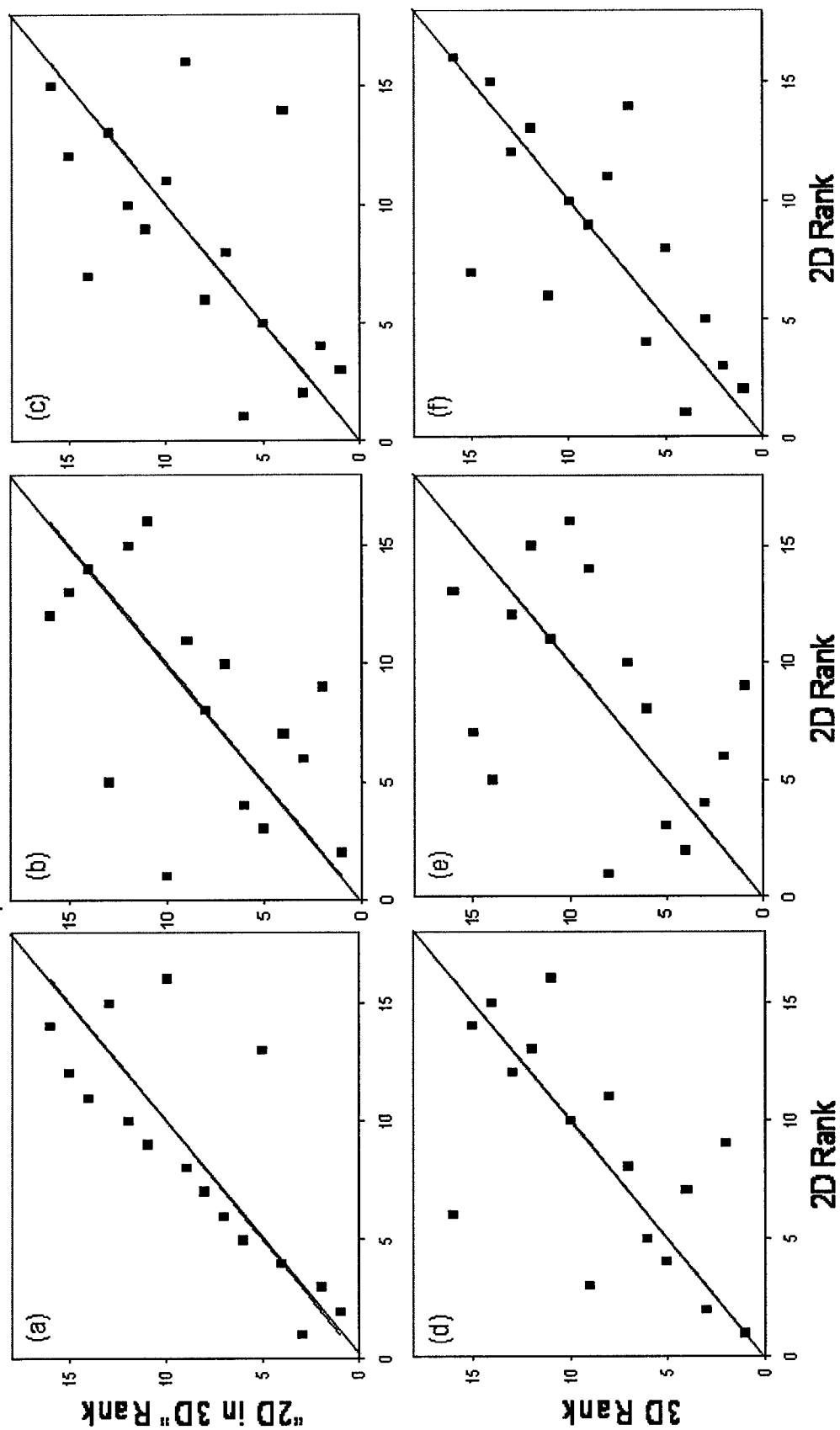


Figure IV.6: Scatterplots of realization ranks based on metric values: (a) 2D v. "2D in 3D" s_{2xx} , (b) 2D v. "2D in 3D" s_{2zz} , (c) 2D v. 3D s_{2xx} , (d) 2D v. 3D s_{2zz} , (e) 2D v. 3D s_{2xx} , (f) 2D v. 3D s_{2zz} .

	s_o^{\max}	σ_{xx}^2	σ_{zz}^2
2-D v. 2-D in 3-D (significance level) ^a	0.788 (99.5%)	0.576 (95%)	0.624 (98%)
2-D v. 3-D (significance level) ^a	0.653 (98.5%)	0.447 (<95%)	0.738 (99.4%)

^a One minus the significance level is the percent likelihood that the calculated correlation is due to chance.

Table IV.5: Spearman rank correlation coefficients for 2-D and 3-D simulation comparisons.

IV.C.3 Variability in the horizontal direction

Performing DNAPL migration and entrapment simulations in 3-D gives the opportunity to investigate spreading behavior in different directions. One potential regulatory compliance alternative to Maximum Contaminant Levels (MCLs) discussed in Chapter I is a regulatory threshold based on contaminant mass flux estimates through a down-gradient plane of compliance [Rao et al., 2002; Stroo et al., 2003; NRC, 2004]. The NAPL saturation distribution in the horizontal direction perpendicular to the direction of groundwater flow is very important to the determination of mass flux [Feenstra et al., 1996; Einarson and Mackay, 2001; Rao et al., 2002; Lemke et al., 2004b]. Typical 2-D models assume a nominal dimension in the direction perpendicular to flow [e.g., Abriola et al., 1992]. Hence, upscaling 2D simulations of source zone dissolution to 3-D is problematic. One logical approach is to assume that horizontal isotropy in permeability will lead to an isotropic source configuration (e.g., $\sigma_{xx}^2 = \sigma_{yy}^2$).

To evaluate this hypothesis, the suite of 16 three-dimensional simulations was analyzed to determine if isotropic variability of permeability in the horizontal direction is associated with a symmetric source configuration. Substituting y for x in equations IV.3 to IV.5 facilitates the calculation of the center of mass in the y -direction (Y_{cm}) and the second spatial moment about that center of mass (σ_{yy}^2). A scatterplot of σ_{xx}^2 v. σ_{yy}^2 for the 16 realizations is shown in Figure IV.7. It is apparent from this figure that there is no correlation between spreading in the x - and y -direction ($\rho = 0.311$). The mean spreading for the suite of realizations in each direction, however, is statistically identical at the 95% confidence level using a paired t-test. These results suggest that spreading in the x - and

y-direction may be different for any realization, but the average spreading in each direction across an ensemble of realizations is expected to be the same.

The variability among realizations observed in Figure IV.7 is possibly due to the release rate or extent (area) of the spill, which extends across approximately $\frac{1}{2}$ the horizontal integral scale of the permeability field. In a 2-D study investigating the influence of source dimensions on spreading, Kueper and Gerhard [1995] found that the degree of lateral spreading was highly dependent on the permeability field near the spill release area for spills with dimensions less than the permeability field integral scale. In a separate numerical experiment, these authors also show that as the rate of release increases both the degree of lateral spreading and the tortuosity of the infiltrating DNAPL path decrease. Hence, the DNAPL mass distribution for any single realization as well as the average spreading over a suite of realizations is expected to become even more symmetric as the spill area or release rate increases. Note, however, for the higher release rate discussed in Section IV.C.1, only a marginal increase ($\sim 4\%$) in the symmetry, denoted as equality between σ_{xx}^2 and σ_{yy}^2 , was observed. Therefore, while the results of this study show that the ensemble average 2-D spreading metric will provide a good approximation to this metric for a symmetric 3-D source zone, symmetric 3-D spreading for an individual realization is likely to be realized only at sites where the source zone area is larger than the integral scale or the release rate is larger than those considered here.

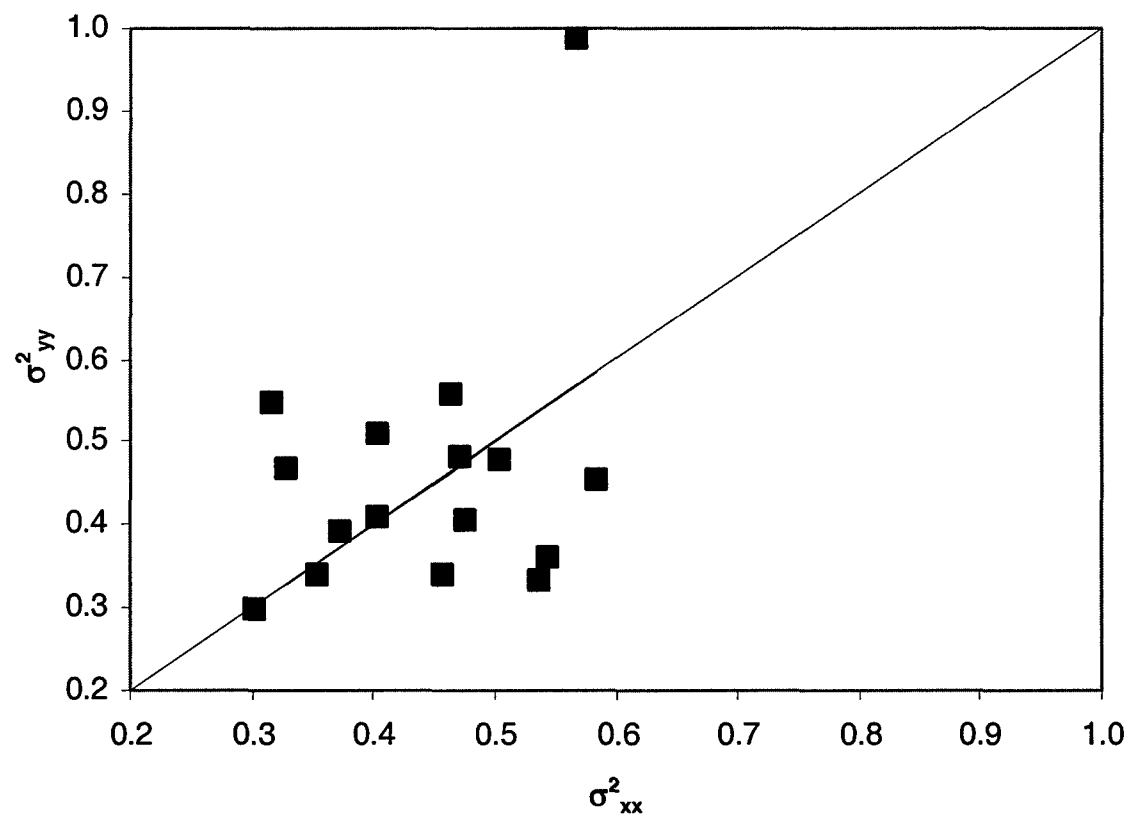


Figure IV.7: Scatterplot of σ^2_{xx} v. σ^2_{yy} metrics for 16 3-D simulations.

IV.C.4 Influence of Increased $\sigma^2 \ln(K)$

The simulations reported previously were for a relatively homogeneous (low variance) porous medium. To explore the influence of increasing nonuniformity on the conclusions reported here, additional simulations were performed with different permeability fields. Three 3-D permeability realizations (chosen based on the *min*, *mean*, and *max* “2-D in 3-D” S_o^{max} values) were transformed from a field where $\sigma^2 \ln(K) = 0.29$, which corresponded to the Bachman aquifer, to one where $\sigma^2 \ln(K) = 1.0$, corresponding to a moderately nonuniform aquifer. The center 2-D cross section was then extracted from the 3-D domain and 2-D and 3-D simulations were performed using UTCHEM. All simulation parameters, other than the permeability field, remained the same.

Although it is difficult to calculate meaningful statistics with three realizations, the results of these simulations are consistent with most of the observations made using the 16 lower variance permeability realizations. Comparison of the metrics calculated for the higher and lower variance realizations (Table IV.6) shows that the maximum saturation and horizontal spreading generally increase with variance, while the GTP mass ratio and the horizontal and vertical centers of mass decrease, regardless of dimensionality. Changes in vertical spreading due to an increase in the variance appear to be dependent on the individual realization, but not on the dimensionality. As with the original set of 16 realizations, the 2-D S_o^{max} , σ_{xx}^2 , and σ_{zz}^2 metric values are generally larger and the GTP mass ratio is generally smaller than the “2-D in 3-D” simulation metric values and the relative rank of the realization for each metric remains unchanged at the higher variance. Comparing the higher variance 2-D and 3-D results shows that, as observed for the ensemble of 16 realizations, the S_o^{max} metric values and GTP mass ratios

are closely related (generally <20% difference). Spreading metrics, however, are more difficult to interpret. 2-D versus 3-D comparisons of lateral spreading are realization dependent and only 2 out of the 3 selected realizations (*min* and *max*) result in 3-D vertical spreading that is smaller than in 2-D. This behavior could be an artifact of the SGS routine used to generate the permeability field or could reflect the fact that these three realizations were selected based on maximum saturations without regard for spreading behavior. SGS routines tend to maximize the entropy in the simulated field [Deutsch and Journel, 1998] and, as observed in Table IV.2 and Figure IV.3, spreading metrics were generally characterized by much greater variability. Thus, the conclusions of this study regarding 2-D and 3-D lateral spreading should be used with caution when considering aquifers characterized by a more highly nonuniform permeability field or a heterogeneous permeability field with discrete, multimodal populations of k values. As the degree of nonuniformity increases, it may become necessary to perform migration and entrapment simulations in 3D domains to capture the degree of lateral and vertical spreading.

Metric	$\sigma^2 \ln(K) =$ Simulation	<i>min</i>		<i>mean</i>		<i>max</i>	
		0.29	1.0	0.29	1.0	0.29	1.0
S_o^{\max}	2-D	0.223	0.521	0.354	0.508	0.440	0.602
	2-D in 3-D ^a	0.134	0.268	0.275	0.464	0.442	0.584
	3-D ^b	0.334	0.618	0.397	0.587	0.442	0.584
X_{cm}	2-D	3.669	3.746	3.758	3.404	3.813	3.254
	2-D in 3-D	4.222	3.989	3.533	2.879	3.531	3.458
	3-D	4.060	4.191	3.865	3.379	3.671	3.488
σ^2_{xx}	2-D	0.388	0.479	1.115	0.952	0.402	0.868
	2-D in 3-D	0.389	0.438	0.692	1.347	0.642	0.777
	3-D	0.328	0.534	0.464	1.480	0.546	0.737
Z_{cm}	2-D	4.725	5.744	3.575	2.925	4.270	4.110
	2-D in 3-D	3.880	3.317	2.660	2.844	3.749	3.230
	3-D	3.629	3.132	3.164	3.013	3.469	3.098
σ^2_{zz}	2-D	8.107	9.891	2.882	1.852	5.655	4.799
	2-D in 3-D	5.385	3.448	1.971	2.005	4.371	3.713
	3-D	4.691	2.805	2.613	2.893	4.009	2.839
GTP	2-D	14.26	1.79	3.63	1.22	14.91	1.76
	2-D in 3-D	∞	4.89	8.83	2.54	8.39	2.31
	3-D	9.03	1.49	11.69	1.88	9.22	2.13

^a Metrics calculated for center 2-D x-z cross section in 3D simulation

^b Metrics calculated for entire 3-D domain

Table IV.6: Statistics for saturation distribution metrics in 2-D and 3-D realizations with $\sigma^2 \ln(K) = 0.29$ and 1.0. A GTP mass ratio = ∞ indicates the maximum saturation is less than the residual organic saturation in all cells in the domain.

IV.D CONCLUSIONS

The influence of dimensionality on the simulation of realistic DNAPL source zone saturation distributions was investigated by conducting numerical simulations in 16 alternative realizations of a three dimensional, statistically homogeneous, nonuniform permeability field using the multiphase flow simulator, UTCHEM. This work appears to be the first to document use of the hysteretic entrapment model in UTCHEM, although coding corrections were required for its proper implementation (see Appendix A).

A reduction in dimensionality from 3-D to 2-D was shown to have a reasonably consistent impact on the predicted characteristics of the DNAPL source zone. Direct scaling of these metrics from 2-D to 3-D is not possible, however, based on the results of this study. 2-D simulations tended to have a 20-30% higher maximum NAPL saturation and increased spreading in the horizontal (x) and vertical (z) directions when compared to equivalent 2-D cross-sections extracted from 3-D domains. The maximum saturations simulated in 2-D and the fully 3-D domains were shown to be statistically identical at the 95% confidence level. A comparison of GTP mass ratios for 2-D and 3-D simulations demonstrated that the simulated distribution of mass between pools and ganglia in 2-D was positively correlated to the mass distribution simulated in 3-D. Variability in 2-D and 3-D NAPL saturation distributions across realizations was shown to be similar, thus indicating that extreme behavior in a 3-D realization will often be reflected in simulations conducted in 2-D slices extracted from the same 3-D realization. Horizontal isotropic variability (x versus y) did not result in a symmetric x - y saturation distribution for any individual 3-D realization. However, *average* spreading in the horizontal direction was symmetric for the 16 simulated realizations. This suggests that ensembles of 2-D

realizations can be analyzed to infer average DNAPL infiltration and entrapment behavior along 2-D transects, irrespective of their orientation, when horizontal isotropy and bedding can be assumed.

The observations reported above were also found to be valid for a small subset of realizations with an increased variance in the permeability field ($\sigma^2 \ln(K) = 1$). However, as the variance in the permeability field increased, lateral spreading of the DNAPL was enhanced in the 3-D simulations to a greater extent than in the 2-D simulations. This observation suggests that it may be necessary to perform 3-D simulations to capture the increased lateral spreading in highly variable formations.

For statistically homogeneous, nonuniform permeability fields generated using SGS, the implications of this work are that DNAPL saturation distributions simulated in 2-D capture the essential characteristics, as quantified by the selected metrics, of a more realistic 3-D DNAPL saturation distribution. Hence, for the analysis of DNAPL infiltration and entrapment behavior using the selected metrics, the more computationally efficient 2-D simulations can provide a good approximation to the fully 3-D simulation. However, caution must be used when considering highly nonuniform aquifers or aquifers that do not have horizontal bedding. In Chapter V, the saturation distributions simulated here will be used to investigate whether equivalent migration and entrapment behavior simulated in 2-D and in 3-D will lead to equivalent aqueous phase concentrations and mass recovery.

CHAPTER V

DIMENSIONALITY EFFECTS ON SIMULATIONS OF DNAPL MASS RECOVERY IN NONUNIFORM POROUS MEDIA

V.A INTRODUCTION

The numerical investigation presented in Chapter IV suggested that DNAPL saturation distributions simulated in two dimensions (2-D) will have properties similar to those simulated in three dimensions (3-D). This investigation did not, however, consider the influence of dimensionality on DNAPL dissolution and mass recovery. Estimated benefits of partial mass removal and source zone bioremediation will depend heavily on the simulated aqueous phase concentrations due to dissolution. If it can be shown that 2-D simulations of the aqueous phase concentrations in a DNAPL source zone provide reasonable approximations to 3-D simulations, then the use of 2-D simulations to investigate the benefits of partial mass removal and to simulate source zone bioremediation will be supported.

In this chapter, a suite of 2-D and 3-D realizations corresponding to that investigated in Chapter IV are used to determine the influence of dimensionality on DNAPL dissolution and mass recovery. The 2-D and 3-D simulations are compared using several common DNAPL source zone mass removal metrics: down gradient

contaminant concentrations, contaminant mass flux through a down gradient control plane, and source longevity [Anderson et al., 1992; Brown et al., 1994; Chrysikopoulos, 1995; Mayer and Miller, 1996; Berglund, 1997; Dekker and Abriola, 2000b; Einarson and Mackay, 2001; Sale and McWhorter, 2001, 2003; Rao et al., 2002; Saenton et al., 2002; Saenton and Illangasekare, 2003; Rao and Jawitz, 2003; Lemke and Abriola, 2003; Lemke et al., 2004b]. These metrics were selected specifically for their applicability to practitioners' efforts to quantify the benefits of partial mass removal in the field [e.g., Rao et al., 2002; Stroo et al., 2003; NRC, 2004].

Quantifying mass removal metrics has been the subject of a number of modeling studies. Simplified analyses have investigated mass removal metrics using analytical solutions to transport equations for idealized source zone configurations [e.g., Anderson et al., 1992; Sale and McWhorter, 2001; Rao and Jawitz, 2003]. Alternative analyses have employed numerical multiphase compositional simulators that incorporate rate-limited mass transfer and spatial variability in aquifer properties [e.g., Mayer and Miller, 1996; Dekker and Abriola, 2000b; Whittaker et al., 2000; Saenton et al., 2002; Parker and Park, 2004; Lemke et al., 2004b]. However, as discussed in Section IV.1, the computational effort required to solve the multiphase, multicomponent flow and transport problem generally limits these numerical investigations to 2-D, cross-sectional (x - z) domains [e.g., Mayer and Miller, 1996; Dekker and Abriola, 2000b; Lemke and Abriola, 2003; Lemke et al., 2004b] or to the use of methods that rely on simplified algorithms to generate the initial DNAPL saturation distribution [Parker and Park, 2004]. Implicit in the use of 2-D simulations of DNAPL mass recovery are the assumptions that DNAPL dissolution and dissolved phase contaminant transport will be relatively unaffected by the

restriction of flow to the nominal 2-D domain width and that subsurface property variability in the third dimension can be neglected.

While several studies have modeled dissolution in a 3-D domain [Brown et al., 1994; Unger et al., 1998; Dela Barre et al., 2002; Saenton et al., 2002; Parker and Park, 2004], Guarnaccia and Pinder [1998] appear to be the only researchers to examine the effect of increasing dimensionality from 2-D to 3-D on DNAPL mass recovery. Using a single, three phase (gas, aqueous, NAPL) homogeneous realization at the lab scale (1m x 1m x 0.3m), they showed that there were minor differences in the down gradient contaminant concentration that were likely caused by differences in the 2-D and 3-D DNAPL saturation distribution. Yet, the results from Chapter IV suggest that for a nonuniform saturated system, the 2-D and 3-D saturation distributions are approximately equivalent. Therefore, it is possible that 2-D simulations will provide good approximations to 3-D simulations of aqueous phase contaminant concentrations in saturated, nonuniform aquifers. Furthermore, investigating differences between 2-D and 3-D mass recovery simulations facilitates the interpretation of existing [e.g., Rathfelder et al., 2001] and future modeling studies, and may potentially lead to the development of upscaled effective mass transfer correlations [e.g., Parker and Park, 2004].

V.B METHODS

V.B.1 Model Equations

Initial attempts to use UTCHEM to simulate mass recovery had extended simulation times and poor numerical stability. Thus, mass recovery simulations were performed using the version of MT3DMS [Zheng and Wang, 1999] modified by Parker

and Park [2004] to simulate DNAPL dissolution followed by dissolved phase contaminant transport (see Section III.E.2). This model solves a three-dimensional component mass balance equation (equation III.5) for the aqueous phase contaminant concentration (C_a^c):

$$\phi \frac{\partial C_a^c}{\partial t} + \nabla \cdot \phi (C_a^c V_a - D_a^c \nabla C_a^c) = \phi E_{ao}^c \quad (\text{V.1})$$

where the aqueous phase contaminant concentration (C_a^c) is related to the mole fraction in equation III.5 by:

$$C_a^c = x_a^c MW_c \rho_a S_a \quad (\text{V.2})$$

Aqueous phase reactions are neglected and all other parameters are as given in section III.C.

Within MT3DMS, the groundwater flow field (V_a -field) is computed using a version of MODFLOW [McDonald and Harbaugh, 1988] modified to update hydraulic conductivities at each time step in response to changes in relative permeability [Parker and Park, 2004]. The Brooks and Corey [1964] - Burdine [1953] capillary pressure-saturation-relative permeability model (equations III.9 and III.15) is used to update the relative permeability as the immobile DNAPL dissolves.

A linear driving force expression (equation III.16) coupled with the Powers et al. [1994] lumped mass transfer coefficient (i.e., equation III.19) is used to simulate the dissolution process. As described in Section III.D.3.i, a comparison of various lumped mass transfer coefficients [e.g., Miller et al., 1990; Imhoff et al., 1994; Powers et al., 1994; Saba and Illangasekare, 2000] demonstrated that the difference resulting from the selection of a particular mass transfer correlation is only observed at high mass removal levels (>90% mass removal) [Mayer and Miller, 1996; Unger et al., 1998; Zhu and Sykes,

2000]. This difference in simulation results at high mass removal will likely affect source longevity estimates and flux averaged concentrations at late times, two of the metrics analyzed in this chapter. There is no evidence, however, that the effect of mass transfer coefficient selection will differ with simulation dimensionality (2-D versus 3-D). Thus, use of the Powers et al. [1994] lumped mass transfer correlation (equation III.19) was judged appropriate.

V.B.2 Numerical Simulations

Using the model described in Section V.B.1, DNAPL dissolution and mass recovery were simulated in sixteen two- and three-dimensional statistically homogeneous, nonuniform permeability fields. These fields correspond directly to the realizations used in the Chapter IV investigation. They are representative of a natural formation located in Oscoda, Michigan, USA, at the site of a former dry cleaning business with a known PCE DNAPL source zone. This site was the location of a recent pilot-scale surfactant enhanced aquifer remediation (SEAR) test [Abriola et al., 2002; Abriola et al., 2005]. As described in detail in Section IV.B.2, these realization domains were sized to be consistent with the extent of the installed remediation system (7.925m long (x) by 7.925m wide (y) by 9.754m deep (z)) and were oriented so that the center x - z cross section lay along the flow path from the SEAR extraction well to the center injection well [Lemke et al., 2004a]. The level of discretization used in these dissolution studies was the same as that used for the migration and entrapment studies. This level of discretization is consistent with the sample support size from 167 vertical and directional cores at the Oscoda site [Lemke et al., 2004a]. The center x - z cross section of each 3-D

realization was used in the corresponding 2-D simulation to facilitate direct comparisons of mass recovery behavior.

MT3DMS was solved on a block-centered grid using an implicit finite difference scheme with first-order upstream weighting of the advection term. The top, bottom, front, and back boundaries of the domain were specified as no flow and the side boundaries were specified to be constant hydrostatic pressure (Figure V.1). At time zero, the concentration of contaminant in the aqueous phase was assumed negligible ($C_a^c = 0$) and 2-D and 3-D DNAPL saturation distributions were as simulated in Chapter IV. An example initial saturation distribution for a 3-D simulation and its corresponding 2-D simulation are shown in Figure V.1.

For each initial DNAPL saturation distribution (16 2-D and 16 3-D) the MT3DMS model was used to simulate mass recovery (99.9999% mass removal) under natural dissolution conditions (hydraulic gradient = 0.01). DNAPL saturations were updated after each time step by computing the change in DNAPL mass. The updating of relative permeability due to changes in saturation were lagged one time step and the time step size was adjusted dynamically to ensure the change in relative permeability remained small [Parker and Park, 2004]. Model verification was performed by comparing down gradient flux-averaged concentrations generated using MT3DMS to those generated using MISER, as summarized in Section III.E.2 and shown in Figure III.3. The model parameters used in the generation of the initial DNAPL saturation distribution are summarized in Table IV.1 and the model parameters used during the simulation of mass recovery are summarized in Table V.1.

Parameter	
Mean hydraulic conductivity, \bar{K} (m/d) ^a	16.8
Lognormal transformed \bar{K} variance $\sigma^2 \ln(K)$ ^a	0.29
Applied hydraulic gradient, (m/m)	0.01
Longitudinal dispersivity, α_L (m) ^a	0.30
Horiz. transverse dispersivity, α_{TH} (m) ^d	0.10
Vert. transverse dispersivity, α_{TV} (m) ^d	0.0075
Median grain size, d_{50} (μm) ^a	295
Uniformity index, U_i ^a	1.86
Porosity ^a	0.36
Δx (m)	0.3048
Δy (m)	0.3048
Δz (m)	0.0726

^a Lemke et al. [2004a]

^b Dekker and Abriola [2000b]

^c Horvath [1982]

^d EPA [1986]

Table V.1: Numerical simulation input parameters for 2-D and 3-D mass recovery simulations in non-uniform permeability fields.

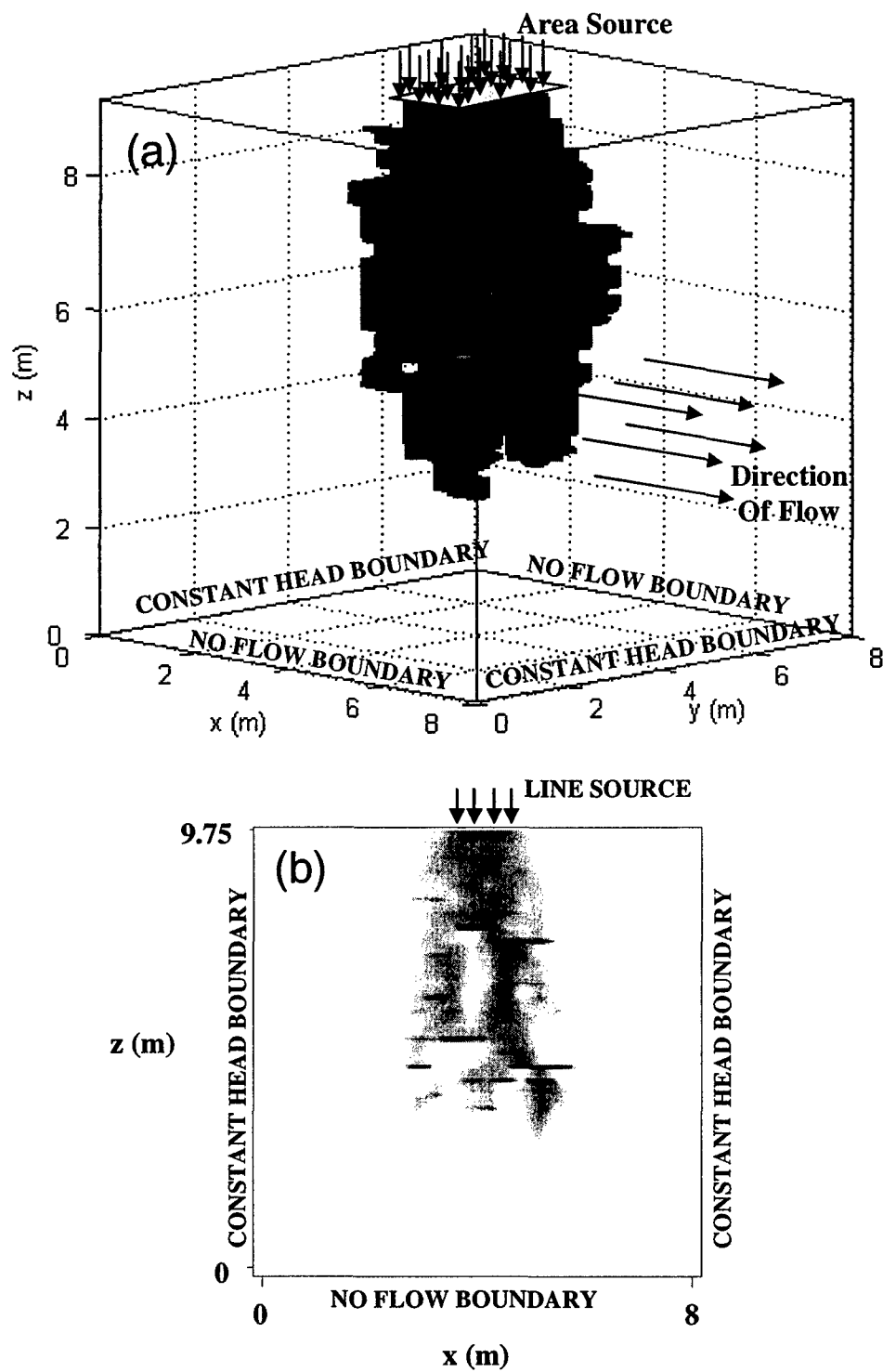


Figure V.1: Representative initial saturation distributions in (a) 3-D and (b) 2-D. Boundary conditions and contaminant release zones are also depicted.

Several source zone metrics were used to evaluate source zone behavior. Flux-averaged concentrations and DNAPL mass remaining were recorded at each time step. The concentration distribution at the down gradient boundary (y-z cross section) and the saturation distribution in the entire domain were recorded every 20 time steps. Flux-averaged concentrations were plotted as a function of percent mass removal and compared for all 2-D and 3-D realizations. In addition, the relationship between flux reduction and mass reduction was considered as an alternative metric of evaluating the benefits of partial mass removal [Stroo et al., 2003; NRC, 2004] and the influence of reduced dimensionality. The source longevity for 2-D simulations was compared to that for 3-D simulations. A recently proposed analytical mass recovery model [Parker and Park, 2004], which accounts for rate-limited dissolution as well as mixing due to the nonuniform flow field through a single upscaled mass transfer coefficient, was also used. Upscaling methods that fit effective field-scale mass transfer coefficients (κ_{eff}) to flux-averaged concentration curves provide an alternative method of comparing 2-D and 3-D concentration curves that spans the entire range of % mass removal.

V.C RESULTS AND ANALYSIS

Figure V.2 shows the temporal evolution of the 3-D saturation distribution and the concentration field in a 2-D plane (y-z) at the down gradient boundary of the domain for a single 3-D realization. At early times, the initial DNAPL mass is distributed over a large area at saturations below the maximum residual organic saturation, resulting in high (near solubility) contaminant concentrations at the down gradient boundary (Figure V.2a). Over time, these low saturation zones consisting predominantly of DNAPL ganglia

dissolve leaving a much smaller area of relatively high saturation pools, which lead to a more discontinuous concentration profile (Figure V.2b). Eventually, only a handful of pools remain that continue to slowly dissolve, leading to a plane of discontinuous low concentration cells at the down gradient boundary (Figure V.2c). Figure V.3 shows that the corresponding 2-D simulation results in similar temporal behavior. Note that in both 2-D and 3-D simulations, up gradient contaminated cells dissolve earlier than down gradient cells, as one might expect.

V.C.1 Flux-weighted Concentration versus % Mass Removal

A common method for quantifying the benefits of partial mass removal is to plot the flux-weighted contaminant concentration at a down gradient boundary against the percent mass removal [Sale and McWhorter, 2001; Lemke and Abriola, 2003; Lemke et al., 2004b]. Such plots typically exhibit a transition region, in which the flux-weighted concentration begins to drop with increasing mass removal [Lemke et al., 2004b]. A transition region reflects the transition of the source zone from a distribution dominated by low saturation ganglia contaminated zones that result in high contaminant flux, to one that is dominated by discrete, high saturation pools that generally result in a low contaminant flux. An estimation of the level of mass removal that coincides with the beginning of the transition region is important because it will dictate what level of treatment will be required before appreciable reductions in down gradient concentrations will be realized [Rao and Jawitz, 2003; Stroo et al., 2003; Lemke et al., 2004b].

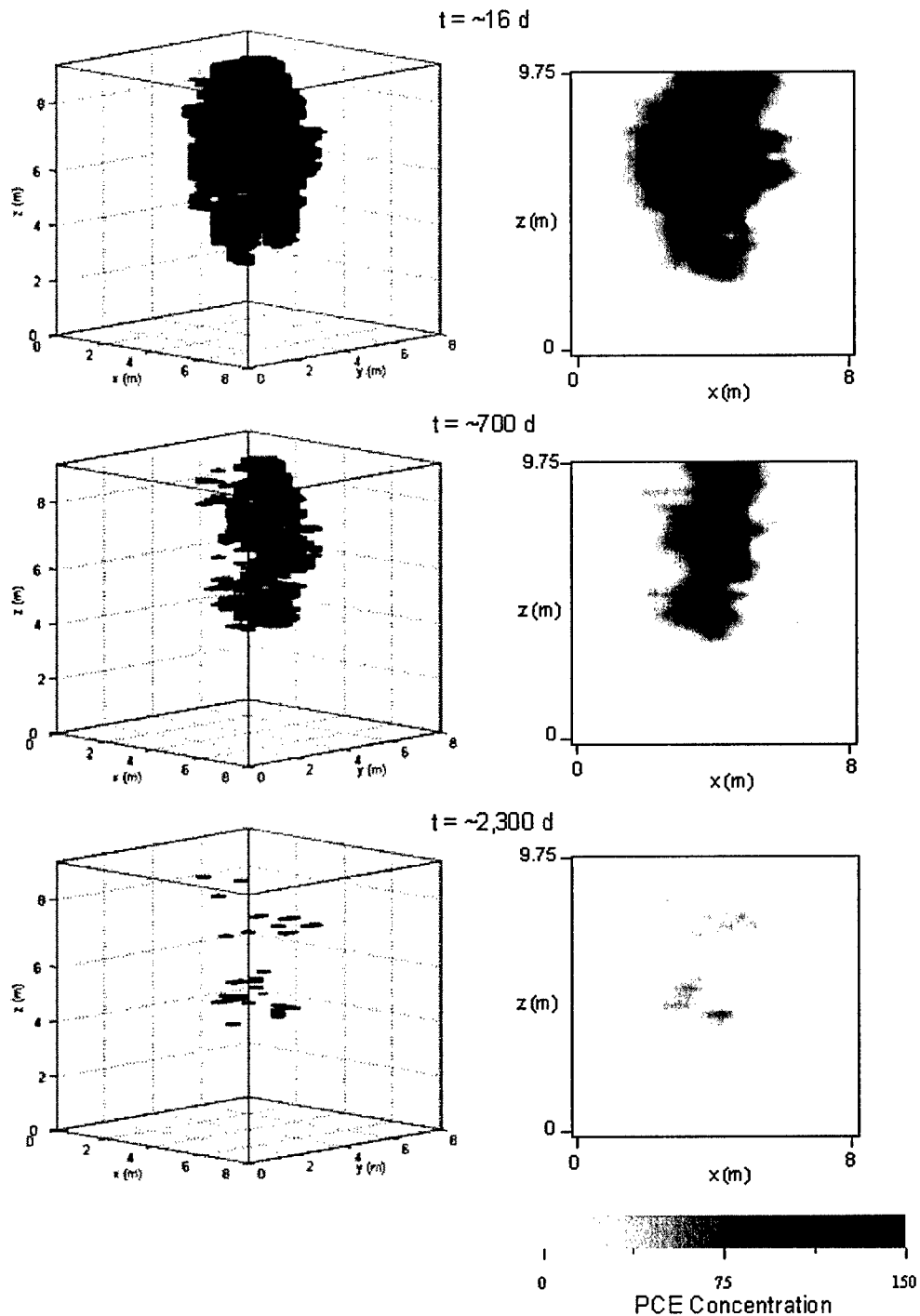


Figure V.2: Temporal evolution of a 3-D DNAPL source zone under natural gradient dissolution conditions (gradient = 0.01). 3-D saturation distributions are depicted in the left column of the figure, while concentration profiles at the down gradient boundary are depicted on the right. Travel time from the center of the source zone to the down gradient boundary is approximately 25 days.

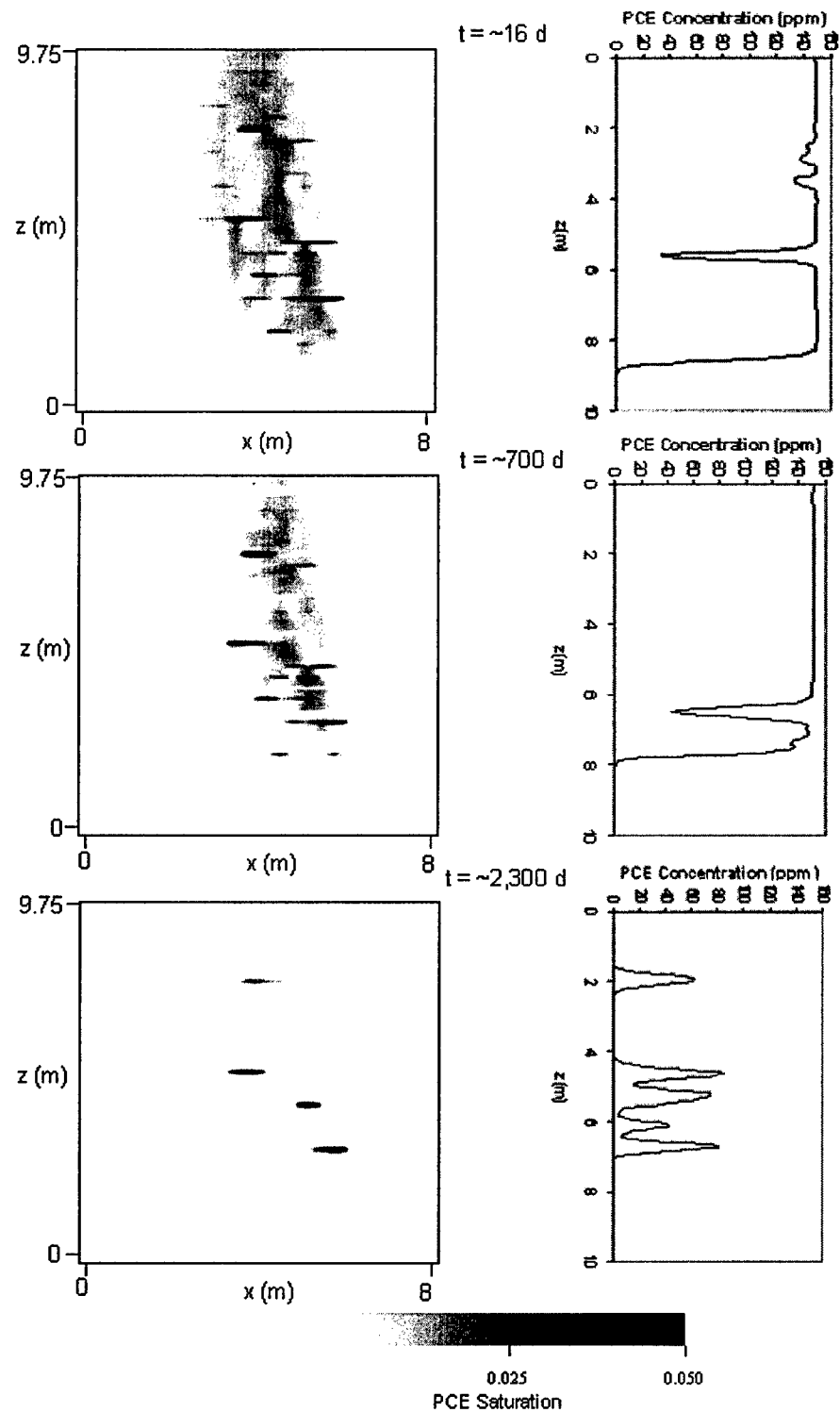


Figure V.3: Temporal evolution of a 2-D DNAPL source zone under natural gradient dissolution conditions (gradient = 0.01). 2-D saturation distributions are depicted in the left column of the figure, while concentration profiles at the down gradient boundary (1-D) are depicted on the right. Travel time from the center of the source zone to the down gradient boundary is approximately 25 days.

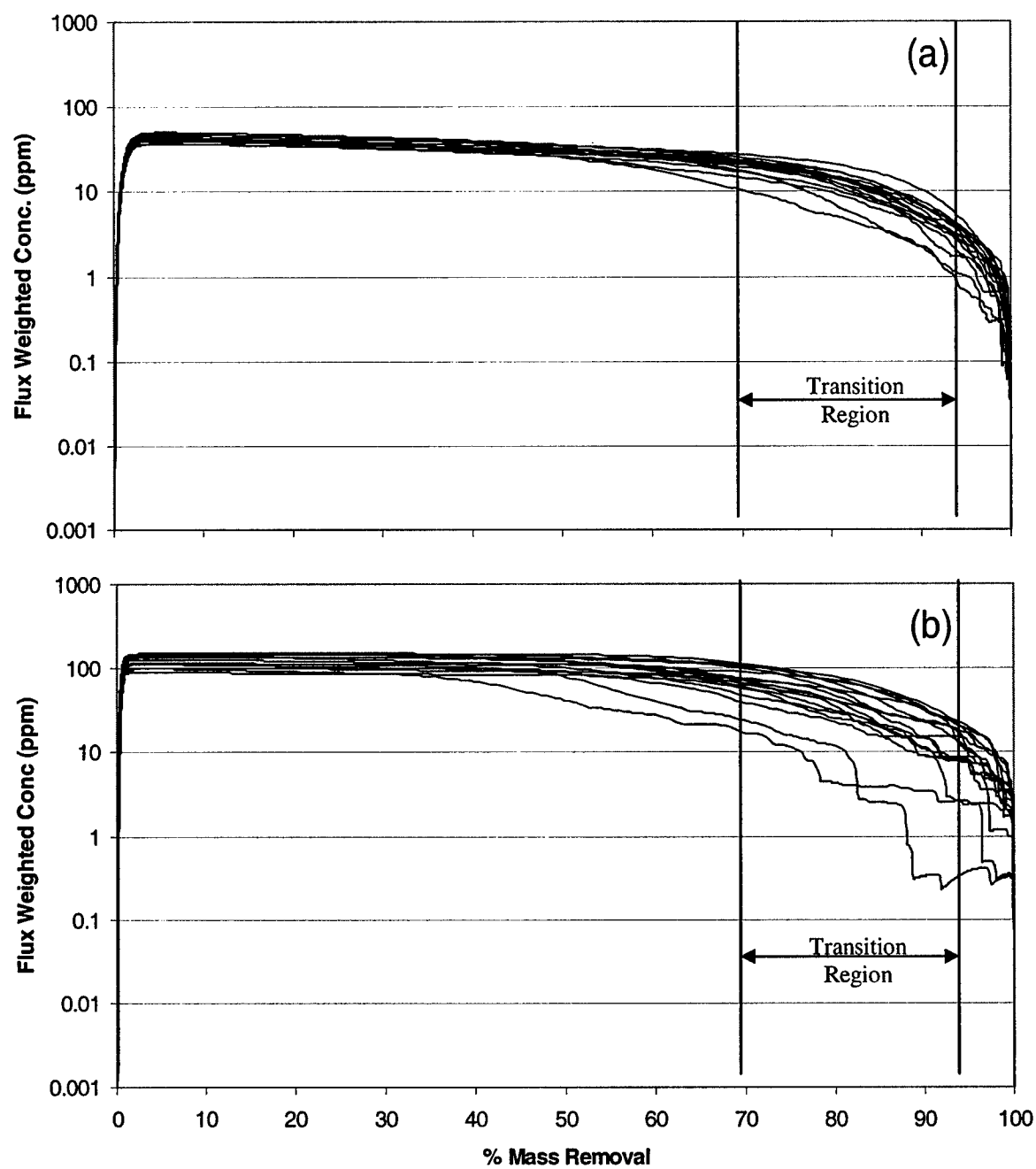


Figure V.4: Flux-weighted concentration at the effluent boundary plotted as a function of percent mass removal for all 16 (a) 3-D and (b) 2-D realizations.

In Figure V.4, flux-weighted contaminant concentrations are plotted for all 16 2-D and 3-D realizations. Initially, at very low percent mass removal, there is a sharp rise in the flux-weighted contaminant concentration as dissolution and transport of contaminant begins. This rise quickly ends, reaching a plateau that can be characterized as a “pseudo-steady-state” condition. Although the saturation distribution is changing as the DNAPL dissolves, the change in the flux averaged concentration is relatively small until the transition region of the curve is reached. The transition from a ganglia-dominated to a pool-dominated saturation distribution results in a rapid reduction of contaminant concentration in response to increased mass removal [Lemke et al., 2004b]. The concentration approaches zero only after the vast majority of the contaminant has been removed from the more persistent high saturation pools, however.

The influence of dimensionality on predictions of flux-weighted contaminant concentrations can be examined by inspection of Figure V.4. With the exception of two of the 2-D simulations, it appears that the transition region in the 2-D simulations (70-95% DNAPL mass removal) is approximately the same as that identified in the 3-D simulations. A paired t-test [Devore, 1995] showed that the beginning of this region, approximated as the % mass removal point at which the flux averaged concentration has declined to approximately one half the pseudo-steady-state concentration, is statistically the same in 2-D and 3-D simulations at the 95% confidence level. An important difference to note, however, is the magnitude of the flux-weighted contaminant concentration in the 2-D and 3-D simulations (compare Figures V.4a and b). The 2-D simulations tend to result in initial flux-weighted contaminant concentrations approximately 3.5 times larger than those in the 3-D simulations. Some portion of this

difference is due to groundwater bypassing the contaminated source zone in the third dimension due to the presence of the organic phase. Another factor is the dilution of the flux-averaged concentration at the down gradient boundary. In 2-D, contaminant concentrations are averaged over a 1-D boundary composed of 128 cells. In 3-D, contaminant concentrations are averaged over a 2-D plane with 3,328 (128 x 26) cells. Hence, there is a likelihood that many more zero concentration values will be averaged in a 3-D simulation than a 2-D simulation when the down gradient boundary area exceeds the contaminant plume dimensions. Figure V.5 compares 3-D and 2-D simulation results for 4 of the 16 realizations (the remaining 12 are plotted in Appendix D). Also, included in each plot is a third flux-weighted contaminant concentration curve, calculated using concentration data from the center x - z cross section of the 3-D domain only. This cross section has the same permeability field as the 2-D simulation and initial saturation distribution metrics that were shown to be approximately equivalent to those obtained in the 2-D simulation (see Chapter IV). Figure V.5 demonstrates that flux-weighted concentrations are generally within 10-30% when computed over equivalent down gradient areas for the 2-D and 3-D simulations, suggesting that aqueous phase contaminant concentrations are similar in 2-D and 3-D, with dilution at the down gradient boundary, not flow by-passing due to relative permeability reductions, being the major contributor to the difference between the predicted 2-D and 3-D flux-averaged contaminant concentrations.

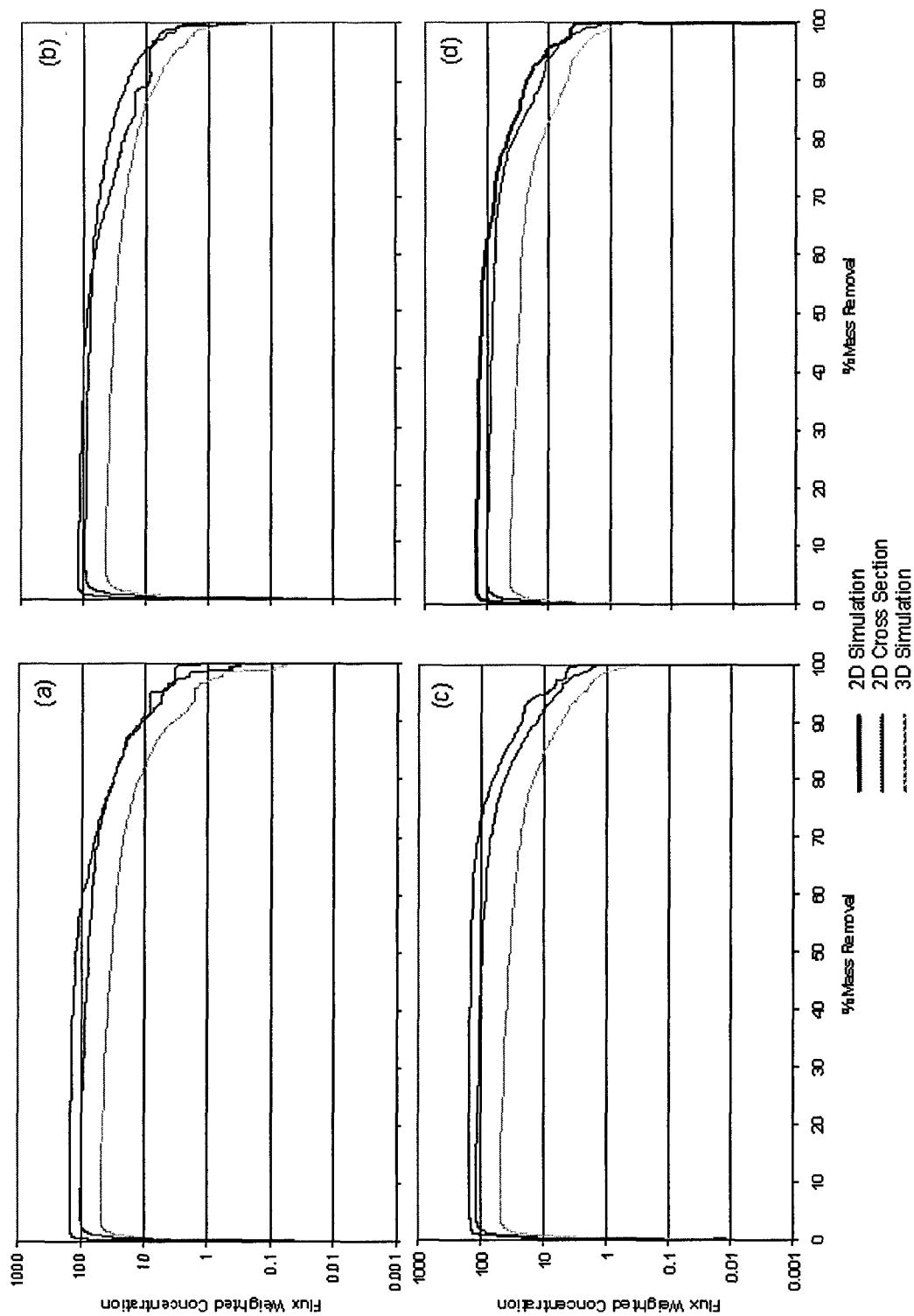


Figure V.5: Flux-weighted concentration at the effluent boundary as a function of percent mass removal for (a) realization 3, (b) realization 6, (c) realization 15, and (d) realization 10. Results from 2D, 3D, and the center cross-section (x-z) extracted from the 3D simulation are displayed on each plot.

V.C.2 % Flux reduction versus % mass removal

An alternative method that has been used to quantify the benefits of partial mass removal from DNAPL source zones is the comparison of % flux reduction versus % mass removal [e.g., Rao and Jawitz, 2003; Stroo et al., 2003]. For the scenarios considered herein, there is actually an increase in the contaminant flux as the DNAPL begins to dissolve into the aqueous phase (Figure V.4). To avoid confusion due to this initial dissolution phase, in the following analysis, the mass remaining and the contaminant flux at day 100 of the simulation were taken as the baseline. A 100 day start is consistent with that used in other numerical modeling studies [Lemke et al., 2004b] and corresponds to the approximate time when the contaminant flux has stabilized.

Figure V.6 plots flux reduction versus mass reduction for 2-D, 2-D cross sections extracted from 3-D, and 3-D simulations for the same 4 realizations presented in Figure V.5. A comparison of the 2-D cross section curves to the 3-D curves shows that, in contrast to the flux averaged concentration (Figure V.5), the flux reduction metric is relatively insensitive to mixing (dilution) down gradient of the source zone. 2-D and 3-D simulation results are compared by computing the average ($\bar{\Delta}$), maximum (Δ_{max}), and average of the squared (ASD) difference between the 2-D and 3-D contaminant flux curves using 150 distinct % mass removal points. The comparison metrics for these and the additional 12 realizations are presented in Table V.2. For three out of the four realizations depicted in Figure V.6 (a, b, and d), the % flux reduction predicted in 2-D is found to be on average within 1 to 4 % of the flux reduction predicted using the 3-D simulation. The relatively low ASD values indicate that the 2-D curves are good approximations to the 3-D curves at all percent mass removals. In the case where the 2-D

and 3-D simulation results differ by more than 30% (Figure V.6c), the 2-D simulation may be considered conservative since it predicts lower % flux reduction at moderate % mass removals. In fact, Table V.2 demonstrates that, out of the 16 realizations considered, only 3 resulted in 2-D simulation behavior that would be considered nonconservative, i.e., higher % flux reduction predictions at a given percent mass removal. These three realizations correspond to the realizations that enter the transition region first in Figure V.4b.

A comparison of 2-D simulations across the ensemble of realizations demonstrates that predictions of contaminant flux in 2-D appear to be more variable than those in 3-D (see Figure V.6). This variability can be quantified by computing the variance in the % flux reduction at a given % mass removal. For example, at the point of 50% mass removal the variance in the ensemble of 2-D % flux reduction curves is an order-of-magnitude greater than the variance in the ensemble of 3-D curves. Additionally, the 2-D flux reduction curves commonly plateau at high (>80%) percent mass removals (e.g., Figure V.6b). These plateaus likely correspond to times when the mass flux is dominated by dissolution from multiple high saturation regions, which are slow to dissolve. In contrast, 3-D curves appear to exhibit very little variability across the ensemble of realizations.

The dissolution behavior depicted in these 3D simulations is consistent with data extrapolated from a field-demonstration of co-solvent flushing at Dover AFB, DE [Rao et al., 2002; Stroo et al., 2003] and, in contrast to curves generated using a simplified analytical model [Sale and McWhorter, 2001], these curves predict appreciable reductions in contaminant mass flux at moderate percent mass removals. However, as

Sale and McWhorter [2003] caution and Figure V.4 suggests, achieving concentrations consistent with MCLs will still require significant reductions in DNAPL mass.

V.C.3 Influence of Increased $\sigma^2 \ln(K)$ and Natural Gradient

The simulations presented in the previous sections were performed using a single hydraulic gradient in a relatively homogeneous porous medium. To explore the influence of gradient and degree of spatial variability on the conclusions presented above, six additional scenarios were investigated in both 2-D and 3-D. Three saturation distributions (see Table V.2, realizations 6, 10, and 15) generated in a nonuniform permeability field with a $\sigma^2 \ln(k)$ scaled from 0.29 to 1.0 (see Section IV.C.4) were used as initial conditions for the three additional simulations. These simulations corresponded to realizations with the min, mean, and max S_o^{max} value in the center cross-section of the 3-D domain. A separate realization with approximately average source zone characteristics (Table V.2, realization 6) was also selected from the original set of 16 realizations and used to simulate dissolution under three different hydraulic gradients ($\Delta h/\Delta L = 0.001, 0.01, 0.1$), representative of the range of conditions that might be encountered from natural gradient to induced pumping scenarios.

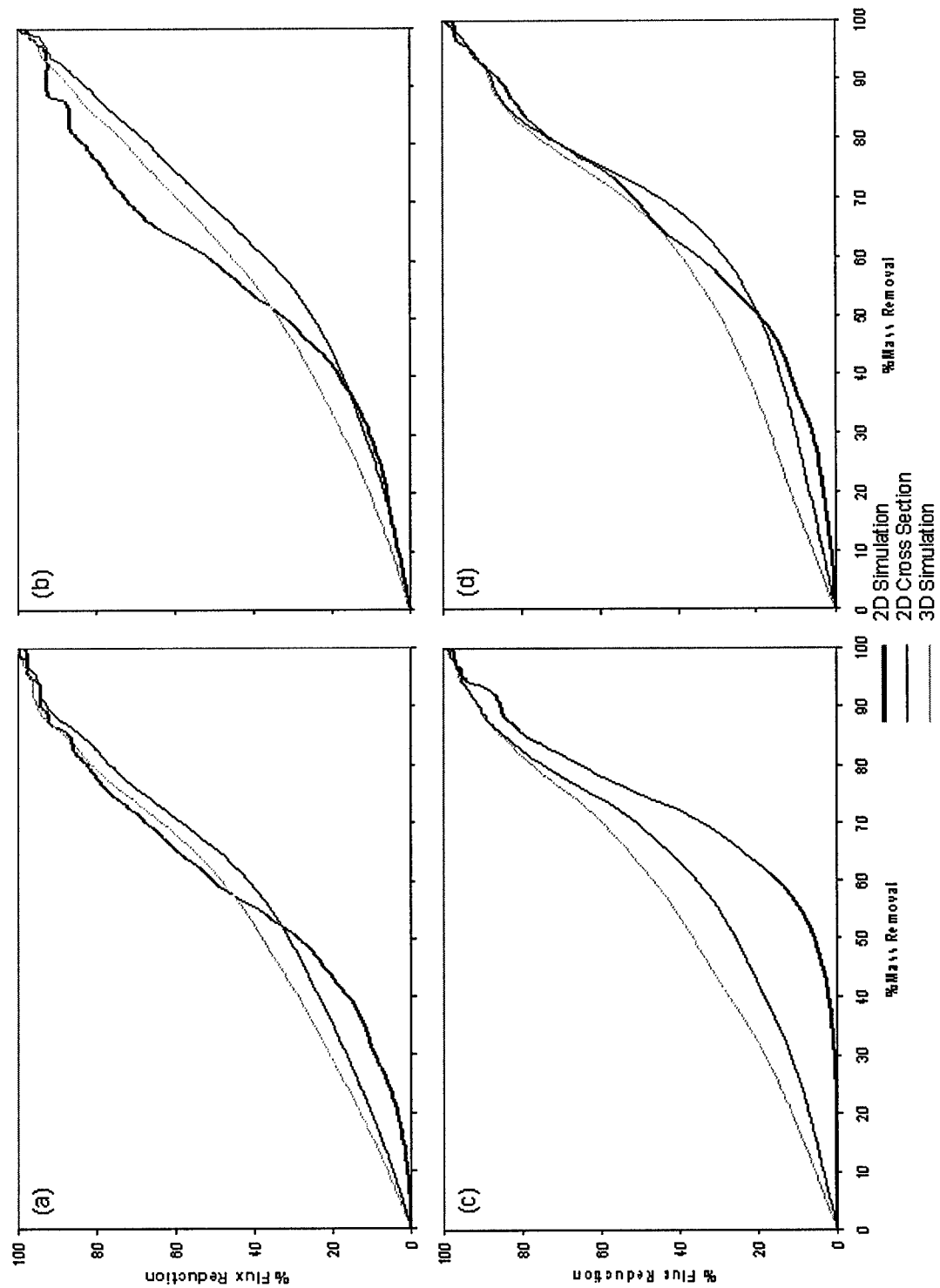


Figure V.6: Percent flux reduction at the effluent boundary as a function of percent mass removal for (a) realization 3, (b) realization 6, (c) realization 15, and (d) realization 10. Results from 2D, 3D, and the center cross-section (x - z) extracted from the 3D simulation are displayed on each plot.

Realization	$\bar{\Delta}$ (%)	Δ_{\max} (%)	ASD
1	7.55	17.58	82.75
2	4.97	14.07	44.92
3	2.65	12.96	26.96
4	-3.27	-22.47	61.49
5	8.48	17.17	99.96
6	-1.06	-13.42	33.86
7	3.92	15.43	39.84
8	8.62	25.79	183.75
9	8.25	19.40	107.08
10	3.97	11.46	29.51
11	2.86	19.91	60.22
12	9.49	20.08	129.84
13	-1.72	-15.52	28.07
14	5.99	25.53	113.84
15	7.89	31.83	162.48
16	3.79	17.35	53.99
Mean	4.52	18.75	78.66

A value less than 0 indicates the 2-D simulation predicted a % flux reduction greater than the 3-D simulation on average ($\bar{\Delta}$) or at a given % mass removal corresponding to the maximum difference (Δ_{\max}).

Table V.2: Average difference $\bar{\Delta}$ in percent, maximum difference Δ_{\max} in percent, and average of the squared difference (ASD) between 2-D and 3-D percent flux reduction curves.

These additional simulations suggest that the observations made previously can be generalized to a wider range of aquifer conditions. Shown in Figure V.7 is the flux-weighted contaminant concentration and the % flux reduction for one realization (realization 15) with a scaled variance in the lognormal transformed hydraulic conductivity field ($\sigma^2 \ln(k) = 1.0$). These results conform to the general behavior shown in Figures V.5 and V.6. The flux-weighted concentration reaches an early plateau and then gradually declines within a transition region. The scaled variance flux-weighted concentration curve, however, has a % mass removal transition region of larger extent (35 – 95% mass removal) in comparison with the unscaled realization (compare Figure V.7a with Figure V.5d). This extended range is likely due to the fact that the saturation distribution simulated in the higher variance permeability field is characterized by higher maximum DNAPL saturations and increased pooling (see Section IV.C.4). Thus, the saturation distribution transitions from a ganglia-dominated to a pool-dominated distribution at lower percent mass removals.

Figure V.8 compares the flux-weighted contaminant concentration in 2-D and 3-D at the three levels of hydraulic gradient tested. These curves also exhibit the same shape as those presented in Figure V.5. For the range of gradients examined, the flux-weighted contaminant concentration curves are insensitive to the imposed gradient. Note, however, that the time to cleanup is reduced by approximately one order of magnitude for each order of magnitude increase in the hydraulic gradient. These results suggest that for a given saturation distribution, the flux-weighted contaminant concentration is primarily a function of the percent mass removal, not the intensity of the mass removal process.

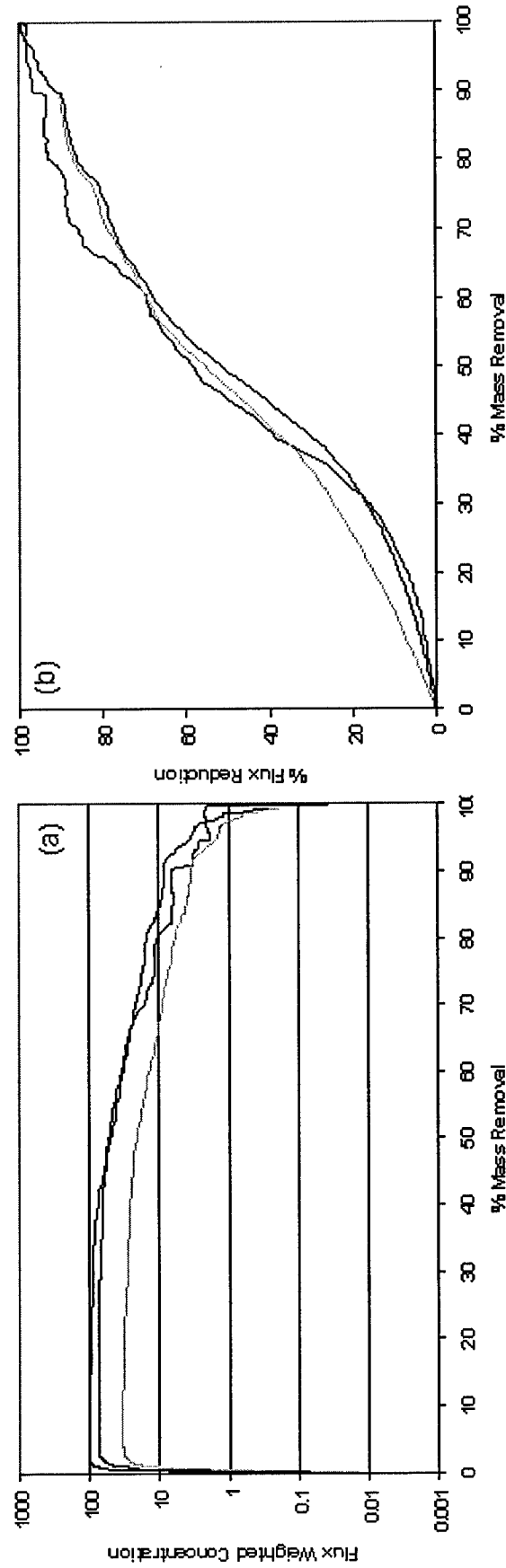


Figure V.7: (a) Flux-weighted concentration and (b) percent flux reduction at the effluent boundary as a function of percent mass removal for a representative realization with $\sigma^2 \ln(k)$ scaled to 1.0. With the exception of the scaled variance, this realization is the same as shown in Figures V.5d and V.6d. Line weights are as given in Figures V.5 and V.6.

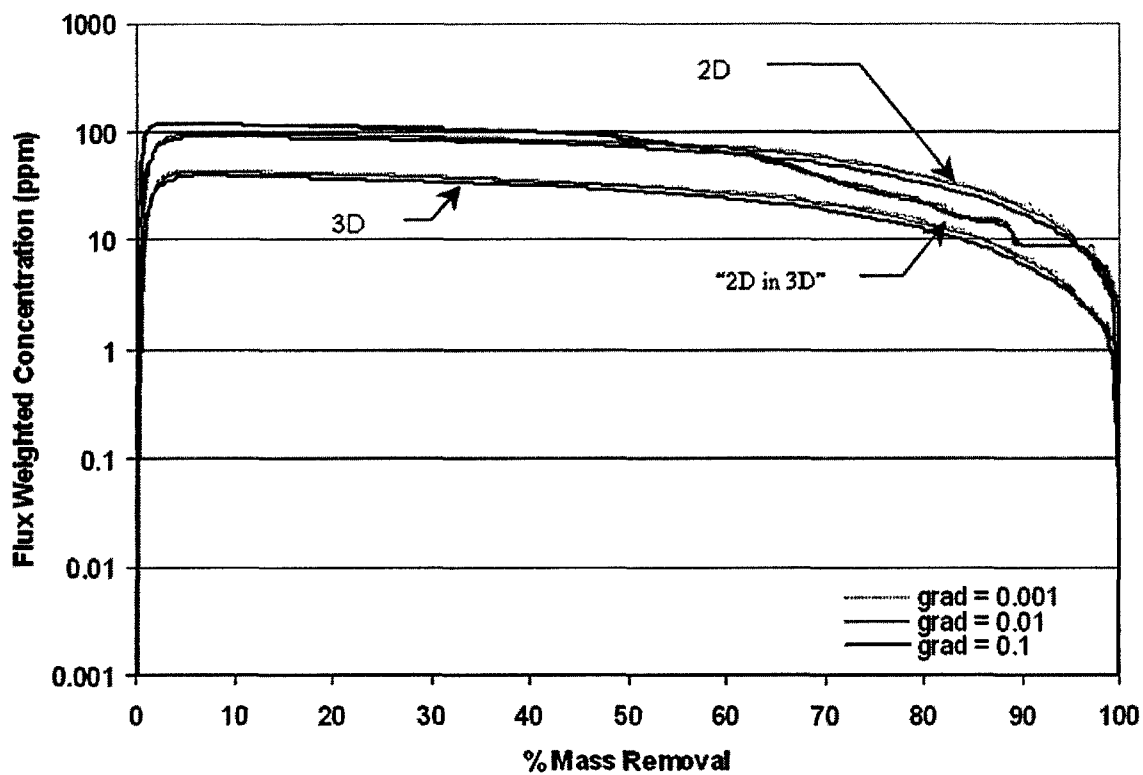


Figure V.8: Flux-weighted concentration at the effluent boundary as a function of percent mass removal for 2-D and 3-D simulations at three different hydraulic gradients (0.001, 0.01, and 0.1).

	MIN	MEAN	MEDIAN	MAX	STD DEV
2-D	8.7 yr	42.9 yr	25.2 yr	211.5 yr	52.1 yr
3-D	14.4 yr	32.3 yr	19.0 yr	98.1 yr	26.8 yr

Table V.3: 2-D and 3-D source longevity statistics for mass recovery simulations.

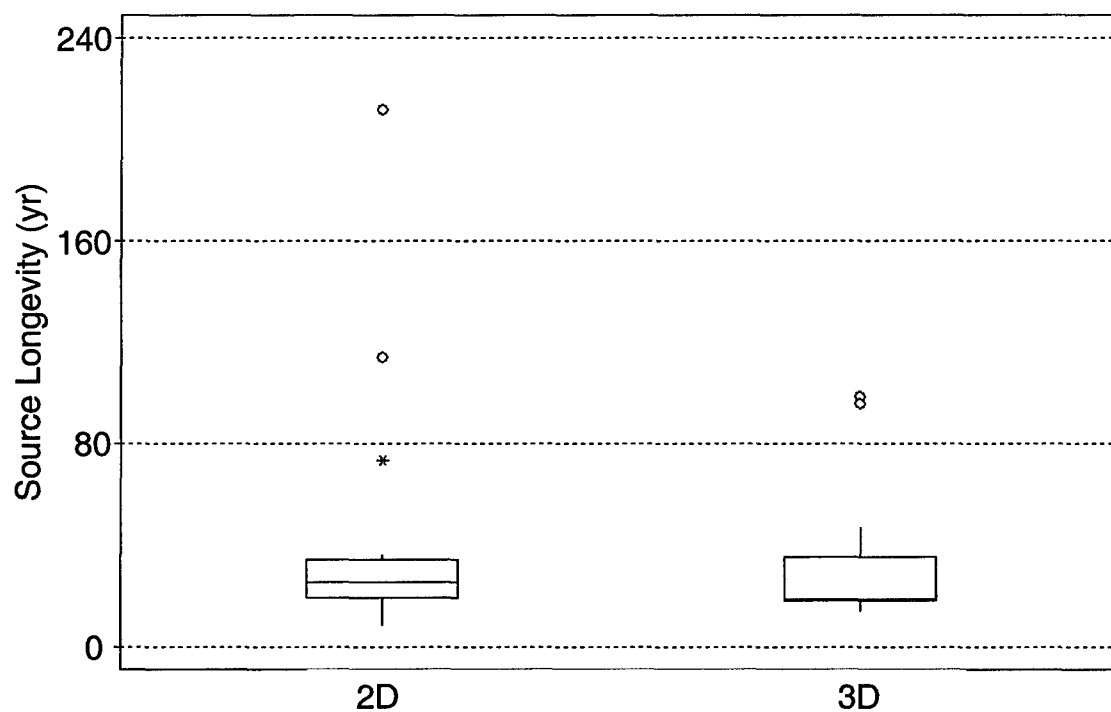


Figure V.9: Box plot of source longevity for the ensemble of two and three dimensional simulations. The box extends from the $q_{0.25}$ to the $q_{0.75}$ quartile (inter quartile range - IQR) and is separated by the median. The whiskers extend from the box to the min and max metric value within $1.5 \cdot \text{IQR}$. An asterisk indicates a probable outlier (metric value $> 3 \cdot \text{IQR}$). (*) indicates a possible outlier and (o) indicates a probable outlier.

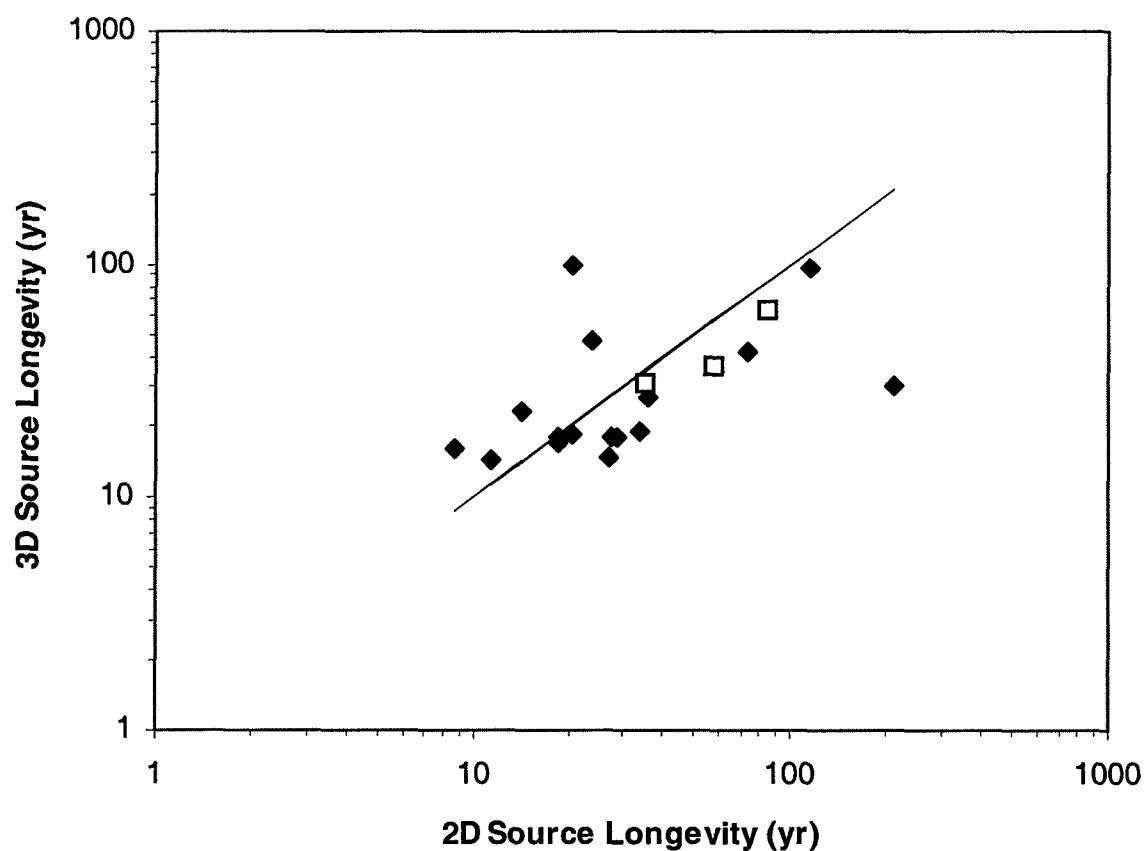


Figure V.10: Scatterplot of 2-D versus 3-D source longevity values. The open boxes correspond to the three $\sigma^2 \ln(k) = 1.0$ realizations and indicate that the higher variance permeability field did not significantly influence these results. The solid line represents the 45° bisector.

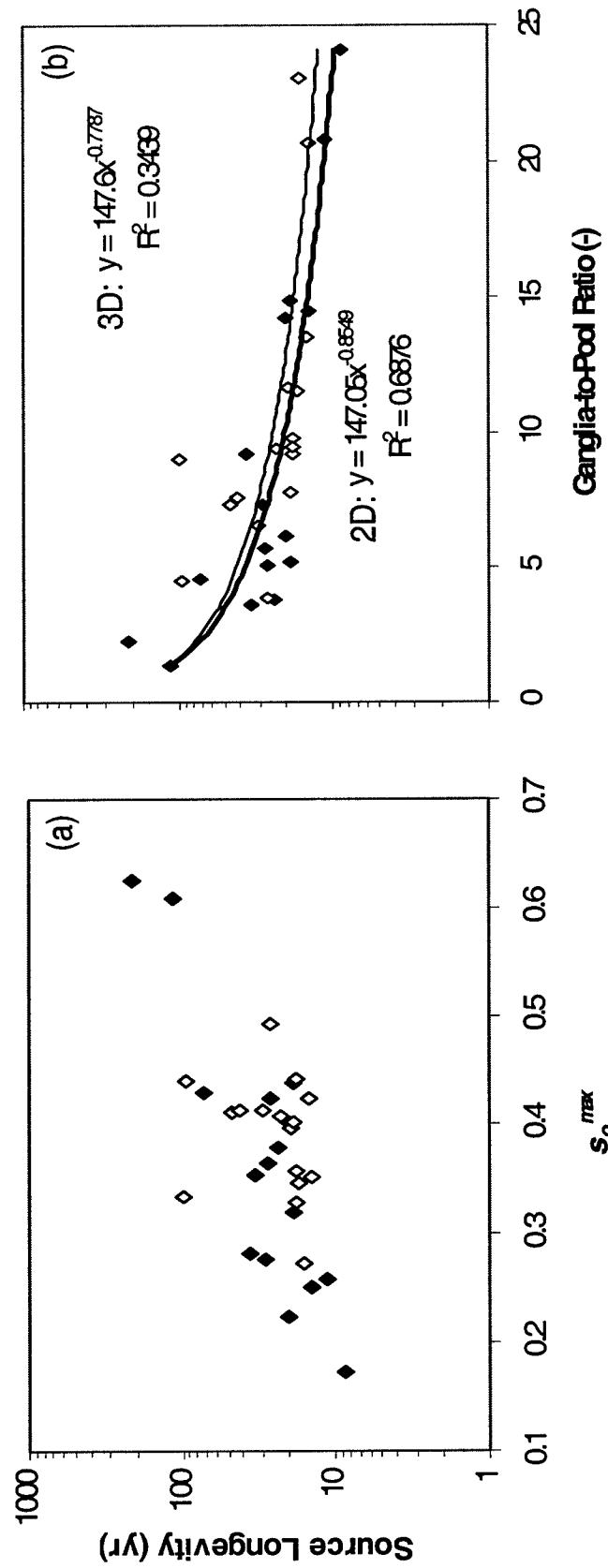


Figure V.11: Source longevity plotted against (a) the maximum organic saturation and (b) the initial ganglia-to-pool Mass ratio. Open symbols correspond to 2D simulations. Closed symbols correspond to 3D simulations.

V.C.4 Source Longevity

In addition to contaminant concentrations and contaminant flux, remediation site managers are generally interested in the persistence of the source. A precise definition of longevity is somewhat difficult to formulate, because contamination may persist at very low concentrations even after all of the NAPL is removed due to dissolution from low permeability regions and desorption [e.g., Sardin et al., 1991]. As described in Section V.B.2, source longevity is defined herein as the time required to remove 99.9999% of the DNAPL mass. At this level of removal, the contaminant is present only in the dissolved phase. Note that, in this analysis, sorption/desorption has been neglected. Thus, the longevity values may be overly optimistic, but should be comparable across dimensionalities. Additionally, recall simulation results are potentially influenced at late times by the extrapolation of the lumped Powers mass transfer correlation to cells with initial DNAPL saturations greater than the entrapped residual saturation (see Sections III.D.3.i.1 and V.B.1).

Source longevity statistics for the ensemble of sixteen 2-D and 3-D realizations are presented in Table V.3. To aid in the assessment of source longevity, the 2-D and 3-D distribution of source longevity values are also plotted in Figure V.9. In this figure, each box represents the inter-quartile range and is separated by the median. The vertical lines extend to the minimum and maximum metric values and the points represent outliers as described in the figure caption. Table V.3 and Figure V.9 show that, with the exception of several outliers, the distribution of source longevity values in 2-D and 3-D are within 10%. A paired t-test was used to determine that the mean difference between the 2-D and 3-D source longevity values was not significantly different from zero at the

95% confidence level [Devore, 1995]. These results suggest that, on average, the source longevity simulated in 2-D realizations is approximately equal to the source longevity simulated in 3-D simulations. However, as indicated by the outliers in Figure V.9, equivalent mean values of source longevity for the ensemble of 2-D and 3-D realizations do not translate into equivalent source longevity values for an individual realization. This observation is better visualized in Figure V.10, which is a scatterplot of source longevity for 2D and 3D simulations. In this figure, the closed diamonds represent the original ensemble of 16 realizations and the open boxes are for the 3 simulations conducted at the increased value of $\sigma^2 \ln(K)$. This plot shows that the predicted source longevity for 2-D and 3-D simulations in a given realization will usually be different. However, there is a statistically significant (p-value = 0.0077) positive correlation (0.6387) between the 2-D and 3-D predictions of source longevity, indicating that a higher source longevity value predicted in 3-D will generally be replicated by a higher value in 2-D.

The results of a recent numerical modeling study indicate that flux-weighted concentration curves that enter the transition zone at lower % mass removals (e.g., 35 to 55%) correspond to those realizations which have a large percentage of mass in high saturation pools [Lemke et al., 2004b]. Thus, to explore how mass distribution may affect the prediction of source longevity in 2-D and 3-D, the relationship of predicted source longevity to two metrics calculated for the initial saturation distributions in Chapter IV, S_o^{max} and the ganglia-to-pool (GTP) mass ratio, was assessed. A statistical analysis of the linear correlation between 2-D predictions of source longevity and S_o^{max} showed that there was a statistically significant positive correlation (Figure V.11a). In 3-D, there is also a positive correlation; however, it is not statistically significant. A

comparison of 2-D and 3-D source longevity values to GTP mass ratios revealed that a simple power expression ($y = fx^y$) resulted in the best fit to the data (Figure V.11b). Although neither of these fits was statistically significant, their parameters were within 10% of each other and as observed with the S_o^{max} analysis, the 2-D predictions of source longevity appeared to be better correlated to the GTP mass ratio than the 3-D predictions (higher r^2 value).

V.C.5 Upscaling and effective mass transfer

In Section V.C.1, 2-D and 3-D flux-weighted concentration curves were compared at a single flux-weighted concentration corresponding to the start of the transition region. In this section, the simplified model developed by Parker and Park [2004] is used to estimate flux-weighted concentration curves at all % mass removal points. This method employs a best-fit domain averaged (i.e., upscaled) mass transfer coefficient (κ_{eff}) derived by assuming pseudo-steady-state conditions, replacing the actual heterogeneous domain with an “equivalent” homogeneous domain, subject to the same average hydraulic flux ($\overline{q_a}$), and fitting the one dimensional advection-dispersion equation (steady state, 1D version of equation V.1) to the flux-averaged effluent contaminant concentration ($\overline{C_a^c}$) at the down gradient boundary ($L = N_x \Delta x$). Neglecting transverse dispersion and molecular diffusion, enforcing a type 1 boundary condition ($\overline{C_a^c} = 0$ at $x = 0$) and Type 2 boundary condition ($d\overline{C_a^c}/dx = 0$ at $x = L$), and assuming that $\alpha_L/L < 0.1$ give the solution:

$$\frac{\overline{C_a^c}(L)}{C_a^{c-sol}} = 1 - \exp\left(\frac{-\kappa_{eff} L}{\overline{q_a}}\right) \quad (V.3)$$

where C_a^{c-sol} is taken to be the contaminant solubility and $\overline{C}_a^c(L)$ is the flux-weighted concentration evaluated over the entire down gradient boundary. Parker and Park [2004] show that for $\kappa_{eff} L / \overline{q}_a \ll 1$, $\overline{C}(L) / C^{eq} \approx \kappa_{eff} L / \overline{q}_a$. However, in the analysis presented here, the constraint on κ_{eff} may not be satisfied at all times, requiring the use of the full solution (equation V.3). Parker and Park [2004] evaluate κ_{eff} by assuming it conforms to a field-scale mass transfer correlation, analogous to those presented for local scale models (e.g., Miller et al., 1998):

$$\kappa_{eff} = \kappa_o \left(\frac{\overline{q}}{\overline{K}} \right)^{\beta_1} \left(\frac{M}{M_o} \right)^{\beta_2} \quad (V.4)$$

where \overline{K} is the average saturated hydraulic conductivity, M is the mass at a point in time (or specified level of mass removal), M_o is the original amount of mass in the DNAPL source zone ($t = 0$), and κ_o , β_1 , and β_2 are correlation fitting parameters. Parker and Park [2004] used a single geostatistical realization evaluated at three different hydraulic gradients to obtain the following values for the fitting parameters: $\kappa_o = 0.0024 - 0.049$, $\beta_1 = 1.00$, $\beta_2 = 0.4 - 1.4$, whose exact values depend on the region of the domain (ganglia-dominated, pool-dominated, and full domain) modeled [Parker and Park, 2004].

In the dimensionality comparison presented here, a nonlinear, least squares fitting routine was used to fit equation V.3 and a slightly modified version of equation V.4 to the simulated, normalized effluent concentration at the down gradient boundary of each 2D, 2D cross section in 3D, and 3D simulation. β_1 in equation V.4 was set equal to 1.0 after a sensitivity analysis showed that the variability in the average hydraulic flux term ($\overline{q}_a / \overline{K}$)

was insufficient to fit κ_o and β_l independently. Thus, only two parameters (κ_o' and β_2) were fit:

$$\kappa_{eff} = \kappa_o' \left(\frac{M}{M_o} \right)^{\beta_2} \quad \text{where} \quad \kappa_o' = \kappa_o \left(\frac{\bar{q}}{K} \right)^{1.0} \quad (\text{V.5})$$

Although the assumed value of $\beta_l = 1.0$ is larger than the exponents generally fit using laboratory data [Miller et al., 1998], this value is consistent with the 3D numerical modeling study of Parker and Park [2004], which considered an average hydraulic flux that spanned two orders of magnitude. Additionally, as explained above, any combination of κ_o and β_l that results in κ_o' gives an equally good fit to the simulated data.

Parameter values for 2-D, 2-D cross section in 3-D, and 3-D simulations are summarized in Table V.4. The fitted 2-D parameter values were found to be within the range of values reported in the laboratory and numerical modeling literature. In the literature, κ_o values vary by several orders of magnitude depending on the functional form of the mass transfer correlation (e.g., parameterize the Schmidt number or normalized grain size), β_l values range between 0.6 and 1.0, and β_2 values range between 0.6 and 1.4 [Miller et al., 1998; Parker and Park, 2004]. The 3-D parameter values are also within the range of values reported in the literature. However, κ_o values calculated in this work are several orders of magnitude greater than the values calculated by Parker and Park [2004]. In their simulation, only approximately 0.42% of the model cells had been infiltrated by DNAPL. In the present study, this value is closer to 15%. This characteristic is a likely explanation for the larger κ_o values calculated in this work. Another potential explanation relates to the method of generating the initial DNAPL

	2D	2D in 3D	3D
κ_o' (d ⁻¹)	7.82x10 ⁻² (±2.75)	2.63x10 ⁻² (±0.36)	8.20x10 ⁻³ (±0.06)
κ_o (d ⁻¹)	7.82 (±2.75)	2.63 (±0.36)	0.82 (±0.06)
β_1 (dimensionless)	1.0	1.0	1.0
β_2 (dimensionless)	1.25 (±0.20)	0.84 (±0.07)	0.85 (±0.07)

Table V.4: Mean (± 95 % Confidence Interval) 2-D and 3-D mass transfer parameter values obtained by fitting equations (V.3) to (V.5) to the ensemble of 16 2-D and 16 3-D flux-weighted concentration curves.

saturation distribution. The present study used a hysteretic multiphase compositional simulator (UTCHEM) to generate the saturation distributions. Parker and Park [2004] used a simplified model based on percolation theory to generate the initial DNAPL saturation distribution. Their model resulted in an average saturation in contaminated cells one order of magnitude greater than that generated using the multiphase flow code used here.

A comparison of effective field scale mass transfer coefficients (κ_{eff}) in 2-D and 3-D for a range of percent mass removal levels (M/M_o) demonstrates that the 2-D κ_{eff} is typically one order of magnitude greater than the 3-D κ_{eff} (see Table V.4 and equation V.4). This difference could be due to a lack of flow by-passing due to relative permeability reductions in 2-D. However, as discussed in Section V.C.1, this effect is more likely due to dilution at the down gradient boundary of the 3-D domain. To examine the influence of dilution, a “2D in 3D” effective field scale mass transfer coefficient was computed using the center x - z cross section from the 3-D domain. Table V.4 reveals that, by considering only the center x - z cross section in the 3-D domain, the correlation parameter κ_o' is of the same order of magnitude as the 2-D simulation. The “2-D in 3-D” κ_o' remains smaller than that for the 2-D simulation, but this is likely due, at least in part, to additional dilution in this cross-section, due to the exchange of contaminant mass with adjacent cross sections. The “2-D in 3-D” β_2 parameter changed very little from the 3-D β_2 parameter, which was approximately 30% lower than the 2-D β_2 parameter, suggesting that source zone saturation distributions will influence the relationship between mass removal and effective concentration.

The ability of the simplified model (equations V.3 to V.5) to approximate the numerical simulation output of MT3DMS is examined in Figure V.12. Figure V.12a compares output from numerical simulations of the flux weighted concentration curve to output from the upscaled modeling approach for the 2-D and 3-D realization corresponding to the mean saturation distribution realization in Chapter IV (Realization 10, Table V.2). The simplified model compares very well with the numerical simulation (<10% difference) up to approximately 70% mass removal. Beyond this point, the flux weighted concentration is dominated by dissolution from a few discrete pools. The upscaling methodology fails to account for this change in the source zone architecture and predicts concentrations that differ by a factor of 2 or more from the numerical simulation output. Figure V.12b demonstrates that this difference is exaggerated when the mass transfer correlations developed using lower variance simulations are applied to higher variance simulations ($\sigma^2 \ln(K) = 1.0$). At a higher variance, the flux weighted concentration in both 2D and 3D is up to 30% lower than that predicted using the lower variance-based upscaled models (equations V.3 and V.5, Table V.4). Additionally, 2-D and 3-D saturation distributions transition to a pool dominated scenario at lower percent mass removals (see discussion in Section V.C.3). These characteristics result in an even poorer prediction of the flux weighted concentration, suggesting that upscaled models that do not account for the transition from a ganglia dominated to a pool dominated saturation distribution have limited applicability.

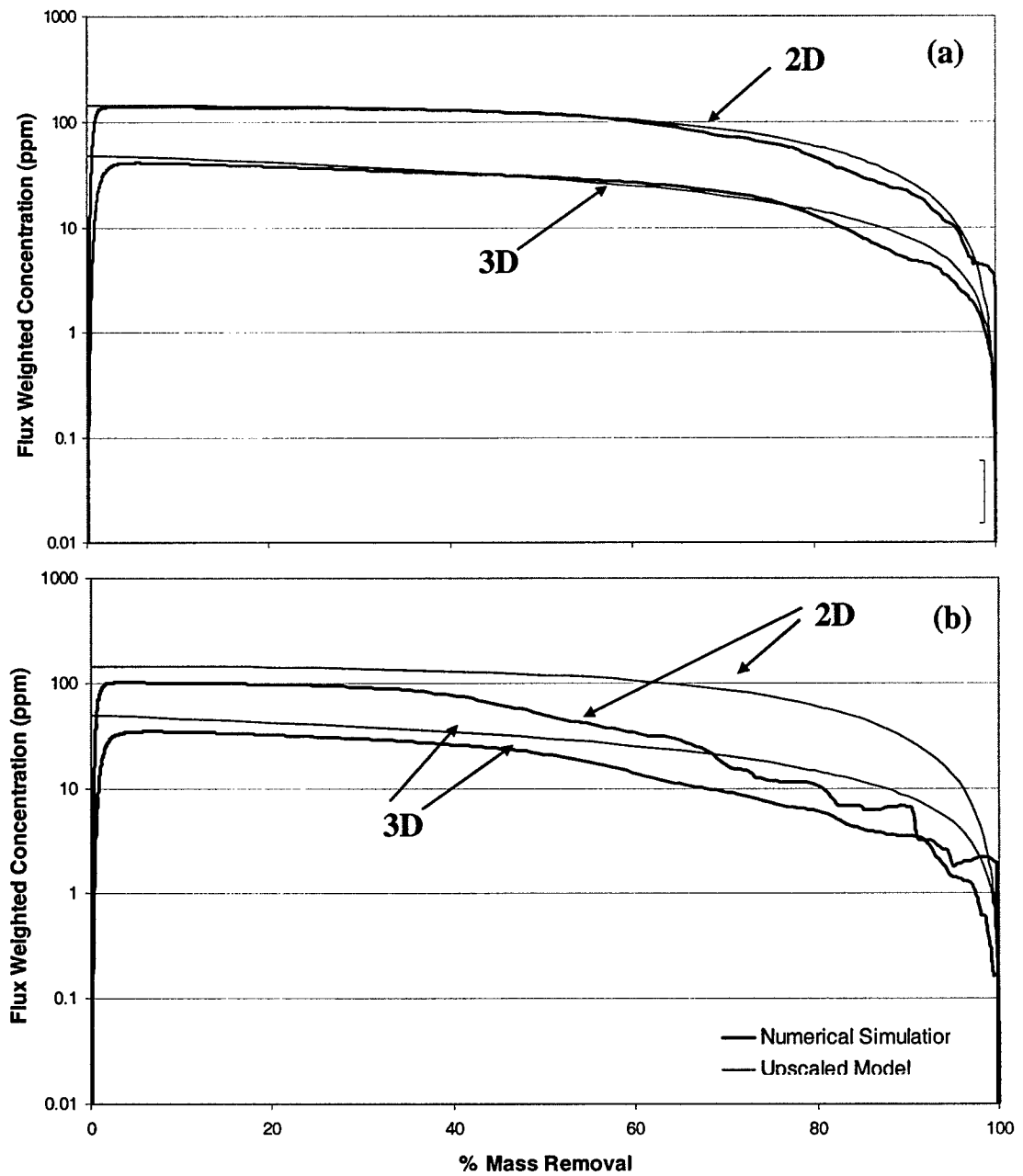


Figure V.12: Numerical simulation (bold line) and upscaled mode (solid line) of the flux weighted concentration at the effluent boundary as a function of percent mass removal for 2-D and 3-D simulations in (a) realization 10 ($\sigma^2 \ln(K) = 0.29$) and (b) realization 10 with $\sigma^2 \ln(K)$ transformed to 1.0.

V.D CONCLUSIONS

The impact of dimensionality on the numerical simulation of mass recovery from realistic DNAPL saturation distributions was investigated by computing and comparing metrics that have recently been proposed as methods for quantifying the benefits of partial mass removal from DNAPL source zones. Mass recovery was simulated in 16 2-D and 16 3-D statistically homogeneous, nonuniform permeability fields with saturation distributions generated using a hysteretic multiphase flow code, UTCHEM. The permeability field was based on the geostatistical parameters developed in support of a recent pilot-scale SEAR demonstration in Oscoda, MI. A modified version of MT3DMS was used to incorporate rate-limited NAPL dissolution. This set of realizations provided the opportunity to make direct realization to realization comparisons, as well as comparisons between average behavior in ensembles of 2D and 3D realizations.

Of the three metrics considered, flux-weighted down gradient contaminant concentration, flux reduction through a down gradient plane of compliance, and source longevity, contaminant flux reduction appeared to be the least sensitive to dimensionality effects. The average difference in the % flux reduction predicted in 2-D and 3-D at a given % mass removal was less than 5% (Table V.2). Flux-weighted concentrations in 2-D were generally 3.5 times greater than those simulated in 3-D. This difference, however, is attributable primarily to dilution across the down gradient boundary and not to flow by-passing in the third dimension due to the presence of a DNAPL. Thus, the aqueous phase concentration in an individual numerical grid-block will be approximately the same in 2-D and 3-D simulations. On average, predictions of source longevity using 2-D simulations tended to give good approximations of 3-D values. Correlations

between source longevity and metrics used to quantify DNAPL saturation distributions (maximum saturation and ganglia-to-pool mass ratio) demonstrated that zones of higher saturation tended to result in increased source longevity predictions, regardless of dimensionality. The 3-D simulations, however, appeared to be less sensitive than the 2-D simulations to the distribution of mass between high and low saturation regions. Upscaled effective mass transfer correlations of a form proposed by Parker and Park [2004] were used to calculate field-scale mass transfer in two and three dimensions. 2-D effective field-scale mass transfer coefficients were found to be approximately one order of magnitude greater than those obtained using 3-D data. This effect was attributed primarily to dilution at the down gradient boundary rather than flow by-passing in the groundwater flow field.

The implications of this work, when combined with the results of Chapter IV, are that (1) 2-D numerical simulations of DNAPL migration, entrapment, and dissolution provide reasonable approximations to simulations conducted in a fully three dimensional domain, (2) 2-D and 3-D predictions of mass recovery metrics will be approximately equivalent when computed over equivalent down gradient boundaries (i.e., corrected for dilution), and (3) the aqueous phase concentration of a numerical grid-block will be approximately the same when simulated in 2-D and 3-D, suggesting that 2-D models may be used to simulate aqueous phase contaminant remediation processes (e.g., source zone bioremediation). Although substantial differences in some metrics (e.g., source longevity) can be observed in comparisons of a single 2-D and 3-D realization, on average, over an ensemble of realizations, mass recovery metrics simulated in 2-D will provide conservative (higher flux-weighted contaminant concentration, longer source

longevity) approximations of 3-D behavior. These findings are important given the large computational requirements associated with 3-D simulations and the fine grid resolution needed to capture capillary behavior at textural interfaces, resulting in 3-D simulation execution times on the order of 10 to 100 times longer than 2-D simulation execution times.

Furthermore, to the authors' knowledge, this is the first study to investigate mass recovery metrics using an ensemble of nonuniform 3D domains. Thus, it provides an opportunity to assess the utility of mass recovery metrics for quantifying the benefits of DNAPL source zone treatment. Before applying the results of this study, however, the reader is cautioned that these results are based on a source zone with low-to-moderate DNAPL saturations (e.g., <0.5) in a relatively homogeneous aquifer with horizontal bedding. Although increased heterogeneity was investigated, a more thorough analysis should be undertaken to explore behavior in highly heterogeneous permeability fields, source zones with high NAPL saturations, and aquifers with non-horizontal bedding.

CHAPTER VI

MODELING METABOLIC REDUCTIVE DECHLORINATION IN BATCH SYSTEMS

VI.A INTRODUCTION

Stimulating metabolic reductive dechlorination in a DNAPL source zone following aggressive mass removal using technologies such as SEAR has been proposed as an efficient method for reducing the longevity of residual DNAPL mass and controlling aqueous phase contaminant concentrations. Simulating this process requires the development of kinetic expressions that quantify the dissolution, production, and degradation rates of relevant substrates and the growth rates of microbial populations.

Several models have been developed that are capable of simulating metabolic reductive dechlorination [e.g., Tandoi et al., 1994; Cirpka, 1995; Fennell and Gossett, 1998]. These models have been applied to estimate dechlorination kinetic coefficients for single-phase experimental systems. However, as described below, these models are limited in their application to DNAPL source zone scenarios due to various simplifying assumptions and the lack of an organic phase. Only a single model has been developed to simulate dechlorination in an aqueous-organic two-phase system [Carr et al., 2000]. This model assumes dechlorination kinetics is first-order and that the aqueous and

organic phases are at equilibrium. These assumptions were valid for the simplified experimental system used to evaluate the model, that is, a continuously stirred tank reactor with a small volume of two component NAPL consisting of $x_o^{PCE} = 0.13$ in an insoluble tridecane carrier phase. Due to the lack of non-linear dechlorination kinetics and rate-limited dissolution, the application of this model to experimental systems more representative of DNAPL source zone scenarios would likely lead to errors in parameter estimation. Thus, there is a need to develop a dechlorination kinetic model capable of simulating experimental systems designed to reproduce typical DNAPL source zone conditions. The application of the model can lead to an improved understanding of the effects of contaminant dissolution and the presence of an organic phase on metabolic reductive dechlorination kinetics.

Section III.D.4 briefly reviewed the general framework for modeling microbial degradation. In this chapter, this framework is extended to model metabolic reductive dechlorination in a DNAPL source zone (i.e., two-phase system). A batch dechlorination kinetic model is developed and coupled with an optimization algorithm to illustrate the ability of the kinetic model to simulate experimental systems with and without chloroethene-DNAPL. The model is used to estimate contaminant dissolution and dechlorination kinetic coefficients in single- and two-phase batch experimental systems. This batch model is integrated into an existing multiphase compositional simulator in Chapter VII to facilitate the simulation of metabolic reductive dechlorination in DNAPL source zones.

VI.B MODEL DEVELOPMENT

VI.B.1 Background and Conceptual Box Model

Metabolic reductive dechlorination (i.e., chlororespiration) was reviewed in detail in Section II.C. Therefore, the following review is intended only to highlight those processes that are important in the development of the metabolic reductive dechlorination model. Metabolic reductive dechlorination is a strictly anaerobic, energy-deriving process that couples the oxidation of an electron donor to the sequential reduction of chlorinated contaminants (e.g., PCE \rightarrow trichloroethene (TCE) \rightarrow dichloroethene (DCE) \rightarrow vinyl chloride (VC) \rightarrow ethene) [Holliger et al, 1998; Loeffler et al., 1996, 1999; Smidt and de Vos, 2004]. The possibility of stimulating this process across a range of chloroethene concentrations, including concentrations near solubility, has been demonstrated in recent years [Sharma and McCarty, 1996; Cirpka et al., 1999; Nielsen and Kiesling, 1999; Carr et al., 2000; Cope and Hughes, 2001; Yang and McCarty, 2000, 2002; Sung et al., 2003]. This ability to dechlorinate high concentrations of PCE and TCE is distributed across a range of bacterial groups [Janssen et al., 2001; Bradley, 2003; Smidt and de Vos, 2004], however, existing evidence suggests that only a single bacterial group, *Dehalococcoides*, is capable of *cis*-DCE and/or VC dechlorination [Maymo-Gatell et al., 1997, 2001; Hendrickson et al., 2002; He et al., 2003a,b; Cupples et al., 2003, 2004] and that this population may be inhibited at high chloroethene concentrations [Yang and McCarty, 2002; Adamson et al., 2004].

Electron donors, such as H_2 or acetate, which support the dechlorination reaction, can be added directly [e.g., Adamson et al., 2004; Clapp et al., 2004] or derived from the fermentation of organic substrates (e.g., lactate, formate, butyrate, propionate, benzoate,

ethanol) by syntrophic microorganisms [Bradley, 2003]. The non-specificity of the electron donor, however, typically leads to competition between dechlorinating and hydrogen-utilizing populations (e.g., methanogens) [Fennell and Gossett, 1998; Carr and Hughes, 1998; Yang and McCarty, 1998, 2002; He et al., 2002]. Fortunately, dechlorinating populations have a competitive advantage over other microbial populations due to their high affinity for the electron donor hydrogen [Smatlak et al., 1996; Löffler et al., 1999], suggesting that amendments that result in the sustained release of hydrogen at low concentrations (nM) are preferable [Smatlak et al., 1996; Ballapragada et al., 1997; Fennell et al., 1997; He et al., 2002]. Additionally, high chlorinated ethene concentrations may be inhibitory to competitor populations [Nielsen and Keasling 1999; Yang and McCarty, 2000], though a recent modeling study suggests these inhibitory effects may be restricted to areas directly adjacent to an organic phase which are at near saturation concentrations [Chu et al., 2003].

This brief background suggests that a conceptual model of metabolic reductive dechlorination should account for the presence of four microbial populations, a fermentative, a PCE-to-*cis*-DCE dechlorinator, a *cis*-DCE-to-ethene dechlorinator (i.e., *Dehalococcoides*), and a competitor (e.g., methanogens), and eight chemical components, a primary fermentable substrate (e.g., lactate), electron donor (e.g., hydrogen), PCE, TCE, *cis*-DCE, VC, ethene, and a competitor product (e.g., methane). The interrelationship among these microbial populations and chemical components is diagrammed in Figure VI.1.

The conceptual model depicted in Figure VI.1 differs from existing dechlorination models in several fundamental ways. The fermentation of a primary substrate to

hydrogen is rarely modeled. Typically, models assume direct addition of an electron donor (e.g., hydrogen), foregoing the need to model the fermentation step [Tandoi et al., 1994; Cirpka, 1995; Chu et al., 2003, 2004; Clapp et al., 2004]. Although the direct addition of electron donor may be possible in the field [Adamson et al., 2003], a more likely scenario requires the addition of fermentable substrates [Ellis et al., 2000; Major et al., 2002; Lendvay et al., 2003]. Competition for electron donor is another commonly neglected process [Tandoi et al., 1994; Tonnaer et al., 1997; Chu et al., 2003]. As mentioned previously, ignoring competitors may be appropriate for systems with high levels of uniform contamination (due to competitor inhibition) or laboratory systems with pure cultures, however, a complex microbial ecology [e.g., Chappelle, 2001] and non-uniform contaminant distribution [e.g., Lemke et al., 2004a; Phelan et al., 2004] are more likely in the field. Separation of the dechlorinating population into two distinct groups, one that converts PCE to *cis*-DCE via TCE and the other that converts *cis*-DCE to ethene via VC, is an increasingly common assumption [Bagley, 1998; Lee et al., 2004; Clapp et al., 2004] based on recent evidence demonstrating a shift in the microbial community during the transition from PCE to *cis*-DCE dechlorination [Flynn et al., 2000] and the growth of *Dehalococcoides* populations on *cis*-DCE and VC [Maymo-Gatell et al., 2001; Hendrickson et al., 2002; Cupples et al., 2003; He et al., 2003a, b].

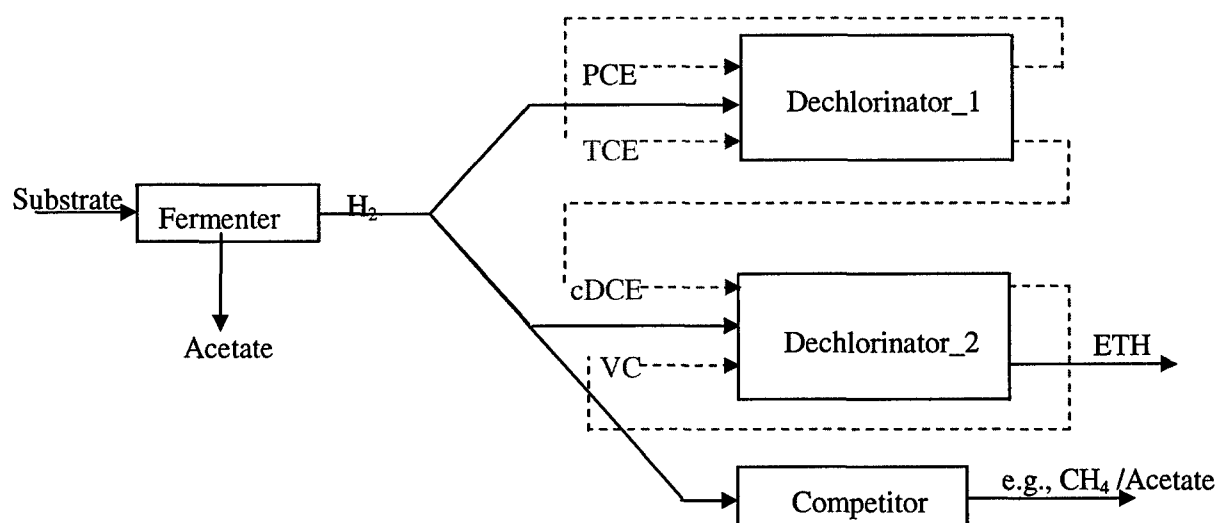


Figure VI.1: Conceptual model of metabolic reductive dechlorination, synergistic, and competing processes.

The kinetic models developed in Fennell and Gossett [1998], Bagley et al. [1998] and Lee et al. [2004] most closely approximate the conceptual model developed here (Figure VI.1). These models account for the processes depicted in Figure VI.1 plus additional fermentative [Fennell and Gossett, 1998; Bagley et al., 1998; Lee et al., 2004] and competitor populations [Bagley et al., 1998]. Although these additional populations may be important in some systems, they are supplementary to the actual dechlorination process. Furthermore, it was judged that the added solution complexity introduced by the addition of two to three microbial populations and chemical components in a multi-dimensional flowing system (note the referenced models were solved for a batch system), a task undertaken in the following chapter, would increase the computational effort unnecessarily.

VI.B.2 Metabolic Reductive Dechlorination Kinetics

Solving for the spatial-temporal distribution of microbial populations and chemical components diagrammed in Figure VI.1 requires the formalization of the conceptual model in a mathematical framework. As stated in Section III.D.4, this work assumes that the microbial populations are immobile and respond directly to bulk aqueous phase concentrations. These commonly employed assumptions [e.g., Hossain and Corapcioglu, 1994; Cirpka, 1995; Tonnaer et al., 1997; Clement et al., 1998] eliminate the need to assume and parameterize the biomass geometrical configuration (i.e., biofilm or microcolonies) [Baveye and Valocchi, 1989; Clement et al., 1996; Lensing, 1998] and to model the concentration gradient between the aqueous and biomass phases [Odencrantz et al., 1990]. Therefore, the reaction terms can be

represented as internal sources/sinks in the aqueous phase flow and transport governing equations.

Formalization of the conceptual model (Figure VI.1) into a mathematical framework (i.e., R_{α}^j) made use of the commonly implemented Monod kinetic expressions (see Section III.D.4):

$$R_a^{c'} = k_{\max}^c X_j \left(\frac{x_a^c}{K_S^c \cdot I^c + x_a^c} \right) \left(\frac{x_a^H - x_a^{H-thresh-j}}{K_S^{H-j} + (x_a^H - x_a^{H-thresh-j})} \right) \quad (VI.1a)$$

where k_{\max}^c is the maximum utilization rate, K_S^c is the component c half-saturation constant, I^c is the inhibition coefficient, and $x_a^{H-thresh-j}$ is the hydrogen utilization threshold concentration for microbial population j . Table VI.1 summarizes expressions used to represent I^c and presents the molar rate of biological degradation of component c in the α -phase for each component (R_a^c). The mass rate of degradation (R_a^{c*}) can be computed using R_a^c and the component molecular weight (MW_c). Equation VI.1a has been modified to include (1) hydrogen thresholds to reflect the hydrogen utilization efficiency of individual populations [Fennell and Gossett, 1998; Löffler et al., 1999; Clapp et al., 2004; Lee et al., 2004], (2) electron acceptor competition between *cis*-DCE and VC [Tonnaer et al., 1997; Garant and Lynd, 1998; Chu et al., 2004; Clapp et al., 2004; Cupples et al., 2003; Lee et al., 2004; Yu and Semprini, 2004; Yu et al., 2005], (3) inhibition of the second dechlorinating population (X_{dc2}) due to the presence of PCE [Adamson et al., 2004], and (4) inhibition of the competitor population due to the presence of high chloroethene concentrations [Bagley, 1998; Nielsen and Keasling, 1999; Clapp et al., 2004]. Note toxicity effects on dechlorinating cultures due to the presence of high contaminant concentrations associated with an organic phase are not included in

equation VI.1. Although recent evidence suggests that some dechlorinating cultures may lose the ability to dechlorinate contaminant concentrations above a threshold concentration [Ben Amos, Georgia Institute of Technology, Personal Communication], a number of published studies have demonstrated PCE-to-*cis*-DCE dechlorination in the presence of NAPL with aqueous phase concentrations at or near contaminant solubility. If future studies indicate that toxicity effects play a substantial role in the rate and extent of dechlorination, the developed model can be easily modified to incorporate these effects.

The growth of each biomass population is a function of the relevant degradation rates, the yield of biomass grown on component *c* (Y^c), and first-order endogenous decay (k_b):

$$\frac{dX_f}{dt} = -Y^c R_a^{PS} - k_b X_f \quad (\text{VI.2a})$$

$$\frac{dX_{dc1}}{dt} = Y^{PCE} R_a^{PCE'} + Y^{TCE} R_a^{TCE'} - k_b X_{dc1} \quad (\text{VI.2b})$$

$$\frac{dX_{dc2}}{dt} = Y^{DCE} R_a^{DCE'} + Y^{VC} R_a^{VC'} - k_b X_{dc2} \quad (\text{VI.2c})$$

$$\frac{dX_{Comp}}{dt} = -Y^{COMP} R_a^{COMP} - k_b X_{Comp} \quad (\text{VI.2d})$$

As indicated in Figure VI.1, an increase in the fermentative biomass concentration (X_f) is assumed to be due to the consumption of a fermentable substrate (e.g., lactate), dechlorinating biomass concentrations (X_{dc1} and X_{dc2}) are assumed to depend on the degradation of the electron donor and chloroethenes, and the competing biomass (X_{Comp}) is assumed to couple the oxidation of hydrogen to the reduction of carbon dioxide, producing for example methane.

Equations VI.1 and VI.2 form a set of twelve coupled, nonlinear ordinary differential equations that describe the growth of four microbial species due to fermentation, dechlorination, and methanogenesis (or other competitor) processes. As written, these equations assume the contaminant is bioavailable only in the aqueous phase. However, in most experimental batch systems, a gas phase is present to facilitate sampling and in some cases a non-aqueous phase is included to investigate metabolic reductive dechlorination in the presence of a dissolving NAPL. Incorporation of these additional phases requires the specification and solution of additional equations to describe interphase mass transfer.

VI.B.3 Interphase Mass Transfer

Generally, interphase mass transfer is modeled as an equilibrium process in batch experimental systems (e.g., aqueous-gas in Yang and McCarty [1998] or aqueous-NAPL in Carr et al. [2000]). This is a reasonable assumption in well-mixed reactors where the interfacial area separating phases remains relatively constant. For example, addition of contaminant (e.g., PCE) as a small fraction of an insoluble carrier phase results in a constant interfacial area separating the aqueous and organic phases (e.g., Carr et al., 2000). When contaminant is added as a pure-phase (e.g., Yang and McCarty, 2000) or when the system is poorly mixed, however, rate-limitations in interphase mass transfer (i.e., equations III.3 and III.5) must be considered.

Component (<i>c</i>)	Inhibition coefficient (<i>I'</i>)	Rate of degradation (R_a^c)
Primary substrate (PS)	-	$-k^{PS} X_f \left(\frac{x_a^{PS}}{K_S^{PS} + x_a^{PS}} \right)$ (VI.1b)
Hydrogen (H)	-	$F_{PS}R_a^{PS} - (F_{PCE}R_a^{PCE} + F_{TCE}R_a^{TCE} + F_{DCE}R_a^{DCE} + F_{VC}R_a^{VC} + F_{COMP}R_a^{COMP})^a$
(PCE)	1.0	$-R_a^{PCE'}$
(TCE)	1.0	$R_a^{PCE'} - R_a^{TCE'}$
<i>cis</i> -(DCE)	$\left(1 + \frac{x_a^{VC}}{K_I^{VC}} \right)$	$R_a^{TCE'} - R_a^{DCE'}$
(VC)	$\left(1 + \frac{x_a^{DCE}}{K_I^{DCE}} + \frac{x_a^{PCE}}{K_I^{PCE}} \right)$	$R_a^{DCE'} - R_a^{VC'}$
Ethene (ETH)	$\left(1 + \frac{x_a^{DCE}}{K_I^{DCE}} + \frac{x_a^{PCE}}{K_I^{PCE}} \right)$	$R_a^{VC'}$
Methane or acetate (COMP)	$\left(1 + \frac{x_a^{PCE}}{K_I^{PCE}} \right)$	$\frac{-k^{COMP}}{I^{COMP}} X_{COMP} \left(\frac{x_a^H - x_a^{H-thresh-j}}{K_S^H + (x_a^H - x_a^{H-thresh-j})} \right)$...(VI.1c)

^a F_c is the stoichiometric production or use coefficient of hydrogen during the degradation of component *c*.

Table VI.1: Biological degradation expressions

As discussed in Section III.D.3 there are two methods for modeling rate-limited interphase mass transfer, one that uses a mass transfer coefficient that incorporates saturation changes in the correlation and the other that models the mass transfer coefficient and the aqueous-organic interfacial area separately. In the work presented here, the latter method of simulating interphase mass transfer was selected:

$$E_{ao}^c = -E_{oa}^c = \begin{cases} \kappa^c a_{ao} (C_a^{c-sol} - C_a^c) & \text{if } C_a^{c-sol} \geq C_a^c \\ 0 & \text{otherwise} \end{cases} \quad (\text{VI.3})$$

Equation VI.3 is written in terms of the aqueous phase molar concentration, which can be related to the mole fraction used in Chapter III by $C_a^c = x_a^c \rho_a S_a$, and has been modified to neglect back partitioning of dechlorination degradation products to the organic phase. The decision to neglect back partitioning is based on the relatively small volume of NAPL (<50 μL) used in most batch experiments. The aqueous-organic interfacial area is quantified using a modified form of the diminishing sphere model described in Section III.D.3.i.2. Rather than assuming m classes of dissolving spherical blobs, the formulation developed here assumes all of the NAPL in the batch reactor is in a single spherical blob. This assumption is based on visual observations of the NAPL configuration during a two-phase experiment, and facilitates the computation of the interfacial area (equation III.23):

$$a_{ao} = \sum_m 3 \frac{\phi_m^f S_o}{r_m} = 4\pi r_1^2 \quad (\text{VI.4})$$

since for a single fraction of blobs ($m = 1$), $\phi_1^f S_o = V_o = \frac{4}{3}\pi r_1^3$. The change in the radius of the spherical blob as NAPL dissolves is computed using the organic phase mass balance equation:

$$\rho_o \frac{dV_o}{dt} = -E_{oa}^c = -K^c \left(4\pi \left(\frac{3V_o}{4\pi} \right)^{2/3} \right) (C_a^{c-sol} - C_a^c) \quad (VI.5)$$

The right hand side of equation (VI.5) can be substituted into the component c mass balance equation to account for dissolution of component c from the NAPL to the aqueous phase. Note, equation VI.5 assumes that biotransformation reactions only occur in the aqueous phase (i.e., $R_o^c = 0 \ \forall c$) and that no external sources or sinks are present (i.e., $Q_o = 0$).

VI.B.4 Batch Dissolution/Dechlorination Model

Simulating batch metabolic reductive dechlorination experiments with and without NAPL requires the integration of the interphase mass transfer and metabolic reductive dechlorination terms discussed in Sections VI.B.2 and VI.B.3 into phase and component mass balance equations.

VI.B.4.i Batch Phase Mass Balance Equations

In addition to the batch organic phase (NAPL) mass balance equation (equation VI.5) described in Section VI.B.3, gas and aqueous phase mass balance equations may be required. Typically, for batch systems, the gas and aqueous phase are assumed to be at equilibrium and the phase volumes are assumed to remain constant. These assumptions allow the phase mass balance equations for these phases to be ignored. However, some experiments require significant sampling, which can alter the phase volumes by up to forty percent (Ben Amos, personal communication). Accurate simulation of these

experiments requires the incorporation of the phase mass balance equations, written here for a batch system:

$$\rho_a \frac{dV_a}{dt} = \sum_c \sum_\beta E_{a\beta}^c + \sum_c R_a^c + \rho_a Q_a \quad (\text{VI.6})$$

$$\rho_g \frac{dV_g}{dt} = \sum_c \sum_\beta E_{g\beta}^c + \rho_g Q_g \quad (\text{VI.7})$$

If it is assumed that the change in phase mass ($\rho_\alpha V_\alpha$) due to interphase exchange and biotransformation reactions is small compared to the change in phase mass due to sampling, then equations VI.6 and VI.7 can be simplified to:

$$\frac{dV_a}{dt} = -Q_a \quad (\text{VI.8})$$

$$\frac{dV_g}{dt} = Q_g = -\frac{dV_a}{dt} \quad (\text{VI.9})$$

where here it is assumed that the sampling occurs in the aqueous phase and that a reduction in the aqueous phase volume corresponds to an equivalent increase in the gas phase volume (i.e., $V_a + V_g = 1$). Equations VI.8 and VI.9 can be solved analytically to model the change in phase volume due to experimental sampling. In the modeling presented in Section VI.C, $Q_a = Q_g$ are assumed to be constant and equal to the slope of the change in phase volume with respect to time due to sampling.

VI.B.4.ii Batch Component Mass Balance Equations

Typically, when simulating metabolic reductive dechlorination in batch systems, the component mass balance equations (i.e., equation III.5) are simplified to model only the change in mass due to reactions (i.e., equation VI.1). The aqueous phase volume is

assumed to remain constant and the presence of a gas phase is incorporated using Henry's law. While using Henry's law to account for gas-aqueous interphase mass transfer is also appropriate in the experiments simulated here, changes in the gas and aqueous phase volumes due to sampling are modeled. Therefore, the phase volumes are functions of time. Using the chain rule to expand the time derivatives and Henry's law to relate the gas phase concentration to the aqueous phase concentration, the component mass balance equation:

$$\frac{d}{dt}(V_a C_a^c) + \frac{d}{dt}(V_g C_g^c) = E_{ao}^c + R_a^c + Q_a^c \quad (\text{VI.10})$$

can be rewritten

$$\begin{aligned} C_a^c \frac{dV_a}{dt} + V_a \frac{dC_a^c}{dt} + C_g^c \frac{dV_g}{dt} + V_g K_c^H \frac{dC_a^c}{dt} = \\ C_a^c Q_a (K_c^H - 1) + (V_a + V_g K_c^H) \frac{dC_a^c}{dt} = E_{ao}^c + R_a^c + Q_a^c \end{aligned} \quad (\text{VI.11})$$

so that

$$\frac{dC_a^c}{dt} = \frac{E_{ao}^c + R_a^c + C_a^c Q_a (1 - K_c^H) + Q_a^c}{(V_a + V_g K_c^H)} \quad (\text{VI.12})$$

The first term in equation VI.12 accounts for the change in concentration due to interphase partitioning of component c , the second term accounts for the change in concentration due to the reaction of component c in the aqueous phase, the third term accounts for the change in concentration due to the change in the aqueous and gas phase volumes, and the last term accounts for the change in concentration due to external sources and sinks of component c (e.g., loss of component mass due to sampling). Equation VI.12 can be written for each component to simulate coupled dissolution and biotransformation of multiple components. Note, as stated previously equation VI.12

assumes back partitioning of aqueous phase PCE degradation products is negligible (i.e., $E_{oa}^c \approx 0$) since the volume of NAPL added to a typical batch system is relatively small (i.e., less than 0.1% of the aqueous phase volume).

VI.B.4.iii Solution Algorithm

Incorporating equations VI.1 and VI.2 into the batch phase mass balance equations (VI.8 – VI.9) and component transport equations (VI.12) forms a set of fifteen coupled ordinary non-linear differential equations that together have been termed Batch-DECHLOR. As described in Section III.E.3, these equations are solved here using a high-order explicit finite-difference routine (fourth-order Runge-Kutta) that is part of the high-level technical computing framework, MATLAB [Hanselman and Littlefield, 2001]. This routine was selected based on results from a recent numerical investigation that compared Runge-Kutta, Taylor series expansion, forward Euler, and quasi-steady-state solution routines for a system of coupled non-linear ordinary differential equations [Mohamed and Hatfield, 2005]. Runge-Kutta routines were shown to provide the most accurate solutions when compared with existing analytical and numerical solutions. Batch-DECHLOR predictions are compared to experimental results using absolute and root mean squared errors. A MATLAB optimization routine is used to systematically adjust biological kinetic coefficients to minimize the error between the simulated and experimental results.

The optimization routine is based on the simplex optimization method [Hanselman and Littlefield, 2001]. This method is an efficient multi-dimensional optimization routine that minimizes an objective function by systematically evaluating

the function at $k+1$ control points, where k is the number of optimized parameters (e.g., k_{max}^c, K_S^c). The $k+1$ control points form a k -dimensional object termed a simplex. For example, when $k = 2$, the simplex is a triangle (see Figure VI.2). The objective function is evaluated at each vertex of the simplex and the values are ranked. The parameters corresponding to the worst vertex are reflected along a line through a point corresponding to the average of the remaining vertexes (centroid). The objective function is evaluated at this new reflected point. If it is an improvement over the worst point it replaces that point and the simplex shifts in that direction. If it is not an improvement, then the objective function is evaluated at a new point (contraction point) along the same line midway between the worst point and the centroid of the remaining points. In this way the simplex moves throughout the search space until a minimum is reached. Penalty functions are used to ensure the simplex remains within the search space. A limitation to the simplex algorithm is its inability to confirm identification of the global minimum. Therefore, alternative starting control points should be evaluated to ensure the global minimum is obtained.

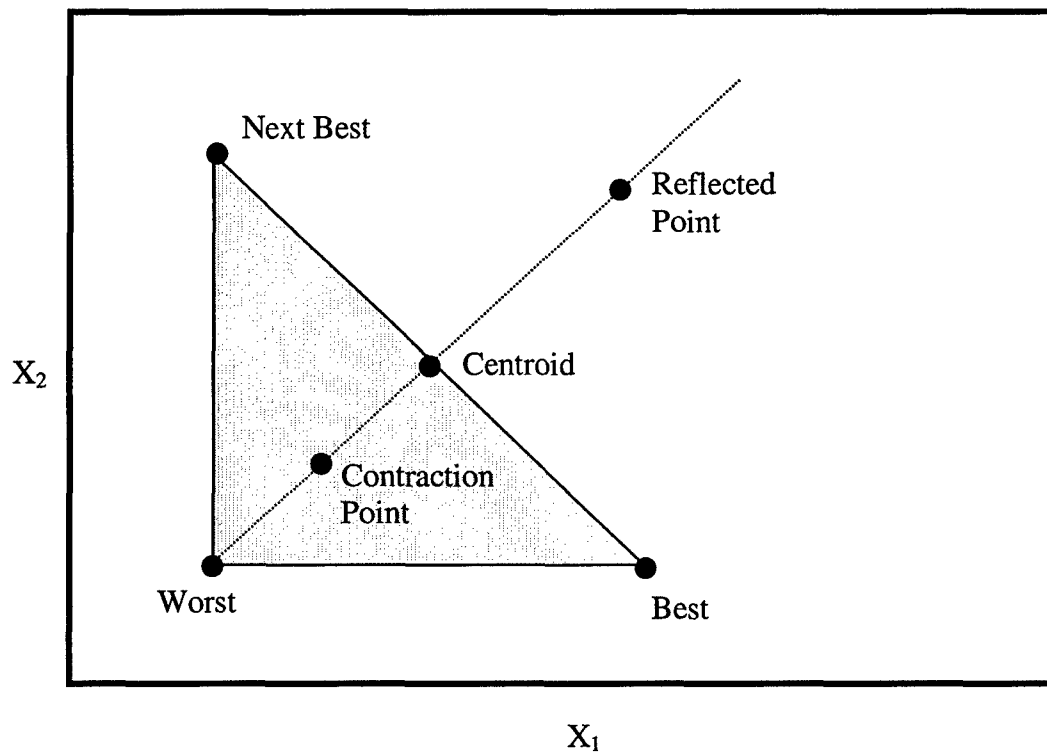


Figure VI.2: Example diagram of simplex optimization method for two parameter ($k = 2$) optimization.

VI.C APPLICATIONS

Batch-DECHLOR, the model described in section VI.B, is applied here to (i) illustrate its ability to simulate batch systems with and without the presence of a non-aqueous phase, and (ii) estimate and compare best-fit kinetic coefficients for a range of experimental conditions. Mixed and pure cultures in the presence and absence of residual source zone flushing solutions (i.e., surfactant) and in the presence of a dissolving organic phase are modeled. Experimental results were either taken from the literature or provided by collaborating colleagues at the Georgia Institute of Technology.

VI.C.1 Single-Phase Batch Systems

In this section experimental results reported by Yang and McCarty [2000] and results provided by collaborating colleagues at the Georgia Institute of Technology are used to quantify metabolic reductive dechlorination kinetics in single-phase batch systems. The dechlorinating ability of two complex and two pure cultures are modeled. The activity of the two pure cultures is also modeled in the presence of a nonionic surfactant that was used at the recent pilot-scale SEAR demonstration in Oscoda, MI [Abriola et al., 2005].

VI.C.1.i Mixed Culture Experiments

Yang and McCarty [2002] carried out batch dechlorination studies at three alternative initial aqueous phase PCE concentrations (0.1mM, 0.3mM, and 1.0mM) to examine the influence of PCE concentration on dechlorinating activity. These experiments were conducted in 120 mL reactors with approximately 60mL of headspace.

An electron donor in the form of hydrogen was added in an amount corresponding to an aqueous phase concentration of approximately 7.0mM. The dechlorinating culture was obtained from a CSTR seeded with a sample collected from a PCE-contaminated aquifer in Victoria, TX. This culture was maintained on near solubility concentrations of PCE for multiple years. The steady-state biomass concentration of this culture was measured at 10 mg volatile suspended solids (VSS)/L. Contaminant samples (250 μ L) were collected from the headspace approximately every 5 days. The small sample volume along with the sparse sampling frequency eliminated the need to account for changes in the phase volume and mass lost due to sampling (i.e., Q_a and Q_a^c).

The batch experiment with an initial PCE concentration equal to 0.3mM was simulated using Batch-DECHLOR. Dimensionless Henry's constants reported by Yang and McCarty [2000] were used to partition the total moles of electron donor and chloroethenes per bottle to aqueous and gas phase concentrations. Although the initial biomass concentration was reported, the fraction of initial biomass associated with each microbial population (i.e., X_{dc1} , X_{dc2} , X_c) was not measured. Therefore, the optimization routine was modified to fit these initial biomass concentrations, with the constraint that the sum of the initial biomass concentrations equaled 10 mg VSS/L. In addition to the biomass concentrations, 10 other parameters were fit, k_{max}^c and K_S^c for PCE, TCE, *cis*-DCE, and VC dechlorination, k_{max}^c for acetogenesis, and K_I for competitor inhibition due to the presence of PCE. All other kinetic model parameters were taken from the literature.

The optimal fit (solid lines) to the Yang and McCarty experimental data (symbols) is shown in Figure VI.3. Simulated electron donor concentrations decline over

the first 15 days of the simulation, with the rate of consumption accelerating between day 10 and day 15 (Figure VI.3a). The reason for the change in the rate of consumption of electron donor is attributable to the rapid growth of acetogens following the dechlorination of PCE (see equation VI.1c). Simulated chloroethene and acetate concentrations shown in Figures VI.3b and c demonstrate that Batch-DECHLOR is capable of matching observed dechlorination and acetogenesis (the competitor process) experimental results quite well. PCE is degraded rapidly to TCE, which accumulates to relatively low concentrations, before being degraded to *cis*-DCE. *cis*-DCE is dechlorinated to VC, however, the electron donor becomes limiting at day 15 (see Figure VI.3a), resulting in incomplete dechlorination of *cis*-DCE and VC to ethene. Although not measured, simulated biomass concentrations are plotted in Figure VI.3d. The model predicts that the PCE-to-*cis*-DCE dechlorinating population grows rapidly during the initial phases of the experiment. Growth of the acetogenic (competitor) population is delayed due to PCE inhibitory processes. The growth rate of the second dechlorinating population is less than the endogenous decay rate, resulting in a gradual decrease in the biomass concentration.

Optimal kinetic coefficients used in the simulation of this experiment are listed in Table VI.2. Also provided in Table VI.2 are ranges of model parameter values obtained from the literature and summarized as part of a recent study [Clapp et al., 2004]. With the exception of the VC kinetic coefficients (k_{max}^{VC} , K_S^{VC}), all of the model parameters are within the range of values reported in the literature. The best-fit values for the VC kinetic coefficients are two to five times less than the minimum reported value, reflecting the lack of VC dechlorination in this experiment.

The second mixed culture experiment simulated was conducted at the Georgia Institute of Technology using a mixed culture collected from the Bachman aquifer in Oscoda, MI [Lendvay et al., 2003]. This experiment differs from the previous experiment in two ways: (i) a fermentable substrate was added in addition to the electron donor hydrogen, and (ii) dechlorination of PCE was complete to ethene. These differences enable the examination of the simulated fermentation process and the last dechlorination step from VC to ethene.

Metabolic reductive dechlorination in a 160mL reactor with a 60mL headspace was initiated using 2mL of the mixed culture. Lactate (5mM) and hydrogen (10 mL) were added to the reactor to supply the necessary electron donors to ensure complete dechlorination of 4 μL of PCE ($\sim 270\mu\text{M}$ aqueous phase concentration). The experiment was run in triplicate and chloroethene concentrations were measured from 1mL aqueous phase samples collected approximately every 7 days. The total change in aqueous (and gas) phase volume over the 46 day experiment was less than 10 percent. Hence, the change in phase and component mass due to sampling was neglected.

The experimental (symbols) and best-fit model (solid line) concentrations for this experiment are plotted in Figure VI.4. Figure VI.4a shows that the lactate is rapidly fermented producing hydrogen, which supports dechlorination and acetogenesis throughout the majority of the experiment. PCE is dechlorinated sequentially through TCE, *cis*-DCE, and VC to ethene over the first 35 days of the experiment (Figure VI.4b). *cis*-DCE and VC are the primary accumulation products. The observation that these components can accumulate to approximately equivalent concentrations supports the need to simulate electron acceptor competition. As in the previous experiment, acetate

concentrations rise rapidly following the depletion of PCE (Figure VI.4c). Acetate concentrations were not measured in this experiment, however, these concentrations ($\sim 2500 \mu\text{M}$) are within a factor of 2 of those measured by Yang and McCarty [2000]. Simulated biomass concentrations are depicted in Figure VI.4d. The fermentative population declines gradually throughout the life of the experiment with an increase in the rate of decay following the depletion of lactate. Both dechlorinating populations decline throughout the life of the experiment, despite the degradation of chloroethenes. This behavior is indicative of a system in which endogenous decay is greater than the yield of microorganisms due to dechlorination. Similar behavior has been reported in simulations by Fennell and Gossett [1998]. Acetogens grow rapidly following the dechlorination of PCE to low levels.

Optimal parameters corresponding to the simulation in Figure VI.4 are reported in Table VI.2. Comparison with the range of values reported in the literature indicates that the simulated best-fit kinetic coefficients are generally low. The optimal values for these parameters may not be unique due to a lack of information on the initial biomass concentrations. The reported values correspond to the best-fit (i.e., lowest root mean squared error between simulated and experimental results) simulation out of several simulations attempted. Changing the initial array of kinetic coefficients, including initial biomass concentrations, resulted in either convergence to the reported solution or failure of the optimization algorithm to find a solution.

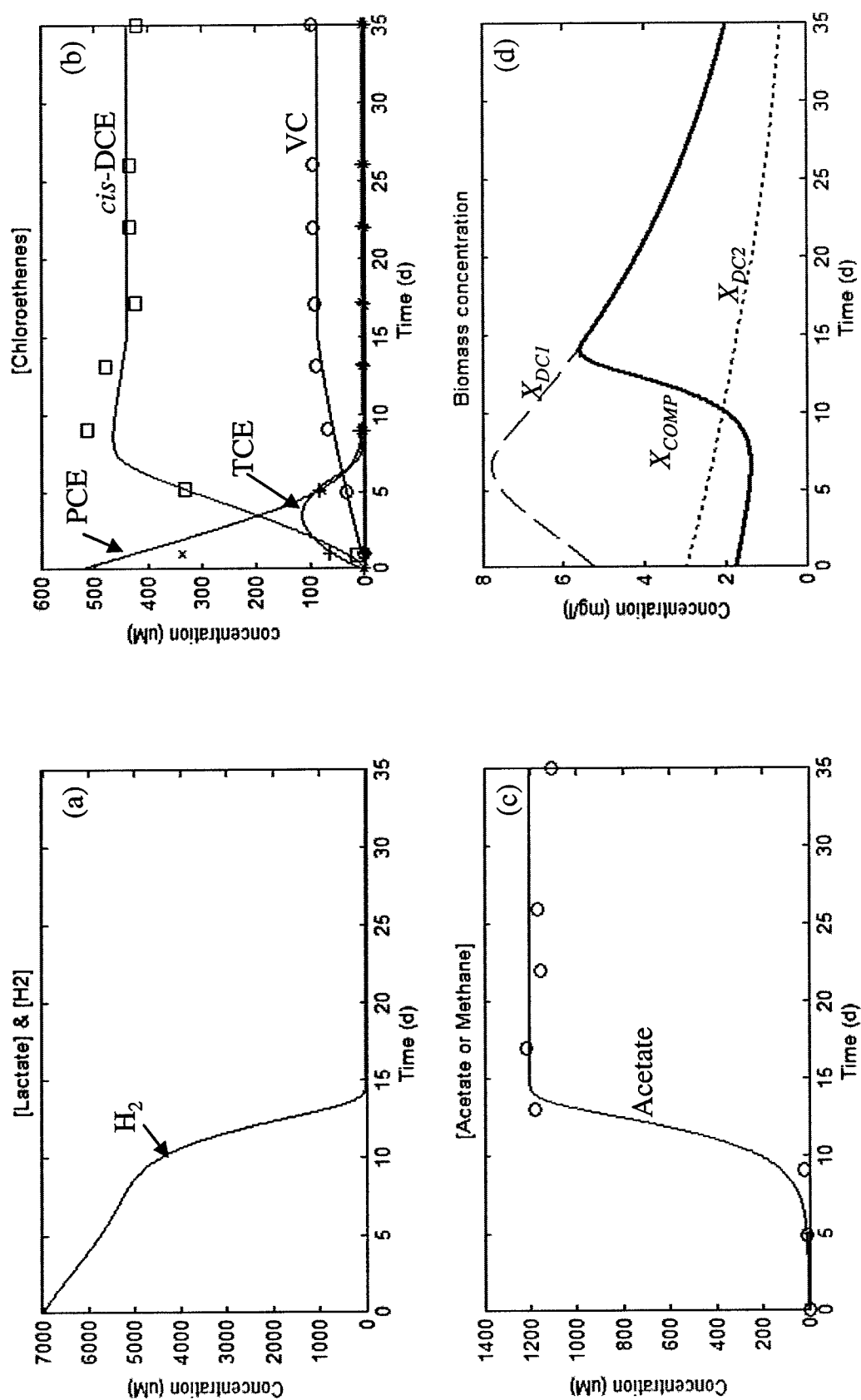


Figure VI.3: (a) Hydrogen, (b) Chloroethene, (c) Acetate, and (d) biomass concentrations as a function of time. Data taken from Yang and McCarty [2000].

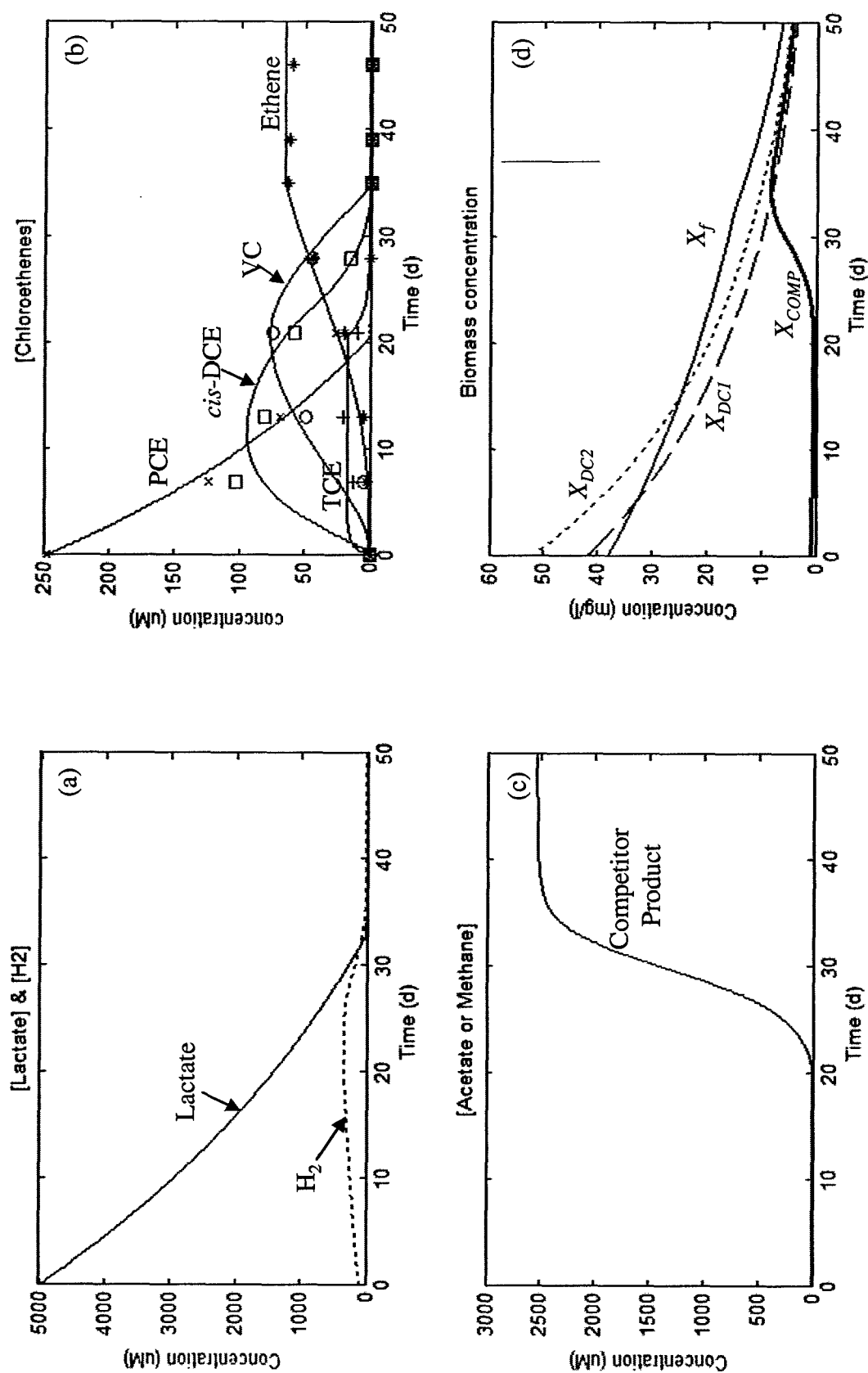


Figure VI.4: (a) Fermentable substrate and Hydrogen, (b) Chloroethene, (c) competitor product, and (d) biomass concentrations as a function of time. Data provided by Ben Amos (Georgia Institute of Technology, unpublished results).

Parameter	Yang & McCarty	Bachman (PCE-ETH)	Multivorans (0 TWEEN)	BAV1	Clapp et al. [2004] Range	Units
System Parameters						
$[H_2]_i$	6200.00	2538.60	5000.00	650.00	-	μM
$[\text{Substrate}]_i$	0.00	5000.00	0.00	5000.00	-	μM
$[\text{PCE}]_i$	336.05	247.70	168.99	$[\text{DCE}]_i = 371.26$	-	μM
Fitted model Parameters						
X_f	-	38.20	-	-	<5000	mg/L
X_{dc1}	5.25	41.99	34.41	-	<5000	mg/L
X_{dc2}	3.00	52.16	-	42.93	<5000	mg/L
X_c	1.75	0.72	-	-	<5000	mg/L
k^{ps}	-	6.13	-	-	-	$\mu\text{mol}/(\text{mg}\cdot\text{d})$
k^{pce}	28.00	0.40	8.56	-	1.4 - 117	$\mu\text{mol}/(\text{mg}\cdot\text{d})$
k^{ice}	15.00	2.49	8.83	-	2.4 - 117	$\mu\text{mol}/(\text{mg}\cdot\text{d})$
k^{dce}	3.00	1.64	-	0.89	1.7 - 22.2	$\mu\text{mol}/(\text{mg}\cdot\text{d})$
k^{vc}	1.00	0.84	-	0.83	2.6 - 22.2	$\mu\text{mol}/(\text{mg}\cdot\text{d})$
k^{comp}	136.00	354.6	-	-	27.0 - 1138.0	$\mu\text{mol}/(\text{mg}\cdot\text{d})$
K_s^{ps}	-	1.26	-	-	-	μM
K_s^{pce}	252.00	0.05	75.78	-	0.11 - 252 ^a	μM
K_s^{ice}	28.00	91.1	13.14	-	0.54 - 100 ^b	μM
K_s^{dce}	0.54	0.19	-	0.13	0.54 - 100 ^b	μM
K_s^{vc}	0.54	0.11	-	0.27	2.6 - 360.0	μM
Assumed model parameters						
K_s^{H-dc1}	0.02	0.02	0.02	0.02	0.015 - 0.10	μM
K_s^{H-dc2}	0.02	0.02	0.02	0.02	0.015 - 0.10	μM
K_s^{H-c}	1.00	1.00	-	-	0.5 - 22.2	μM
K_i^{DCE}	K_s^{vc}	K_s^{vc}	-	K_s^{vc}	-	μM
K_i^{VC}	K_s^{dce}	K_s^{dce}	-	K_s^{dce}	-	μM
K_i^{COMP}	0.30	0.30	-	-	<500	μM
$[H_2]_{\text{thresh-DC}}$	2.00×10^{-3}	2.00×10^{-3}	2.00×10^{-3}	2.00×10^{-3}	<2.00E-3	μM
$[H_2]_{\text{thresh-comp}}$	0.011	0.011	-	-	0.011 - 0.077	μM
Y_{ps}	-	3.51×10^{-3}	3.51×10^{-3}	-	-	mg/ μmol
Y_{dc}	4.86×10^{-3}	4.86×10^{-3}	4.86×10^{-3}	4.86×10^{-3}	3.3 - 9.6×10^{-3}	mg/ μmol
Y_{comp}	4.52×10^{-3}	4.52×10^{-3}	4.52×10^{-3}	-	0.62 - 1.5×10^{-3}	mg/ μmol
K_b	0.05	0.05	0.05	0.05	-	d ⁻¹

^a Maximum value from Nielsen and Keasling [1999]

^b Maximum value from Cirpka [1995]

Table VI.2: Dechlorination kinetic parameters for pure and mixed culture simulations described in Section VI.C.1. Clapp et al. [2004] summarized the range of values published in the literature as of 2004.

VI.C.1.ii Pure Culture Experiments

In addition to the mixed culture experiments simulated in the previous section, pure cultures are commonly evaluated for dechlorinating activity. In this section, Batch-DECHLOR is used to simulate results from two pure culture experiments conducted by collaborating colleagues at the Georgia Institute of Technology, one containing *Sulfurospirillum multivorans* and the other containing *Dehalococcoides etheneogenes* BAV1. *Sulfurospirillum multivorans* is a robust pure culture that is known to convert high concentrations of PCE to *cis*-DCE. *Dehalococcoides etheneogenes* BAV1 is a recently discovered isolate that converts *cis*-DCE to ethene via metabolic dechlorination [He et al., 2003b]. Previous cultures capable of dechlorinating *cis*-DCE to ethene were assumed to do so co-metabolically due to the low rates of dechlorination and lack of microbial yield [Maymo-Gatell et al., 1997]. Simulating these two cultures independently provides a method for investigating the two-step dechlorination process implemented in Bio-DECHLOR.

In the first experiment, which contained a 5mL culture of *Sulfurospirillum multivorans*, pyruvate (5mM) was added to a 160 mL reactor (100mL aqueous phase) with an aqueous phase PCE concentration of approximately 160 μ M. Pyruvate is a unique substrate since it can be used directly as an electron donor as well as be converted to additional fermentable substrates and hydrogen, which further support dechlorination. In this simulation, however, pyruvate was assumed only to be a direct electron donor in that the 0.06 mol H₂/mol pyruvate were neglected. Figure VI.5 presents experimental results that demonstrate that the pure culture is able to dechlorinate PCE to *cis*-DCE within the first day. No significant accumulation of TCE was measured. Best fit kinetic

coefficients are listed in Table VI.2. These coefficients lie within the range of values that have been reported in the literature and are generally higher than the best-fit values for the Bachman mixed culture, but lower than the best-fit values for the Victoria culture.

In the second experiment, 5mL of an active *Dehalococcoides etheneogenes* BAV1 culture were added to a 160 mL reactor (101mL aqueous phase) with an aqueous phase *cis*-DCE concentration of approximately 375 μ M. Acetate (5mM) was added to serve as a carbon source and hydrogen (5 mL) was added to drive the dechlorination process. As shown in Figure VI.6, *cis*-DCE is rapidly converted to VC. VC accumulates to significant concentrations (200 μ M) before degrading to ethene. Best-fit values for the kinetic coefficients for this experiment are listed in Table VI.2. These coefficients are generally within a factor of two of the best-fit kinetic coefficients for the *cis*-DCE to ethene dechlorination population in the Bachman culture. The closeness of the values of these coefficients may be expected since the BAV1 pure culture was isolated from the Bachman mixed culture [He et al., 2003a].

The dechlorinating activity of these pure cultures was also examined under conditions of stress. A nonionic surfactant, TWEEN 80, was added at various concentrations to batch reactors containing either *Sulfurospirillum multivorans* or *Dehalococcoides etheneogenes* BAV1. This surfactant was selected for examination because of its use at the SEAR pilot-scale demonstration in Oscoda, MI [Abriola et al., 2005] and because of its relatively non-toxic effect on microbial activity in previous batch experiments [Yeh et al., 1999; McGuire and Hughes, 2003; Ramsburg et al., 2004].

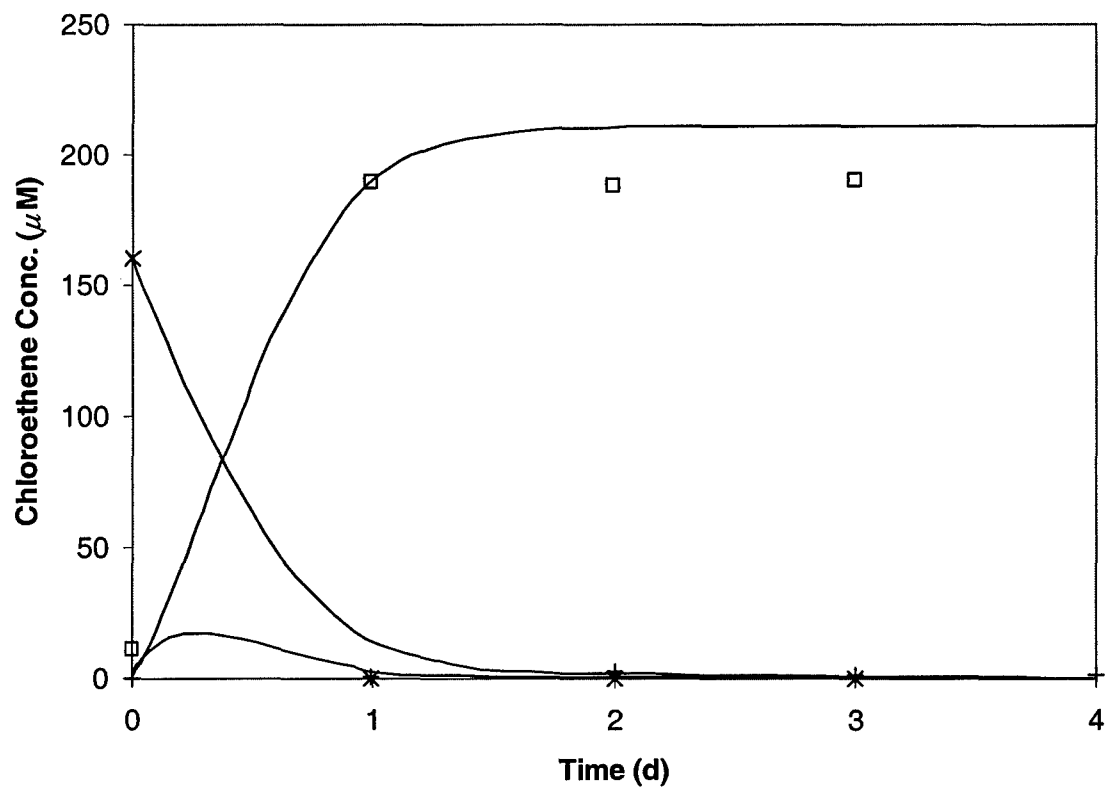


Figure VI.5: Model (solid line) and experimental (symbols) results for PCE dechlorination to cis-DCE by *Sulfurospirillum multivorans* pure culture. PCE (x), TCE(+), and cis-DCE (□).

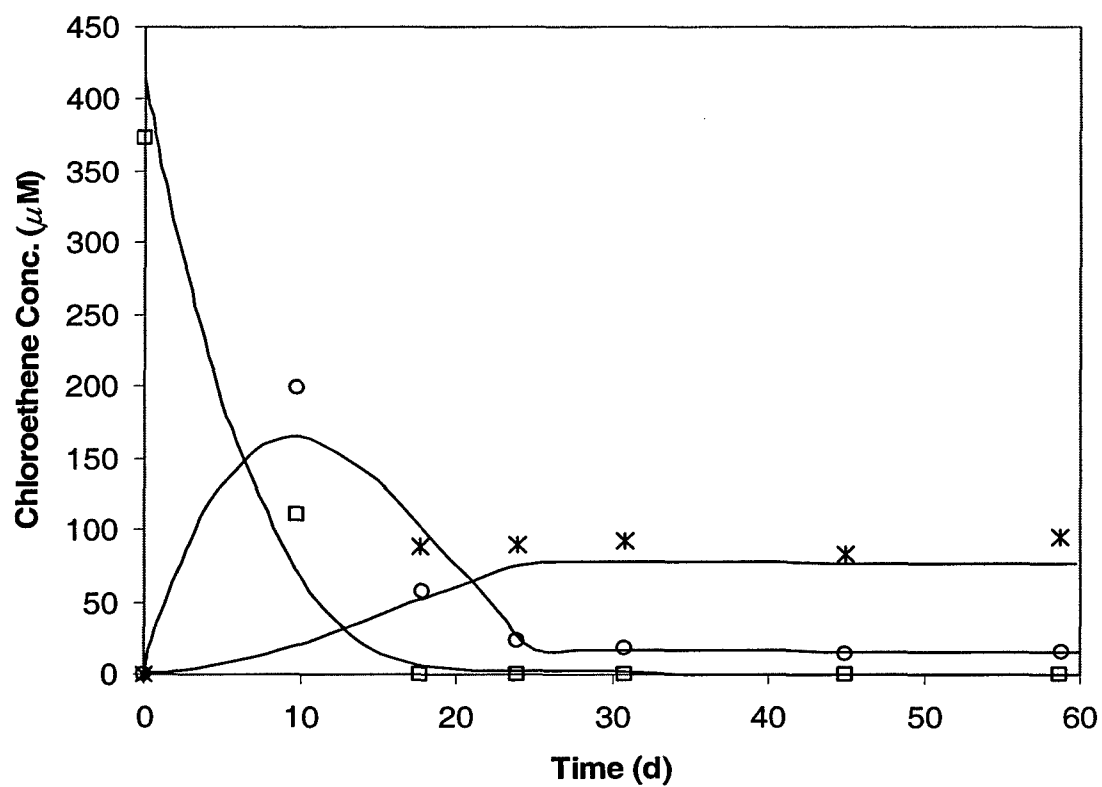


Figure VI.6: Model (solid line) and experimental (symbols) results for *cis*-DCE dechlorination to ethene by *Dehalococcoides etheneogenes* BAV1 pure culture. *cis*-DCE (\square), VC (O), ethane (*).

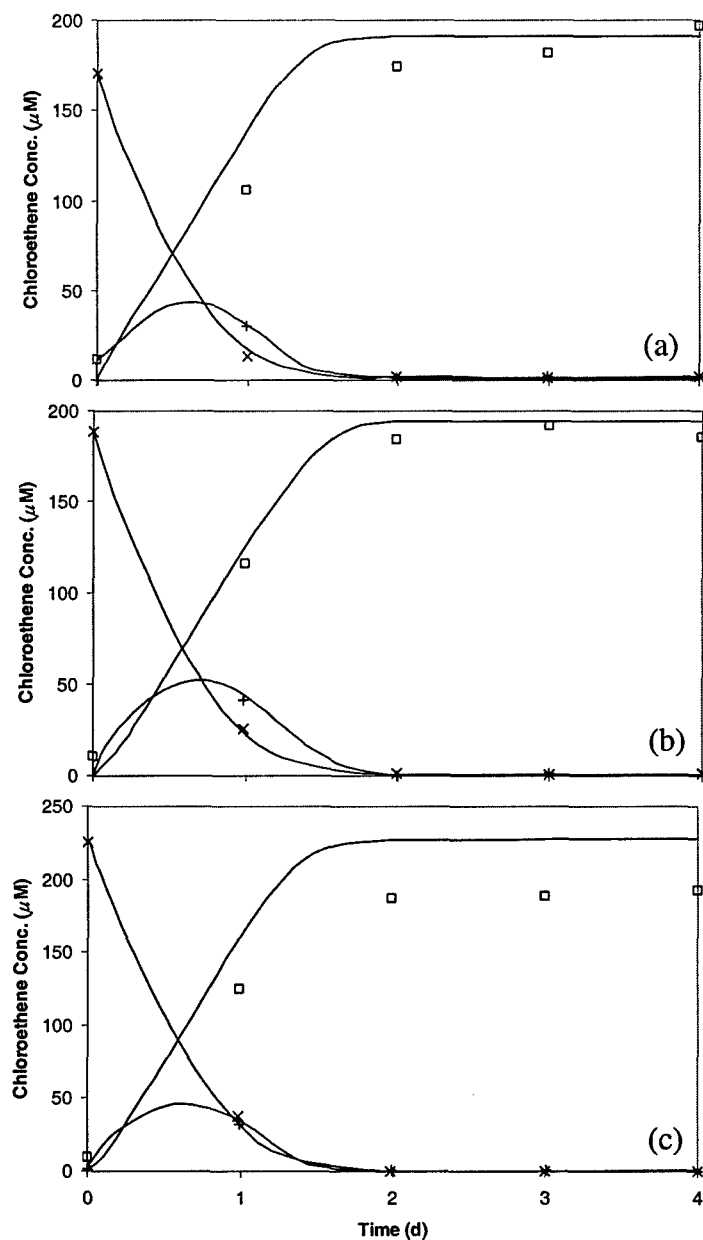


Figure VI.7: Simulated (solid line) and experimental (symbol) chloroethene concentrations during metabolic reductive dechlorination by *Sulfurospirillum multivorans* in the presence of (a) 500 mg/L, (b) 1000 mg/L, and (c) 5000 mg/L of TWEEN 80 surfactant. PCE (x), TCE(+), and cis-DCE (□).

Parameter	Multivorans (0 mg/L TWEEN)	Multivorans (500 mg/L TWEEN)	Multivorans (1000 mg/L TWEEN)	Multivorans (5000 mg/L TWEEN)	Units
System Parameters					
$[PCE]_i$	168.99	169.30	188.40	225.60	μM
Fitted model Parameters					
X_{dcl}	34.41	34.41	34.41	34.41	mg/L
k^{pce}	8.56	10.71	6.26	6.26	$\mu\text{mol}/(\text{mg}\cdot\text{d})$
k^{tce}	8.83	6.56	3.23	4.13	$\mu\text{mol}/(\text{mg}\cdot\text{d})$
K_s^{pce}	75.78	75.78	75.78	75.78	μM
K_s^{tce}	13.14	13.14	13.14	13.14	μM

Table VI.3: Best fit kinetic coefficients for *Sulfurospirillum multivorans* in the presence of 500 mg/L, 1000 mg/L, and 5000 mg/L of TWEEN 80 surfactant. See Table VI.2 for kinetic coefficients not shown.

Three increasing concentrations (500, 1000, and 5000 mg/L) of TWEEN 80 were added to an active culture of *Sulfurospirillum multivorans* [Ramsburg et al., 2004]. These concentrations were selected to span the range of residual surfactant concentrations that may be expected in a DNAPL source zone following SEAR treatment. Figure VI.7 shows experimental (symbols) and simulated (solid line) dechlorination activity at the three surfactant concentrations selected. The distribution of chloroethenes between the gas and aqueous phases was computed using Henry's constants corrected for the presence of surfactant following the methods of Kibbey et al. [2001]. Comparing results reported in Figure VI.7 to the original experimental results where no TWEEN 80 was present (Figure VI.5), the presence of surfactant, even at a concentration of 5000 mg/L, appears to have only a minor effect on the rate of PCE-dechlorination. When surfactant is present, minor amounts of TCE accumulate during the early stages of the experiment slowing the production rate of *cis*-DCE. Table VI.3 compares the dechlorination kinetic coefficients for *Sulfurospirillum multivorans* in the presence of TWEEN 80 at all three concentrations to the original best-fit values. The presence of surfactant appears to reduce the maximum utilization rates of PCE and TCE by approximately 25%. However, the change in maximum utilization rates does not appear to be proportional to the surfactant concentration. Rather, it appears that the presence of surfactant at any concentration inhibits the dechlorination rate equally.

The dechlorinating activity of an active culture of *Dehalococcoides etheneogenes* BAV1 was also examined in the presence of the TWEEN 80 surfactant [Ben Amos, Georgia Institute of Technology, Unpublished data]. In this experiment, only a single surfactant concentration (250 mg/L) was examined. Even at this relatively low

concentration, the surfactant completely inhibited the dechlorination of *cis*-DCE throughout the 75 day period of the experiment [Ben Amos, Georgia Institute of Technology, unpublished data]. This result is consistent with experiments performed by McGuire and Hughes [2003] that demonstrated suppressed dechlorination beyond *cis*-DCE in the presence of TWEEN 80 and field observations reported by Ramsburg et al. [2004] that found *cis*-DCE accumulation despite the presence of *Dehalococcoides* populations.

VI.C.2 Two-phase (aqueous-organic) Batch Systems

While the experiments evaluated in the previous section (Section VI.C.1) are important for the assessment of dechlorinating activity, the application of those results to DNAPL source zone scenarios may be limited due to the absence of a dissolving organic phase (i.e., NAPL) in the batch studies. Only a single published study has attempted to quantify rates of dechlorination in aqueous-organic systems [Carr et al., 2000]. This study, however, employed numerous simplifying conditions and did not attempt to compare dechlorination rates in the presence and absence of a dissolving organic phase. In this section, Batch-DECHLOR is used to simulate dechlorination observations from two-phase (aqueous-organic) batch reactors with cultures corresponding to those evaluated by Yang and McCarty [2000] and collaborating colleagues at the Georgia Institute of Technology. This analysis provides a first-step in quantifying potential effects of an organic phase on metabolic reductive dechlorination rates.

The Yang and McCarty [2000] experiment was conducted using the same methodology described in Section VI.C.1.i for single-phase experiments. For this

experiment, however, PCE ($\sim 10 \mu\text{L}$) was added to a batch reactor in a quantity sufficient to result in aqueous phase PCE concentrations near saturation ($\sim 900 \mu\text{M}$). This experimental setup resulted in the presence of pure phase PCE as well as near saturation aqueous phase PCE concentrations. Yang and McCarty [2000] did not provide any abiotic data that could be used to quantify the PCE mass transfer coefficient (κ^{PCE}). Therefore, the modeling protocol was adjusted so that the mass transfer coefficient was included as an additional fitting parameter.

Experimental (symbols) and simulated (solid line) results are compared in Figure VI.8. The aqueous phase PCE concentrations decline over the first fifteen days of the experiment, producing TCE and *cis*-DCE. After approximately 20 days, TCE is no longer detected and *cis*-DCE begins to accumulate. As PCE continues to transfer from the NAPL to the aqueous phase, *cis*-DCE accumulates until the PCE is depleted. The best fit PCE mass transfer coefficient value for this experiment was 1.74 m/d. Dechlorination kinetics were modeled using the same values for the kinetic coefficients obtained using the single-phase Yang and McCarty [2000] experiment. An initial attempt to use the same initial biomass concentrations resulted in a poor fit to the data. Thus, the initial X_{del} biomass concentration was reduced from 5.25 mg/L to 0.2 mg/L to improve the fit. The observation of a reduction in the biomass concentration suggests that the presence of an organic phase may have a toxic effect on the PCE to *cis*-DCE dechlorinating population. Yet, this effect could not be confirmed since biomass concentrations were not reported.

The Yang and McCarty [2000] two-phase study simulated above used a PCE amendment strategy that resulted in high aqueous phase PCE concentrations along with a

pure PCE phase. Alternatively, PCE can be added as a separate phase to an actively dechlorinating culture [Ben Amos, Georgia Institute of Technology, unpublished results]. In this case, the relative magnitude of the rate of dissolution can be compared to the rate of degradation. If PCE accumulates in the aqueous phase then it can be assumed that the rate of degradation is less than the rate of dissolution. If PCE does not accumulate, however, then dissolution limited conditions may be assumed.

To examine the relative magnitude of the dissolution and dechlorination rate processes, Batch-DECHLOR was used to simulate a two-phase (aqueous-organic) experiment that employed this amendment strategy. Pure PCE (50 μL) was added to biotic and abiotic experimental reactors that were operated under the same conditions as those reported in Section VI.C.1.ii for the *Sulfurospirillum multivorans* pure culture. The simulation of dissolution data measured in the abiotic reactor gave a best-fit PCE mass transfer coefficient value of $k^{PCE} = 2.3 \text{ m/d}$. This mass transfer coefficient was then used as an input parameter in the biotic reactor simulation.

Figure VI.9 shows the experimental and simulated results for both the abiotic and biotic batch reactors. Figure VI.9a shows the best-fit (solid line) and experimental (symbol) aqueous phase PCE concentrations due to dissolution from a PCE-NAPL in an abiotic reactor operated under the same physical conditions as the biotic reactor. The presented simulation results were obtained using the best-fit PCE mass transfer coefficient value. Equilibrium PCE concentrations in this experimental system are not achieved until after approximately 5 days of system operation. Figure VI.9b plots the simulated (solid lines) and experimental (symbols) results for the reactor undergoing active dechlorination (i.e., biotic reactor). Dissolution was modeled using the best-fit

PCE mass transfer coefficient from the abiotic reactor (i.e., Figure VI.9a) and dechlorination was modeled using the same parameters as those used to fit the single-phase experimental results for the *Sulfurospirillum multivorans* pure culture (Table VI.2). Simulation results indicate that dissolution is likely limiting the rate of degradation, since PCE is detected in the aqueous phase only at day 2 when the electron donor became depleted. Following the re-addition of electron donor, dechlorination resumed and the PCE concentration rapidly declined, resulting in the accumulation of *cis*-DCE. Differences in the simulated and experimental *cis*-DCE concentrations depicted in Figure VI.9b may be reduced by directly fitting the mass transfer coefficient for the biotic experiment rather than using the best-fit value obtained in the abiotic experiment. Directly fitting the coefficient resulted in a reduction in the mass transfer coefficient by a factor of approximately two to $\kappa^{PCE} = 1.2$ m/d (Figure VI.9c). Reasons for the apparent reduction in mass transfer include: over-estimation of the aqueous-organic interfacial area due to simplifying assumptions (i.e., single spherical blob), reductions in the mass transfer coefficient due to microbial activity (e.g., Mukherji and Weber [2001]), or reductions in dechlorination activity following electron donor depletion. More work will be needed, however, to examine these and other possible mass transfer limiting effects.

Finally, the estimation error introduced by neglecting sampling losses is depicted in Figure VI.9d. As the experimental data points in Figure VI.9d show, a significant number of samples were collected during the course of the biotic experiment. Each aqueous phase sample had a volume of one to two milliliters, resulting in a loss of approximately 40% of the aqueous phase volume over the time frame of the experiment. Additionally, sampling resulted in the removal of more than 140 μmol (~30% of the

added PCE-NAPL) of chloroethenes from the reactor. Neglecting to account for these losses results in the over-estimation of chloroethene concentrations and could produce inaccurate values for the kinetic coefficients.

VI.D CONCLUSIONS

A metabolic reductive dechlorination model capable of simulating single- and two-phase batch systems (Batch-DECHLOR) was developed and employed to model a variety of published and unpublished dechlorination experiments. Model parameters were either taken from the literature or estimated using an optimization routine that was integrated with the Batch-DECHLOR model.

The simulations of primary substrate fermentation, PCE metabolic reductive dechlorination, and acetogenesis in single-phase pure and mixed culture systems were in close agreement with experimental results. Batch-DECHLOR was able to accurately match the fermentation of a primary substrate to an electron donor that stimulated the degradation of PCE to lesser chlorinated products and the formation of acetate by competitor populations. Optimal values for the model parameters were found to be consistent with the range of values in the published literature. Comparison of the values for kinetic coefficients obtained for a *cis*-DCE to ethene dechlorinating population in a mixed culture and a pure *cis*-DCE to ethene dechlorinating culture indicated that the rate of dechlorination of the pure and mixed culture were comparable (i.e., within a factor of two).

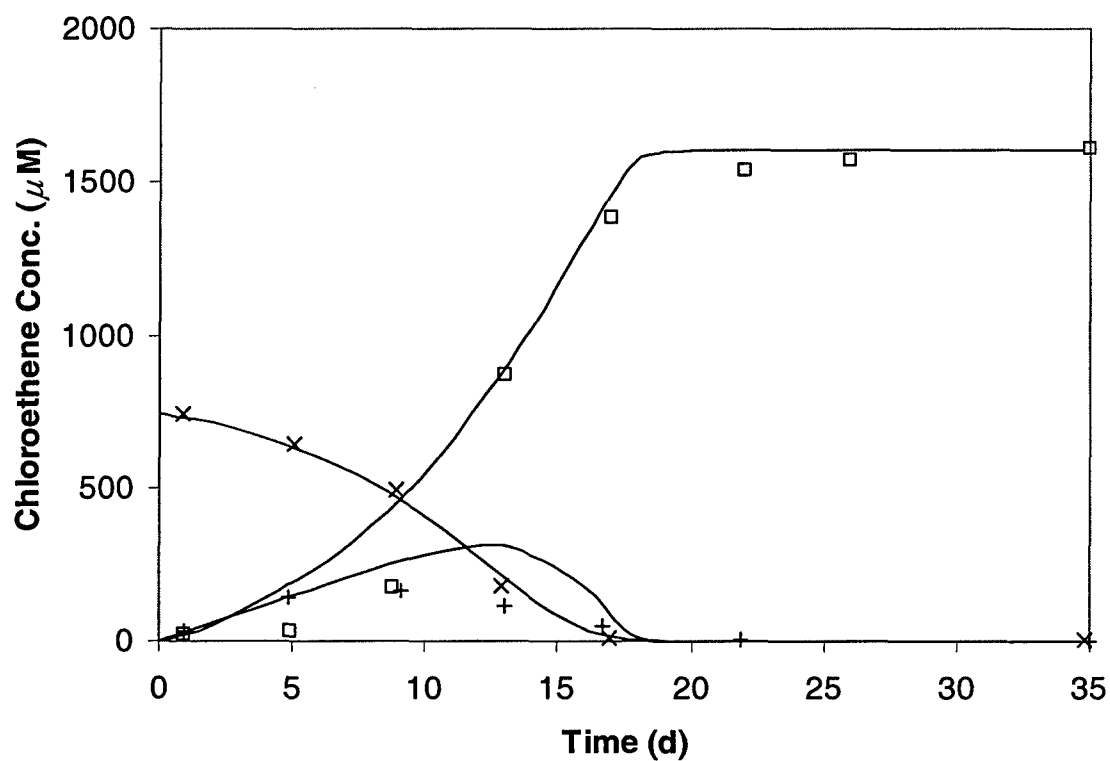


Figure VI.8: Simulated and experimental chloroethene concentrations for aqueous-organic phase batch system of Yang and McCarty [2000]. PCE (x), TCE(+), and *cis*-DCE (□).

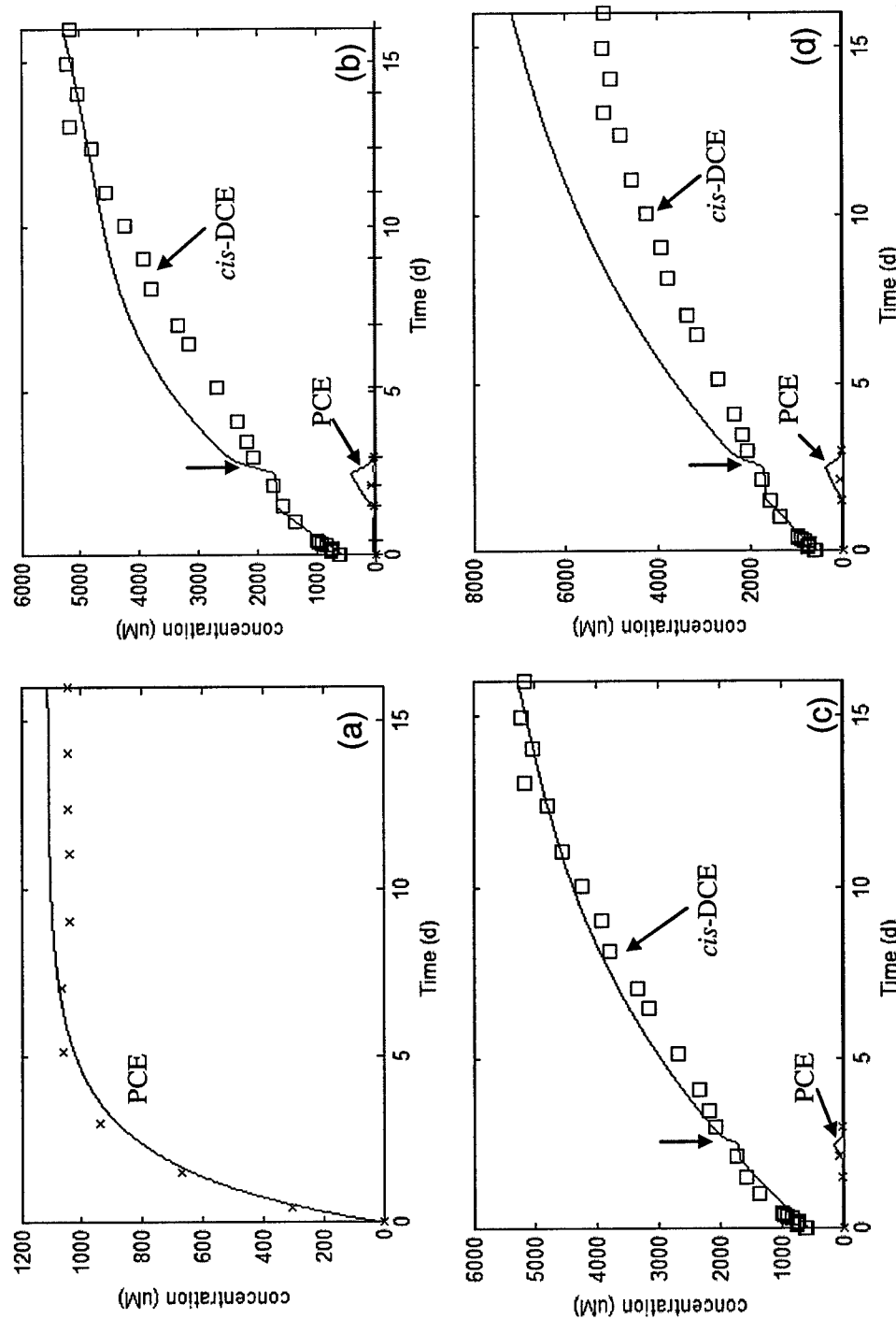


Figure VI.9: Simulated and experimental results for a two-phase (PCE-water) batch experiment. (a) PCE concentration in an abiotic reactor, (b) chloroethene concentrations in two-phase batch reactor with abiotic reactor mass transfer coefficient, (c) Chloroethene concentrations in two-phase batch reactor with best-fit mass transfer coefficient, and (d) chloroethene concentrations in two-phase batch reactor where sampling losses have been neglected in the numerical simulation. Symbols represent data provided by Ben Amos (Georgia Institute of Technology, unpublished results) and solid lines are Batch-DECHLOR simulation results. Arrows signify time of electron donor readjustment.

Given the potential for remediation of DNAPL source zones by coupling aggressive mass removal technologies with post-treatment biostimulation (see Chapter I), the model was used to simulate dechlorination in the presence of the nonionic surfactant TWEEN 80, which had been used at a recent pilot-scale SEAR demonstration [Abriola et al., 2005]. Experimental results indicated that reductions in the rate and extent of PCE to *cis*-DCE dechlorination due to the presence of surfactant were minimal. The best-fit values for the PCE and TCE maximum utilization rates were reduced by approximately 25% in the presence of the surfactant. All other model parameters were unchanged. Further dechlorination of *cis*-DCE to ethene was not modeled, however due to complete inhibition of these dechlorination steps by the surfactant.

Two-phase (aqueous-organic) experiments were also successfully modeled using Batch-DECHLOR. This is the first demonstration of a metabolic reductive dechlorination model capable of simulating dechlorination and rate-limited dissolution simultaneously. Given that the kinetic coefficients obtained from the single-phase experiments were capable of simulating dechlorination in the two-phase experiments, the presence of an organic phase appears to have a minimal impact on the rate of dechlorination in these experimental systems. In both experiments, the degradation of aqueous phase PCE increased the dissolution driving force resulting in the complete dissolution of the PCE NAPL. More work will be needed, however, to investigate potential effects of biological activity on the rate of DNAPL dissolution. The incorporation of sampling effects on simulated results, a process that is typically neglected, was necessary to accurately simulate the two-phase *Sulfurosporillium multivorans* experiment.

The results presented here provide a foundation for future investigations into dechlorination in multiphase systems and present a tool to obtain optimal metabolic reductive dechlorination kinetic parameters from site-specific microcosms that can then be used in the simulation and design of field-scale remediation systems.

CHAPTER VII

MODELING METABOLIC REDUCTIVE DECHLORINATION IN DNAPL SOURCE ZONES

VII.A INTRODUCTION

The stimulation of source zone bioremediation as a sole treatment strategy, or following partial DNAPL mass removal using a physico-chemical process (e.g., SEAR), is thought to lead to *bioenhanced dissolution*, or the enhancement of DNAPL interphase mass transfer, due to (i) increases in the driving force for mass transfer to the aqueous phase and (ii) in the case of PCE-NAPL, increases in aqueous phase chloroethene concentrations due to the transformation of the parent compound to chlorinated products of higher aqueous solubility [NRC, 2004]. These enhancements in dissolution due to microbial activity are expected to reduce DNAPL longevity. For example, in Chapter VI, two-phase experimental results indicated that metabolic reductive dechlorination could lead to the complete dissolution of PCE-NAPL by degrading aqueous phase PCE concentrations to lesser chlorinated products. Bioenhanced dissolution may also reduce contaminant mass flux in systems capable of complete degradation (i.e., no daughter product accumulation). When degradation is incomplete, however, as in the two-phase experiments simulated in Chapter VI, dissolution enhancement may lead to an increase in

the total contaminant mass flux (i.e., mM *cis*-DCE concentrations). Thus, the application of source-zone bioremediation may require a careful balance between alternative remediation objectives: reduction of DNAPL longevity and minimization of down gradient contaminant flux [NRC, 2004].

The quantification of reductions in DNAPL longevity and changes in contaminant mass flux due to bioenhanced dissolution requires the development and application of models capable of simulating metabolic reductive dechlorination in chlorinated DNAPL source zones. The simulation of metabolic reductive dechlorination has heretofore been focused on modeling experimental batch reactors (e.g., Fennell and Gossett, 1998) or transport in single-phase (aqueous) systems (e.g., Schaerlaekens et al., 1999; Wagner et al., 2002). Such models are effective at simulating dechlorination in a migrating plume down-gradient of a source-zone; however, they are incapable of capturing the dynamic interphase mass transfer and dechlorination effects associated with bioenhanced dissolution. Simplified models for the simulation of enhancements in dissolution due to microbial activity have been developed for fully saturated DNAPL pools placed along the flow domain boundary [Seagren et al., 1994; Reitsma and Dia, 2001; Chu et al., 2003, 2004; Gupta and Seagren, 2005] and residual DNAPL (i.e., ganglia) contaminated media [Seagren et al., 1993]. Application of these models to experimental or field-scale systems, however, has been limited due to the use of idealized modeling domains, simplified degradation kinetics, and the assumption of steady-state conditions. Each of these limitations is expected to affect the predicted enhancement in dissolution. Consideration of these limitations will likely require the use of numerical modeling

methods that are capable of simulating the spatial-temporal distribution of multiple components and phases.

Compositional multi-phase simulators originally developed to solve phase and component mass balance equations in abiotic systems may be adapted to facilitate the simulation of source-zone metabolic reductive dechlorination. These simulators have been used to assess a range of alternative physico-chemical source-zone remediation strategies (e.g., Dekker and Abriola, 2000b). Biological reactions have been incorporated into a number of existing multi-phase simulators [Delshad et al., 1996; Abriola et al., 1997; Rathfelder et al., 2000; Battistelli, 2004; Hammond et al., 2005]; however, no compositional multi-phase simulator has been developed and applied to simulate bioenhanced dissolution due to source zone metabolic reductive dechlorination [Stroo et al., 2003, EPA, 2003; NRC, 2004]. In this chapter, the batch dechlorination kinetic model described in Chapter VI is integrated into an existing multiphase compositional simulator, MISER, to provide a compositional multiphase model capable of simulating bioremediation in a spatially heterogeneous chlorinated-DNAPL source zone. This model is used to investigate bioenhanced dissolution in one- and two-dimensional domains. Three-dimensional domains are not considered; however, as was shown in Chapters IV and V, the errors introduced into simulation results by reductions in dimensionality (2-D versus 3-D) are relatively minor.

VII.B MODEL DEVELOPMENT

Integration of metabolic reductive dechlorination kinetics into an existing multiphase compositional simulator requires modifications to the phase and component

mass balance equations. Chapter III outlined the mathematical framework implemented in the original version of MISER. This framework is briefly reviewed below to point out the changes that were made to integrate the metabolic reductive dechlorination kinetic model presented in Chapter VI into MISER.

VII.B.1 Governing Equations

In MISER, bulk fluid phase flow is described using a standard macroscopically averaged equation that incorporates a modified Darcy's law for the specific discharge [Abriola, 1989]:

$$\phi \frac{\partial}{\partial t} (\rho_{\alpha}^* S_{\alpha}) - \nabla \cdot [\rho_{\alpha}^* \lambda_{\alpha} (\nabla P_{\alpha} - \rho_{\alpha}^* g \nabla z)] = \sum_c E_{\alpha\beta}^{c*} + \sum_c R_{\alpha}^{c*} + Q_{\alpha} \quad (\text{VII.1})$$

Parameter definitions for equation VII.1 can be found in Section III.B (i.e., equation III.3). Equation VII.1 accounts for the change in phase mass due to advective fluxes, component mass transfer, component reactions, and sources/sinks. Commonly, changes in phase mass due to component reactions are neglected [e.g., Barry et al., 2002; Gallo and Manzini, 2001]. Although this term was found to be negligible in simulations presented here, it was included in the model to accommodate scenarios that require consideration of phase changes due to reactions.

Within each phase, the fate and transport of component c is computed using a component mass balance equation written in terms of the mole fraction of component c in the α -phase (x_{α}^c):

$$\phi \frac{\partial}{\partial t} (S_{\alpha} \rho_{\alpha} x_{\alpha}^c) + \nabla \cdot \phi S_{\alpha} \rho_{\alpha} (x_{\alpha}^c V_{\alpha} - D_{\alpha}^c \nabla x_{\alpha}^c) = \phi \sum_{\beta} E_{\alpha\beta}^c + R_{\alpha}^c + Q_{\alpha}^c \quad (\text{VII.2})$$

Parameter definitions for equation VII.2 can be found in Section III.C (i.e., equation III.5). Equation VII.2 relates the change in component mass in the α -phase to changes due to advective and dispersive fluxes, interphase mass transfer, biological reactions, and sources/sinks. This equation is an expanded version of equation VI.1 solved in Batch-DECHLOR.

The solution of equations VII.1 and VII.2 enables the simulation of the spatial-temporal distribution of multiple components and phases in a DNAPL source zone. In the original version of MISER, these equations were solved for three components, contaminant, surfactant, and alcohol, in two flowing phases, gas and aqueous. The organic and bio-phases were assumed to be immobile and the soil matrix was assumed to be rigid. Mass transfer was modeled for the aqueous-gas, aqueous-NAPL, aqueous-biophase, and aqueous-solid phase interfaces. To facilitate the simulation of metabolic reductive dechlorination in a DNAPL source zone, MISER was modified to simulate the eight chemical components discussed in Chapter VI: primary substrate, electron donor, PCE, TCE, *cis*-DCE, VC, ethene, and methane or acetate. Flow and transport, however, are restricted to the aqueous phase (i.e., the gas phase is not considered) and microbial populations are assumed to respond directly to bulk aqueous phase concentrations (i.e., no aqueous-biophase mass transfer limitations) [Odencrantz et al., 1990]. These assumptions eliminate the need to solve equations VII.1 and VII.2 for the biophase and greatly simplify the solid and organic component and phase mass balance equations:

$$\phi \frac{\partial}{\partial t} (\rho_{\alpha}^* S_{\alpha}) = \sum_c E_{\alpha\beta}^{c*} \quad \text{for } \alpha = o \text{ and } s \quad (\text{VII.3a})$$

$$\phi \frac{\partial}{\partial t} (S_{\alpha} \rho_{\alpha} x_{\alpha}^c) = \phi \sum_{\beta} E_{\alpha\beta}^c \quad \text{for } \alpha = o \text{ and } s \quad (\text{VII.3b})$$

VII.B.2 Constitutive Relationships

The solution of the governing equations (Section VII.B.1) requires the parameterization of the relative permeability, interphase mass transfer, and molar (or mass) rate of degradation. Forms of each of these relationships were present in the original version of MISER. However, changes to the interphase mass transfer and molar rate of degradation relationships were required to facilitate the simulation of metabolic reductive dechlorination.

The existing relative permeability model was used in the simulations presented here without modification (see Section III.D.3.i.2). This relative permeability function is slightly different than that used in the original version of MISER, however, due to the incorporation of the biomass as a volume occupying component (S_b) into the constraint on saturation (i.e., $S_a + S_o + S_b = 1$). When biomass is not present, the relative permeability function reduces to the standard, abiotic function (equation III.15). When biomass is present, however, the relative permeability is reduced to account for the presence of the biophase (see Section III.D.4).

Rate-limited interphase mass transfer is modeled in MISER using the linear driving force approximation (equation III.16) with the mass transfer coefficient (κ^c) for component c through the controlling aqueous-phase computed using the Powers et al. [1992] correlation (equation III.21) and the interfacial area (a_{ao}) computed using the diminishing sphere model described in Section III.D.3.i.2. Although recent experimental evidence [Mukherji and Weber, 2001] and two-phase batch simulations presented in Section VI.C.2 suggest biological activity may affect the mass transfer coefficient, no attempt was made to modify the Powers et al. [1992] mass transfer correlation to account

for the presence of an actively dechlorinating culture. The rate-limited driving force approximation to mass transfer implemented in MISER had previously been modified however, to neglect mass transfer from the aqueous into the NAPL phase (i.e., back partitioning):

$$E_{ao}^c = \begin{cases} \rho_a K_{ao}^c (x_{ao}^{c-e} - x_a^c) & \text{if } x_{ao}^{c-e} \geq x_a^c \\ 0 & \text{otherwise} \end{cases} \quad (\text{VII.4})$$

Given the low saturations simulated in this work (and found in the field) along with the increasing solubility of the dechlorination daughter products (e.g., *cis*-DCE), back partitioning was assumed to be negligible. Implications of this assumption on the simulation of dissolution enhancement will be investigated further in Section VII.C.

Metabolic reductive dechlorination kinetics are the same as those implemented in the batch dechlorination model presented in Chapter VI. The kinetics in this model form the mathematical framework for the dechlorination conceptual model diagrammed in Figure VI.1. The original version of MISER was developed assuming aerobic degradation of a single organic component by a single microbial population [Abriola et al., 1997]. Therefore, MISER was updated to simulate metabolic reductive dechlorination by including the fermentation of a primary substrate to electron donor, sequential reduction of chlorinated ethenes coupled with the oxidation of the electron donor, and competition for the electron donor by a separate electron donor-utilizing process. Incorporation of these kinetics required significant changes to the existing biological processes implemented in MISER. In addition to changes in the reaction kinetics, new routines were developed to check the magnitude of the component reaction terms (R_a^c) to ensure that the mass reacted over a given time-step did not exceed the mass created over that time step plus the mass present at the beginning of the time-step, which

could lead to negative concentrations. Furthermore, the biological routines were modified to compute the biomass concentration for all four microbial populations included in the metabolic reductive dechlorination conceptual model. These microbial populations were then used to compute a biophase saturation (equation III.30) that altered the aqueous phase saturation, affecting flow. Although the simulations presented in this work assumed uniform initial biomass concentrations, MISER was updated to allow for the possibility of non-uniform initial biomass concentrations.

VII.B.3 Numerical Solution Technique

In the simulations presented in this chapter, the initial organic phase saturation distribution was prescribed based on experimental conditions. However, for field-scale simulations, an immiscible two-phase simulator could be used to solve the phase mass balance equations to determine the organic phase saturation distribution. This non-uniform DNAPL saturation distribution could then be used as an initial condition for the modified version of MISER.

MISER solves the phase and component mass balance equations in two dimensions using a standard Galerkin finite-element approach with linear triangular elements. Minor modifications were made to the original solution algorithm (see Abriola et al., 1997) to facilitate the simulation of source zone bioremediation. Mass matrices were diagonalized using mass lumping to reduce oscillatory behavior and improve computational stability. A dynamic time-step adjustment was incorporated into the solution algorithm used to solve the set of component mass balance equations when biological reactions were lagged a time-step. This adjustment re-computes the biological

reactions using the new mole fractions and compares the new and old time-step solutions to ensure that the error introduced by lagging the biological reactions remains below a user-specified tolerance (i.e., the convergence criteria). The flow, transport, and interphase mass transfer components of MISER have been verified mathematically through mass balance calculations and comparison to other numerical and analytical solutions [Abriola et al., 1997; Rathfelder et al., 2000].

To ensure that the modified version of MISER solved the metabolic reductive dechlorination equations correctly, MISER simulations were compared to an existing 1-D analytical solution for sequential first-order degradation of aqueous phase contaminants [Clement, 2001]. This analytical model forms the foundation of the popular single-phase natural attenuation screening model BIOCHLOR [Aziz et al., 1999]. To facilitate the numerical-analytical comparison, interphase partitioning was neglected and the reaction terms were forced to approximate first-order. Figure VII.1 shows the close agreement between the analytical solution (symbols) and the modified version of MISER (solid lines), providing model verification for simplified reaction kinetics.

For more complex problems that incorporate interphase partitioning and non-linear dechlorination kinetics, no analytical solutions are available and mass balance calculations are useful to evaluate model performance. Cumulative and time-step phase and component mass balances were computed following the methods outlined in Abriola et al. [1997], which generally take the form:

$$\varepsilon_{cum} = 1 - \left| \frac{\sum_{\Delta t} (F_{adv} + F_{mt} + F_{rxn}) \Delta t}{\sum_{\Delta t} (\Delta_{storage}) \Delta t} \right| \quad (\text{VII.5a})$$

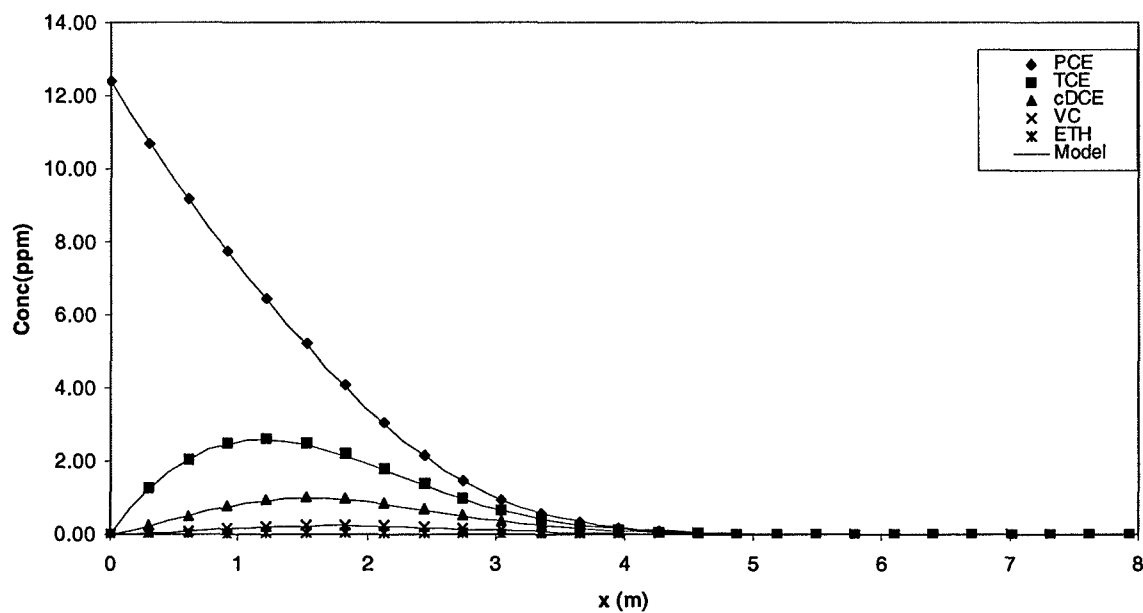


Figure VII.1. Comparison of numerical model developed in this work to analytical solution of Clement [2001]. Symbols represent analytical solution and solid lines represent numerical model results generated using a modified version of MISER.

and

$$\varepsilon_{\Delta t} = 1 - \left| \frac{F_{adv} + F_{mt} + F_{rxn}}{\Delta_{storage}} \right| \quad (\text{VII.5b})$$

for the cumulative (ε_{cum}) and time-step ($\varepsilon_{\Delta t}$) mass balance error, respectively. For each phase and component, $\Delta_{storage}$ represents the change in storage, F_{adv} represents the advective flux, F_{mt} represents changes due to interphase partitioning, and F_{rxn} represents changes due to biological reactions. Using equation VII.5 to evaluate model performance, cumulative (and time-step) phase and component mass balance errors were less than 0.1% for all components with concentrations greater than 1 ng/L.

VII.C SOURCE ZONE DECHLORINATION SIMULATIONS

VII.C.1 Base Case Scenario

The next step in model assessment was to determine the ability of the model to simulate typical trends found in laboratory experiments. Thus, the modified MISER model was used to simulate the results of a laboratory experiment involving metabolic reductive dechlorination and bioenhanced dissolution in a two-phase (aqueous-organic) packed column system [Yang and McCarty, 2002]. The intent of this comparison was not to use the model in a predictive sense, but rather to demonstrate the ability of the model to simulate metabolic reductive dechlorination in a two-phase system using parameter values consistent with those provided in the literature.

Simulated and published experimental chloroethene breakthrough curves were compared for a one-dimensional column packed with aquifer material from a pristine site that was contaminated by hand during packing using a syringe to an approximately

uniform saturation of PCE-DNAPL [Yang and McCarty, 2002]. Two pore volumes of an anaerobic PCE-dechlorinating mixed culture were flushed through the column at the start of the experiment to initiate metabolic reductive dechlorination. Pentanol (3.7 mM) was continuously flushed through the column to provide the necessary fermentable substrate to drive the dechlorination reactions. Retention time in the column was approximately 14 days. Although the column was operated for approximately 300 days, only the first 150 days of column operation are simulated. The column's properties are summarized in Table VII.1 and the fluid properties are summarized in Table VII.2.

Biotransformation kinetic coefficients and initial biomass concentrations are summarized in Tables VII.3 and VII.4. Kinetic coefficients and initial biomass concentrations were taken from a recent study that used the column augmented culture to investigate the rate and extent of dechlorination for several alternative fermentable substrates [Lee et al., 2004]. Pentanol fermentation kinetics were assumed to be the same as those of ethanol utiliziers and methanogenesis kinetics were estimated from the literature [Fennell and Gossett, 1998]. Initial biomass was assumed to be uniformly distributed throughout the column and the PCE maximum utilization rate was adjusted (reduced by approximately one order-of-magnitude) to obtain the best fit to the effluent chloroethene concentrations.

Simulated (solid line) and experimental (closed symbols) breakthrough curves are compared in Figure VII.2. Simulations were consistent with experimental trends in chloroethene breakthroughs. PCE is dechlorinated to *cis*-DCE with no noticeable accumulation of TCE, and dechlorination beyond *cis*-DCE is not observed. The lack of complete dechlorination of PCE to ethene in the experimental system is likely due to the

inhibition of the *cis*-DCE-to-ethene dechlorinating population by the high PCE concentrations, since this culture has demonstrated the ability to effect the complete conversion of PCE to ethene at lower PCE concentrations [Yang and McCarty, 1998; Lee et al., 2004]. These results are consistent with other experimental studies that observed *cis*-DCE accumulation in the presence of PCE-DNAPL (e.g., Adamson et al., 2004). Simulated methane discharge at the effluent boundary ($\sim 2 \mu\text{mol/d}$) was approximately equivalent to the discharge reported by Yang and McCarty [2002] ($\sim 3 \mu\text{mol/d}$), although the model did not predict the significant spikes in discharge ($\sim 20 \mu\text{mol/d}$) that were periodically observed in the experimental results. Recall the model assumed a uniform initial PCE-DNAPL saturation in all elements, which resulted in significant inhibition of methanogens. In the experiment, however, PCE-DNAPL was only approximately uniform. Therefore, methanogens may have thrived in localized areas where PCE concentrations were low [Chu et al., 2003]. If more refined measurements of the PCE-DNAPL distribution had been available, this may have improved model predictions.

Parameter	Value
<i>Soil Properties</i>	
$k \text{ (m}^2\text{)}^a$	2.593×10^{-11}
gradient (-)	4×10^{-4}
$\phi \text{ (-)}^a$	0.34
$\rho_s^* \text{ (g/L)}^b$	1.75×10^3
$\lambda \text{ (-)}^b$	2.077
$\alpha_L \text{ (m)}^b$	0.01
$\alpha_T \text{ (m)}^b$	0.0001
<i>Phase Properties</i>	
$\mu_a \text{ (g/cm-s)}$	0.0112
$S_{ar} \text{ (-)}^a$	0.08
$S_o^{t=0} \text{ (-)}^a$	0.02
<i>Numerical Properties</i>	
N_x	30
N_z	1
$\Delta x \text{ (m)}$	0.01
$\Delta z \text{ (m)}$	0.022

^a estimated from Yang and McCarty [2002]

^b assumed based on Abriola et al. [1993]

Table VII.1: 1-D column properties for base case metabolic reductive dechlorination simulation.

Component	MW_c (g/L) ^a	ρ_a^* (g/L) ^a	D_a^{cM} (m ² /d) ^c	C_{ao}^{c-e} (mM) ^{a,d}	R_c (-) ^b
H ₂	1.01	0.089	3.32×10^{-4}	0.81	1
Pentanol	88.17	0.824		3.06×10^2	1
PCE	165.8	1.6	0.62×10^{-4}	0.862	3.33
TCE	131.4	1.46	0.69×10^{-4}	8.37	2.03
cis-DCE	96.94	1.28	0.78×10^{-4}	8.25	1.21
VC	62.5	0.91	0.92×10^{-4}	40.6	1
ETH	28.05	0.57	1.16×10^{-4}	5.69×10^3	1
MTH	16.04	0.42	1.47×10^{-4}	2.5×10^2	1

^a Verschuieren [2001] and Wiedemeier et al. [1999]

^b Taken from Chu et al. [2004]

^c Taken from Clapp et al. [2004]

^d $C_{ao}^{c-e} = \rho_a x_a^c$ for $x_o^c = 1.0$

Table VII.2: Component c physical properties for metabolic reductive dechlorination simulations.

Biomass Population	$X_j^{t=0}$ (mg/L) ^a	$C_a^{H-thresh-j}$ (nM) ^{b,c}	b (d ⁻¹) ^d
Fermentors (X_f)	0.1	-	0.05
PCE- c DCE Dechlorinators (X_{DC1})	0.015	2.0	0.05
c DCE-ETH Dechlorinators (X_{DC2})	0.015	2.0	0.05
Competitors (X_c)	1.0	11.0	0.05

^a Taken from Lee et al. [2004]

^b Taken from Yang and McCarty [1998]

^c $C_a^{H-thresh-j} = \rho_a x_a^{H-thresh-j}$

^d assumed

Table VII.3: Biomass phase properties for metabolic reductive dechlorination simulations.

Parameter	This Work ^a	Clapp et al. (2004) ^b
<i>Maximum utilization rate (μmol/(mg cell-d))</i>		
PCE (k_{max}^{PCE})	27	1.4-117
TCE (k_{max}^{TCE})	366	2.4-117
cDCE (k_{max}^{DCE})	48	1.7-22.2
VC (k_{max}^{VC})	48	2.6-22.2
Pentanol (k_{max}^{PS})	251.5 ^d	- ^c
Competitor (k_{max}^C)	1500	27-1138
<i>Half-saturation constant (μM)</i>		
PCE (K_S^{PCE})	0.2	0.11-2.8
TCE (K_S^{TCE})	1.4	0.54-1.5
cDCE (K_S^{DCE})	3.3	0.54-3.3
VC (K_S^{VC})	2.6	2.6-360
Pentanol (K_S^{PS})	17 ^e	-
H ₂ – DC1 (K_S^{H-DC1})	0.1	0.015-0.1
H ₂ – DC2 (K_S^{H-DC2})	0.1	0.015-0.1
H ₂ – C (K_S^{H-C})	0.5	0.5-22.2
<i>Inhibition coefficients (μM)^e</i>		
PCE (K_I^{PCE})	0.2	-
DCE (K_I^{DCE})	2.6	-
VC (K_I^{VC})	250	100-500
<i>Yield (mg cell/mmol substrate)</i>		
PCE (Y^{PCE})	11.72	3.3 – 9.6
TCE (Y^{TCE})	11.72	3.3 – 9.6
cDCE (Y^{DCE})	11.72	3.3 – 9.6
VC (Y^{VC})	11.72	3.3 – 9.6
Pentanol (Y^{PS})	6.35	-
Competitor (Y^C)	1.98	-
<i>Stoichiometric coefficients (mol H₂/mol substrate)^f</i>		
PCE (F_{PCE})	1.41	1.03-1.85
TCE (F_{TCE})	1.41	1.03-1.85
DCE (F_{DCE})	1.41	1.03-1.85
VC (F_{VC})	1.41	1.03-1.85
Pentanol (F_{PS})	2.03	-
Competitor (F_C)	4.44	-

^a Parameter values were taken from Lee et al. [2004].

^b Clapp et al. [2004] provided a summary of biological parameters as of early 2004.

^c A dash (-) indicates the parameter was not provided/not simulated in the subject model.

^d Assumed to be equal to ethanol utilizer values reported by Lee et al.[2004].

^e As discussed in Yu et al. [2005], inhibition constants are assumed to take the value of the appropriate half-saturation constant (e.g., $K_I^{DCE} = K_S^{VC}$).

^f The parameter values given in the column *This Work* were derived using the stoichiometric half-reactions ($f_e = 0.7$ for dechlorination and $f_e = 0.9$ for methanogenesis).

Table VII.4: Biological degradation parameters for metabolic reductive dechlorination simulations.

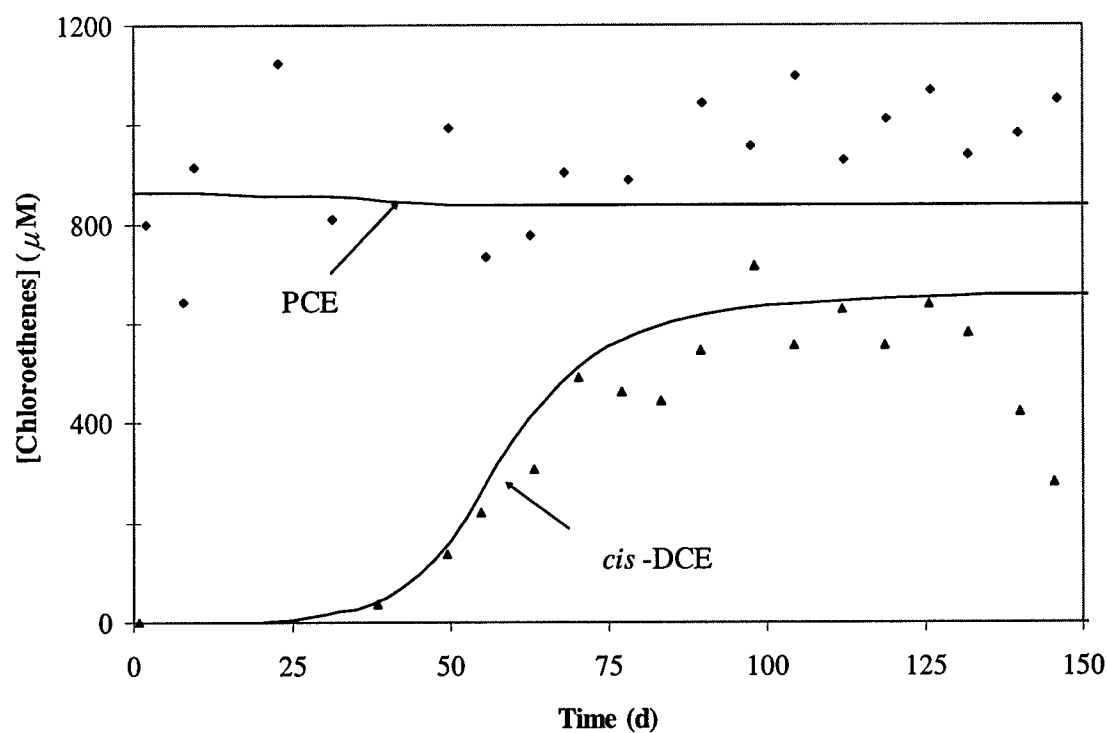


Figure VII.2: Comparison of simulated (solid line) and experimental (filled symbols) results for a one-dimensional column contaminated with PCE-DNAPL [Yang and McCarty, 2002].

Comparison of simulated and experimental breakthrough curves reveals relatively good agreement, except for the trend in *cis*-DCE concentration after approximately 120 days of system operation. Here simulated *cis*-DCE concentrations remain relatively constant while measured *cis*-DCE concentrations decline. Yang and McCarty [2002] attribute the observed decline to the accumulation of biomass and the production of methane gas by competitors. Gas production is not considered in the model developed here. Although bio-clogging is modeled, the biophase saturation did not have a noticeable effect on the aqueous phase relative permeability in this simulation. The discrepancy between the simulation and experimental results, thus, suggests that either (i) the production of methane gas is a significant clogging mechanism in experimental systems or (ii) additional clogging mechanisms associated with biomass growth, such as production of extracellular polysaccharides, should not be neglected. The former explanation is supported by the observation of methane discharge spikes mentioned previously. These spikes occurred at about the same time as the decline in *cis*-DCE concentration. Furthermore, the addition of saturated PCE concentrations to the experimental column influent at day 150 inhibited the spikes in methane production and enabled the recovery of PCE-to-*cis*-DCE dechlorination resulting in *cis*-DCE accumulation [Yang and McCarty, 2002]. Future work will need to determine the likelihood of clogging due to gas production in the field and potentially incorporate these clogging mechanisms into source-zone models. Overall this comparison demonstrates the ability of the model to simulate the dissolution and degradation of PCE and the accumulation of daughter products in a column contaminated with DNAPL.

VII.C.2 Base Case Simulation Assumptions

Simulation results presented in the previous section indicate that the modified version of MISER can successfully simulate bioenhanced dissolution due to metabolic reductive dechlorination in a flowing system. This simulation, however, was based on a number of simplifying assumptions, including (i) the initial biomass concentration is spatially uniform, (ii) the column is at equilibrium at the start of the simulation (i.e., aqueous phase contaminant concentrations equal solubility), and (iii) the biomass density is approximately equivalent to the density of water. To better understand the implications of these assumptions on bioenhanced dissolution predictions, the modified version of MISER was used to simulate the base case scenario with alternative simulation assumptions. A fourth and final simplifying assumption that back partitioning of aqueous phase components into the NAPL is negligible is considered in section VII.C.4.

VII.C.2.i Non-uniform Initial Biomass Concentration

Experimental results reported in the literature indicate that the initial biomass distribution in a one-dimensional column following bioaugmentation is spatially non-uniform. For example, Rogers and Logan [2000] investigated the biomass distribution of two aerobic populations (*Pseudomonas fluorescens* P17 and *P. putida* KT2442) flushed through one-dimensional columns (15 cm x 2.54 cm) contaminated with residual NAPL (toluene). They found that the biomass concentration retained in the column decayed approximately exponentially along the column length. Using clean-bed filtration theory, they developed a model that describes the biomass concentration along the length of the column following bioaugmentation:

$$X_j(L) = X_j^{L=0} \exp[-\lambda_{pv} \alpha L] \quad (\text{VII.6a})$$

where

$$\lambda_{pv} = 1.5\eta_5 \left(\frac{1-\phi}{\phi d_c} \right) \quad (\text{VII.6b})$$

and

$$\eta_5 = 4 \left(\frac{V_{aL} d_c}{D_p} \right)^{-2/3} + 1.5 \left(\frac{d_p}{d_c} \right)^2 + \frac{d_p^2 (\rho_p - \rho_a^*) g}{18 \mu V_{aL}} \quad (\text{VII.6c})$$

where d_c is the soil grain diameter, d_p is the particle size, ρ_p is the particle density, α is the collision efficiency, and D_p is the particle diffusivity, computed using the Stokes-Einstein equation [Logan, 1999]:

$$D_p = \frac{k_B T}{3\pi\mu d_p} \quad (\text{VII.6d})$$

In equation VII.6d, k_B is the Boltzmann constant ($1.38 \times 10^{-16} \text{ g cm}^2 \text{ s}^{-2} \text{ K}^{-1}$) and T is temperature in Kelvins [Logan, 1999; Rogers and Logan, 2000].

To determine the influence of an initially non-uniform biomass concentration on dissolution enhancement, equation VII.6a was integrated into MISER to compute a non-uniform initial biomass distribution. Two alternative collision efficiencies (α) reported by Rogers and Logan [2000] were examined. Model parameters used in these simulations are summarized in Table VII.5.

Parameter	Value	Units
Soil grain diameter (d_c)	0.05	cm
Bacterium diameter (d_p)*	5×10^{-5}	cm
Bacterium density (ρ_p)	1.07	g/cm^3
Aqueous phase density (ρ_a^*)	0.999	g/cm^3
Viscosity (μ)	0.0112	g/cm-s
Temperature (T)	288	K
Pore velocity (V_{aL})	2.48×10^{-5}	cm/s
Collision efficiency (α)	0.015	-
	0.15	-

* Assumed based on reported value of Maymo-Gatell et al. [1997]

Table VII.5: Model parameters used in non-uniform biomass simulations.

Simulations with an initial non-uniform biomass modeled using equations VII.6 were indistinguishable from the simulations that assumed a uniform biomass (i.e., base case simulation). Although minor differences did occur at early times during the biomass growth phase, the non-uniform biomass simulations attained the same steady-state chloroethene concentrations as the uniform biomass simulations. These results indicate that for the conditions considered here, assuming a uniform biomass concentration will result in minimal prediction error.

VII.C.2.ii Contamination Scenario

In Chapter VI, two alternative two-phase batch experiments were investigated. A primary difference between these experiments was the initial aqueous phase contaminant concentration. In the Yang and McCarty [2000] experiment, initial aqueous phase concentrations were in equilibrium with the NAPL phase. In the experiments conducted at the Georgia Institute of Technology, NAPL was added to an actively dechlorinating culture, so that the concentration in the aqueous phase remained approximately zero. In a column experiment, the former method would likely coincide with a scenario in which biomass is added to the column following contamination with NAPL [e.g., Yang and McCarty, 2002]. Adding NAPL to a column already augmented with active biomass would coincide with the later contamination scenario [Cope and Hughes, 2001]. Since both methods may be used, the modified version of MISER was used to investigate the sensitivity of bioenhanced dissolution predictions to the assumed initial condition. Rather than assuming equilibrium between the aqueous and NAPL phase at time $t = 0$, MISER was modified to simulate an initial contaminant concentration in the aqueous

phase equal to zero. Employing this assumption, the contaminant has to first dissolve from the organic phase before being dechlorinated.

Figure VII.3 shows the total chloroethene concentration as a function of time for both the equilibrium and zero contamination initial conditions. Clearly, the simulated concentrations differ at early times. However, over time, the zero initial condition simulation reaches approximately the same total chloroethene concentration as the equilibrium initial condition simulation. The tendency for the concentrations in zero initial condition simulation to lie 1-2% below those in the equilibrium initial condition simulation is attributable to differences in the dechlorination rates at early times, which result in slightly lower steady-state biomass concentrations in the zero initial condition simulations. These results indicate that the contamination scenario will likely have a relatively minor impact on the simulation results. It should be noted, however, that initial contamination conditions could cause large variations in simulations results when considering microbial populations that are negatively affected by contaminant toxicity (see Section VI.B.2).

VII.C.2.iii Biomass Density

Reports of clogging in column experiments are often attributed to biomass growth. As discussed in Section VII.B.2, MISER was modified to compute a biophase saturation that reduces the aqueous phase relative permeability, simulating biological clogging. In the base case simulation, however, biological clogging was not observed. Therefore, the biomass density used in the base case simulation (999 g/L) was reduced to 2 g/L. This value was recently used in a simplified modeling study [Chu et al., 2003] to

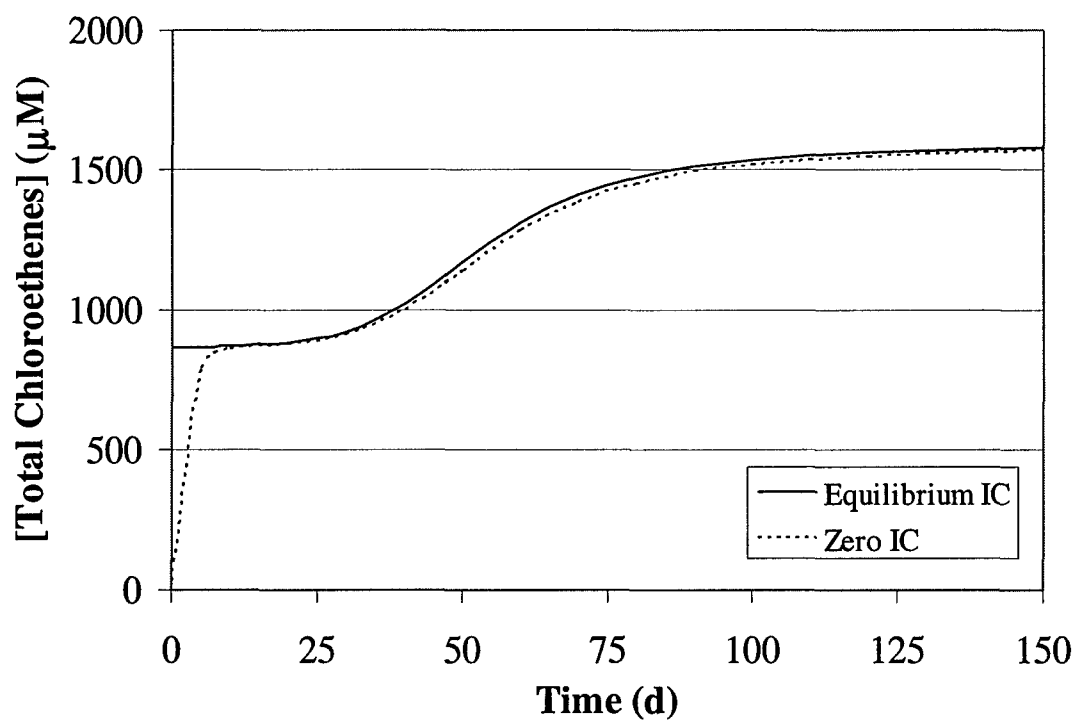


Figure VII.3: Simulation results for the equilibrium initial condition and the zero contaminant concentration initial condition (see Section VII.C.2.ii).

simulate biological clogging. Even at this low density, however, the simulated biophase saturation was less than 1%, indicating that for the experimental conditions considered in this work, the model is relatively insensitive to the assumed biomass density.

VII.C.3 Modeling Bioenhanced Dissolution

The results from the previous two sections demonstrate the ability of the modified version of MISER to simulate bioenhanced dissolution due to metabolic reductive dechlorination at scales consistent with experimental observations. This capability provides a new tool for evaluating factors that may control bioenhanced dissolution at the experimental- and field-scale.

Previous efforts to quantify bioenhanced dissolution have focused on the development of theoretical dissolution enhancement factors [Seagren et al. 1993, 1994; Reitsma and Dia, 2001; Chu et al., 2003; Gupta and Seagren, 2005]. Typically these factors are derived assuming NAPL is distributed as a fully saturated pool along the flow domain boundary. Simplified boundary conditions representing the NAPL are then used to solve a two-dimensional steady-state version of the component mass balance equation, equation (VII.2), with interphase mass transfer set to zero and reaction kinetics approximated as first-order (see Seagren et al., 1994). Substitution of this solution into Fick's first law, which governs the dissolution flux (J), permits the computation of a dissolution enhancement factor as the ratio of the dissolution flux for a biotic (J_{biotic}) and abiotic ($J_{abiotic}$) system (e.g., Seagren et al., 1994). This method of simulating bioenhanced dissolution has been applied to the evaluation of dissolution in an experimental one-dimensional rectangular column with a short (~10% of the column

length) fully saturated NAPL pool (toluene in dodecane) emplaced along the top boundary [Seagren et al., 2002]. Recently, the method was incorporated into a numerical model to simulate non-steady-state dissolution enhancement from multiple, discrete, fully-saturated NAPL pools [Chu et al., 2004]. The majority of experimental studies focused on bioenhanced dissolution, however, have examined systems contaminated by residual NAPL blobs and ganglia entrapped within the porous medium [Cope and Hughes, 2001; Yang and McCarty, 2000, 2002]. Applying models derived assuming that the NAPL is in pools to these scenarios could possibly lead to erroneous dissolution enhancement predictions.

Little work, however, has examined possible dissolution enhancements in ganglia-contaminated media. Seagren et al. [1993] derived an alternative dissolution enhancement factor for a semi-infinite ganglia-contaminated column using a steady-state solution to the one-dimensional component mass balance equation (equation VII.2). E_{ao}^c was computed using equation (VII.7) with a constant mass transfer coefficient ($\kappa^c a_{ao}$), R_a^c was approximated as $k_l x_a^c$ where $k_l \approx \frac{k_{\max}^c X_{dc1}}{K_s^c}$, and boundary conditions were specified as Type III at the inlet and Type II at the outlet (i.e., $x = \infty$). The derived dissolution factor quantified the rate of dissolution in a bioenhanced system as a fraction of the maximum possible rate of dissolution calculated by setting the bulk aqueous phase concentration in equation VII.7 equal to zero. It is relatively straight-forward, however, to rearrange the solutions derived in Seagren et al. [1993] to quantify the dissolution enhancement factor as the ratio of the biotic and abiotic dissolution flux:

$$E = \frac{J_{biotic}}{J_{abiotic}} = \frac{Da_1 w^2 - Da_1^2 \left(w - \left(1 - \exp \left(\frac{Pe}{2} \left(1 - \left(1 + \frac{4w}{Pe} \right)^{1/2} \right) \right) \right) \right)}{w^2 \left(1 - \exp \left(\frac{Pe}{2} \left(1 - \left(1 + \frac{4Da_1}{Pe} \right)^{1/2} \right) \right) \right)} \quad (VII.8)$$

where $Da_1 = \frac{\kappa^c a_{ao} L_x}{V_{aL}}$ is the Damköhler number 1, $Da_2 = \frac{k_1 L_x}{V_{aL}}$ is the Damköhler number

2, $w = Da_1 + Da_2$, and $Pe = \frac{V_{aL} L_x}{D_{ax}^c}$ is the Péclet number. Alternatively, Da_2 can be

computed for a DNAPL source zone assuming zero-order kinetics (i.e., $C_a^c \gg K_s^c$) as

$\left(Da_2 = \frac{2k_0 L_x}{V_{aL}} \right)$ where $k_0 = \frac{k_{\max}^{PCE} X_{DC1}^{avg}}{C_a^{PCE-e}}$ [Gupta and Seagren, 2005]. Equation (VII.8)

provides a simple method for computing the enhancement in dissolution due to dechlorinating activity in a ganglia-contaminated column. Unlike previous equations used to compute dissolution enhancement, which predict an approximately linear unconstrained increase in enhancement as the rate of dechlorination increases (e.g., Gupta and Seagren, 2005), equation VII.8 is constrained at high rates of dechlorination by the rate of dissolution, $E_{max} = Da_1$ [Seagren et al., 1993]. The application of equation VII.8, however, is restricted to steady-state systems with spatially uniform rates of dissolution and dechlorination.

The model developed in this work, however, is capable of simulating spatially non-uniform, non-linear dechlorination kinetics in a transient system. Following the methods used in existing experimental studies (e.g., Yang and McCarty, 2002), the dissolution enhancement in the numerical model is computed using the ratio of the total simulated chloroethene flux (i.e., DNAPL component plus dechlorination products

including ethene) through the down-gradient boundary of a biotic (J_{biotic}) and abiotic ($J_{abiotic}$) system:

$$E = \frac{J_{biotic}}{J_{abiotic}} \quad (VII.9)$$

Computing dissolution enhancement in this manner facilitates the determination of reductions or increases in mass flux due to bioenhanced dissolution, as discussed in Section VII.A.

Equation VII.9 was used to compute the bioenhanced dissolution factor for a series of 1- and 2-D numerical simulation results. Existing experimental work has focused on quantifying dissolution enhancement for various dechlorinating populations and electron donor amendment strategies [Cope and Hughes, 2001; Yang and McCarty, 2002]. Dissolution enhancement predictions in these experimental studies have ranged between one (i.e., no enhancement) and six. Reasons for the differences are likely related to experimental factors that affect the rates of dechlorination and dissolution. Therefore, numerical simulations employed in this work focused on several factors that may affect these rates: the maximum contaminant utilization rate (i.e., k_{max}^{PCE}), the organic phase saturation, the DNAPL zone length, and the DNAPL zone configuration. Predictions made using equations VII.8 and VII.9 were also compared for the base case simulation to examine the errors that could be expected when applying the simplified equations.

VII.C.3.i Base Case Comparison

The application of equation VII.8 to the base case simulation (Section VII.C.1) predicts a dissolution enhancement factor equal to 1.87. Using equation VII.9 and the base case simulation, results in a dissolution enhancement factor equal to 1.74. The

differences in these values are attributable to variations in the dissolution and dechlorination rate simulated using the numerical and simplified models.

The simplified model simulates bioenhanced dissolution from the DNAPL ganglia using a spatially and temporally constant mass transfer coefficient and spatially uniform dechlorination rate. In the multiphase numerical model, however, the dissolution mass transfer coefficient varies along the length of the column, due to preferential dissolution of the upgradient contamination. The rate of dechlorination also varies along the length of the column due to non-uniform biomass concentrations and electron donor depletion along the length of the column. It is likely that these factors contribute to the higher prediction of dissolution enhancement using the simplified steady-state model, equation VII.8. If, for example, dechlorination kinetics in the base case simulation are forced to approximate k_0 , the numerically simulated dissolution enhancement at steady-state is approximately 1.85. This value is remarkably close to the value predicted using equation VII.8 ($E = 1.85$ versus 1.87), indicating that, for the conditions of this simulation, the primary difference between the simplified model and the numerical simulator is related to constraints on the rate of dechlorination.

The differences in the numerical and analytical model predictions will likely become exaggerated at higher rates of dechlorination, however. In the simplified model dechlorination rate limitations are neglected. Hence, the only limitation on dissolution enhancement as the rate of dechlorination increases is the maximum rate of dissolution, Da_1 . In the numerical model, however, the rate of dechlorination is constrained due to limitations on biomass growth and insufficient electron donor. Therefore, when dechlorination is rate-limited, the simplified model will tend to over-predict dissolution

enhancement. For the base case simulation considered here, sufficient electron donor was present. Increasing the influent electron donor concentration by one order-of-magnitude (37.0 mM) had a minimal effect on the predicted dissolution enhancement ($E = 1.84$). For higher rates of dechlorination, however, dechlorination rate limitations may play a role.

VII.C.3.ii Dechlorination Rate (k_{max}^{PCE})

The experimental work published to date has considered the role of the dechlorination rate on dissolution enhancement only indirectly through the use of different dechlorinating cultures. According to the range in values listed in Table VII.5, the dechlorination rate may vary over an order-of-magnitude or more. Therefore, simulations were performed with k_{max}^{PCE} an order-of-magnitude greater than and less than the base case simulation value listed in Table VII.5. The bioenhanced dissolution as a function of simulation time for each of these scenarios as well as for the base case scenario is plotted in Figure VII.4. According to the simplified model (equation VII.8), an order-of-magnitude increase in the dechlorination rate should lead to an approximately 5-fold increase ($E = 9.43$) in dissolution enhancement and an order-of-magnitude decrease in the dechlorination rate should lead to a 0.6-times decrease ($E = 1.09$) in the enhancement factor. The lower dechlorination rate simulation demonstrates essentially no enhancement as predicted by the simplified equation. In this scenario, the rate of dechlorination is too slow to affect the rate of dissolution. Simulation results for the higher dechlorination rate presented in Figure VII.4, however, indicate that the simplified equation over-predicts the dissolution enhancement ($E = 1.86$ in numerical simulation).

As discussed in the previous section, the failure to account for dechlorination rate limitations in the simplified model leads to overly-optimistic dissolution enhancement predictions.

VII.C.3.iii NAPL Zone Length (L_x)

In experimental studies, NAPL zone length can vary due to column dimensions and NAPL emplacement techniques. Published experimental studies have used column lengths ranging from 22 to 30 cm [Yang and McCarty, 2000, 2002; Cope and Hughes, 2001]. NAPL emplacement techniques have included addition of NAPL to a residual saturation using a syringe [Yang and McCarty, 2000, 2002] or NAPL imbibition followed by column flushing till a residual saturation is reached [Cope and Hughes, 2001]. Section VII.C.2.ii investigated the effect of the emplacement scenario on the simulation initial conditions. The emplacement technique may also affect the NAPL zone length. The length of the NAPL zone is expected to influence the predicted enhancement in dissolution due to changes in the contact time between the NAPL and aqueous phase.

To examine the affect of NAPL zone length on dissolution enhancement, the length of the base case simulation NAPL zone was doubled to 60cm and reduced from 30cm (i.e., the entire column) to 20cm and 10cm (see Figure VII.5 a-c). All other parameters were kept constant. Simulation results are plotted in Figure VII.6. As expected, reductions in the NAPL zone length lead to reductions in dissolution enhancement. Or, put another way, increases in the NAPL zone length (e.g., 20 cm versus 10 cm) lead to increases in dissolution enhancement. However, unlike the simplified model that predicts an approximately linear increase in dissolution

enhancement over the range of NAPL lengths considered here (e.g., $E = 1.29$ for $L_x = 10\text{cm}$, $E = 1.58$ for $L_x = 20\text{cm}$, and $E = 1.87$ for $L_x = 30\text{cm}$), increases in dissolution enhancement with NAPL length appear to decline in the numerical simulations, suggesting the existence of a maximum dissolution enhancement corresponding to the length at which electron donor becomes depleted.

VII.C.3.iv NAPL Configuration

A significant advantage to modeling dissolution enhancement using a macro-scale model is the ability to simulate dissolution from a non-uniform DNAPL saturation distribution. Despite the likelihood of non-uniformities in saturation and NAPL configuration in experimental and field systems, little work has considered the effect of non-uniformities in the saturation distribution on dissolution enhancement predictions. In this section, two alternative initial organic phase saturations, two additional 10 cm DNAPL source-zone configurations in the one-dimensional column (Figure VII.5d and e), and a hypothetical two-dimensional 15 cm DNAPL source zone (Figure VII.5f) are considered. These scenarios were selected to examine the effect of DNAPL saturation, total NAPL length, and system dimensionality on dissolution enhancement.

An increase in the uniform DNAPL saturation distributed along the length of the column reduces the rate at which the mass transfer coefficient decreases as DNAPL dissolves. Changes in the interfacial area as DNAPL dissolves occur more slowly in a system with higher initial organic saturations [Powers et al., 1992]. This phenomenon leads to sustained rates of high mass transfer, which result in an increase in the simulated dissolution enhancement. For example, using the base case scenario with a uniform

DNAPL saturation of 0.2 rather than 0.02 (column retention time was kept at ~14 days), resulted in a dissolution enhancement prediction of 1.9. This value represents about a 10% increase in the predicted bioenhanced dissolution factor. Increasing the organic saturation to $S_o = 0.5$ resulted in a further increase in dissolution enhancement to 2.14.

Changing the location of the 10 cm NAPL zone from the influent end of the column to the center of the column (Figures VII.75c and d) delayed the initial on-set of dissolution enhancement, however, the impact on the predicted steady-state dissolution enhancement was minimal (Figure VII.7). Although the microbial competitors thrive in the initial 10 cm of the column in the absence of high PCE concentrations, sufficient electron donor was present to drive the dechlorination reactions in the DNAPL zone. Dissecting the 10 cm NAPL zone into two 5 cm NAPL zones separated by a 5 cm zone that was initially uncontaminated (Figure VII.5 e) increased the dissolution enhancement ($E = 1.33$ versus $E = 1.2$) (Figure VII.7). Although NAPL was not present in the 5cm zone separating the NAPL zones, dechlorination continued, resulting in reduced PCE concentrations that increased the dissolution driving force in the down gradient NAPL zone. This same observation appears to hold for two-dimensional systems. As shown in Figure VII.7 for a hypothetical laboratory scale two-dimensional domain (Figure VII.5 f), with a 20 cm long non-uniform source-zone (10 cm NAPL length), the predicted dissolution enhancement is greater than that expected for a 10 cm NAPL zone length. This observation is important given the likelihood that DNAPL will be distributed non-uniformly due to tortuous migration paths and DNAPL fingering [NRC, 2004].

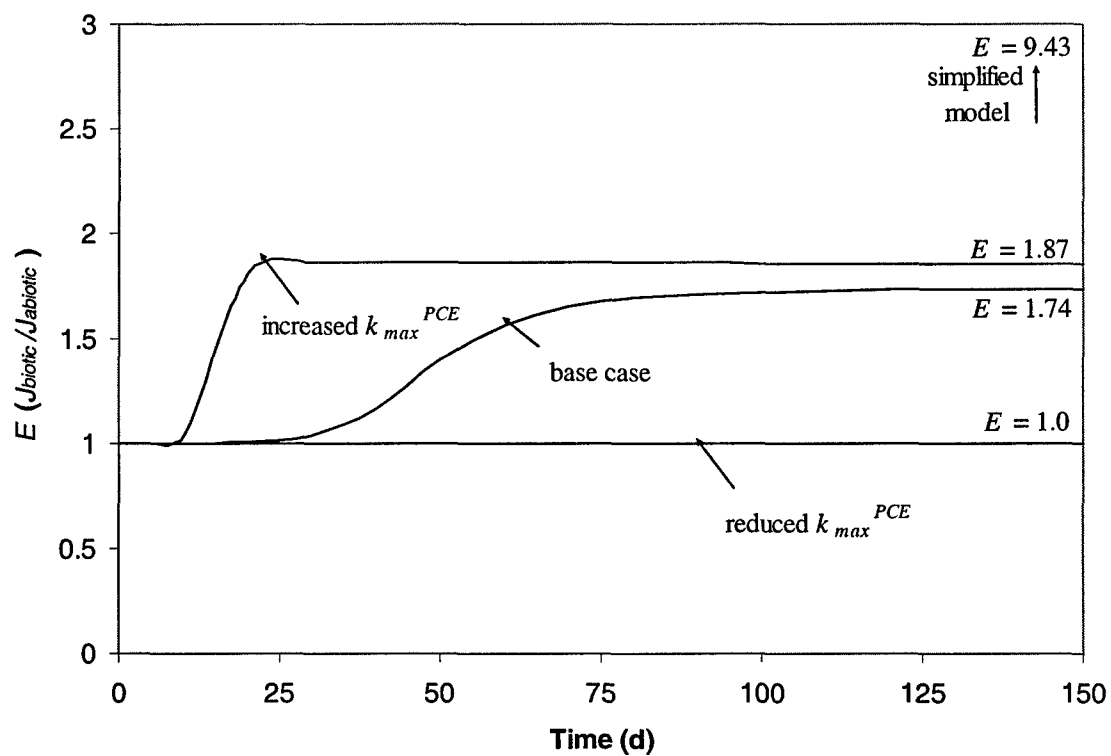


Figure VII.4: Dissolution enhancement as a function of time for three alternative k_{max}^{PCE} values. All other simulation parameters remain unchanged.

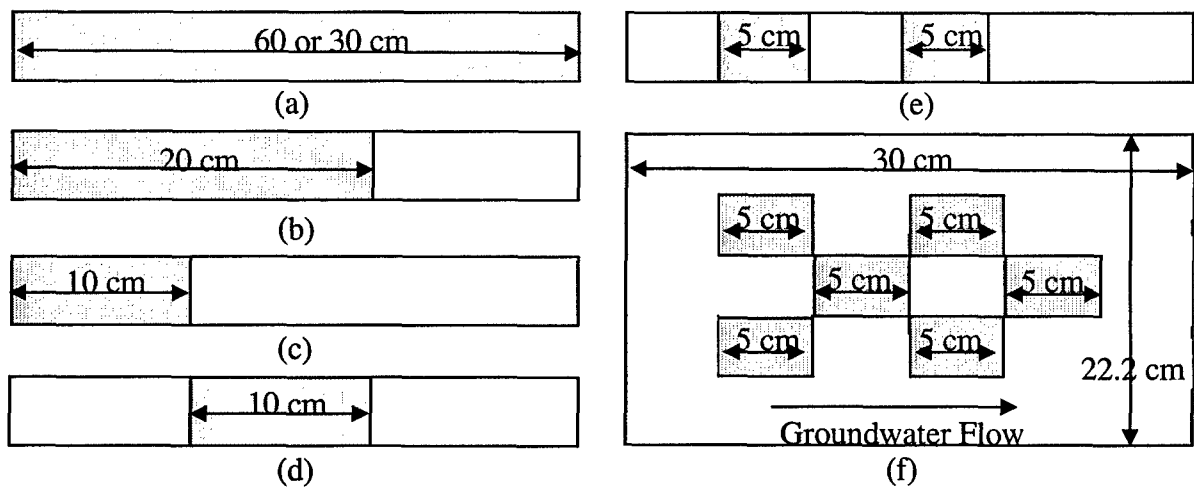


Figure VII.5: NAPL configuration (shaded area) for simulations in Sections VII.C.3.iii and VI.C.3.iv.

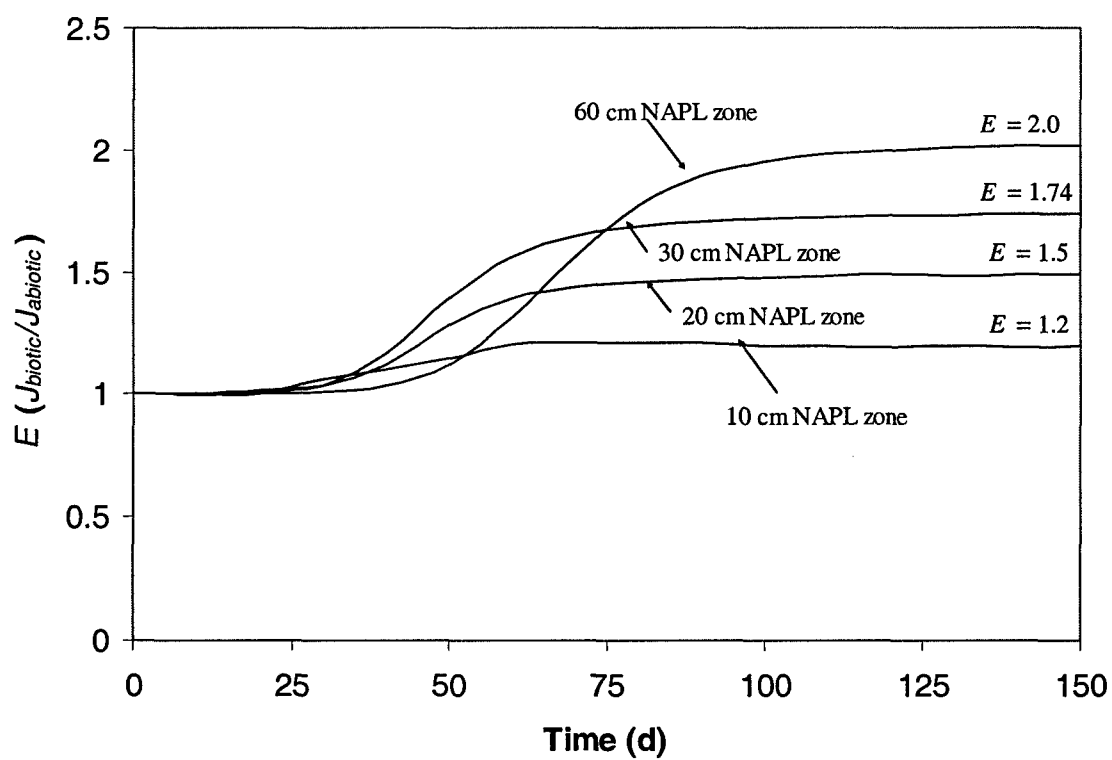


Figure VII.6: Dissolution enhancement factor as a function of time for the 60 cm, 30 cm, 20 cm, and 10 cm NAPL zone length.

Furthermore, the 2-D results indicate that for the saturation distribution considered here, dimensionality has a minimal effect on dissolution enhancement predictions (dissolution enhancement reduced by approximately 5 percent in 2-D versus 1-D). The differences between 1- and 2-D simulation results could be caused by flow by-passing due to relative permeability reductions and mixing due to transverse dispersion. The simulation of the NAPL configuration depicted in Figure VII.5f with an increase in the organic phase saturation from 0.02 to 0.2, however, resulted in a 10% increase in the predicted dissolution enhancement ($E = 1.39$). This result is consistent with the 1-D simulation results, indicating that for these relatively low saturations, flow by-passing has a minimal effect. Likewise, the simulation of the 2-D NAPL zone configuration (Figure VII.5f) with a two order-of-magnitude increase in transverse dispersion ($\alpha_T = 0.01$ m) resulted in approximately the same level of dissolution enhancement at steady-state ($E = 1.25$), indicating, that for these experimental conditions, mixing due to transverse dispersion had a minimal effect on dissolution enhancement. Simulating a 2-D source zone with the NAPL configuration shown in Figure VII.5f shifted 5cm to the left, however, resulted in a predicted dissolution enhancement factor equal to 1.36. This value is consistent with the 1-D value, suggesting that electron donor depletion in the 5-10 cm separating the left boundary and the NAPL zone could cause reductions in dissolution enhancement. The extension of these 2-D observations to other experimental systems containing DNAPL pools, however, should not be attempted since aqueous phase flow through a DNAPL pool is known to be small, flow by-passing will be significant, and transverse dispersion will likely have a significant effect on DNAPL pool dissolution [e.g., Anderson et al., 1992].

VII.C.3.v Dissolution Time

The time required to completely dissolve residual NAPL in 1-D column experiments has typically exceeded the time-frame of an experiment. Thus, bioenhanced dissolution factors published in the literature generally represent the quasi-steady-state value. Although the time required to reach this steady-state value may be on the order of 50 to 100 days, relatively short compared to the longevity of the NAPL source, existing efforts have failed to consider the length of time the system remains at the quasi-steady-state value. As NAPL dissolves, the rate of dissolution will change, leading to a reduction in the dissolution enhancement factor. Figure VII.8 demonstrates the eventual decline in the dissolution enhancement factor as the source-zone length (L_x) decreases due to dissolution. Eventually the system becomes dissolution limited and the bioenhanced dissolution factor is reduced to 1.0 (see 10 cm NAPL length curve in Figure VII.8). A failure to consider this behavior could lead to the erroneous estimation of source longevity at a site with active microbial reductive dechlorination. For example, in the 10 cm NAPL zone simulation, bioenhanced dissolution is sustained at the quasi-steady-state value for less than 50% of the time required to effect DNAPL removal. Failing to account for this transient effect could lead to overly-optimistic predictions of reductions in DNAPL source longevity due to bioenhanced dissolution.

Including a dissolution enhancement factor that declined linearly as a function of % mass removal in the source zone bioremediation and SEAR plus bioremediation illustrative calculations performed in Section II.E resulted in an estimated source longevity three times greater than that estimated using a constant bioenhanced dissolution factor (Figure VII.9). Using these newly simulated source longevity values,

implementing source zone bioremediation would result in a 40% reduction in time to cleanup and implementing SEAR plus bioremediation would result in a 70% reduction in cleanup time. These enhancements are significant, but not as large as those estimated using the constant dissolution enhancement factor in Section II.E (Table II.2).

VII.C.4 Future Modeling Applications

In this final section, the ability of the modified version of MISER to simulate mixed NAPL systems is demonstrated. These systems arise in chlorinated DNAPL source zones due to partitioning of chlorinated daughter products into the NAPL. They also are of interest to recently proposed remediation methods that attempt to partition fermentable substrate into the NAPL to serve as a slow release of electron donor.

VII.C.4.i Contaminant Back Partitioning

As discussed in section VII.B.2, interphase partitioning in MISER neglects back partitioning of contaminant degradation products into the NAPL phase. Low DNAPL saturations present in column studies, as well as the increasing solubility of dechlorination products (see Table VII.3), make neglecting back partitioning a reasonable assumption. To test this impact of this assumption on dissolution enhancement factor predictions, the interphase mass transfer model implemented in MISER was modified:

$$E_{ao}^c = \rho_a K_{ao}^c (x_{ao}^{c-e} - x_a^c) \quad (\text{VII.7})$$

Equation VII.7 may act as a source of component c in the aqueous phase equation when $x_a^c < x_{ao}^{c-e}$ and a sink in the aqueous phase equations when $x_a^c > x_{ao}^{c-e}$. The rate of back partitioning may be significant at early times when the equilibrium mole fraction (x_{ao}^{c-e})

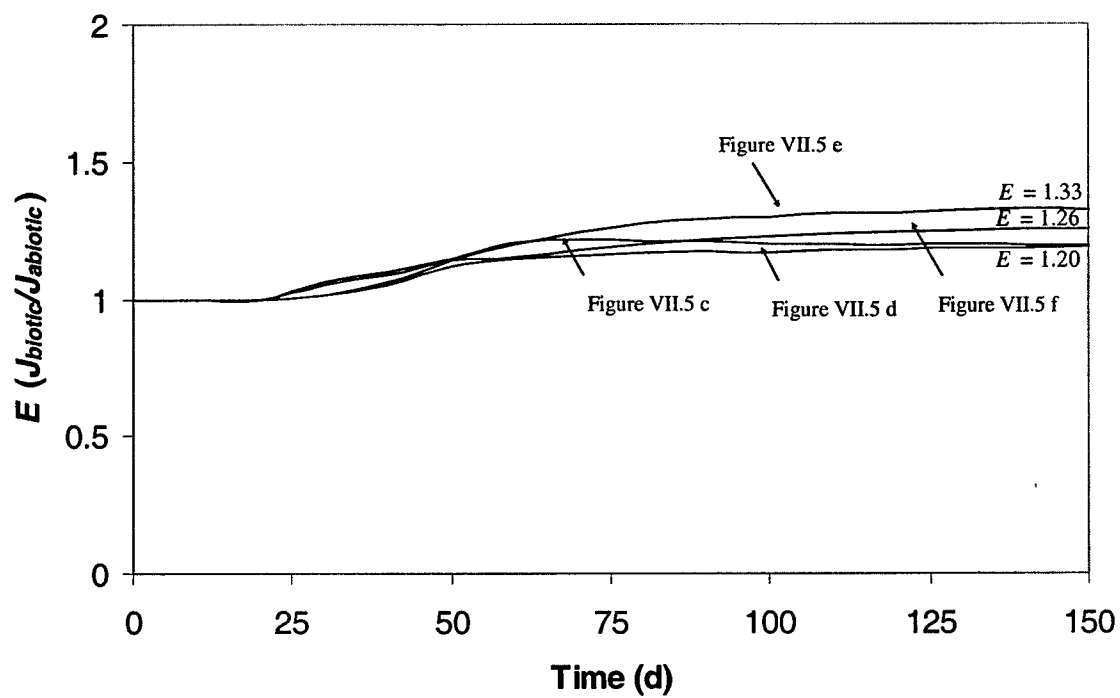


Figure VII.7: Dissolution enhancement factor as a function of time for alternative NAPL source configurations. See Figure VII.V c – f.

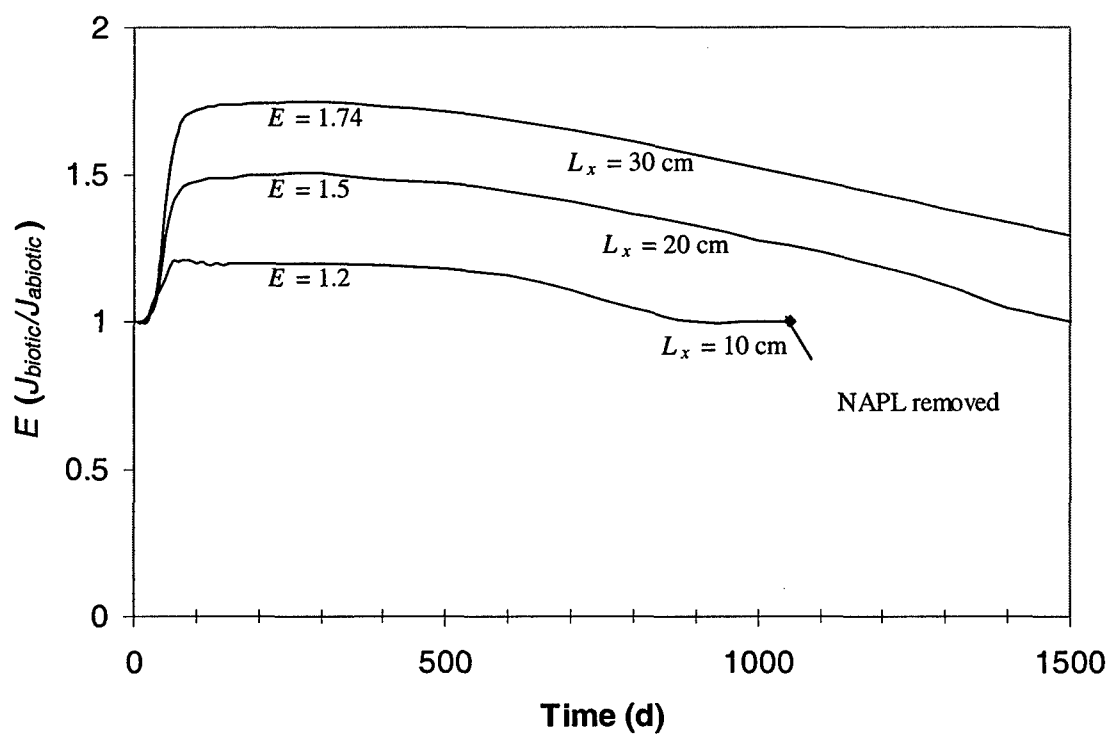


Figure VII.8: Bioenhanced dissolution as a function of time for 30 cm (Base case), 20 cm, and 10 cm NAPL zone lengths. Point on 10cm NAPL length curve indicates the time when NAPL was completely dissolved.

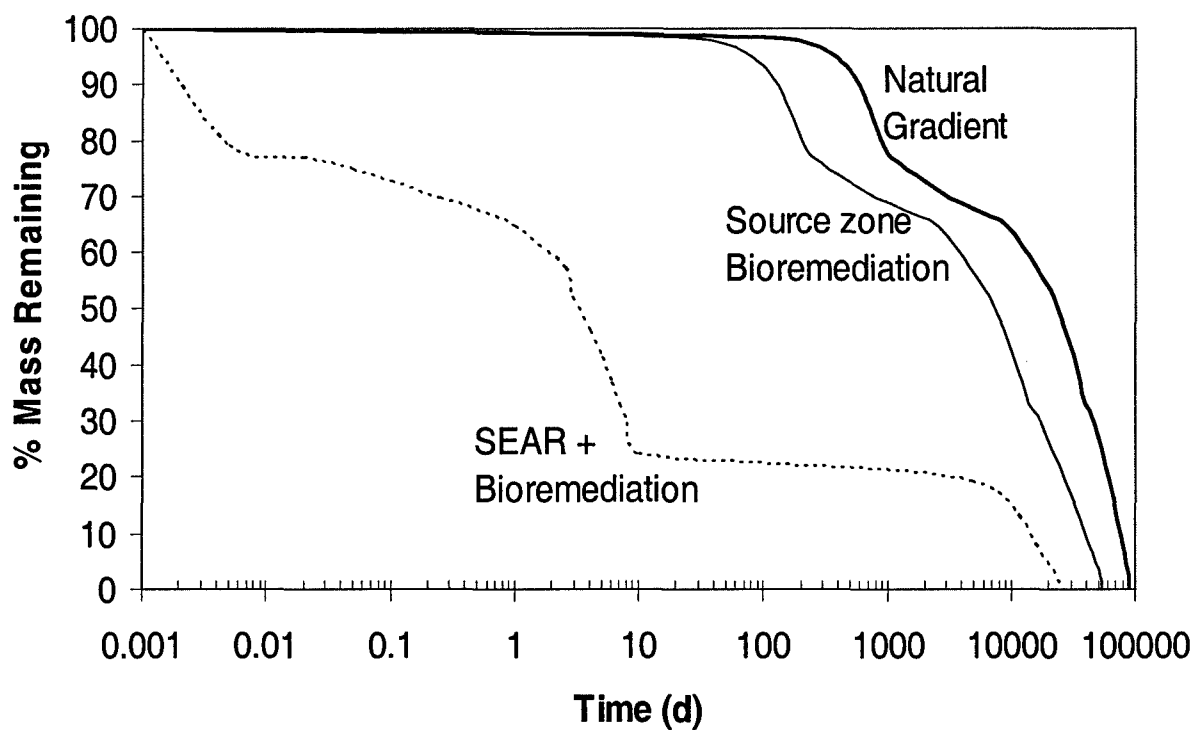


Figure VII.9: Percent of DNAPL mass remaining as a function of time for three alternative remediation strategies in the LGP scenario (Figure II.2) with a transient bioenhanced dissolution factor.

is near zero due to a lack of contaminant degradation products in the organic phase. Over time, equation VII.7 will lead to a NAPL mixture at equilibrium with the aqueous phase contaminant concentrations.

To determine the impact of back partitioning on simulation results, the base case scenario was simulated using equation VII.7. Dissolution and back partitioning were modeled using the dissolution mass transfer correlation given by equation (III.21) [Powers et al., 1992]. Simulation results are shown in Figure VII.10. When back partitioning is simulated, the total chloroethene concentration in the column effluent is significantly lower than the base case simulation where back partitioning was neglected. The reduction in the total chloroethene concentration in this simulation is due to the partitioning of *cis*-DCE into the PCE-NAPL along the length of the column. Back partitioning of *cis*-DCE into the NAPL results in a direct reduction in the aqueous phase effluent *cis*-DCE concentration and a slight reduction in the aqueous phase PCE concentration due to a reduction in the PCE solubility as the PCE mole fraction in the organic phase is reduced. Ultimately, for these simulation conditions, neglecting back partitioning results in a 30% error in the predicted total chloroethene concentration.

Simulation of back partitioning using equation VII.7, however, assumes (i) that the dissolution mass transfer coefficient (equation III.21) can be used to quantify the rate of back partitioning, and (ii) that Raoult's law can be used to compute the equilibrium mole fraction in the multi-component mixture. These assumptions could possibly lead to an estimated one- to two-order-of-magnitude over-prediction of the back partitioning rate. An alternative scenario is that the rate of back partitioning will be controlled by mass transfer resistance internal to the NAPL phase in the form of component diffusion

away from the NAPL interface. This rate-limiting process could be several orders-of-magnitude slower than the contaminant dissolution rate, resulting in a decrease in degradation product losses due to back partitioning. Unfortunately, little work has considered these processes. These issues will need to be investigated experimentally before the simulation of back partitioning can be accomplished with confidence.

VII.C.4.ii Electron Donor Supply

In several of the simulations presented in the previous sections, modest enhancements in dissolution were attributed to electron donor limitations. In all of those simulations, electron donor was supplied as a component in the aqueous phase at the influent end of the column. This method of application results in significant dechlorination in the first 30 to 50 percent of the column, with little dechlorination occurring thereafter. An alternative strategy that could improve the NAPL length over which dechlorination actively occurs is to augment the NAPL with a fermentable substrate using either a substrate designed to partition into the NAPL or a substrate that is injected into the subsurface as a NAPL. Dissolution of both components from the NAPL leads to a targeted amendment strategy capable of supplying electron donor in the NAPL zone throughout the length of the column. This amendment strategy has been demonstrated in the laboratory for a PCE/olive oil mixture [Yang and McCarty, 2002].

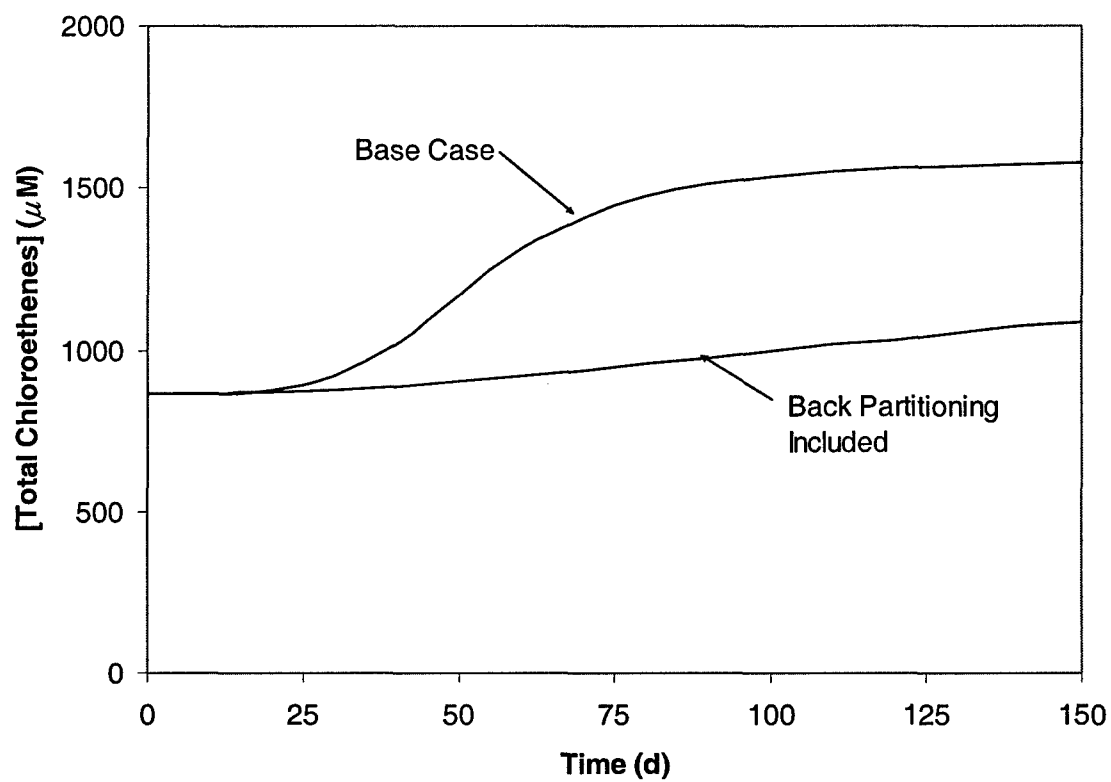


Figure VII.10: Total chloroethene concentration as a function of time for base case simulation and a simulation that includes back partitioning of dechlorination products (e.g., *cis*-DCE) into the residual PCE-NAPL.

To examine this amendment strategy, MISER was used to simulate bioenhanced dissolution from a mixed NAPL comprised of a 1:1 v/v mixture of PCE and pentanol ($x_o^{PCE} = 0.42$ and $x_o^{PS} = 0.58$) emplaced in the NAPL configuration depicted in Figure VII.5e. Initially, the NAPL saturation was assumed to be the same as that used in the original simulation ($S_o = 0.02$). The simulation results, however, indicated that the pentanol was depleted from the organic phase before significant dechlorination could occur. Therefore, the simulation was rerun with $S_o = 0.2$. The chloroethene concentrations at the effluent boundary for this simulation are shown in Figure VII.11. The PCE concentration rises rapidly at the effluent boundary as contaminant migrates from the NAPL zone down gradient. After approximately 25 days, *cis*-DCE begins to accumulate. The lag in the accumulation of *cis*-DCE is attributable to the time required for the primary substrate to dissolve from the NAPL and stimulate the dechlorinating populations to appreciable levels. From day 50 to day 80, PCE concentrations begin to decline due to the dechlorination of PCE to *cis*-DCE. After approximately 80 days, however, the primary substrate is depleted from the NAPL, resulting in the decline in *cis*-DCE and the increase in PCE concentrations to near saturation concentration levels. These results are consistent with the experimental observations of Yang and McCarty [2002] and illustrate that the addition of a primary substrate to the contaminant NAPL can stimulate dechlorination. Design of the primary substrate-NAPL mixture, however, will need to account for the longevity of the NAPL within the source as well as the aqueous phase primary substrate concentrations within the NAPL zone.

VII.D CONCLUSIONS

Simulating bioenhanced dissolution due to metabolic reductive dechlorination in DNAPL source-zones requires the use of a model capable of simulating rate-limited dissolution and sequential reductive dechlorination. Previous modeling efforts have focused on the simulation of dissolution enhancements from fully-saturated horizontal DNAPL pools placed along the flow-domain boundary. The majority of source-zone bioremediation experiments, however, have investigated dissolution enhancement in systems contaminated with a residual DNAPL. DNAPL saturation distributions in the field are likely to exhibit both residual DNAPL saturations and DNAPL pooling. Therefore, to enable the simulation of dissolution enhancement in field-scale DNAPL source zones and to facilitate the simulation of dissolution enhancement for typical experimental conditions, this work developed a new source-zone bioremediation model. This model is capable of simulating the spatial-temporal evolution of a chloroethene-DNAPL source-zone influenced by metabolic reductive dechlorination. This model is based on an existing multi-phase compositional simulator that has been modified to account for fermentative, dechlorinating, and competitor (e.g., methanogenesis) microbial processes. The model was validated against an existing analytical dechlorination model, BIOCHLOR, and results from a one-dimensional two-phase column experiment. The model was used to examine several factors that may affect dissolution enhancement predictions in experimental-scale systems, including the dechlorination rate, electron donor supply, NAPL source-zone length, NAPL saturation, and NAPL configuration. The numerical simulator was also used to examine a newly formulated analytical model capable of predicting dissolution enhancement due to biological activity in a ganglia-

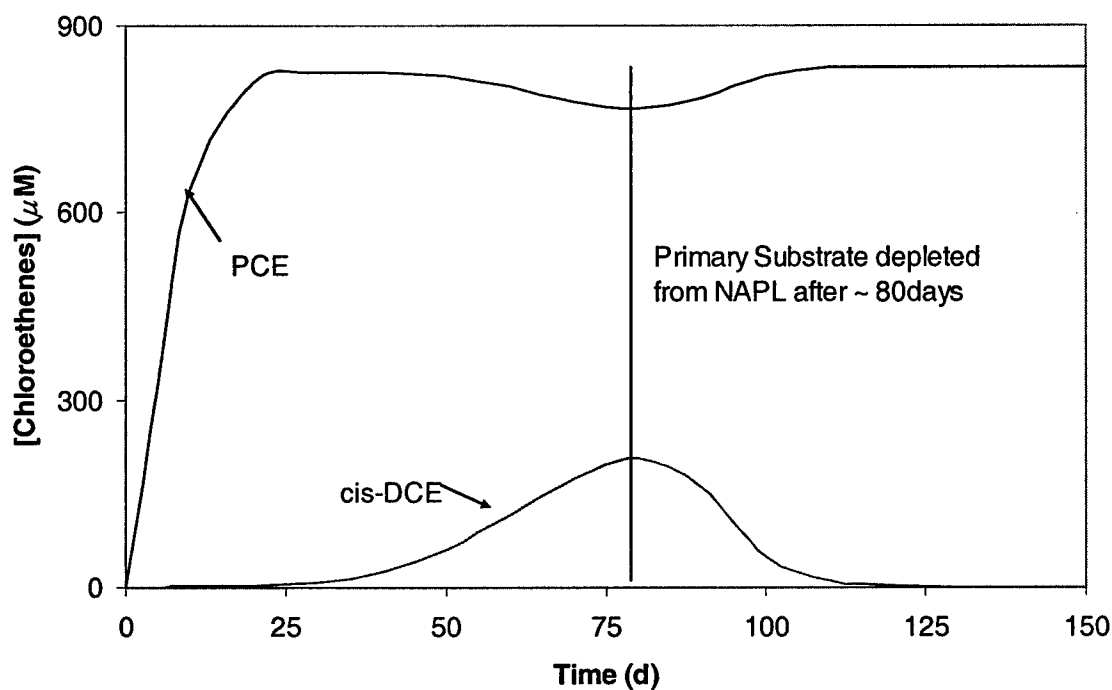


Figure VII.11: PCE and *cis*-DCE concentrations for the alternative primary substrate amendment strategy simulation discussed in Section VII.C.4.ii.

contaminated source-zone. This model was found to provide reasonable bioenhanced dissolution predictions for systems that did not have rate-limited dechlorination. Systems that were rate-limited, however, resulted in the over-estimation of bioenhanced dissolution using the simplified model.

Using the numerical simulator to investigate factors that affect bioenhanced dissolution predictions indicated that increases in the dechlorination rate and length of the DNAPL source-zone will tend to increase dissolution enhancement. The increases are relatively small, however, due to physical factors limiting dechlorination rates, such as insufficient amounts of electron donor. Altering the NAPL saturation and NAPL configuration was found to either increase the predicted level of dissolution enhancement or have no effect. The simulation of a DNAPL source zone with relatively high residual DNAPL saturations ($S_o = 0.2$) and source-zones with non-uniform DNAPL distributions, for example NAPL zones separated by an uncontaminated zone, were shown to increase the dissolution enhancement factor. Increasing the dimensionality from 1-D to 2-D had a minimal affect on dissolution enhancement predictions for the contamination scenario considered here.

Simulation results also demonstrated that the time the system is operating at quasi-steady-state conditions may be a relatively small fraction (e.g., $\frac{1}{2}$) of the DNAPL source longevity. This finding is important given the desire to use a constant dissolution enhancement factor consistent with the quasi-steady-state value to simulate bioenhanced dissolution over the life of a DNAPL source zone. Simulation of dissolution enhancement using a constant value could lead to significant under-prediction of the DNAPL source longevity.

Finally, the utility of the model to simulate mixed NAPL systems was demonstrated by considering chlorinated daughter product back partitioning and a primary substrate amendment strategy that utilized a mixed (two-component) NAPL to deliver primary substrate. The simulation of chlorinated daughter product partitioning into the NAPL demonstrated that neglecting back partitioning could result in the overestimation of the dissolution enhancement factor by 30%. The simulation of a substrate/PCE mixed NAPL system demonstrated that dechlorination will be limited by the mass of substrate in the organic phase, suggesting implementation of this amendment strategy will require a balance between the need to partition sufficient primary substrate into the aqueous phase to drive dechlorination and the need to sustain dechlorination throughout the life of the NAPL source.

Future work will focus on the use of this model as a tool to aid in the design and evaluation of existing and future experimental studies and to simulate bioenhanced dissolution in field-scale non-uniform DNAPL source zones. Quantifying the benefits of DNAPL source zone bioremediation relative to alternative source zone remediation technologies will be essential to the acceptance of this technology as a viable source zone management strategy.

CHAPTER VIII

CONCLUSIONS AND RECOMMENDATIONS FOR FUTURE WORK

VIII.A CONCLUSIONS

Quantifying the benefits of partial contaminant mass removal from DNAPL source zones is a leading objective in the environmental engineering and science community. Research has focused on (i) the application of existing models to the simulation of mass recovery from DNAPL source zones under natural and engineered conditions and (ii) the development of complementary technologies, such as source zone bioremediation, to reduce the DNAPL source longevity and contaminant mass flux eluting from the source zone. The application of existing models to these problems, however, has been limited due to computational difficulties associated with the simulation of DNAPL source zone processes in three dimensions and a lack of models capable of simulating biological processes in a DNAPL source zone. Work presented in this dissertation focused on remedying these limitations through the modification and application of existing compositional multiphase numerical simulators.

A general mathematical framework for the simulation of migration, entrapment, dissolution, and degradation of DNAPLs in non-uniform permeability fields was presented in Chapter III. This mathematical framework formed the foundation for the

numerical models applied in Chapters IV and V and the numerical models developed and applied in Chapters VI and VII. In Chapter IV, an existing compositional multiphase simulator (UTCHEM) was used to investigate the impact of reductions in dimensionality (three dimensions (3-D) versus two dimensions (2-D)) on simulations of DNAPL migration and entrapment. Dimensionality effects on DNAPL mass recovery from these 2- and 3-D DNAPL saturation distributions were investigated in Chapter V using a modified version of MT3DMS. In Chapter VI, a numerical model (Batch-DECHLOR) was developed to simulate metabolic reductive dechlorination in single- and two-phase batch systems. The model was successfully coupled with an optimization algorithm to facilitate the quantification of dechlorination kinetic parameters. This dechlorination model was integrated into an existing multiphase compositional simulator (MISER) in Chapter VII. This newly developed model permits the simulation of bioenhanced DNAPL dissolution due to source zone metabolic reductive dechlorination. This is the first model to simulate these processes using macroscopically averaged flow and transport equations.

Computational difficulties associated with the implementation of multi-phase compositional simulators in 3-D have lead many researchers to perform simulations in more computationally efficient 2-D domains. No study, however, has performed a systematic investigation of dimensionality effects on DNAPL migration, entrapment, and mass recovery to determine the validity of using the 2-D domains to represent 3-D behavior. Research presented in Chapters IV and V considered this effect for an ensemble of 2- and 3-D statistically homogeneous, non-uniform permeability fields

conditioned to actual field-data collected during a recent pilot-scale investigation.

Conclusions from this study are as follows:

- Reductions in dimensionality from 3D to 2D were found to have a minor impact on predicted characteristics of the simulated DNAPL saturation distributions. Hence, for the analysis of DNAPL infiltration and entrapment behavior, the more computationally efficient 2D simulations can provide reasonable approximations to fully 3D simulations.
- Simulations of DNAPL migration and entrapment in 2D tend to predict saturation distributions with maximum saturations approximately equivalent to those simulated in 3D, but with lateral and vertical spreading greater than in 3D. The 2D and 3D distributions of DNAPL mass within the source zone, quantified using ganglia-to-pool (GTP) mass ratio metrics, is correlated (~ 0.7), with 2D simulations tending to predict lower GTP mass ratios than 3D simulations, suggesting 2D simulations provide more conservative source longevity estimates due to the higher percentage of DNAPL mass residing in high saturation pools.
- Rank correlation results indicate that 2D and 3D saturation distribution ensembles are similar, that is, extreme behavior in a 3D realization is typically manifested in the corresponding 2D realization.
- Analysis of horizontal isotropy in 3D simulations indicated that, while an isotropic permeability field did not translate to an approximately symmetric (x - y) DNAPL source area for an individual realization, average lateral spreading was symmetric for the ensemble of simulations. This suggests that ensembles of 2D realizations

may be analyzed to infer average DNAPL infiltration and entrapment behavior along 2D transects of a 3D domain, irrespective of their orientation.

- Examination of dimensionality affects on three alternative DNAPL source zone mass recovery metrics presented in the literature (flux-weighted down gradient concentration, contaminant flux reduction through a down-gradient boundary, and source longevity) demonstrated dimensionality primarily impacted flux-weighted concentration predictions. Contaminant flux reductions and source longevity were shown to generally be within 5% in 2D and 3D simulations.
- 2D flux-weighted concentration predictions were found to be approximately 3.5 times greater than those simulated in 3D. Reasons for this difference, however, were attributable to dilution and not dimensionality. Comparing flux-weighted concentrations from the center 2D cross-section of a 3D simulation with a 2D simulation demonstrated that the aqueous phase concentrations in a given cross-section are approximately equivalent, i.e., concentrations in 2D and 3D simulations are similar at the numerical grid block scale. Therefore, simulated concentrations in 2D are approximately equivalent to those simulated in 3D when corrected for dilution, supporting the use of more computationally efficient 2D simulators to examine DNAPL source zone behavior.
- Alternative spill characteristics such as the volume and spill rate (e.g., volume, rate), and increases in the degree of non-uniformity ($\sigma^2 \ln(k)$) in the permeability field had only a minimal impact on the conclusions presented previously.
- The hysteretic entrapment subroutine in UTCHEM (version 9.0) required coding corrections (see Appendix A) to successfully simulate DNAPL migration and

entrapment. These coding corrections have been forwarded to the code developers to be incorporated in the next version of the widely used UTCHEM compositional multiphase simulator.

Recent experimental evidence has suggested that stimulation of microbial populations in DNAPL source zones may reduce DNAPL source longevity by enhancing dissolution. Among the most promising is the stimulation of metabolic reductive dechlorinating populations due to the ubiquity of chlorinated solvent source zones and the tolerance of these dechlorinating populations at high contaminant concentrations. Unfortunately, a lack of models capable of simulating these processes has limited its investigation. Research presented in Chapters VI and VII takes a first step toward remedying this limitation by developing and applying numerical models capable of simulating metabolic reductive dechlorination in multiphase batch, one-dimensional, and two-dimensional systems. The batch model presented in Chapter VI is the first model to be developed that is capable of simulating metabolic reductive dechlorination in a two-phase system with rate-limited DNAPL dissolution. Integration of this dechlorination model into the existing multiphase simulator, MISER, in Chapter VII, provides the first macro-scale compositional multiphase model capable of simulating enhancements in DNAPL dissolution due to metabolic reductive dechlorination, a research need identified by several recent expert panels. Application of Batch-DECHLOR and the modified version of MISER to experimental and hypothetical scenarios has led to the following conclusions:

- Batch-DECHLOR is able to simulate fermentation of a primary substrate to an electron donor, metabolic reductive dechlorination of PCE to ethene, and electron

donor-scavenging processes (e.g., acetogenesis) in single and two-phase batch experimental systems using best-fit parameters consistent with kinetic coefficients published in the literature.

- Evaluation of dechlorinating mixed and pure cultures demonstrated that the rate of dechlorination of the pure culture was consistent with the rate obtained for the mixed culture, suggesting that for the experimental conditions considered here, kinetic coefficients obtained for pure cultures may be applied to mixed cultures containing those same populations.
- Simulation of metabolic reductive dechlorination experiments spiked with the surfactant TWEEN 80, a common amendment used in SEAR, demonstrated that dechlorination kinetics were negatively affected (reduced by 25%) due to the presence of the surfactant, but that the reduction was independent of the surfactant concentration.
- Comparison of best-fit kinetic coefficients for single and two-phase experimental systems demonstrated that coefficients obtained from single-phase (i.e., aqueous phase only) experiments could be used to simulate two-phase experiments.
- Simulation of the two-phase experiments demonstrated the capacity for metabolic reductive dechlorination in the aqueous phase to increase the dissolution driving force, resulting in the complete dissolution of PCE-NAPL.
- Successful integration of the dechlorination kinetics into an existing multi-phase flow and transport simulator (MISER) was demonstrated using mass balance calculations, comparison with results from an existing analytical solution, and

simulation of experimental chloroethene breakthrough curves measured in a 1-D column contaminated with residual PCE-NAPL.

- Investigation of the simplifying assumptions used in the simulation of the 1-D experimental column indicated that for the conditions considered here, assuming equilibrium between the aqueous and organic phase and assuming a uniform biomass concentration at the start of the simulation had a minimal affect on simulation results. Likewise, simulation results were relatively insensitive to the magnitude of the biomass density (generally assumed to be equivalent to water). Simulation of back partitioning, however, was found to have a potentially significant effect on predicted chloroethene breakthrough curves. Including back partitioning in the model resulted in a 30% reduction in the simulated *cis*-DCE effluent concentration. A lack of data on the rate of back partitioning, however, limits the successful application of this process.
- Comparison of simulation results with an analytical model newly derived to simulate dissolution enhancement in systems contaminated with residual NAPL ganglia indicate that the simplified model will tend to over-estimate dissolution enhancement due to its failure to incorporate dechlorination rate-limiting processes.
- Application of the modified model to hypothetical experimental scale scenarios indicated that increases in the rate of dechlorination, NAPL saturation, and source zone length will result in greater dissolution enhancement. The increases in dissolution enhancement are relatively small, however, due to dechlorination rate limitations caused by insufficient electron donor. Consideration of dimensionality

effects demonstrated that for the scenario considered here, increasing dimensionality from 1-D to 2-D had a relatively minor effect.

- Using the model to simulate a novel substrate amendment strategy that assumes a component in the NAPL can serve as a fermentable substrate demonstrated the potential for this technology to stimulate metabolic reductive dechlorination. In the scenario simulated, however, dechlorination was modest due to the rapid depletion of primary substrate from the NAPL.

VIII.B FUTURE WORK

The corrected version of UTCHEM used in Chapter IV provides a powerful tool for the simulation of DNAPL migration and entrapment in 2D and 3D permeability fields. This tool may prove very useful for the future investigation of DNAPL source zone behavior. Future research that may benefit from the use of this model includes:

- Investigation of dimensionality effects on DNAPL migration and entrapment simulations in higher heterogeneity permeability fields with potentially non-horizontal bedding characteristics. The research presented in Chapters IV and V was restricted to a relatively homogeneous permeability field. While simulations in a higher variance permeability field supported the general conclusions presented in this work, these results suggested that these conclusions may become tenuous as the heterogeneity of the permeability field increases.
- Simulation of alternative source zone remediation strategies (e.g., air sparging, chemical oxidation, thermal treatment) using the DNAPL saturation distributions developed in this work. Difficulties with simulating hysteretic infiltration and

entrapment in 3D domains have led most researchers to assume a correlation between the DNAPL saturation and soil property field. These assumed distributions are then used during the simulation of DNAPL mass recovery. Given that the basis for these correlations is weak, use of the saturation distributions developed in this work, or new distributions developed using the modified version of UTCHEM, provide an opportunity to investigate DNAPL mass removal under more realistic source zone conditions.

The batch metabolic reductive dechlorination model and modified version of MISER developed as part of this dissertation provide new research tools that enable the quantification of dissolution enhancements due to metabolic reductive dechlorination. Future endeavors suggested by the work contained in Chapters VI and VII include:

- Simulation of existing and future batch experimental studies to further refine changes in dechlorination kinetics due to systems stresses such as, the presence of a residual surfactant, or dissolution from an organic phase. In particular, it will be important to determine solvent toxicity effects on biological activity and how aqueous phase biological activity may affect the mass transfer rate coefficient.
- Examine the sensitivity of bioenhanced dissolution predictions to the initial biomass concentration and the proportion of the fermentative, dechlorinating, and competitor populations that make up the total biomass concentration. Understanding the importance of microbial ecology on the success of source zone bioremediation will aid in the identification of subsurface microbial conditions that require the amendment of additional microbial populations.

- Simulation of 2D non-uniform, field-scale DNAPL source zones similar to those presented in Chapter IV. DNAPL source zone containment (i.e., natural gradient dissolution), aggressive mass removal (e.g., SEAR), source zone metabolic reductive dechlorination (i.e., bioenhanced dissolution), and aggressive mass removal followed by source zone metabolic reductive dechlorination have all been suggested as potential source zone management strategies. The modified version of MISER developed as part of this work may facilitate the simulation of these alternative management strategies to determine under what conditions one management strategy outperforms (i.e., reduced source longevity and contaminant mass flux) the other.
- Investigation of back partitioning of contaminant degradation daughter products. Preliminary analyses presented in Chapter VII suggest that back partitioning may play an important role in the effectiveness of bioenhanced dissolution. Little work, however, has attempted to quantify the rate of back partitioning and the equilibrium distribution of contaminants in a multi-component mixture. Incorporation of experimentally validated rates into the modified version of MISER could prove useful for the simulation of bioenhanced dissolution.
- Examination of alternative source zone amendment strategies. As demonstrated in the simulations presented in Chapter VII, electron donor limitations will typically affect the rate of dechlorination. The modified version of MISER may be used to aid in the design of electron donor delivery strategies including the novel alternative in which primary substrate is partitioned into the NAPL to provide a slow release of fermentable substrates in the immediate vicinity of the dissolving contaminant.

APPENDICES

APPENDIX A

UTCHEM VALIDATION

A.A INTRODUCTION

This appendix summarizes an examination of the capability of the University of Texas Chemical Flood Simulator (UTCHEM 9.0) to model two-phase immiscible infiltration and entrapment using hysteretic saturation-capillary pressure-relative permeability relationships. UTCHEM results were evaluated through comparison to equivalent simulations performed with the Michigan-Vertical and Lateral Organic Redistribution (MVALOR) simulator (see section III.E for model description).

For this comparison, UTCHEM and MVALOR model input was forced to be equivalent. The same field-scale x - z domain (7.9 x 1.0 x 9.8 m) was used in both models (see Figure A.1a). No-flow boundary conditions were specified at the top and bottom of the domain, and constant head conditions were specified at the left and right boundaries (no horizontal gradient). Sequential Gaussian Simulation was used to generate a heterogeneous permeability field ($\sigma^2 \ln(K) = 0.29$) on a 0.3048 x 0.3048 x 0.3048 m grid, which was then translated to a two-dimensional mesh with 26 x 1 x 128 cells and corresponding dimensions of 0.3048 x 1.0 x 0.0762 m. Permeability in the y -direction was set near 0 (0.001) and permeability in the z -direction was set to 0.5 that in the x -direction. Sensitivity analyses showed simulation results were insensitive to the y -permeability.

The spill event was modeled using the hysteretic Brooks and Corey [1964] – Burdine [1953] (BCB) capillary pressure – relative permeability framework (see section

III.D). 96 l of PCE were released in the top four center cells of the domain over a 400 day period, followed by a 330-day redistribution period. In UTCHEM the Peaceman well model was used to simulate a constant flux condition [UTCHEM, 2000].

A summary of fluid and matrix properties as well as constitutive expression parameters is provided in Tables A.1 & A.2. The ability of UTCHEM to consider complex phase behavior and mass transfer was disabled by assuming the concentration at the plait point is 1.0 (vol/vol) and by setting the organic solubility to 0.0 [UTCHEM, 2000]. An attempt was made to eliminate geochemical reactions involving cation and anion components by setting the concentrations in the domain to 0.0. However, numerical stability suffered, resulting in negative saturations. Therefore, the ion concentration was made negligible ($C < 0.0001$ meq/ml). Sensitivity analyses confirmed that with these model settings, simulation results were insensitive to all other complex phase behavior, solubility, and geochemical parameters.

MVALOR simulations developed by Lemke et al. [2004a] were used as a benchmark to investigate and validate UTCHEM results. Simulation parameters were based on Lemke et al. [2004a] and were equivalent to those described above (Tables A.1 and A.2). An example MVALOR simulation is presented in Figure A.1b.

A.B ANALYSIS

Initially, UTCHEM was used to simulate the described spill event using a non-hysteretic formulation of the saturation-capillary pressure-relative permeability framework. Ignoring hysteresis (i.e., organic phase entrapment due to saturation path reversal) is common in the multiphase modeling literature. This UTCHEM simulation is

compared to a hysteretic BCB simulation performed using MVALOR in Figure A.2. Visual inspection of figure A.2 demonstrates the same general infiltration path is followed in both formulations. However, the lack of entrapment in the non-hysteretic UTCHEM simulation results in greater vertical migration, ultimately resulting in organic pooling along the bottom low permeability layer. Comparison to the hysteretic simulation indicates that ignoring hysteresis will result in the over-prediction of the organic phase depth of penetration.

UTCHEM was then used to simulate the hysteretic saturation – capillary pressure – relative permeability model. Simulation results at day 120 are shown in Figure A.3. The simulation was terminated after 120 days due to an excessive run time and apparent errors in the simulation results. Close inspection of the saturation profile depicted in Figure A.3 shows saturation values equal to the input maximum residual organic saturation ($s_{or} = 0.151$) in all cells behind the migrating front. Investigation of the temporal evolution of this profile demonstrated that during the simulation, organic was trapped in a cell until the maximum residual organic saturation was reached. This behavior differs from MVALOR as well as the theory developed by Parker and Lenhard [1987]. Based on the review of Miller et al. [1998] it appears that the entrapment model implemented in UTCHEM resembles that proposed by Luckner et al. [1989], in which the entrapped organic saturation is equal to the existing organic saturation up to the maximum residual organic saturation.

Parameter		Units
Organic liquid density (PCE)	1.625	g/cm ³
Organic viscosity	0.89	cP
Water density	0.999032	g/cm ³
Water viscosity	1.121	cP
Organic compressibility	0.0	Pa ⁻¹
Water compressibility	4.4 x 10 ⁻¹⁰	Pa ⁻¹
Interfacial tensions		
Air/Water	72.75	dynes/cm
PCE/Water	47.8	dynes/cm
Irreducible water sat (s_{wr})	0.080	
Residual organic sat (s_{or}^{max})	0.151	
Initial water saturation	1.0	
Porosity	0.36	
Δx	0.3048	m
Δy	1.0	m
Δz	0.0726	m
Anisotropy factor (k_x/k_z)	0.5	
Nx	26	
Ny	1	
Nz	128	

Table A.1: Fluid and matrix properties for numerical simulation experiments. All values are taken from the literature.

Parameter		Units
Reference permeability	19.7	darcies
Reference porosity	0.36	-
P_b	2.809	kPa
λ	2.0773	-
PCE volume released	96	liters
PCE release rate/cell	6.0×10^{-2}	d^{-1}

Table A.2: Constitutive relation properties for model simulations (see Section III.D for definitions).

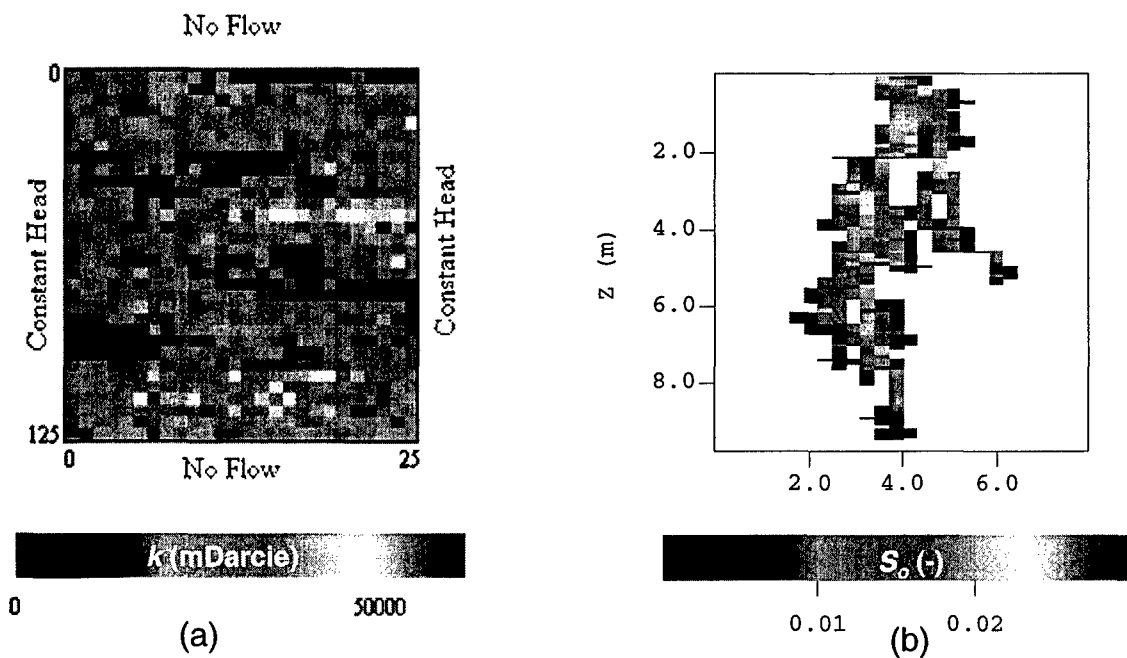


Figure A.1: (a) Hydraulic conductivity field used in reported simulations and (b) M-VALOR hysteretic benchmark simulation.

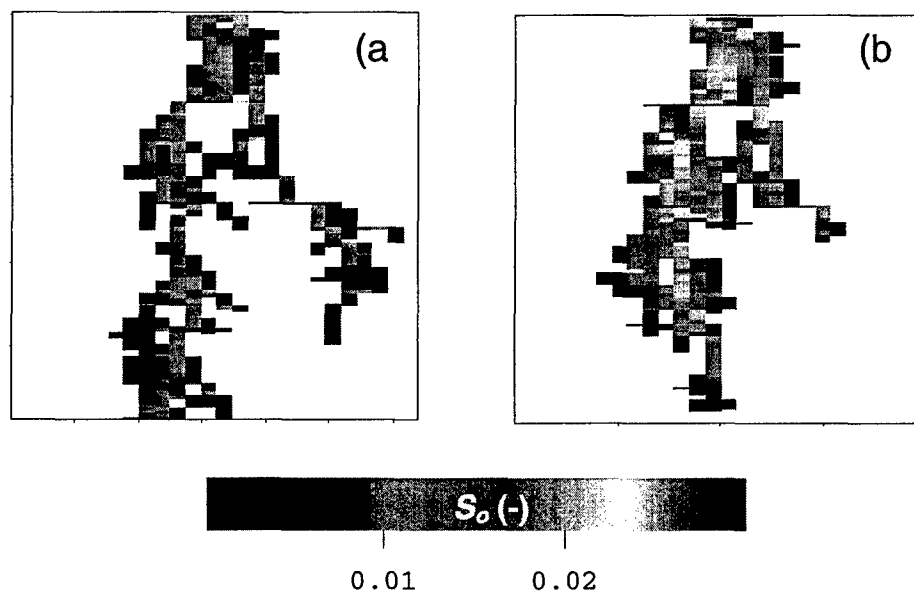


Figure A.2: (a) Non-hysteretic saturation – capillary pressure – relative permeability model simulation using UTCHEM and (b) hysteretic simulation using MVALOR.

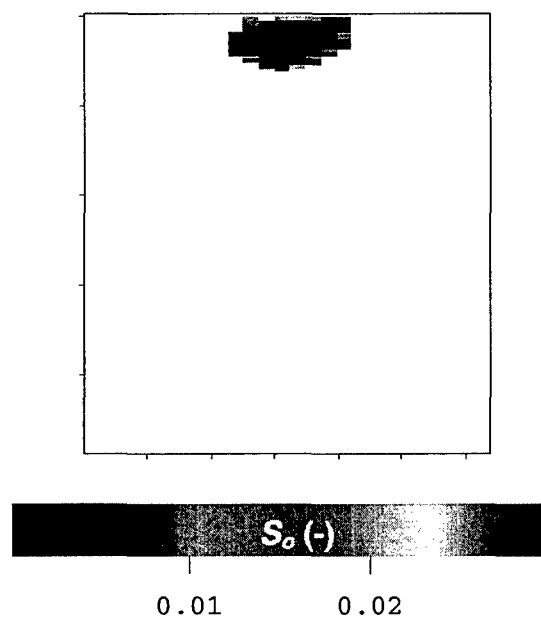


Figure A.3: Saturation profile for hysteretic simulation using the unmodified version of UTCHEM.

To examine the reasons for this behavior the entrapment subroutines in UTCHEM and MVALOR were compared. This comparison resulted in the discovery of errors in the computation of the Land equation (see section III.D), which is used to calculate the maximum entrapped organic saturation, and in the if-then loop used to compute the actual trapped organic saturation.

In UTCHEM the maximum residual water and organic saturation vary between the actual water or organic saturation and the maximum residual phase saturation input by the user:

$$S_{wr}^{max} = \text{MIN}(S_w, S_{wr}^{max}) \quad S_{or}^{max} = \text{MIN}(S_o, S_{or}^{max}) \quad (\text{A.1})$$

(hyswwg.f, Line 94&95)

This expression does not matter in the aqueous saturation case since the maximum residual water saturation is always smaller than the actual water saturation for the realizations considered in this work. However, this expression has great influence on the calculation of the residual organic saturation, which in turn has significant influence on the calculation of the maximum entrapped organic saturation as calculated by the Land equation:

$$\bar{S}_{or} = \frac{1 - \bar{S}_w^{\min}}{1 + R(1 - \bar{S}_w^{\min})} \quad \text{where} \quad R = \frac{1 - S_{rw}}{S_{or}^{\max}} - 1 \quad (\text{A.2})$$

(hyswwg.f, Line 177 & 183)

Generally the S_o in a cell is much lower than the user defined S_{or}^{max} , resulting in a large R -value and a small maximum entrapped saturation. In Land's original paper, and also in the UTCHEM technical documentation [2000], it is clear that the R -term is a function of the maximum residual phase saturations and should not vary. The resultant behavior of

this error is reduced entrapment, however, it does not explain the behavior shown in Figure A.3.

The behavior exhibited in Figure A.3 can be attributed to a programming error in the if-then loop used to calculate the actual entrapped organic saturation \bar{S}_{ot} . In subroutine hyswwg.f of UTCHEM the following statements begin the if-then loop used to calculate the trapped organic saturation (hyswwg.f lines 196 & 197):

$$\begin{aligned} &\text{IF } S_o \leq S_{or}^{max} \text{ THEN} \\ &\quad \bar{S}_{ot} = S_o / (1 - S_{wr}^{max}) \\ &\text{ELSEIF ...} \end{aligned} \tag{A.3}$$

where S_{or}^{max} is based on equation (A.1), which can easily be shown to always be true when organic saturations are below S_{or}^{max} . Therefore, as organic enters a cell it is immediately entrapped and it remains entrapped until enough organic has entered the cell to overcome the maximum residual organic saturation, at which time organic can move on to the next cell. This explains the behavior seen in Figure A.3.

To correct this behavior the lines of code represented by equation (A.3) were removed and the maximum residual saturations were set equal to the user input values. The saturation profile calculated using this modified form of UTCHEM is shown in Figure A.4. The original MVALOR profile is also shown for comparison purposes. The similarity between the saturation profiles generated using these two different models is excellent. It appears that there is slightly less "dispersion" using the modified UTCHEM code, but overall the saturation profiles are difficult to distinguish (differences in the saturation distributions were quantified in section IV.D).

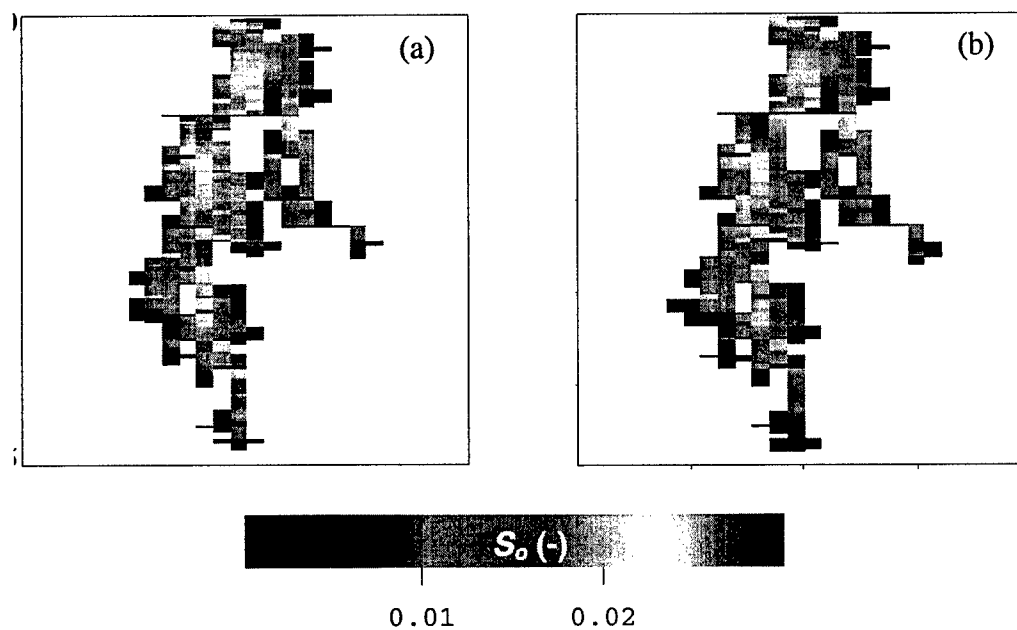


Figure A.4: Organic saturation profile simulated using (a) the modified version of UTCHEM and (b) MVALOR.

APPENDIX B

MISER SOLUTION SCHEME

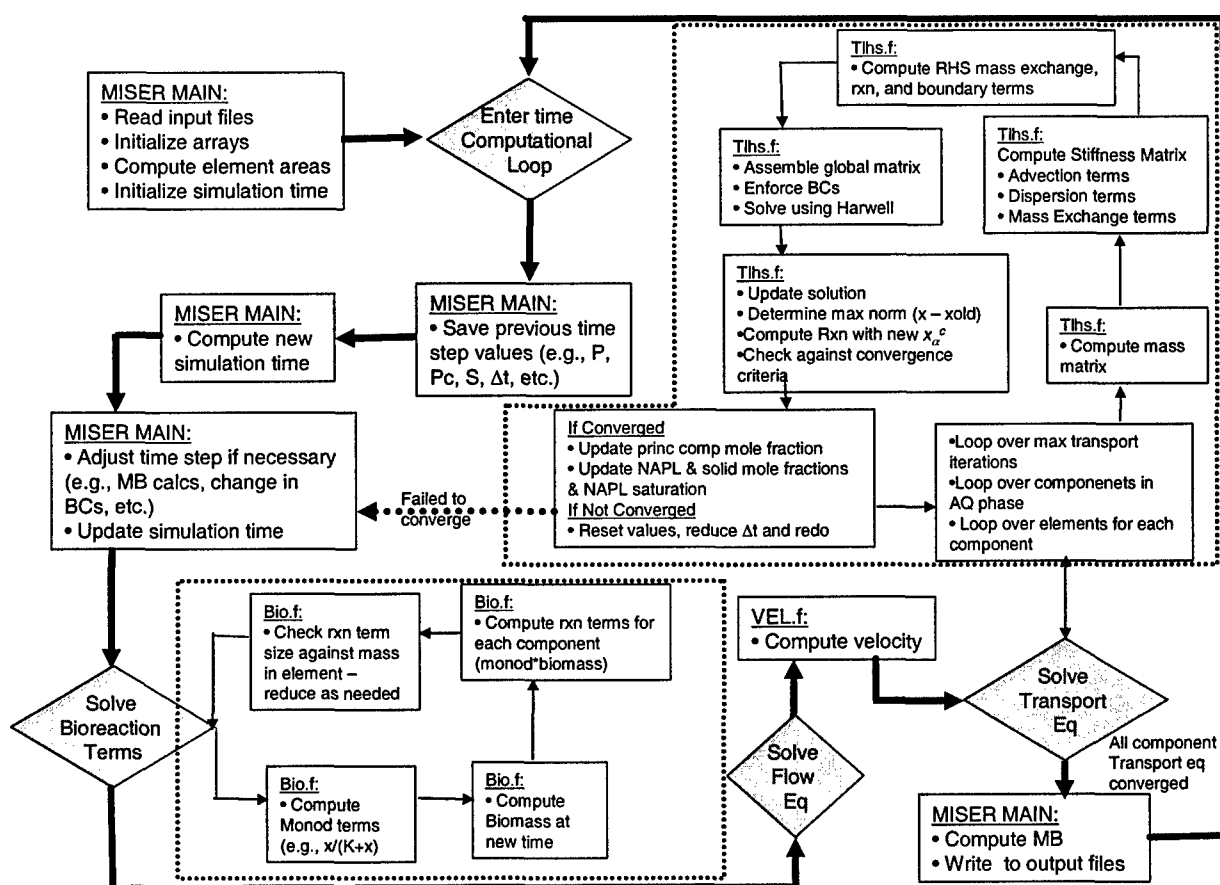


Figure B.1: Solution scheme used in version of MISER modified to simulate DNAPL source zone metabolic reductive dechlorination.

APPENDIX C

SATURATION DISTRIBUTION COMPARISON

Realization	3D				2D			
	Avg_So (-)	Max_So (-)	σ^2_{xx}	σ^2_{zz}	Avg_So (-)	Max_So (-)	σ^2_{xx}	σ^2_{zz}
SGS_02	0.013	0.153	0.453	3.126	0.015	0.261	0.500	4.410
SGS_13	0.012	0.161	0.291	4.799	0.013	0.172	0.296	6.312
SGS_17	0.013	0.324	0.336	3.837	0.019	0.379	0.452	7.856
SGS_23	0.014	0.284	0.540	2.927	0.021	0.625	1.320	3.061
SGS_25	0.013	0.179	0.378	3.843	0.014	0.258	0.330	5.730
SGS_26	0.014	0.275	0.692	1.971	0.018	0.350	1.038	2.576
SGS_27	0.014	0.273	0.392	4.669	0.017	0.275	0.653	4.457
SGS_30	0.014	0.220	0.467	4.965	0.016	0.297	0.570	5.800
SGS_36	0.013	0.402	0.701	3.464	0.016	0.352	1.047	3.724
SGS_37	0.015	0.442	0.642	4.371	0.015	0.446	0.376	5.032
SGS_39	0.014	0.424	0.328	4.855	0.017	0.433	0.526	4.037
SGS_41	0.015	0.268	0.475	2.675	0.018	0.274	0.273	6.171
SGS_43	0.018	0.400	0.365	2.349	0.028	0.578	0.465	2.221
SGS_44	0.015	0.183	0.510	2.293	0.018	0.441	1.722	2.714
SGS_45	0.012	0.134	0.389	5.385	0.015	0.226	0.367	7.216
SGS_49	0.013	0.312	0.717	2.963	0.017	0.344	1.007	2.193

Table C.1: 2D and 3D saturation distribution metrics for all 16 realizations.

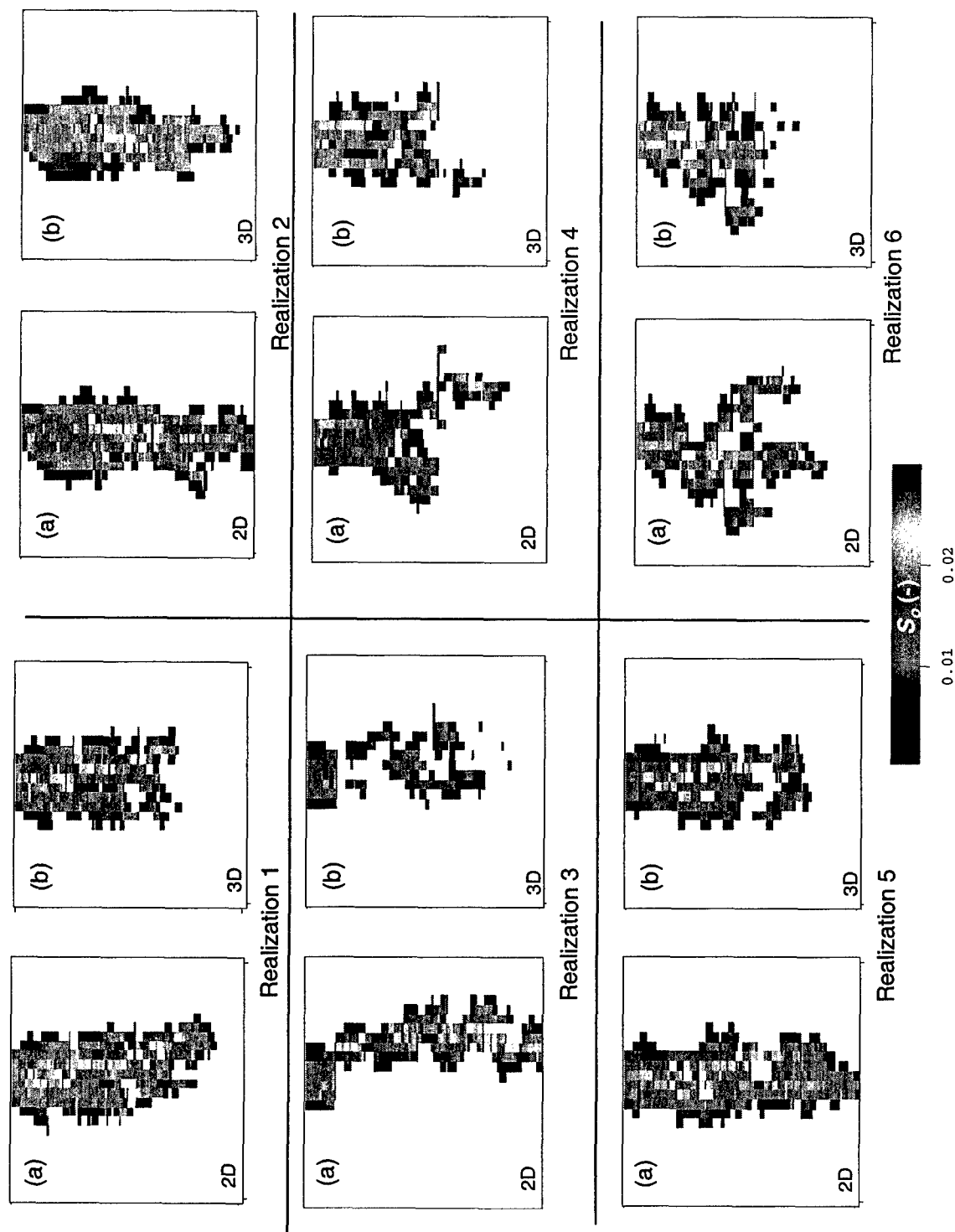


Figure C.1: Saturation profiles simulation in (a) 2D and (b) the same 2D slice extracted from 3D using UTCHEM.

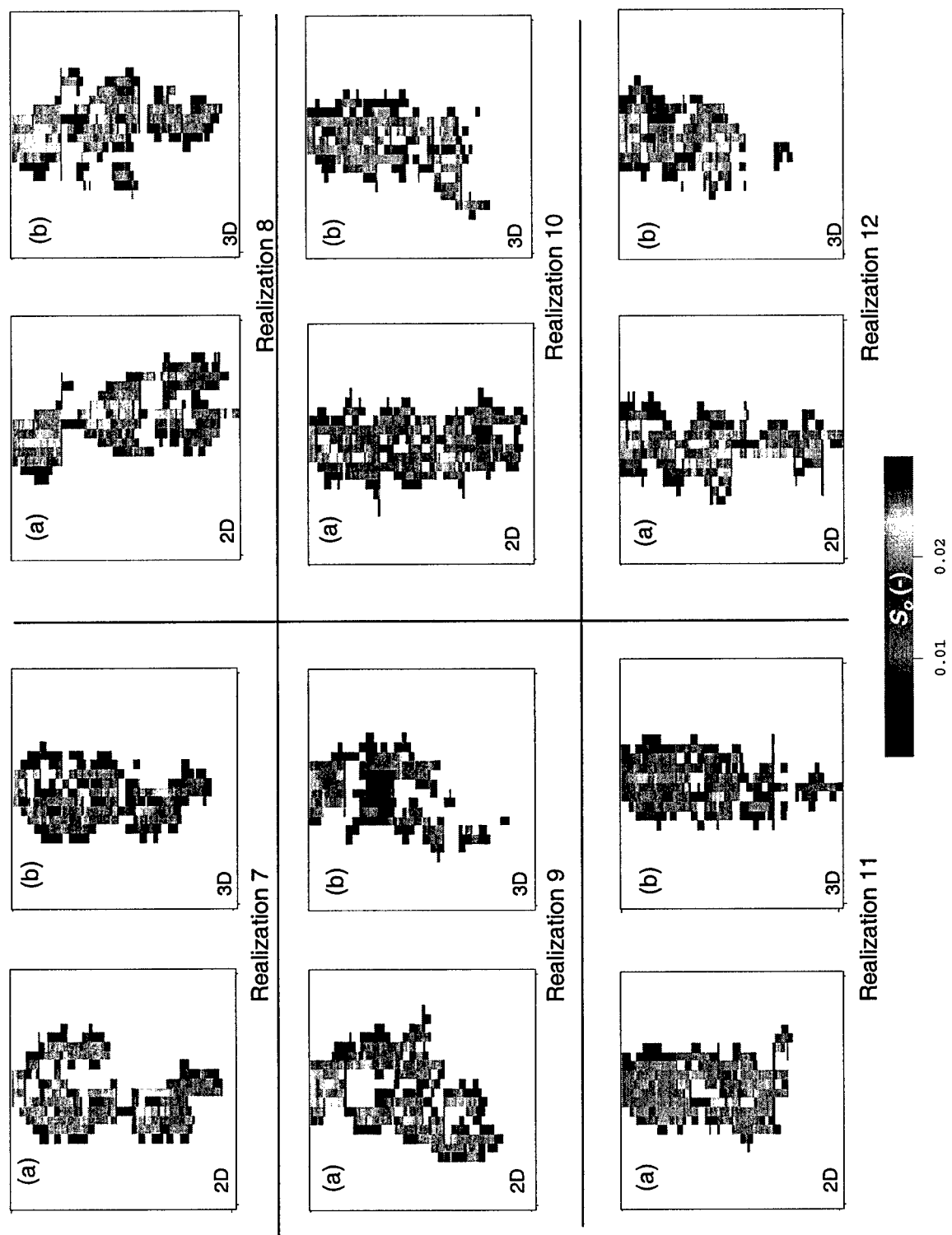


Figure C.1 (cont): Saturation profiles simulation in (a) 2D and (b) the same 2D slice extracted from 3D using UTCHEM.

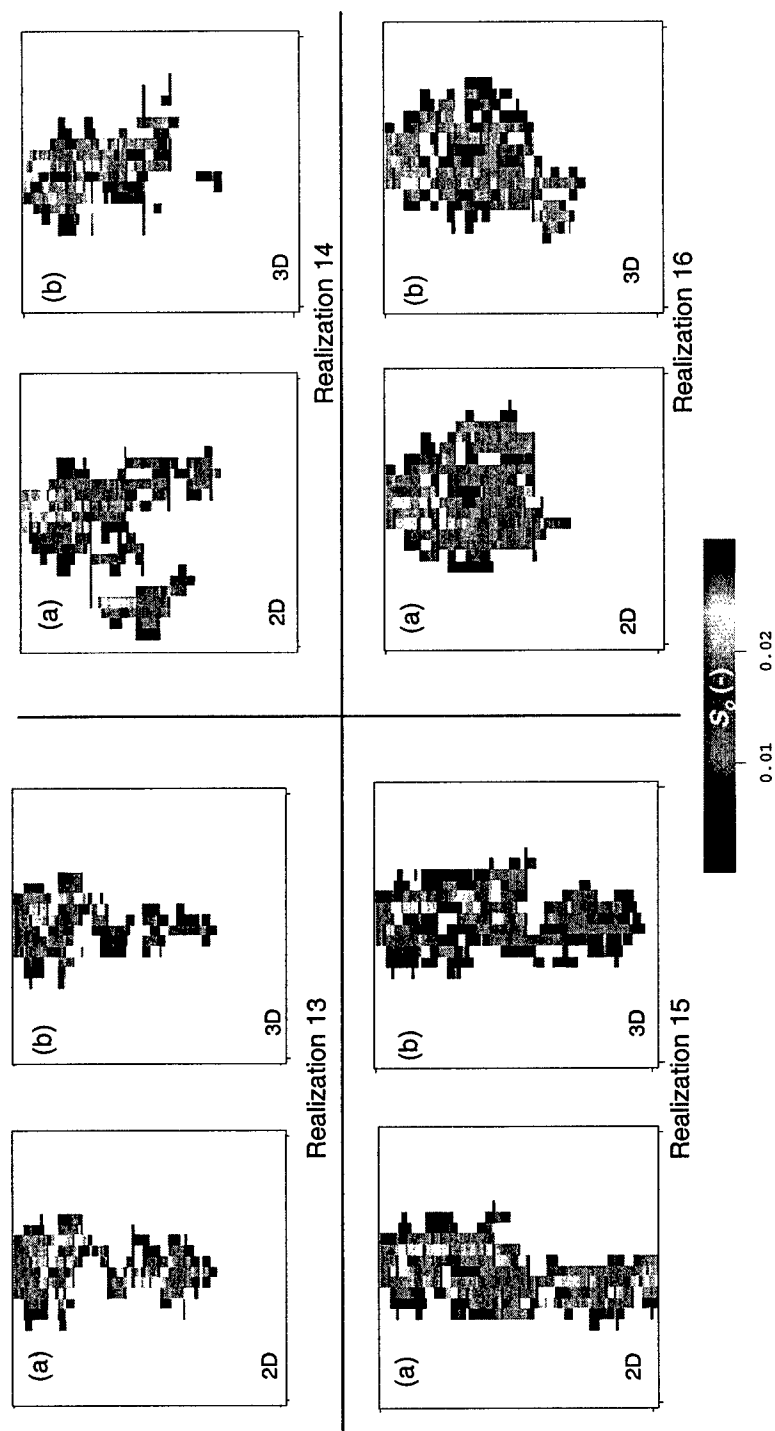


Figure C.1 (cont): Saturation profiles simulation in (a) 2D and (b) the same 2D slice extracted from 3D using UTCHEM.

APPENDIX C

FLUX-AVERAGED CONCENTRATIONS

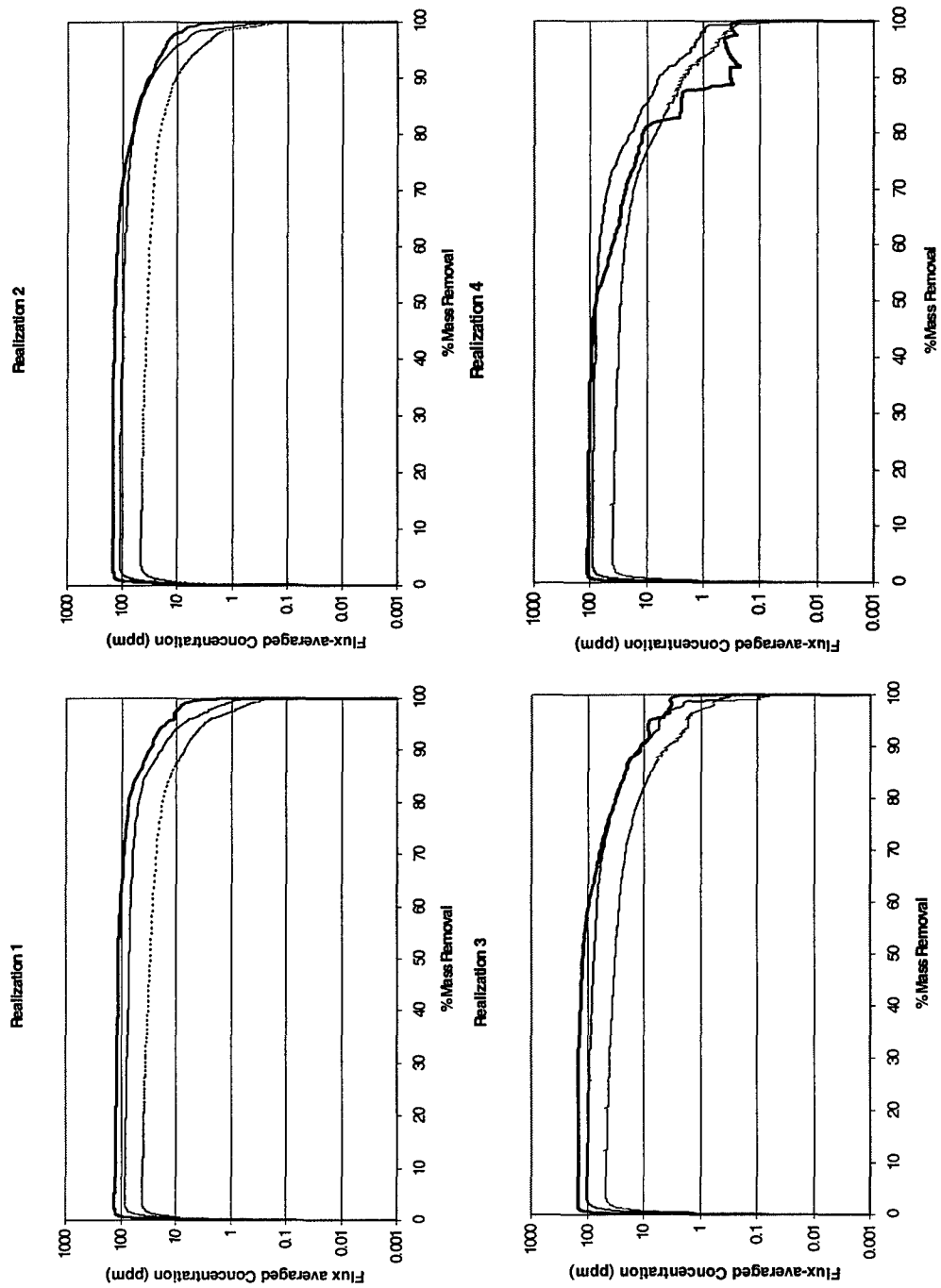


Figure D.1: Flux-averaged concentration curves for all 16 realizations

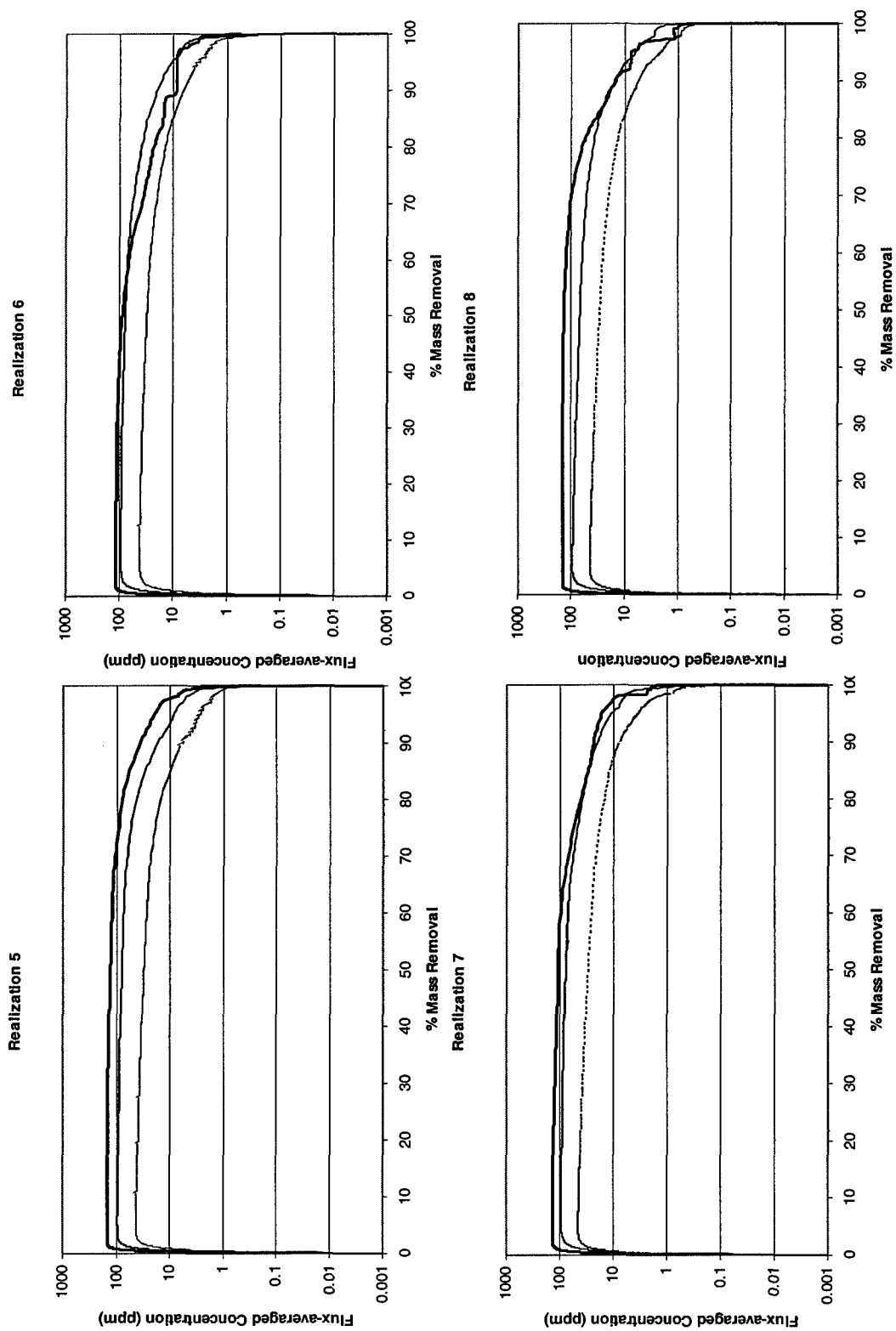


Figure D.1 (cont.): Flux-averaged concentration curves for all 16 realizations

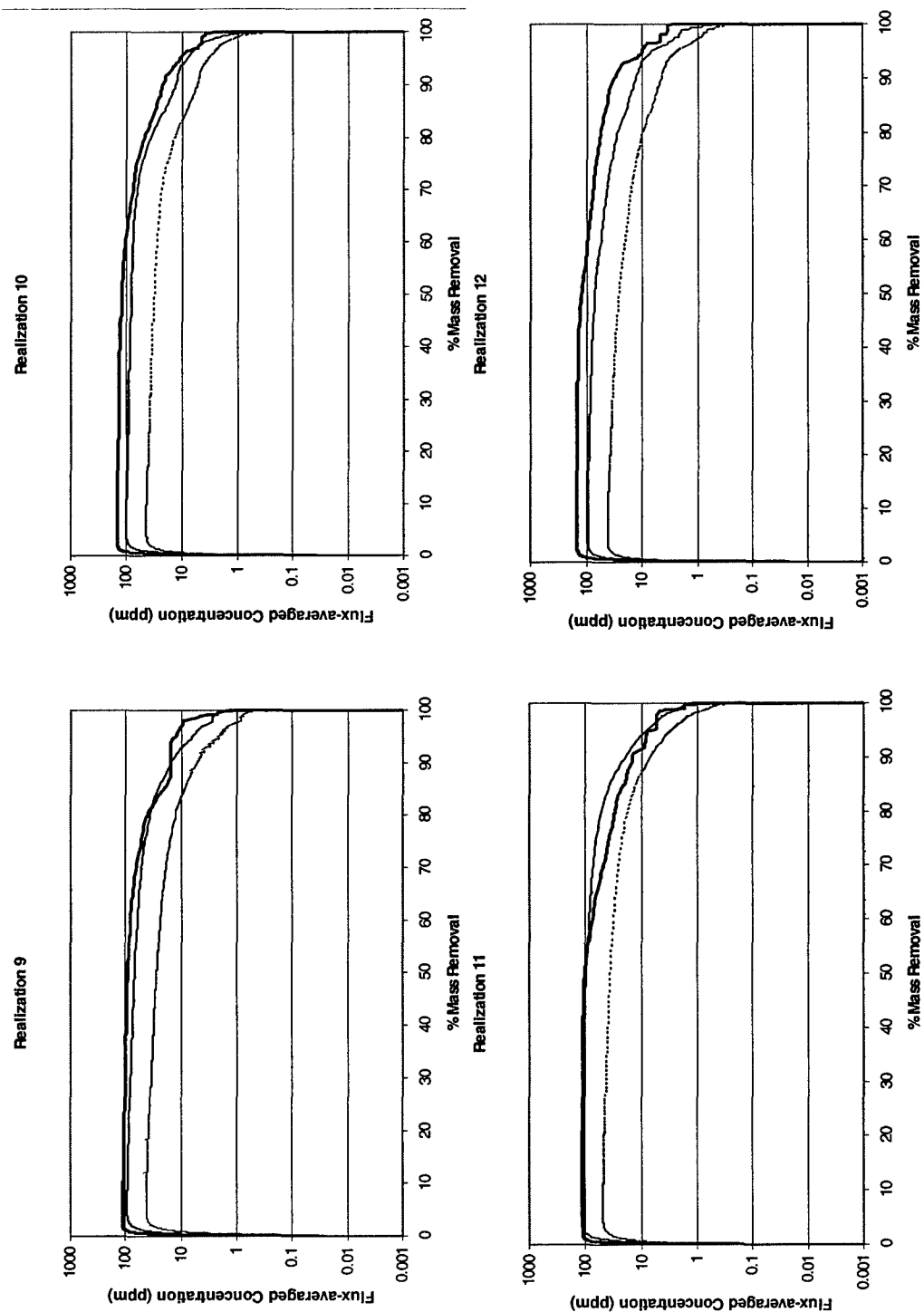


Figure D.1 (cont.): Flux-averaged concentration curves for all 16 realizations

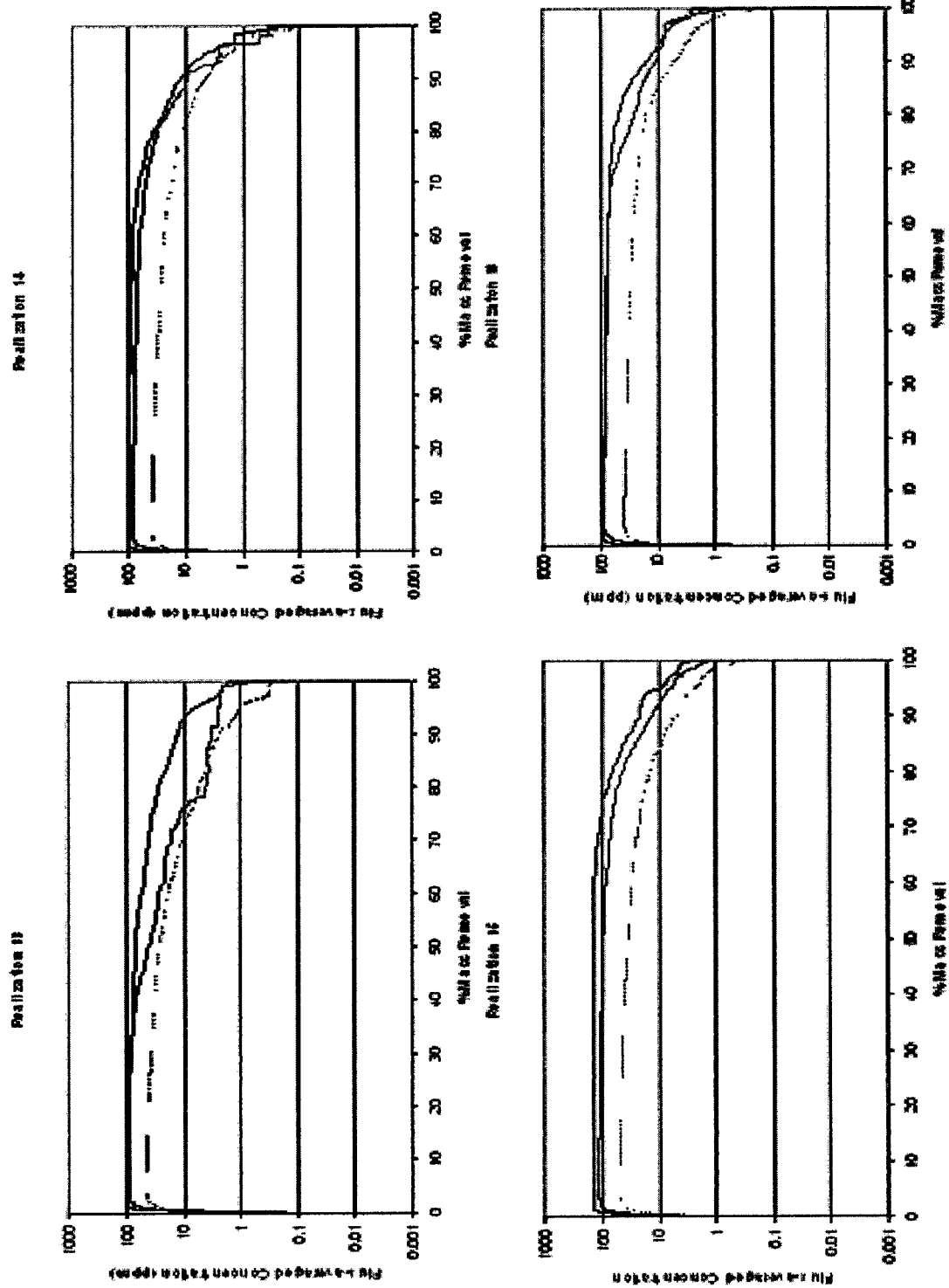


Figure D.1 (cont.) Flux-averaged concentration curves for all 16 realizations

BIBLIOGRAPHY

- Abelson PH. 1990. Volatile contaminants of drinking water. *Science* 247: 141.
- Abriola LM, Pinder GF. 1985a. A multiphase approach to the modeling of porous media contamination by organic compounds 1. Equation development, *Water Resources Research* 21: 11-18.
- Abriola LM, Pinder GF. 1985b. A multiphase approach to the modeling of porous media contamination by organic compounds 2. Numerical Simulation, *Water Resources Research* 21: 19-26.
- Abriola, L. M. 1989. Modeling multiphase migration of organic chemicals in groundwater systems – A review and assessment, *Environmental Health Perspectives*, 83: 117-143.
- Abriola LM, Chen Y-M, Vogel TM. 1991. Investigation and prediction of the biodegradation of benzene, toluene, and xylene (BTX) in sandy aquifer materials. In *Proceedings of the International Hydrology and Water Resources Symposium*, Perth, Australia, 2-4 Oct.1991, p. 429-434.
- Abriola, L.M., K. Rathfelder, S. Yadav, and M. Maiza. 1992. VALOR code version 1.0: a PC code for simulating subsurface immiscible contaminant transport. Final Report, EPRI TR-101018, Electric Power Research Institute, Palo Alto, CA.
- Abriola LM, Rathfelder K. 1993. Mass balance errors in modeling two-phase immiscible flows: causes and remedies, *Advances in Water Resources* 16: 223-239.
- Abriola LM, Dekker TJ, Pennell KD. 1993. Surfactant-Enhanced solubilization of residual dodecane in soil columns. 2. Mathematical modeling, *Environmental Science & Technology* 27: 2341-2351
- Abriola LM, Lang J, Rathfelder K. 1997. Michigan Soil Vapor Extraction Remediation (MISER) Model: A computer program to model soil vapor extraction and bioventing of organic chemicals in unsaturated geological material, EPA/600/R-97/099, pp. 239.
- Abriola LM, Drummond CD, Hahn EJ, Kibbey TCG, Lemke LD, Pennell KD, Petrovskis EA, Ramsburg CA, Rathfelder KM. 2005. A pilot-scale demonstration of surfactant-enhanced PCE solubilization at the Bachman road site: (1) Site characterization and test design. *Environmental Science and Technology* 39: 1178-1790.
- Adamson DT, McDade JM, Hughes JB. 2003. Inoculation of a DNAPL source zone to initiate reductive dechlorination of PCE. *Environmental Science and Technology* 37: 2525-2533.
- Adamson DT, Lyon DY, Hughes JB. 2004. Flux and product distribution during biological treatment of tetrachloroethene dense non-aqueous-phase liquid. *Environmental Science and Technology* 38: 2021-2028.

- Anderson, M. R., R. L. Johnson, and J. F. Pankow. 1992. Dissolution of dense chlorinated solvents into groundwater. 3. Modeling contaminant plumes from fingers and pools of solvent, *Environmental Science and Technology* 26: 901-908.
- Anderson JE, McCarty PL. 1994. Model for treatment of trichloroethylene by methanotrophic biofilms. *Journal of Environmental Engineering* 120: 379-400.
- Anderson JE, McCarty PL. 1997. Transformation yields of chlorinated ethenes by a methanotrophic mixed culture expressing particulate methane monooxygenase. *Applied and Environmental Microbiology* 63: 687-693.
- Aziz CE, Newell CJ, Gonzales AR, Hass P, Clement TP, Sun Y. 1999. *BIOCHLOR Natural Attenuation Decision Support System User's Manual*. Prepared for the Air Force Center for Environmental Excellence, Brooks AFB: San Antonio, TX.
- Bagley, D.M. 1998. Systematic approach for modeling tetrachloroethene biodegradation. *Journal of Environmental Engineering* 124: 1076-1086.
- Ballapragada BS, Stensel HD, Puhakka JA, Ferguson JF. 1997. Effect of hydrogen on reductive dechlorination of chlorinated ethenes. *Environmental Science and Technology* 31: 1728-1734.
- Barry DA, Prommer H, Miller CT, Engesgaard P, Brun A, Zheng C. 2002. Modelling the fate of oxidisable organic contaminants in groundwater. *Advances in Water Resources* 25: 945-983.
- Battistelli, A. 2004. Modeling biodegradation of organic contaminants under multiphase conditions with TMVOCBio. *Vadose Zone Journal* 3: 875-883.
- Baveye P, Valocchi A. 1989. An evaluation of mathematical models of transport of biologically reacting solutes in saturated soils and aquifers. *Water Resources Research* 25: 1413-1421.
- Baehr AL, Corapcioglu MY. 1987. A compositional multiphase model for groundwater contamination by petroleum products, 2. Numerical solution, *Water Resources Research* 23: 201-214.
- Bear, J. 1972, *Dynamics of Fluids in Porous Media*, Elsevier, New York.
- Berglund S. 1997. Aquifer remediation by pumping; a model for stochastic-advective transport with nonaqueous phase liquid dissolution, *Water Resources Research* 33, 399-405.

- Bouwer EJ. 1994. Bioremediation of chlorinated solvents using alternate electron acceptors. In: *In Situ Bioremediation* second edition (Rittmann BE, Seagren E, Wrenn BA, Valocchi AJ, Ray C, Raskin L, eds). New Jersey: Noyes Publication, 149-168.
- Bradford, S.A., L.M. Abriola, and K.M. Rathfelder. 1998. Flow and entrapment of dense nonaqueous phase liquids in physically and chemically heterogeneous aquifer formations, *Advances in Water Resources* 22: 117-132.
- Bradley PM, Chapelle. 1996. Anaerobic mineralization of vinyl chloride in Fe(III)-reducing aquifer sediments. *Environmental Science and Technology* 30: 2084-2086.
- Bradley PM, Landmeyer JE, Dinicola RS. 1998. Anaerobic oxidation of [1,2-¹⁴C]Dichloroethene under MN(IV)-reducing conditions. *Applied and Environmental Microbiology* 64: 1560-1562.
- Bradley PM. 2003. History and ecology of chloroethene biodegradation: A review. *Bioremediation Journal* 7: 81-109.
- Broholm, K., S. Feenstra, and J.A. Cherry. 1999. Solvent release into a sandy aquifer. 1. Overview of source distribution and dissolution behavior, *Environmental Science & Technology* 33: 681-690.
- Broholm K, Feenstra S, Cherry JA. 2005. Solvent release into a sandy aquifer. 2. Estimation of DNAPL mass based on a multiple-component dissolution model, *Environmental Science & Technology* 33: 681-690.
- Brooks RH, Corey AT. 1964. Hydraulic Properties of Porous Media, *Hydrology Papers No. 3*, Colorado State University, Fort Collins, CO.
- Brown CL, Pope GA, Abriola LM, Sepehrnoori K. 1994. Simulation of surfactant-enhanced aquifer remediation, *Water Resources Research* 30: 2959-2977.
- Brusseau ML. 1996. Evaluation of simple methods for estimating contaminant removal by flushing. *Ground Water* 34: 19-22.
- Brusseau ML, Zhang Z, Nelson NT, Cain RB, Tick GR, Oostrom M. 2002. Dissolution of nonuniformly distributed immiscible liquid: Intermediate-scale experiments and mathematical modeling, *Environmental Science & Technology* 36: 1033-1041.
- Burdine HT. 1953. Relative permeability calculations from pore-size distribution data. *Trans. Soc. Pet. Eng. AIME* 198: 71-77.
- Carr CS, Hughes JB. 1998. Enrichment of high-rate PCE dechlorination and comparative study of lactate, methanol, and hydrogen as electron donors to sustain activity. *Environmental Science and Technology* 32: 1817-1824.

Carr CS, Garg S, Hughes JB. 2000. Effect of dechlorinating bacteria on the longevity and composition of PCE-containing nonaqueous phase liquids under equilibrium dissolution conditions. *Environmental Science and Technology* 34: 1088-1094.

Chapelle, F.H. 2001. *Ground-Water Microbiology and Geochemistry*. 2nd ed. New York: Wiley. 424.

Chauhan S, Barbieri P, Wood TK. 1998. Oxidation of trichloroethylene, 1,1-dichloroethylene, and chloroform by toluene/o-xylene monooxygenase from *Pseudomonas stutzeri* OX1. *Applied and Environmental Microbiology* 64: 3023-2024.

Chen Y-M, Abriola LM, Alvarez PJ, Anid PJ, Vogel TM. 1992. Modeling transport and biodegradation of benzene and toluene in sandy aquifer material: comparisons with experimental measurements, *Water Resources Research* 28: 1833-1847.

Cherry JA, Feenstra S, Mackay DM. 1997. Developing rational goals for in situ remedial technologies. In: *Subsurface Restoration* (Ward CH, Cherry JA, Scalf MR, eds). Chelsea, MI: Ann Arbor Press, 75-98.

Chrysikopoulos CV. 1995. Three-dimensional analytical models of contaminant transport from nonaqueous phase liquid pool dissolution in saturated subsurface formations, *Water Resources Research* 31: 1137-1145.

Chrysikopoulos CV, Kim T-J. 2000. Local mass transfer correlations for nonaqueous phase liquid pool dissolution in saturated porous media, *Transport in Porous Media* 38: 167-187.

Chu M, Kitanidis PK, McCarty PL. 2003. Effects of biomass accumulation on microbially enhanced dissolution of a PCE pool: a numerical simulation. *Journal of Contaminant Hydrology* 65: 79-100.

Chu, M., P.K. Kitanidis, and P.L. McCarty. 2004. Possible factors controlling the effectiveness of bioenhanced dissolution of non-aqueous phase tetrachloroethene. *Advances in Water Resources* 27: 601-615.

Cirpka, O.A. 1995. *Influence of hydraulic aquifer properties on reductive dechlorination of tetrachloroethylene*, in *Bioremediation of Chlorinated Solvents*, R.E. Hinchee, A. Leeson, and L. Semprini, Editors. Battelle Press: Columbus, OH. p. 25-34.

Clapp, L.W., M.J. Semmens, P.J. Novak, and R.M. Hozalski. 2004. Model for in situ perchloroethene dechlorination via membrane-delivered hydrogen. *Journal of Environmental Engineering* 130: 1367-1381.

Clement TP, Hooker BS, Skeen RS. 1996. Macroscopic models for predicting changes in saturated porous media properties caused by microbial growth. *Ground Water* 34: 934-942.

Clement TB, Johnson CD, Sun Y, Klecka GM, Bartlett C. 1998. Natural attenuation of chlorinated ethene compounds: model development and field-scale application at the Dover site. *Journal of Contaminant Hydrology*, 42: 113-140.

Clement TP. 2001. Generalized solution to multispecies transport equations coupled with a first-order reaction network. *Water Resources Research* 37: 157-163.

Cole JR, Fathepure BZ, Tiedje JM. 1995. Tetrachloroethene and 3-chlorobenzoate activities are co-induced in *Desulfomonile tiedjei* DCB-1. *Biodegradation* 6: 167-172.

Coleman NV, Mattes TE, Gossett JM, Spain JC. 2002a. Biodegradation of *cis*-Dichloroethene as the sole carbon source by a β -Proteobacterium. *Applied and Environmental Microbiology* 68: 2726-2730.

Coleman NV, Mattes TE, Gossett JM, Spain JC. 2002b. Phylogenetic and kinetic diversity of aerobic vinyl chloride-assimilating bacteria from contaminated sites. *Applied and Environmental Microbiology* 68: 6162-6171.

Cope N, Hughes JB. 2001. Biologically-enhanced removal of PCE from NAPL source zones. *Environmental Science and Technology* 35: 2014-2021.

Corapcioglu MY, Baehr AL. 1987. A compositional multiphase model for groundwater contamination by petroleum products, 1. Theoretical considerations, *Water Resources Research* 23: 191-200.

Corapcioglu Y, Hossain MA, Hossain A. 1991. Methanogenic biotransformation of chlorinated hydrocarbons in ground water. *Journal of Environmental Engineering* 117: 47-65.

Cupples AM, Spormann AM, McCarty PL. 2003. Growth of *Dehalococcoides*-like microorganism on vinyl chloride and *cis*-dichloroethene as electron acceptors as determined by competitive PCR. *Applied and Environmental Microbiology* 69: 953-959.

Cupples AM, Spormann AM, McCarty PL. 2004. Vinyl chloride and *cis*-dichloroethene dechlorination kinetics and microorganism growth under substrate limiting conditions. *Environmental Science and Technology* 38: 1102-1107.

de Blanc PC, Brown CL, McKinney DC, Speitel GE, Pope GA. 1997. Surfactant flushing and bioremediation – striking a balance. In: *In Situ and On-Site Bioremediation: Volume 2* (Alleman BC, Leeson A, eds.). Columbus, Ohio: Battelle Press, 565.

Dekker, T.J. 1996. An assessment of the effects of field-scale formation heterogeneity on surfactant-enhanced aquifer remediation, Doctoral Dissertation, University of Michigan, Ann Arbor, MI.

Dekker TJ, Abriola LM. 2000a. The influence of field-scale heterogeneity on the infiltration and entrapment of dense nonaqueous phase liquids in saturated formation. *Journal of Contaminant Hydrology* 42: 187-218.

Dekker, T.J. and L.M. Abriola. 2000b. The influence of field-scale heterogeneity on the surfactant-enhanced remediation of entrapped nonaqueous phase liquids, *Journal of Contaminant Hydrology* 42: 219-251.

Dela Barre, B.K., T.C Harmon, and C.V. Chrysikopoulos. 2002. Measuring and modeling the dissolution of nonideally shaped dense nonaqueous phase liquid pools in saturated porous media, *Water Resources Research* 38: doi: 10.1029/2001WR000444.

Delshad, M., G.A. Pope, and K. Sepehrnoori. 1996. A compositional simulator for modeling surfactant enhanced aquifer remediation, 1 formulation, *Journal of Contaminant Hydrology* 23: 303-327.

Delshad M, Yeh L, Holzmer FJ. 2000. Design of the surfactant flood at Camp Lejeune, in *Treating Dense Nonaqueous Phase Liquids (DNAPLs): Remediation of Chlorinated and Recalcitrant Compounds*, edited by G.B. Wickramanayake, A.R. Gavaskar, N. Gupta, Batelle Press, Columbus, OH, 203-210.

Demond AH, Rathfelder K, Abriola LM. 1996. Simulation of organic liquid flow in porous media using estimated and measured transport properties, *Journal of Contaminant Hydrology* 22: 223-239.

Deutsch CV, Journel AG. 1998. *GSLIB Geostatistical Software Library and User's Guide*, second edition, Oxford University Press, New York.

Devore JL. 1995. *Probability and Statistics for Engineering and the Sciences*, fourth edition, Wadsworth Publishing Company, Belmont, CA.

DiStefano TD, Gossett JM, Zinder SH. 1992. Hydrogen as an electron donor for dechlorination of tetrachloroethene by an anaerobic mixed culture. *Applied and Environmental Microbiology* 58: 3622-3629.

Dupin HJ, McCarty PL. 2000. Impact of colony morphologies and disinfection on biological clogging in porous media. *Environmental Science & Technology* 34: 1513-1520.

Edwards M.G, Delshad M, Pope GA, Sepehrnoori K. 1999. A high-resolution method coupled with local grid refinement for three-dimensional aquifer remediation, *In Situ* 23: 333-377.

Einarson, M.D. and D.M. Mackay. 2001. Predicting impacts of ground water contamination. *Environmental Science & Technology* 35: 67A-73A.

Ellis DE, Lutz EJ, Odom JM, Buchanan Jr. RJ, Bartlett CL, Lee MD, et al. 2000. Bioaugmentation for accelerated in situ anaerobic bioremediation. *Environmental Science and Technology* 34: 2254-2260.

Ensign SA, Hyman MR, Arp DJ. 1992. Cometabolic degradation of chlorinated alkenes by alkene monooxygenase in a propylene-grown *Xanthobacter* strain. *Applied and Environmental Microbiology* 58: 3038-3046.

Environmental Protection Agency. 1986. *Background document for the ground-water screening procedure to support 40 CFR Part 269: Land disposal*, EPA/530-SW-86-047, US EPA, Washington, DC.

Environmental Protection Agency. 1990. Laboratory investigation of residual liquid organics from spills, leaks, and disposal of hazardous wastes in groundwater. EPA/600/6-90/004. Washington DC: U.S. Environmental Protection Agency.

Environmental Protection Agency. 2003. *The DNAPL remediation challenge: Is there a case for source depletion?* Vol. EPA 600/R-03/143. Washington D.C.: US Environmental Protection Agency.

Essaid HI, Hess KM. 1993. Monte Carlo simulations of multiphase flow incorporating spatial variability of hydraulic properties. *Ground Water* 31: 123-134.

Essaid HI, Herkelrath WN, Hess KM. 1993. Simulation of fluid distributions observed at a crude oil spill site incorporating hysteresis, oil entrapment, and spatial variability of hydraulic properties. *Water Resources Research* 29: 1753-1770.

Falta RW, Pruess K, Javandel I, Witherspoon PA. 1992. Numerical modeling of steam injection for the removal of nonaqueous phase liquids from the subsurface 1. Numerical formulations, *Water Resources Research* 28: 433-449.

Fathepure BZ, Boyd SA. 1988a. Dependence of tetrachloroethylene dechlorination on methanogenic substrate consumption by *Methanosarcina* SP Strain DCM. *Applied and Environmental Microbiology* 54: 2976-2980.

Fathepure BZ, Boyd SA. 1988b. Reductive dechlorination of perchloroethylene and the role of methanogens. *FEMS Microbiology Letters* 49: 149-156.

Faust CR. 1985. Transport of immiscible fluids within and below the unsaturated zone: A numerical model, *Water Resources Research* 21: 587-596.

Faust, C.R., J.H. Guswa, and J.W. Mercer. 1989. Simulation of three-dimensional flow of immiscible fluids within and below the unsaturated zone, *Water Resources Research* 25: 2449-2464.

Feenstra, S., J. A. Cherry, and B. L. Parker. 1996. Conceptual models for the behavior of nonaqueous phase liquids (DNAPLs) in the subsurface, in *Dense Chlorinated Solvents and Other DNAPLs in Groundwater*, edited by J. F. Pankow and J.A. Cherry, Waterloo Press, Portland, OR, 53-88.

Fennell DE, Gossett JM, Zinder SH. 1997. Comparison of butyric acid, ethanol, lactic acid, and propionic acid as hydrogen donors for the reductive dechlorination of tetrachloroethene. *Environmental Science and Technology* 31: 918-926.

Fennell DE, Gossett JM. 1998. Modeling the production of and competition for hydrogen in a dechlorinating culture. *Environmental Science and Technology* 32: 2450-2460.

Flynn, S.J., F.E. Loffler, and J.M. Tiedje. 2000. Microbial community changes associated with a shift from reductive dechlorination of PCE to reductive dechlorination of cis-DCE and VC. *Environmental Science and Technology* 34: p. 1056-1061.

Fountain JC, Waddell-Sheets C, Lagowski A, Taylor C, Frazier D, Byrne M. 1995. Enhanced removal of dense nonaqueous-phase liquids using surfactants: capabilities and limitations from field trials. In: *Surfactant-enhanced subsurface remediation: Emerging technologies* (Sabatini DA, Knox RC, Harwell JH, eds). ACS Symposium Series, No. 594 Washington, D.C.: American Chemical Society, 177-190.

Freeze GA, Fountain JC, Pope GA, Jackson RE. 1995. Modeling the surfactant-enhanced remediation of perchloroethylene at the Borden test site using the UTCHEM compositional simulator. In *Surfactant-Enhanced Subsurface Remediation*, edited by: D.A. Sabatini, R.C. Knox, and J.H. Harwell, Washington DC, p. 191-200.

Freeze RA, McWhorter DB. 1997. A framework for assessing risk reduction due to DNAPL mass removal from low-permeability soils. *Ground Water* 35: 111-123.

Freeze RA. 2000. *The Environmental Pendulum*. University of California Press.

Fried JJ, Muntzer P, Zilliox L. 1979. Ground-water pollution by transfer of oil hydrocarbons, *Ground Water* 17: 586-594.

Frind EO, Molson JW, Schirmer M, Guiger N. 1999. Dissolution and mass transfer of multiple organics under field conditions: The Borden emplaced source, *Water Resources Research* 35: 683-694.

Gallo C, Hassanizadeh SM. 2000. Influence of biodegradation on NAPL flow and dissolution in groundwater. in XIII International Conference on Computational Methods in Water Resources. Alberta, Canada.

Gallo C, Manzini G. 2001. A fully coupled numerical model for two-phase flow with contaminant transport and biodegradation kinetics. *Communication in Numerical Methods in Engineering* 17: 325-336.

Gallo C, Hassanizadeh SM. 2002. Modeling NAPL dissolution and biodegradation interactions: effect of toxicity and biomass growth limitations. in XIV International Conference on Computational Methods in Water Resources. Delft, The Netherlands.

Garant H, Lynd L. 1998. Applicability of competitive and noncompetitive kinetics to the reductive dechlorination of chlorinated ethenes. *Biotechnology and Bioengineering* 57: p. 751-755.

Geller JT, Hunt JR. 1993. Mass transfer from nonaqueous phase organic liquids in water-saturated porous media, *Water Resources Research* 29: 833-845

Glass RJ, Conrad SH, Peplinski W. 2000. Gravity-destabilized nonwetting phase invasion in macroheterogeneous porous media: Experimental observations of invasion dynamics and scale analysis, *Water Resources Research* 36: 3121-3137.

Goovaerts P. 1997. *Geostatistics for Natural Resources Evaluation*, Oxford University Press, New York.

Guarnaccia I, Pinder G. 1998. On the importance of dimensionality in the simulation of Dense Non-Aqueous Liquid migration in the subsurface. In *Soil and Aquifer Pollution Non-Aqueous Phase Liquids-Contamination and Reclamation*, edited by H. Rubin, N. Narkis, and J. Carberry, Springer-Verlag, New York, 209-219.

Gupta S, Seagren EA. 2005. Comparison of bioenhancement of nonaqueous phase liquid pool dissolution with first- and zero-order biokinetics. *Journal of Environmental Engineering* 131: p. 165-169.

Hammond GE, Valocchi AJ, Lichtner PC. 2005. Application of Jacobian-free Newton-Krylov with physics-based preconditioning to biogeochemical transport. *Advances in Water Resources* 28: 359-376.

Hanselman D, Littlefield B. 2001. *Mastering Matlab 6, A comprehensive tutorial and reference*. Prentice-Hall: New Jersey.

Hartmans S, DeBont JAM, Tramper J, Luyben KCAM. 1985. Bacterial-degradation of vinyl-chloride. *Biotechnology Letters* 7: 383-388.

Hartmans S, deBont JA. 1992. Aerobic vinyl chloride metabolism in *Mycobacterium aurum* L1. *Applied and Environmental Microbiology* 58: 1220-1226.

Haston ZC, McCarty PL. 1999. Chlorinated ethene half-velocity coefficients (K_s) for reductive dehalogenation. *Environmental Science and Technology* 33: 223-226.

Haverkamp R, Parlange JY. 1986. Predicting the water-retention curve from particle-size distributions: 1. Sandy soils without organic matter, *Soil Science* 142, 325-339.

He J, Sung Y, Dollhopf ME, Fathepure BZ, Tiedje JM, Löffler FE. 2002. Acetate versus hydrogen as direct electron donors to stimulate the microbial reductive dechlorination process at chloroethene-contaminated sites. *Environmental Science and Technology* 36: 3945-3952.

He J, Ritalahti KM, Aiello MR, Löffler FE. 2003a. Complete detoxification of vinyl chloride by an anaerobic enrichment culture and identification of the reductively dechlorinating population as a *Dehalococcoides* species. *Applied and Environmental Microbiology* 69: 996-1003.

He J, Ritalahti KM, Yang K-L, Koenigsberg SS, Löffler FE. 2003b. Detoxification of vinyl chloride to ethene coupled to growth of an anaerobic bacterium. *Nature* 243: 62-65.

Hendrickson ER, Payne JA, Young RM, Starr MG, Perry MP, Fahnestock S, et al. 2002. Molecular analysis of *Dehalococcoides* 16S ribosomal DNA from chloroethene-contaminated sites throughout North America and Europe. *Applied and Environmental Microbiology* 68: 485-495.

Henry SM, Hardcastle CH, Warner, SD. 2003. Chlorinated solvent and DNAPL remediation: An overview of physical, chemical, and biological processes. In: Chlorinated Solvent and DNAPL Remediation: Innovative Strategies for Subsurface Cleanup (Henry SM, Warner SD, eds). ACS Symposium Series, No. 837. Washington, D.C.:American Chemical Society, 1-20.

Higgins IJ, Best DJ, Hammond RC. 1980. New findings in methane-utilizing bacteria highlight their importance in the biosphere and their commercial potential. *Nature* 286: 561-564.

Holliger C, Wohlfarth G, Diekert G. 1998. Reductive dechlorination in the energy metabolism of anaerobic bacteria. *FEMS Microbiological Reviews* 22: 383-398.

Hollinger C, Schraa G, Stamms AJ, Zhender AJBA. 1993. Highly purified enrichment culture couples the reductive dechlorination of tetrachloroethylene to growth. *Applied and Environmental Microbiology* 59: 2991-2997.

Hopkins GD, Semprini L, McCarty PL. 1993. Microcosm and in situ field studies of enhanced biotransformation of trichloroethylene by phenol-utilizing microorganisms. *Applied and Environmental Microbiology* 59: 2277-2285.

Horvath, A.L. 1982. *Halogenated Hydrocarbons Solubility – Miscibility with Water*, Marcel Dekker, New York.

Hossain MA, Corapcioglu MY. 1994. Anaerobic biotransformation and transport of chlorinated hydrocarbons in groundwater. *Bioremediation of Chlorinated and Polycyclic Aromatic Hydrocarbon Compounds*, edited by R.E. Hinchee, A. Leeson, L. Semprini, and S.K. Ong, CRC Press, Boca Raton, FL, p. 86-98.

Hutson, S.S., N.L. Barber, J.F. Kenny, K.S. Linsey, D.S. Lumia, and M.A. Maupin. 2004. Estimated use of water in the United States in 2000. USGS Circular 1286, U.S. Geological Survey.

Imhoff, P.T., P.R. Jaffe, and G.F. Pinder. 1994. An experimental study of complete dissolution of a nonaqueous phase liquid in saturated porous media, *Water Resources Research* 30: 307-320.

Janssen DB, Oppentocht JE, Poelarends GJ. 2001. Microbial dehalogenation. *Current Opinions in Biotechnology* 12: 254-258.

Jawitz JW, Sillan RK, Annable MD, Rao PSC, Warner K. 2000. In-situ alcohol flushing of a DNAPL source zone at a dry cleaner site. *Environmental Science and Technology* 34: 3722-3729.

Johnson RL, Pankow JF. 1992. Dissolution of dense chlorinated solvents into groundwater. 2. Source functions for pools of solvent. *Environmental Science and Technology* 26: 3896-3901.

Journel, A.G. and C.J. Huijbregts. 1978. *Mining Geostatistics*, Academic Press: New York.

Kaluarachchi JJ, Parker JC. 1992. Multiphase flow with a simplified model for oil entrapment, *Transport in Porous Media* 7: 1-14.

Kengen SWM, Breidenbach GC, Felske A, Stams AJM, Schraa G, De Vos, WM. 1999. Reductive dechlorination of tetrachloroethene to *cis*-1,2-dichloroethene by a thermophilic anaerobic enrichment culture. *Applied and Environmental Microbiology* 65: 2312-2316.

Kibbey TCG, Pennell KD, Hayes KF. 2004. Application of sieve-tray air strippers to the treatment of surfactant-containing wastewaters. *AIChE Journal* 47: 1461-1470.

Kim T-J, Chrysikopoulos CV. 1999. Mass transfer correlations for nonaqueous phase liquid pool dissolution in saturated porous media, *Water Resources Research* 35: 449-460.

Krumholtz LR, Sharp R, Fishbain SS. 1996. A freshwater anaerobe coupling acetate oxidation to tetrachloroethylene dehalogenation. *Applied and Environmental Microbiology* 62: 4108-4113.

Kueper BH, Frind EO. 1991. Two-phase flow in heterogeneous porous media 2. Model Application, *Water Resources Research* 27: 1059-1070.

Kueper, B.H., D. Redman, R.C. Starr, S. Reitsma, and M. Mah. 1993. A field experiment to study the behavior of tetrachloroethylene below the water table: spatial distribution of residual and pooled DNAPL, *Ground Water* 31: 756-766.

Kueper, B.H. and J.I. Gerhard. 1995. Variability of point source infiltration rates for two-phase flow in heterogeneous porous media, *Water Resources Research* 31: 2971-2980.

Land CS. 1968. Calculation of imbibition relative permeability for two- and three-phase flow from rock properties, *Trans. Am Inst. Min. Metall. Pet. Eng.* 243: 149-156.

Lang JR. 2000. Self adaptive hierarchic finite element solution of multiphase/multicomponent transport with microbial growth and degradation. Doctoral Dissertation. The University of Michigan, Ann Arbor, MI.

Lee I-S, Bae J-H, Yang Y, McCarty PL. 2004. Simulated and experimental evaluation of factors affecting the rate and extent of reductive dehalogenation of chloroethenes with glucose. *Journal of Contaminant Hydrology* 74: p. 313-331.

Lemke LD, Abriola LM. 2003. Predicting DNAPL entrapment and recovery: the influence of hydraulic property correlation. *Stochastic Environmental Research and Risk Assessment* 17: 408-418.

Lemke LD, Abriola LM, Goovaerts P. 2004a. DNAPL source zone characterization: Influence of hydraulic property correlation on predictions of DNAPL infiltration and entrapment. *Water Resources Research* 40: W01511, doi: 10.1029/2003WR001980.

Lemke LD, Abriola LM, Lang JR. 2004b. DNAPL source zone remediation: Influence of source zone architecture on predictions of DNAPL recovery and contaminant mass flux. *Water Resources Research* 40, W12417, doi: 10.1029/2004WR003061.

Lenhard RJ, Parker JC, Kaluarachchi JJ. 1991. Comparing simulated and experimental hysteretic two-phase transient fluid flow phenomena, *Water Resources Research* 27: 2113-2124.

Lenhard RJ, Oostrom M, White MD. 1995. Modeling fluid flow and transport in variably saturated porous media with the STOMP simulator. 1. Verification and validation exercises, *Advances in Water Resources* 18: 365-373.

Lendvay JM, Löffler FE, Dollhopf M, Aiello MR, Daniels G, Fathepure BZ, et al. 2003. Bioreactive barriers: A comparison of bioaugmentation and biostimulation for chlorinated solvent remediation. *Environmental Science and Technology* 37: 1422-1431.

Lensing HJ. 1998. Modeling of microbially mediated processes in the subsurface – an evaluation of several modeling concepts. In *Computational methods in contamination and remediation of water resources*, edited by: V.N. Brganos, G.P. Karatzas, A.C. Payatakes C.A. Brebbia, W.G. Gray, G.F. Pinder, Computational Mechanics Publications, Boston, MA, p. 279-286.

Leverett, M.C. 1941: Capillary behavior in porous solids. *Trans. Am. Inst. Min. Metall. Eng. Pet. Eng. Div.* 142: 152-169.

Löffler FE, Sanford RA, Tiedje JM. 1996. Initial characterization of a reductive dehalogenase from *Desulfitobacterium chlororespirans* Co23. *Applied and Environmental Microbiology* 62: 3809-3813.

Löffler FE, Tiedje JM, Sanford RA. 1999. Fraction of electrons consumed in electron acceptor reduction and hydrogen thresholds as indicators of halorespiratory physiology. *Applied and Environmental Microbiology* 65: 4049-4056.

Löffler FE, Sun Q, Li J, Tiedje JM. 2000. 16S rRNA gene-based detection of tetrachloroethene-dechlorinating *Desulfuromonas* and *Dehalococcoides* species. *Applied and Environmental Microbiology* 66: 1369-1374.

Löffler FE, Cole JR, Ritalahti KM, Tiedje JM. 2003. Diversity of dechlorinating bacteria. In *Dehalogenation: Microbial Processes and Environmental Applications* (Häggblom MM, Bossert ID, eds). New York: Kluwer Academic, 53-87.

Logan, B.E. 1999. *Environmental Transport Processes*. New York: John Wiley & Sons.

Londergan JT, Meinardus HW, Mariner PE, Jackson RE, Brown CL, Dwarakanath V, Pope GA, Ginn JS, Taffinder S. 2001. DNAPL removal from a heterogeneous alluvial aquifer by surfactant-enhanced aquifer remediation. *Ground Water Monitoring and Remediation* 21(4):57-67.

MacDonald TR, Kitanidis PK, McCarty PL, Roberts PV. 1999. Mass-transfer limitations for macroscale bioremediation modeling and implications on aquifer clogging. *Ground Water* 37: 523-530.

Mackay DM, Cherry JA. 1989. Groundwater contamination: pump-and-treat remediation. *Environmental Science and Technology* 23: 630-636.

Mackinnon RJ, Schimmel KA, Loehr CA, Best JF, Wolfram JH. 1997. Scaling in situ bioremediation problems by application of multiphase, multicomponent transport theory. *Chemical Engineering Communications* 158: 123-156.

- Malliard J, Schumacher W, Vazquez F, Regeared C, Hagen WR, Hollinger C. 2003. Characterization of the coronoid iron-sulfur protein tetrachloroethene reductive dehalogenase of *Dehalobacter restrictus*. *Applied and Environmental Microbiology* 69: 4628-4638.
- Major D, McMaster ML, Cox EE, Edwards EA, Dworatzek SM, Hendrickson ER, et al. 2002. Field demonstration of successful bioaugmentation to achieve dechlorination of tetrachloroethene to ethane. *Environmental Science and Technology* 36: 5106-5116.
- Major D, Edwards E, McCarty P, Gossett J, Hendrickson E, Löffler F, et al. 2003. Discussion of Environment vs. bacteria or let's play, 'name that bacteria.' *Ground Water Monitoring and Remediation* 23: 32-48.
- Malone DR, Kao C-M, Borden RC. 1993. Dissolution and bioremediation of nonaqueous phase hydrocarbons: model development and laboratory evaluation. *Water Resources Research* 29: 2203-2213.
- Martel R, Gelinas PJ, Saumure L. 1998. Aquifer washing by micellar solutions: 3 Field test at the Thouin Sand Pit (L'Assomption, Quebec, Canada). *Journal of Contaminant Hydrology* 30: 33-48.
- Maymo-Gatell X, Chien Y-t, Gossett JM, Zinder SH. 1997. Isolation of a bacterium that reductively dechlorinates tetrachloroethene to ethene. *Science* 276: 1568-1571.
- Maymo-Gatell X, Nijenhuis I, Zinder SH. 2001. Reductive dechlorination of *cis*-1,2-dichloroethene and vinyl chloride by "*Dehalococcoides ethenogenes*." *Environmental Science and Technology* 35: 516-521.
- Mayer AS, Miller CT. 1996. The influence of mass transfer characteristics and porous media heterogeneity on nonaqueous phase dissolution. *Water Resources Research* 32: 1551-1568.
- McCarty PL, Semprini L. 1994. Groundwater treatment for chlorinated solvents. In: *In situ bioremediation* second edition (Rittmann BE, Seagran E, Wrenn BA, Valocchi AJ, Ray C, Raskin L, eds). New Jersey: Noyes Publication, 87-110.
- McDonald MG, Harbaugh AW. 1988. A modular three-dimensional finite difference groundwater flow model, in *Modeling Techniques, Techniques Water Resour. Invest. U.S. Geol. Surv.*, book 6.
- McGuire T, Hughes JB. 2003. Effects of surfactant on the dechlorination of chlorinated ethenes. *Environmental Toxicology and Chemistry* 22: 2630-2638.
- Mercer JW, Cohen RM. 1990. A review of immiscible fluids in the subsurface: properties, models, characterization and remediation. *Journal of Contaminant Hydrology* 6: 107-163.

- Miller CT, Poirier-McNeill MM, Mayer AS. 1990. Dissolution of trapped nonaqueous phase liquids: Mass transfer characteristics, *Water Resources Research* 26: 2783-2796.
- Miller CT, Christakos G, Imhoff PT, McBride JF, Pedit JA, Trangenstein JA. 1998. Multiphase flow and transport modeling in heterogeneous porous media: challenges and approaches, *Advances in Water Resources* 21: 77-120.
- Millington RJ, Quirk JP. 1961. Permeability of porous media. *Transactions of the Faraday Society* 57: 1200-1207.
- Mohamed M.M, Hatfield K. 2005. Modeling microbial-mediated reduction in batch reactors. *Chemosphere* 59: 1207-1217.
- Molz FJ, Widdowson MA, Benefield LD. 1986. Simulation of microbial growth dynamics coupled to nutrient and oxygen transport in porous media. *Water Resources Research* 22: 1207-1216.
- Mravik SC, Sillan RK, Wood AL, Sewell GW. 2003. Field evaluation of the solvent extraction residual biotreatment technology. *Environmental Science and Technology* 37: 5040-5049.
- Mukherji S, Weber WJ Jr. 2001. Mass transfer effects on microbial uptake of naphthalene from complex NAPLs. *Biotechnology and Bioengineering* 60: 750-760.
- Nambi IM, Powers SE. 2000. NAPL dissolution in heterogeneous systems: an experimental investigation in a simple heterogeneous system, *Journal of Contaminant Hydrology* 44: 161-184.
- Nambi IM, Powers SE. 2003. Mass transfer correlations for nonaqueous phase liquid dissolution from regions with high initial saturations, *Water Resources Research* 39: 1030, doi:10.1029/2001WR000667.
- National Research Council (NRC). 2004. *Contaminants in the Subsurface: Assessment and Remediation*. Washington, D.C.: National Academy Press.
- Nielsen RB, Keasling JD. 1999. Reductive dechlorination of chlorinated ethene DNAPLS by a culture enriched from contaminated groundwater. *Biotechnology and Bioengineering* 62: 160-165.
- Odenchantz JE, Valocchi AJ, Rittmann BE. 1990. *Modeling solute transport with different biodegradation kinetics*. in *Proceedings of Petroleum Hydrocarbons and Organic Chemicals in Groundwater: Prevention, Detection, and Restoration*. 1990: National Water Well Association and American Petroleum Institute.

- Oostrom M, Hofstee C, Walker RC, Dane JH. 1999. Movement and remediation of trichloroethylene in a saturated heterogeneous porous medium 2. Pump-and-treat and surfactant flushing. *Journal of Contaminant Hydrology* 37: 179-197.
- Osborne M, Sykes J. 1986. Numerical modeling of immiscible organic transport at the Hyde-Park landfill. *Water Resources Research* 22: 25-33.
- Ouyang Y, Cho JS, Mansell RS. 2002. Simulated formation and flow of microemulsions during surfactant flushing of contaminated soil, *Water Research* 36: 33-40.
- Panday S, Wu YS, Huyakorn PS, Springer EP. 1994. A three-dimensional multiphase flow model for assessing NAPL contamination in porous and fractured media, 2. Porous medium simulation examples, *Journal of Contaminant Hydrology* 16: 131-156.
- Parker JC, Lenhard RJ. 1987. A model for hysteretic constitutive relations governing multiphase flow 1. Saturation-pressure relations, *Water Resources Research* 23: 2187-2196.
- Parker JC, Park E. 2004. Field-scale DNAPL dissolution kinetics in heterogeneous aquifers, *Water Resources Research*, 40, W05109, doi: 10.1029/2003WR002807.
- Pennell KD, Abriola LM, Weber WJ Jr. 1993. Surfactant-enhanced solubilization of residual dodecane in soil columns. 1. Experimental investigation. *Environmental Science and Technology* 27: 2332-2340.
- Phelan TJ, Lemke LD, Bradford SA, O'Carroll DM, Abriola LM. 2004. Influence of textural and wettability variations on predictions of DNAPL persistence and plume development in saturated porous media, *Advances in Water Resources* 27: 411-427.
- Pouslen MM, Kueper BH. 1992. A field experiment to study the behavior of tetrachloroethylene in unsaturated porous media, *Environmental Science and Technology* 26: 889-895.
- Powers SE, Loureiro CO, Abriola LM, Weber Jr WJ. 1991. Theoretical study of the significance of nonequilibrium dissolution of nonaqueous phase liquids in subsurface systems, *Water Resources Research* 27: 463-477.
- Powers SE, Abriola LM, Weber WJ Jr. 1992. An experimental investigation of nonaqueous phase liquid dissolution in saturated subsurface systems: Steady state mass transfer rates, *Water Resources Research* 28: 2691-2705.
- Powers SE, Abriola LM, Weber WJ Jr. 1994. An experimental investigation of nonaqueous phase liquid dissolution in saturated subsurface systems: Transient mass transfer rates, *Water Resources Research* 30: 321-332.

Powers SE, Nambi IM, Curry GW Jr. 1998. Non-aqueous phase liquid dissolution in heterogeneous systems: Mechanisms and a local equilibrium modeling approach, *Water Resources Research* 34: 3293-3302.

Pruess K, Battistelli A. 2003. TMVOC, a simulator for multiple volatile organic chemicals. TOUGH symposium, Berkely, CA 12-14 May 2003.

Ramsburg CA, Pennell KD, Abriola LM, Daniels G, Drummond CD, Gamache M, Hsu H-l, Petroskis E, Rathfelder KM, Ryder J, Yavaraski T. 2005. A pilot-scale demonstration of surfactant-enhanced PCE solubilization at the Bachman Road site: (2) System operation and evaluation, *Environmental Science and Technology*, 39: 1791-1801.

Ramsburg CA, Abriola LM, Pennell KD, Löffler FE, Gamache M, Amos BK, Petrovskis EA. 2004. Stimulated microbial reductive dechlorination following surfactant treatment at the Bachman road site. *Environmental Science and Technology* 38: 5902-5914 DOI: 10.1021/es049675i.

Rao P.S., J.W. Jawitz, G.C. Enfield, R.W. Falta, M.D. Annable, and A.L. Wood. 2002. Technology integration for contaminated site remediation: clean-up goals and performance criteria, In *Groundwater Quality: Natural and Enhanced Restoration of Groundwater Pollution*, edited by S. F. Thornton and S. E. Oswald, IAHS Publication No. 275, International Association of Hydrological Sciences, Wallingford, Oxfordshire, United Kingdom, 571-578.

Rao PSC, Jawitz JW. 2003. Comment on "Steady state mass transfer from single-component dense nonaqueous phase liquids in uniform flow fields" by T.C. Sale and D.B. McWhorter. *Water Resources Research* 39: 1068, doi: 10.1029/2001WR000599.

Rathfelder, K. and L.M. Abriola. 1998. The influence of capillarity in numerical modeling of organic liquid redistribution in two-phase systems, *Advances in Water Resources* 21: 159-170.

Rathfelder KM, Lang JR, Abriola LM. 2000. A numerical model (MISER) for the simulation of coupled physical, chemical and biological processes in soil vapor extraction and bioventing systems. *Journal of Contaminant Hydrology* 43: 239-270.

Rathfelder KM, Abriola LM, Taylor TP, Pennell KD. 2001. Surfactant enhanced recovery of tetrachloroethylene from a porous medium containing low permeability lenses: 2. Numerical simulations. *Journal of Contaminant Hydrology* 48: 351-374.

Rathfelder KM, Abriola LM, Singletary MA, Pennell KD. 2003. Influence of surfactant-facilitated interfacial tension reduction on chlorinated solvent migration in porous media: Observations and numerical simulations, *Journal of Contaminant Hydrology* 64: 227-252.

- Reitsma S, Dai QL. 2001. Reaction-enhanced mass transfer and transport from non-aqueous phase liquid source zones. *Journal of Contaminant Hydrology* 49: p. 49-66.
- Rivett MO, Feenstra S. 2005. Dissolution of an emplaced source of DNAPL in a natural aquifer setting, *Environmental Science and Technology* 39: 447-455, doi: 10.1021/es040016f.
- Roeder E, Falta RW. 2001. Modeling unstable alcohol flooding of DNAPL-contaminated columns, *Advances in Water Resources* 24: 803-819.
- Rogers B, Logan BE. 2000. Bacterial transport in NAPL-contaminated porous media. *Journal of Environmental Engineering* 126: 657-666.
- Ryoo D, Shim H, Arengi FLG, Barbieri P, Wood TK. 2001. Tetrachloroethylene, trichloroethylene, and chlorinated phenols induce toluene-o-xylene monooxygenase activity in *Pseudomonas stutzeri* OX1. *Applied Microbiology and Biotechnology* 56: 545-549.
- Saba T, Illangasekare TH. 2000. Effect of groundwater flow dimensionality on mass transfer from entrapped nonaqueous phase liquid contaminants, *Water Resources Research* 36: 971-979.
- Saenton S, Illangasekare TH, Soga K, Saba TA. 2002. Effects of source zone heterogeneity on surfactant-enhanced NAPL dissolution and resulting remediation endpoints *Journal of Contaminant Hydrology* 59: 27-44.
- Saenton S, Illangasekare TH. 2003. Evaluation of benefits of partial source zone treatment using intermediate-scale physical model testing and numerical analysis, in *Groundwater Engineering-Recent Advances*, (Kono, Nishigaki and Komatsu, eds.), 25-35.
- Sale TC, McWhorter DB. 2001. Steady state mass transfer from single-component dense nonaqueous phase liquids in uniform flow fields. *Water Resources Research* 37: 393-404.
- Sale TC, McWhorter DB. 2003. Reply to comment by P.S.C. Rao and J.W. Jawitz on "Steady state mass transfer from single-component dense nonaqueous phase liquids in uniform flow fields", *Water Resources Research* 39: 1068, doi: 10.1029/2001WR000599.
- Sardin M, Schweich D, Leij FJ, Van Genuchten MTh. 1991. Modeling the nonequilibrium transport of linearly interacting solutes in porous media: A review, *Water Resources Research* 27: 2287-2307.
- Schaerlaekens J, Mallants D, Simunek J, van Genuchten MTh, Feyen J. 1999. Numerical simulation of transport sequential biodegradation of chlorinated aliphatic hydrocarbons using CHAIN_2D. *Hydrological Processes*, 13: p. 2847-2859.

- Schink B. 1997. Energetics of syntrophic cooperation in methanogenic degradation. *Microbiology and Molecular Biology Reviews* 61: 262-280.
- Schwarzenbach RP, Gschwend PM, Imboden DM. 2003. *Environmental Organic Chemistry*. New York, NY: Wiley.
- Seagren EA, Rittmann BE, Valocchi AJ. 1994. Quantitative evaluation of the enhancement of NAPL-pool dissolution by flushing and biodegradation. *Environmental Science & Technology* 28: 833-839.
- Seagren EA, Rittmann BE, Valocchi AJ. 1993. Quantitative evaluation of flushing and biodegradation for enhancing in situ dissolution of nonaqueous-phase liquids. *Journal of Contaminant Hydrology* 12: 103-132.
- Seagren EA, Rittmann BE, Valocchi AJ. 2002. Bioenhancement of NAPL pool dissolution: experimental evaluation. *Journal of Contaminant Hydrology* 55: 57-85.
- Seki K, Miyazaki T. 2001. A mathematical model for biological clogging of uniform porous media. *Water Resources Research* 37: 2995-2999.
- Sharma PK, McCarty PL. 1996. Isolation and characterization of a facultatively aerobic bacterium that reductively dehalogenates tetrachloroethene to *cis*-1,2-dichloroethene. *Applied and Environmental Microbiology* 62: 761-765.
- Shim H, Ryoo D, Barbieri P, Wood TK. 2001. Aerobic degradation of mixtures of tetrachloroethylene, trichloroethylene, dichloroethylenes, and vinyl chloride by toluene-o-xylene monooxygenase of *Pseudomonas stutzeri* OX1. *Applied Microbiology and Biotechnology* 56: 265-269.
- Sleep BE, Sykes JF. 1993. Compositional simulation of groundwater contamination by organic compounds 1. Model development and verification, *Water Resources Research* 29: 1697-1708.
- Smatlak CR, Gossett JM, Zinder SH. 1996. Comparative kinetics of hydrogen utilization for reductive dechlorination of tetrachloroethene and methanogenesis in an anaerobic enrichment culture. *Environmental Science and Technology* 30: 2850-2858.
- Smidt H, de Vos WM. 2004. Anaerobic microbial dehalogenation. *Annual Reviews in Microbiology* 58: 43-73.
- Soerens TS, Sabatini DA, Harwell JH. 1998. Effects of flow bypassing and nonuniform NAPL distribution on the mass transfer characteristics of NAPL dissolution, *Water Resources Research* 34: 1657-1673.
- Statistix. 1996. *Statistix for Windows User's Manual*, Analytical Software, Tallahassee, FL.

Stroo, H.F., M. Unger, C.H. Ward, M.C. Kavanaugh, C. Vogel, A. Leeson, J.A. Marqusee, and B.P. Smith. 2003. Remediating chlorinated solvent source zones, *Environmental Science and Technology* 37: 224A-230A.

Sung Y, Ritalahti KM, Sanford RA, Urbance JW, Flynn SJ, Tiedje JM, Löffler FE. 2003. Characterization of two tetrachloroethene-reducing, acetate-oxidizing anaerobic bacteria and their description as *Desulfuromonas michignensis* sp. nov. *Applied and Environmental Microbiology* 69: 2964-2974

Tandoi V, DiStefano TD, Bowser PA, Gossett JM, Zinder SH. 1994. Reductive dehalogenation of chlorinated ethenes and halogenated ethanes by a high-rate anaerobic enrichment culture. *Environmental Science & Technology* 28: 973-979.

Taylor SW, Jaffe PR. 1990. Substrate and biomass transport in porous medium. *Water Resources Research* 26: 2181-2194.

Taylor SW, Milly PCD, Jaffe PR. 1990. Biofilm growth and the related changes in physical properties of a porous medium 2. Permeability. *Water Resources Research*, 26: 2161-2169.

Taylor TP, Pennell KP, Abriola LM, Dane JH. 2001. Surfactant enhanced recovery from a porous medium containing low permeability lenses 1. Experimental studies. *Journal of Contaminant Hydrology* 48: 325-350.

Terzenbach DP, Blaut M. 1994. Transformation of tetrachloroethylene to trichloroethylene by homoacetogenic bacteria. *FEMS Microbiology Letters* 123: 213-218.

Tonnaer H, Spuij F, Gerritse J, Gottschal JC. 1997. *Modeling of anaerobic dechlorination of chloroethenes for in situ bioremediation*, in *In-Situ and On-Site Bioremediation*, B.C. Alleman and A. Leeson, Editors. Battelle Press: Columbus, OH. p. 591-596.

Unger AJA, Forsyth PA, Sudicky EA. 1998. Influence of alternative dissolution models and subsurface heterogeneity on DNAPL disappearance times, *Journal of Contaminant Hydrology* 30: 217-242.

UTCHEM. 2000. *Version 9.0 Technical Documentation*, Center for Petroleum and Geosystems Engineering, The University of Texas at Austin, Austin, TX 78712.

Vandevivere P, Baveye P, deLozada DS, DeLeo P. 1995. Microbial clogging of saturated soils and aquifer materials: Evaluation of mathematical models. *Water Resources Research* 31: 2173-2180.

van Genuchten MTh. 1980. A closed-form equation for predicting the hydraulic conductivity of unsaturated soils. *Sci. Soc. Am J.* 44: 892-898.

- Vayenas DV, Michalopoulou E, Constantinides GN, Pavlou S, Payatakes AC. 2002. Visualization experiments of biodegradation in porous media and calculation of the biodegradation rate. *Advances in Water Resources* 25: 203-219.
- Verce MF, Ulrich RL, Freedman DL. 2000. Characterization of an isolate that uses vinyl chloride as a growth substrate under aerobic conditions. *Applied and Environmental Microbiology* 66: 3535-3542.
- Verce MF, Ulrich RL, Freedman DL. 2001. Transition from cometabolic to growth-linked biodegradation of vinyl chloride by a *Pseudomonas* sp. isolated on ethane. *Environmental Science and Technology* 35: 4242-4251.
- Verschueren K. 2001. *Handbook of environmental Data on organic chemicals (4th edition)*. New York: John Wiley & Sons.
- Vogel TM, Criddle CS, McCarty PL. 1987. Transformation of halogenated aliphatic compounds. *Environmental Science and Technology* 21: 722-736.
- Wagner C, Schafer W, Jager W, Wittum G, Kohlmeier E. 2002. Simulating a field case of reactive chloroethene transport. *Comput. Visual Sci.* 5: 149-163.
- Weber WJ, DiGiano FA. 1996. *Process Dynamics in Environmental Systems*. New York, New York: John Wiley & Sons, 943.
- White MD, Oostrom M, Lenhard RJ. 1995. Modeling fluid flow and transport in variably saturated porous media with the STOMP simulator, 1. Nonvolatile three-phase model description, *Advances in Water Resources* 18: 353-364.
- Whittaker J, Teutsch G, Grathwohl P. 2000. DNAPL spill and plume migration in a naturally heterogeneous aquifer analogue, *IAHS Publication No. 265*, 455-460.
- Wiedemeier TH, Rifai HS, Newell CJ, Wilson JT. 1999. *Natural attenuation of fuels and chlorinated solvents in the subsurface*. New York: John Wiley and Sons.
- Wilson DJ. 1989. Soil cleanup by in-situ surfactant flushing: 1. mathematical modeling, *Separation Science and Technology* 24: 863-892.
- Wilson DJ, Clarke AN. 1991. Soil cleanup by in-situ surfactant flushing. IV. A two component mathematical model, *Separation Science and Technology* 26: 1177-1194.
- Yang Y, McCarty PL. 1998. Competition for hydrogen within a chlorinated solvent dehalogenating anaerobic mixed culture. *Environmental Science and Technology* 32: 3591-3597.

Yang Y, McCarty PL. 2000. Biologically enhanced dissolution of tetrachloroethene DNAPL. *Environmental Science and Technology* 34: 2979-2984.

Yang Y, McCarty PL. 2002. Comparison between donor substrates for biologically enhanced tetrachloroethene DNAPL dissolution. *Environmental Science and Technology* 36: 3400-3404.

Yeh DH, Pennell KD, Pavlostathis SG. 1999. Effect of TWEEN surfactants on methanogenesis and microbial reductive dechlorination of hexachlorobenzene. *Environmental Toxicology and Chemistry* 18: 1408-1416.

Yu, S. and L. Semprini. 2004. Kinetics and modeling of reductive dechlorination at high PCE and TCE concentrations. *Biotechnology and Bioengineering* 88: 451-464.

Yu, S., M.E. Dolan, and L. Semprini. 2005. Kinetics and inhibition of reductive dechlorination of chlorinated ethylenes by two different mixed cultures. *Environmental Science & Technology*, 39: p. 195-205.

Zheng, C. and P.P. Wang. 1999. *MT3DMS: A modular three-dimensional multispecies transport model for simulation of advection, dispersion, and chemical reactions of contaminants in groundwater systems; Documentation and user's guide*. Contract Report SERDP-99-1, U.S. Army Engineer Research and Development Center, Vicksburg, MS.

Zhu J. and J.F. Sykes. 2000. The influence of NAPL dissolution characteristics on field-scale contaminant transport in subsurface, *Journal of Contaminant Hydrology* 41: 133-154.

Zhu J. and J.F. Sykes. 2004. Simple screening models of NAPL dissolution in the subsurface, *Journal of Contaminant Hydrology* 72: 245-258.

Zoller U. 1998. In situ bioremediation of residual entrapped NAPL in aquifers by a biodegradable nutrient-surfactant mix. In: *Soil and Aquifer Pollution* (Rubin H, Narkis N, Carberry J, eds). Heidelberg: Springer-Verlag, 322-334.

Zoller U, Rubin H. 2001. Feasibility of in situ NAPL-contaminated aquifer bioremediation by biodegradable nutrient-surfactant mix. *Journal of Environmental Science and Health – Part A* 36: 1451-1471.